DOE-ER-0313/50
Distribution
Categories
UC-423, -424

FUSION MATERIALS
SEMIANNUAL PROGRESS REPORT
FOR THE PERIOD ENDING

June 30, 2011

Prepared for
DOE Office of Fusion Energy Sciences
(AT 60 20 10 0)

DATE PUBLISHED: August 2011

Prepared by
OAK RIDGE NATIONAL LABORATORY
Oak Ridge, Tennessee 37831
Managed by
UT-Battelle, LLC
For the
U.S. DEPARTMENT OF ENERGY

FOREWORD

This is the fiftieth in a series of semiannual technical progress reports on fusion materials science activity supported by the Fusion Energy Sciences Program of the U.S. Department of Energy. It covers the period ending June 30, 2011. This report focuses on research addressing the effects on materials properties and performance of exposure to the neutronic, thermal and chemical environments anticipated in the chambers of fusion experiments and energy systems. This research is a major element of the national effort to establish the materials knowledge base for an economically and environmentally attractive fusion energy source. Research activities on issues related to the interaction of materials with plasmas are reported separately.

The results reported are the products of a national effort involving a number of national laboratories and universities. A large fraction of this work, particularly in relation to fission reactor irradiations, is carried out collaboratively with partners in Japan, Russia, and the European Union. The purpose of this series of reports is to provide a working technical record for the use of program participants, and to provide a means of communicating the efforts of fusion materials scientists to the broader fusion community, both nationally and worldwide.

This report has been compiled under the guidance of F. W. (Bill) Wiffen and Betty Waddell, Oak Ridge National Laboratory. Their efforts, and the efforts of the many persons who made technical contributions, are gratefully acknowledged.

G. R. Nardella
Research Division
Office of Fusion Energy Sciences

TABLE OF CONTENTS

1. FERRITIC/MARTENSITIC STEELS

See also items 4.1, 5.1, and 8.1.

1.1 Selected Reduced Activation Ferritic-Martensitic (RAFM) Steels For HFIR Experiments JP-30/31 — 1
L. Tan (Oak Ridge National Laboratory)

Three heats of RAFM steels were selected for HFIR experiments. A modified-NF616 was also selected for comparison. Tensile tests of the heats were performed at temperatures of 23°C, 300°C, 400°C, and 650°C, which showed tensile properties comparable to the oxide dispersion strengthened (ODS) steel PM2000. Microstructural analysis indicates that fine lath boundaries with nano-precipitates had been developed in the heats by the specific thermomechanical treatment.

1.2 On the Structure and Chemistry of Complex Oxide Nanofeatures in Nanostructured Ferritic Alloy U14YWT — 5
D. Bhattacharyya, P. Dickerson, S. A. Maloy, A. Misra, M. A. Nastasi *(Los Alamos National Laboratory)* and G. R. Odette *(University of California Santa Barbara)*

The remarkable radiation damage resistance of nanostructured Ferritic alloys (NFAs) is attributed to the large numbers of matrix nano-features (NFs) of various types, which can enhance the recombination of displacement defects and trap transmutant helium in fine scale bubbles. Conventional and high resolution transmission electron microscopy and energy dispersive spectroscopy were used to characterize the various types of NF and larger oxide phases in a model 14Cr-3W-0.4Ti-0.25Y_2O_3 NFA (14YWT) Hot Isostatic Pressed (HIP-ed) at 1150°C. Large $CrTiO_3$ precipitates (50-300 nm) and small diffracting NFs (< 5 nm) were found in this alloy. One major new result is the observation of an additional type of nano-feature (10-50 nm), orthorhombic in structure, with a square center cross section, that constitutes a new kind of Y-Ti oxide phase with lattice parameters different from those of known Y and Ti complex oxides. The interfaces of these particles seem to be semicoherent, while manifesting a possible orientation relationship with the BCC matrix. The ratio of Y to Ti varies between < 1 and 2 for these larger NFs.

1.3 Transmission Electron Microscopy Characterization of the Structure and Composition of the Nanofeatures in Nanostructured Ferritic Alloy MA957 — 25
Y. Wu, E. Haney, N. Cunningham and G. R. Odette *(Univ. of California Santa Barbara)*

Bright field transmission electron microscopy (TEM), high resolution TEM (HRTEM), scanning TEM (STEM) and energy dispersive X-ray (EDX) spectroscopy were combined to comprehensively characterize the Ti-Y-O enriched nano-scale features (NF) in a nanostructured ferritic alloy (NFA), MA957. The characterization included the NF number densities, size distributions, volume fractions, crystal structures and compositions. In foil

TABLE OF CONTENTS

measurements were complemented by studies of NF on extraction replica foils. The conditions examined included: two heats of extruded MA957; one of these heats following long-term thermal aging at 1000°C for 19.53 kh; and two friction-stir-weld variants. The study revealed the presence of diffracting complex oxide phases that varied somewhat with the feature size. However, the smallest features, with diameters (d) < 5 nm, were found to be consistent with cubic pyrochlore $Y_2Ti_2O_7$ complex oxides with average Y/Ti ratios of ≈ 1. Long-term thermal aging coarsened the NF, while friction stir welding had relatively little effect on their number density and size distribution.

APT studies were carried out at the University of California Santa Barbara (UCSB), University of Leoben (UL) in Austria, Oxford University (OU) in England and University of Rouen (UR) in France. The tools used at UCSB, OU and LU were all Cameca (previously Imago) HR3000X-HR Local Electrode Atom Probes (LEAPs), while the fourth instrument at Rouen was a Camaca Laser Assisted Wide Angle Tomographic Atom Probe (LAWATAP). The measurements reported by the various APT groups are in remarkable agreement with one another. The bulk average compositions (at.%) for Fe, Cr, Ti, Y and O are: 83.6±0.39, 14.8±0.46, 0.771±0.059, 0.064±0.022 and 0.273±0.031, respectively. The corresponding matrix Fe, Cr, Ti, Y and O are, respectively: 84.1±0.283, 14.7±0.212, 0.636±0.021, 0.017±0.001 and 0.109±0.020. The average NF compositions, based only on their Y, Ti and O contents (at.%), are 13.9±0.92 Y, 41.6±3.34 Ti and 45.4±4.77 O, respectively. The corresponding average NF number density (N) and average diameter (<d>) are: $5.1\pm1.06\times10^{23}/m^3$ and 2.72±0.56 nm, respectively.

The effects of bulk O variations on the characteristics of the grain structure, nanofeatures (NFs) and microhardness of nanostructured ferritic alloys (NFA) were investigated. The grain structures were characterized by optical metallography and transmission electron microscopy (TEM). The NFs were characterized by TEM, atom probe tomography (APT) and small angle neutron scattering (SANS). Based on bulk chemical analysis of the milled powders, the O content ranged from 0.065 to 0.249 (wt.%). The variations in O resulted from differences in the milling conditions. The low O powders (OW3) were milled with a procedure that minimized contamination, while the high O powders (OW1), that initially had a low O content in the as atomized condition, were contaminated with both N and O during milling. The intermediate O powders (OW4) minimized this contamination while increasing O with additions of FeO during milling. The three powder batches were all consolidated by hot

TABLE OF CONTENTS

isostatic pressing (HIPing) at 1150°C and 200 MPa. All the consolidated alloys had bimodal distributions of grain sizes, that were characterized by the two average large and small sizes ($d_{s,l}$) and the relative fraction of the small grains (f_s). The NFs were Y-Ti-O enriched phases characterized by their number density (N), size distributions and average diameter (<d>), composition (especially the Y/Ti ratio) and phase structure (not evaluated in this study). Both the large and small grain sizes decreased with increasing O contents, while the fraction of small grains increased. The size of the NFs decreased and their number density increased with increasing O. TEM energy dispersive x-ray (EDX) studies indicated the low O alloy contained fewer and coarser features compared to alloys with higher O. TEM showed that the low O features were much more highly enriched in Y compared to Ti, including a majority that contained no Ti. However, APT showed that NFs in the low O alloy with <d> ≈ 5 nm had Y/Ti ratios < 1 that is only slightly larger than found in the other cases. The Vickers microhardness (H_v) of the alloys increased significantly with increasing O, reflecting both the effects of differences in the grain size and scale dispersion strengthening features. The H_v increased systematically with the volume fraction of NFs measured by SANS.

1.6 **Effects of Neutron Irradiation on Hardness Properties of Friction Stir Processed ODS Ferritic Steel** — **58**
Sanghoon Noh (Kyoto University), M. A. Sokolov (Oak Ridge National Laboratory), Ryuta Kasada, Akihiko Kimura (Kyoto University) and Takuya Nagasaka (National Institute for Fusion Science)

Oxide dispersion strengthened ferritic steels (ODS-FS) have been considered as one of the most promising structural materials for advanced nuclear systems such as fusion reactors and next generation fission reactors, because of its excellent elevated temperature strength, corrosion and radiation resistance. Especially, irradiation resistance is a critical issue for the high performance of ODS-FS. In this study, effects of the irradiation on hardness properties of friction stir processed (FSP) ODS-FS were investigated. FSP technique was employed on ODS-FS. A plate specimen was cut out from the cross section and irradiated to 1.2 dpa at 573K in the High Flux Isotope Reactor (HFIR). To investigate the effect of neutron irradiation on processed area, the hardness distributions were evaluated on the cross section. Hardness of FSP ODS-FS was various with each microstructure after irradiation to 1.2 dpa at 573K. The increase of Vickers hardness was significant in the stirred zone and heat affected zone. Base material exhibited the lowest hardening about 38HV. Since nano-oxide particles in stirred zone showed identical mean diameter and number density, it is considered that hardening differences between stirred zone and base material is due to differences in initial dislocation density.

1.7 **Joining of 14YWT and F82H by Friction Stir Welding** — **62**
D. T. Hoelzer, M. A. Sokolov and Z. Feng, ORNL

A sample was prepared for the initial joining study using friction stir welding (FSW) that consisted of 4 specimens of the advanced oxide dispersion strengthened (ODS) 14YWT-SM6 ferritic alloy, 15 mm long, 6 mm wide and 2.86 mm thick each, that were spot welded in a corresponding slot that was machined in an F82H plate. The FSW run was successfully performed on the sample using a polycrystalline boron nitride tool (PCBN) that resulted in joints showing good bonding between specimens of 14YWT-SM6 and between 14YWT-SM6 and F82H. The joints were characterized by light microscopy and SEM analysis and were observed to be relatively narrow in width. However, porosity was observed in the thermomechanically affected zone (TMAZ) of 14YWT-SM6 on the advancing side of the FSW joint and at the interface between F82H and 14YWT-SM6. Further refinements in the FSW process will be required to minimize defects including porosity.

2. CERAMIC COMPOSITE STRUCTURAL MATERIALS

See also items 5.1 and 8.2.

2.1 Tensile Properties of Unidirectional CVI SIC/SIC Minicomposites with a Multilayer interphase and Near-Stoichiometric SIC Fibers — **76**
K. Ozawa, Y. Katoh, L. L. Snead (Oak Ridge National Laboratory), T. Nozawa, H. Tanigawa (Japan Atomic Energy Agency)

Tensile properties of unidirectional single tow SiC/SiC minicomposites reinforced with Hi-Nicalon™ Type-S and Tyranno™-SA3 were evaluated. The interphase structure was pyrolytic carbon (PyC) / SiC multilayer and the thickness of the innermost PyC layer was varied (~70, ~240 and ~1150 nm). Only the Hi-Nicalon Type-S minicomposites with ~240 and ~1150 nm-thick PyC interphases exhibited the pseudo-ductile behavior; others reinforced with Tyranno-SA3 and the Hi-Nicalon Type-S composite with 70 nm-thick PyC interphase underwent brittle to near-brittle fracture behavior. The brittle failure behavior for those composites was attributed primarily to the quite low fiber volume fraction (5-10%). The Hi-Nicalon Type-S minicomposites with ~240 nm-thick PyC interphase exhibited ultimate tensile strength equivalent to 79-104% of the fiber bundle strength but only 70-85% of the strength for the ~1150 nm interphase for a given gauge length. Based on the analysis of the hysteresis loops recorded during the tensile loading and unloading sequences, the sliding stress estimated for the ~1150 nm-thick interphase appeared to be about 0.7 times that of the ~240 nm-thick interphase. This shows that both composites satisfied the global load sharing condition, but the composite with the thicker interphase could not achieve its fiber bundle strength, probably due to the lower interfacial sliding stress.

2.2 Low Activation Joining of SiC/SiC Composites for Fusion Applications — **87**
C. H. Henager, Jr., R. J. Kurtz (Pacific Northwest National Laboratory, Richland, WA 99336, USA), and M. Ferraris, (Politecnico di Torino, Torino, Italy)

The use of SiC composites in fusion environments likely requires joining of plates using reactive joining or brazing. One promising reactive joining method uses solid-state displacement reactions between Si and TiC to produce Ti_3SiC_2 + SiC. We continue to explore the processing envelope for this joint for the TITAN collaboration in order to produce optimal joints to undergo irradiation studies in HFIR. The TITAN collaboration has designed miniature torsion joints for preparation, testing, and irradiation in HFIR. PNNL synthesized 40 miniature torsion joints and several were tested for shear strength prior to irradiation testing in HFIR. The resulting tests indicated that 1) joint fixture alignment problems cause joint strengths to be lower than optimal, 2) that non-planar torsion test failures may limit th

TABLE OF CONTENTS

TABLE OF CONTENTS

4. OTHER STRUCTURAL AND SPECIAL PURPOSE MATERIALS

4.1 Effects of Neutron Irradiation on Hardness of W-ODS Ferritic Steel Joints — Sanghoon Noh (Kyoto University), M. A. Sokolov (Oak Ridge National Laboratory), Ryuta Kasada, Akihiko Kimura (Kyoto University) and Takuya Nagasaka (National Institute for Fusion Science) **111**

In present study, the effects of neutron irradiation on the hardness of W-coated ODS steels were investigated. Vacuum plasma spraying (VPS) technique was employed to fabricate W layer on the surface of substrates. Substrate materials were K1-, K4-ODS ferritic steels and F82H steel, which are 3mm thick plates. Tungsten powder of 99.9% high purity was used for VPS process. The powders were sprayed by the plasma jet of argon and hydrogen mixture to the surface of substrates pre-annealed at 773K. VPS-W coated specimens were irradiated at 723K to 4.5, 9.6 dpa in the High Flux Isotope Reactor (HFIR), respectively. To investigate the effect of neutron irradiation on joint area, the hardness distributions were evaluated on the cross section using a micro Vickers hardness tester. Microstructure analysis revealed that W was successfully coated on each substrate by VPS process, in spite of mismatch of the CTE between these materials. The hardness of W was significantly varied from 260 to 480Hv because inhomogeneous cooling rate during the process. After irradiations, irradiation hardening was occurred in the VPS-W, while substrate materials did not.

5. CORROSION AND COMPTIBILITY

5.1 COMPATIBILITY OF MATERIALS EXPOSED TO ISOTHERMAL Pb-Li — B. A. Pint and K. A. Unocic (Oak Ridge National Laboratory, USA) **115**

Characterization of wrought and oxide dispersion strengthened (ODS) Fe-Cr alloys after exposure to Pb-Li in isothermal capsule experiments is in progress. Oxide precipitates appear to coarsen near the surface perhaps due to the loss of metallic substrate. To further investigate the performance of Al-rich coatings, a time series of exposures in Pb-Li is being conducted and results are compared to observations for uncoated Fe-Cr specimens. Measurement of the Al profile after 500h suggests that there is an initial Al loss from the coating on exposure. Dissimilar metal experiments with SiC capsules and Fe and SiC specimens have been completed and the mass change data suggests a large difference in behavior for the Fe specimens after 1000h at 700°C. Unfortunately, the SiC specimens chipped during loading/unloading resulting in unreliable mass change data.

TABLE OF CONTENTS

In order to further understand the behavior of specimens exposed in the loop, microstructural characterization is being performed on the V-4Cr-4Ti tensile specimens that showed dynamic strain aging at 500°C. Initial results are presented. Also, further characterization on the dual layer MHD coatings is planned.

6. THEORY AND MODELING

The properties of ½<111> screw dislocations in $W_{1-x}Tm_x$ alloys with different transition metal, Tm, concentrations within the local density approximation of density functional theory was investigated. The electronic structure of alloys was described within the virtual crystal approximation. It was demonstrated that alloying of W with transition metals from group VIII modifies the properties of screw dislocation similar to the effect of alloying with Re. Specifically, the alloying changes the dislocation core from symmetric to asymmetric and reduces the value of the Peierls barrier and Peierls stress. These modifications are caused by filling of d-electron states of W.

The thermal desorption spectra of helium from single crystalline iron samples was obtained as a function of implantation conditions using the Berkeley thermal helium desorption spectroscopy (THDS). The implantation conditions were He ion implantation energies of 10, 20, or 40 keV at a consistent dose level $1x10^{15}$ He/cm^2. Constant rate heating ramps were employed to thermally desorb the implanted helium. The present results, in which the single crystalline iron has a lower carbon content, indicate a significant effect of carbon on the helium desorption behavior, when compared to our previous measurements. The results

TABLE OF CONTENTS

indicate that major helium releasing peaks of the iron samples with higher purity show up at lower temperatures. A spatially dependent cluster dynamics model is utilized to reproduce the helium spectrum in BCC region. Meanwhile it provides an opportunity to optimize the basic thermodynamic and kinetic energy parameters of helium and small helium-vacancy clusters. The combination of the modeling and THDS measurement allows identification of possible mechanisms (e.g. shrinkage of He_3V_2) responsible for the measured helium desorption peaks. Furthermore, the model is also used to predict the depth dependence of helium and helium-defect clusters as a function of time and temperature during the THDS measurement. The samples with the implantation condition of 40 keV, $1x10^{15}$ He/cm^2 have been measured by positron annihilation spectroscopy, as an initial attempt to correlate a second experimental technique of the vacancy cluster population against the modeling predictions. Good agreement is obtained between the positron lifetime analysis and the modeling calculation. The recent work provided an overview of the self-consistency of the model predictions based on the assumptions made in the helium-point defect binding and interaction energies and diffusivities.

In a recent coordinated effort, we have studied defect cluster dynamics in nanometer-thick molybdenum foils under 1 MeV Krypton ion irradiation at 80°C through both cluster dynamics computation and in-situ TEM experiments. By making direct one-to-one comparisons with experimentally observed cluster number density and size distribution as functions of foil thickness and irradiation dose and dose rate, significant validation and optimization of the model have been conducted in terms of both physical contents (damage production mode, identities of mobile defects) and parameterization (diffusivities of mobile defects). The optimized model exhibits excellent agreement with the current set of experiments both qualitatively and quantitatively, while further validation of the model and parameterization will continue to be pursued in the future with respect to Kr ion irradiation at varied temperatures and neutron irradiations on Mo.

7. IRRADIATION AND EXPERIEMNTAL METHODS AND ANALYSIS

No contributions this period.

8. IRRADIATION EXPERIMENTS AND TEST MATRICES

An experiment has been designed, fabricated and assembled to irradiate disk compact tension (DCT) specimens of F82H in the flux trap of the High Flux Isotope Reactor (HFIR).

TABLE OF CONTENTS

Twelve DCT specimens with an outer diameter of 12.5 mm are exposed directly to HFIR coolant flow. The specimens are separated by perforated spacers to ensure cooling flow to the upper and lower surfaces of the specimens. Another experiment will use a perforated capsule to irradiate bend bar and tensile specimens to supplement this irradiation experiment, and provide the other specimen geometries for comparison with the DCT specimen data.

In order to examine the high-dose and high-temperature neutron irradiation effects on (1) mechanical properties of SiC, SiC/SiC composites and the fiber/matrix (F/M) interface, and (2) microstructural change of pyrolytic carbon (PyC) as the F/M interphase, new HFIR irradiation experiments were planned. Two types of rabbit capsules were designed: (1) composites' compact flexure rabbits for macro-strength evaluation and (2) mini-composites' rabbits for the F/M interfacial evaluation.

1.1 Selected Reduced Activation Ferritic-Martensitic (RAFM) Steels For HFIR Experiments JP-30/31 — L. Tan (Oak Ridge National Laboratory)

OBJECTIVE

Characterize the tensile properties and microstructure of selected RAFM steels to ensure their initial condition suitable for neutron irradiation assessment and prepare specimens for the HFIR experiments JP-30/31.

SUMMARY

Three heats of RAFM steels were selected for HFIR experiments. A modified-NF616 was also selected for comparison. Tensile tests of the heats were performed at temperatures of 23°C, 300°C, 400°C, and 650°C, which showed tensile properties comparable to the oxide dispersion strengthened (ODS) steel PM2000. Microstructural analysis indicates that fine lath boundaries with nano-precipitates had been developed in the heats by the specific thermomechanical treatment.

PROGRESS AND STATUS

Introduction

The fast decay characteristics of induced radioactivity in RAFM steels have promoted the development of this category of FM steels. The Japanese F82H and the European heat EUROFER 97 are two promising examples of RAFM steels. Recent FM steel development at ORNL showed significant strengthening capability by means of specific thermomechanical treatment (TMT) [1]. This approach is also applicable to RAFM steels, which had shown refined lath boundaries and precipitates, leading to enhanced hardness and tensile properties [2]. However, irradiation resistance of the RAFM steels needs to be assessed. Progress of the neutron irradiation experiments using HFIR at ORNL is reported here.

Heats Preparation and Evaluation

Three RAFM steels, together with a modified-NF616 steel, were selected for the HFIR experiments JP30/31. Their nominal compositions in weight percentage (wt%) are listed in Table 1. The steels were in wrought condition. To produce expected FM microstructure, specific TMTs were applied to wrought steels. The selection of normalization and tempering temperatures of the steels was guided by computational thermodynamics. Using heat 1539 as an example, Figure 1 shows the calculated phase mole fraction as a function of temperature. The heat 1539 was normalized at 1100°C for 1 h followed by tempering at 750°C and air cooling. A deformation of ~60% was applied to the heat at the normalization temperature to refine microstructure and promote precipitation.

Table 1. Nominal composition (wt%) of the heats.

Heat	Cr	Mn	V	Si	W	Ta	Mo	Nb	Ni	Cu	C	N
1537	9.0	0.5	0.3	0.25	1.1						0.02	0.06
1538	9.0	0.5	0.3	0.25	1.1	0.1					0.02	0.06
1539	9.0	0.5	0.3	0.25	1.1	0.1					0.1	0.06
Modified-NF616	8.5	0.4	0.3	0.15	2.2		0.1	0.1	0.4	0.1	0.01	0.08

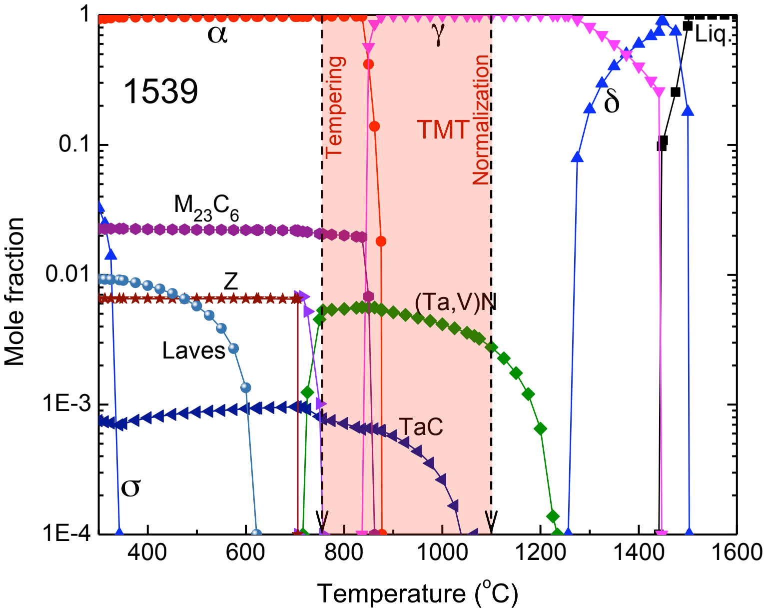

Figure 1. Example of calculated mole fraction of phases in heat 1539 as a function of temperature.

The microstructure of the processed heats was characterized by optical microscopy and transmission electron microscopy (TEM). The optical images (not shown here) showed typical FM microstructure with prior-austenite grains and dense lath packets and boundaries in the samples. Figure 2 shows the TEM images in both bright-field (BF) and dark-field (DF) mode of the heats 1538, 1539, and modified-NF616. In addition to the fine lath boundaries, many (Ta,V)N and (Nb,V)N in nanometers and Cr-rich carbides in sub-micrometers were developed in the materials. Additionally, ultra-fine nano-precipitates with a density in the order of 1022/m3 were observed in the heats 1538 and modified-NF616, as shown in their respective DF images, which may benefit irradiation resistance. The chemical composition of these ultra-fine nano-precipitates was not able to be characterized. Unlike the ultra-fine nano-precipitates primarily decorating lath boundaries as shown in the DF image of the heat 1538, the ultra-fine nano-precipitates are dispersed in the matrix of the modified-NF616.

Miniature tensile specimens (type SS-J3: 16 x 4 x 0.76 mm) were prepared from the processed heats using electric discharge machining (EDM) for tensile tests. Figure 3 shows the yield strength and total elongation of the specimens tested at 23°C, 300°C, 400°C, and 650°C that are consistent with the targeted neutron irradiation temperatures. The results of F82H [3], NF616 [4], and ODS steel PM2000 [5] are also included in Figure 3 for comparison. The samples of the RAFM heats and the modified-NF616 showed tensile properties comparable to the ODS steel PM2000 and greater strength than the F82H and NF616.

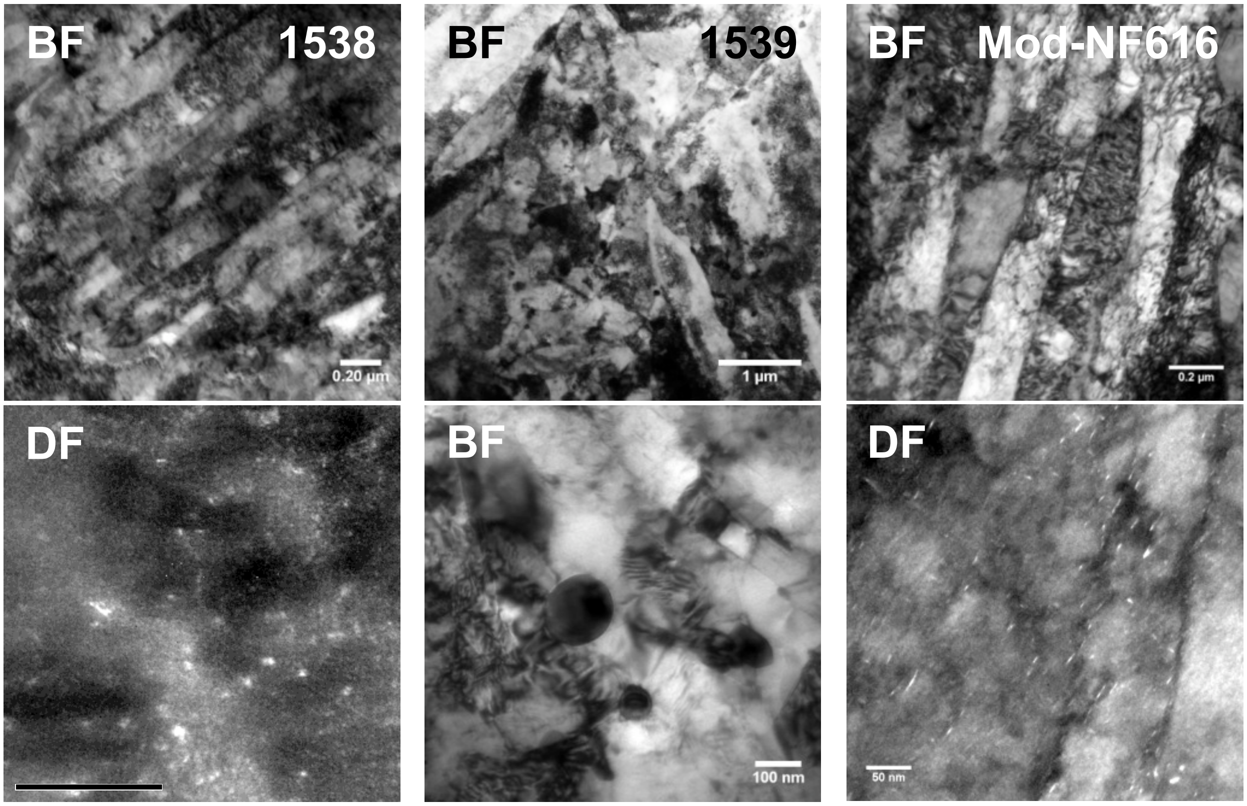

Figure 2. Bright-field (BF) and dark-field (DF) TEM images of heats 1538, 1539, and modified-NF616 at low (upper row) and high (lower row) magnifications.

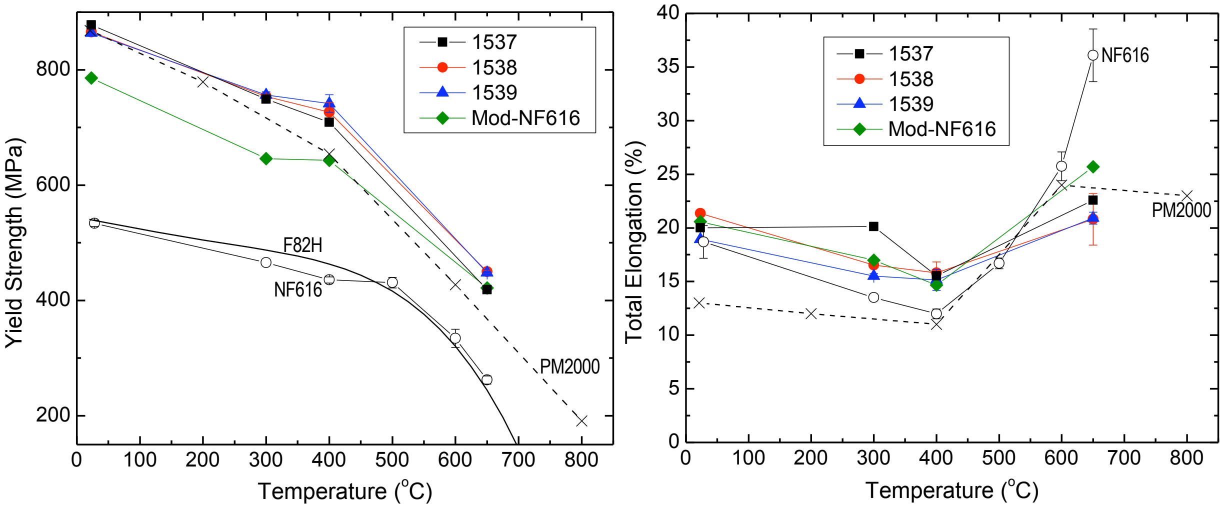

Figure 3. Yield strength and total elongation of the heats 1537, 1538, 1539, and modified-NF616.

Specimens Preparation for the HFIR Experiments JP-30/31

Four types of specimens were prepared for the HFIR experiments JP-30/31 using EDM. They are type SS-J3 miniature tensile specimens, 3-notch or 5 notch bend bars (M3PCCVN 36 x 3.3 x 1.65 mm and M5PCCVN 54 x 3.3 x 1.65 mm), specimens for preparing atom probe samples (APFIM 16 x 1.14 x 0.5 mm), and TEM disks (∅3 x 0.25 mm). The numbers of the specimens for the four heats (1537, 1538, 1539, and modified-NF616) are listed in Table 2.

Table 2. Specimens prepared for the HFIR experiments JP-30/31.

JP30/31	Specimen Type	Heat 1539	1538	1537	Mod-NF616	Total Number
300°C	SS-J3	4	3	3		10
	M3PCCVN	3	3	3		9
	APFIM	1	1	1	1	4
	TEM disk	3	3	3	3	12
400°C	SS-J3	3	3	2		8
	M5PCCVN	2				2
	APFIM	1	1	1	1	4
	TEM disk	3	3	3	3	12
650°C	SS-J3	2	2	2		6
	M5PCCVN	2				2
	APFIM	1	1	1	1	4
	TEM disk	3	3	3	3	12

REFERENCES

[1] R. L. Klueh, N. Hashimoto, P. J. Maziasz, *Scripta Mater.* **53** (2005) 275-280.
[2] L. Tan, D. T. Hoelzer, J. T. Busby, M. A. Sokolov, R. L. Klueh, submitted to *J. Nucl. Mater.* 2011.
[3] S. J. Zinkle, J. P. Robertson, R. L. Klueh, Fusion Materials - Semiannual Progress Report for Period Ending June 30, 1998 (DOE/ER-0313/24), pp. 135-143.
[4] L. Tan, J. T. Busby, P. J. Maziasz, Y. Yamamoto, submitted to *J. Nucl. Mater.* 2011.
[5] R. L. Klueh, J. P. Shingledecker, R. W. Swindeman, D. T. Hoelzer, *J. Nucl. Mater.* **341** (2005) 103-114.

1.2 On the Structure and Chemistry of Complex Oxide Nanofeatures in Nanostructured Ferritic Alloy U14YWT

— D. Bhattacharyya, P. Dickerson, S. A. Maloy, A. Misra, M. A. Nastasi *(Los Alamos National Laboratory)* and G. R. Odette *(University of California Santa Barbara)*

OBJECTIVE

The objective of this work is to characterize the different types of precipitates in a UCSB model nanostructured ferritic alloy U14YWT, in the hot-isostatically pressed condition, in order to understand their distribution, morphology, chemical composition and crystal structure.

SUMMARY

The remarkable radiation damage resistance of nanostructured Ferritic alloys (NFAs) is attributed to the large numbers of matrix nano-features (NFs) of various types, which can enhance the recombination of displacement defects and trap transmutant helium in fine scale bubbles. Conventional and high resolution transmission electron microscopy and energy dispersive spectroscopy were used to characterize the various types of NF and larger oxide phases in a model 14Cr-3W-0.4Ti-0.25Y_2O_3 NFA (14YWT) Hot Isostatic Pressed (HIP-ed) at 1150°C. Large $CrTiO_3$ precipitates (50-300 nm) and small diffracting NFs (< 5 nm) were found in this alloy. One major new result is the observation of an additional type of nano-feature (10-50 nm), orthorhombic in structure, with a square center cross section, that constitutes a new kind of Y-Ti oxide phase with lattice parameters different from those of known Y and Ti complex oxides. The interfaces of these particles seem to be semicoherent, while manifesting a possible orientation relationship with the BCC matrix. The ratio of Y to Ti varies between < 1 and 2 for these larger NFs.

BACKGROUND

The compelling need to reduce mankind's reliance on fossil fuels and the consequent deleterious effects on the environment, while meeting a rapidly growing demand for energy has generated a worldwide interest in advanced fission and fusion energy [1-2]. The viability of nuclear energy systems will ultimately depend on developing new high performance structural materials that can provide extended life under extremely hostile conditions, characterized by combinations of high temperatures, large time varying stresses, chemically aggressive environments and intense neutron radiation fields [1, 3]. The lifetime goals for some reactor components will require tolerance of up to 400 displacements-per-atom (dpa). Displacement damage produces excess concentrations of defects consisting of vacancies and self-interstitial atoms (SIAs). Neutron irradiation also generates a wide range of transmutation products, most notably insoluble helium. These sources of primary damage interact to drive complex microstructural, dimensional and microchemical evolutions, which in turn typically degrade a host of performance-sustaining material properties [1, 3-4]. Complex irradiation effects depend on the *combination* of the irradiation temperature, dpa, dpa rate and He/dpa ratio, as well as the composition and starting microstructure of the material.

We focus here on potentially transformational nanostructured ferritic alloys (NFAs) that show promise of meeting many of these challenges. Note that NFAs derive from earlier roots in oxide dispersion strengthened (ODS) steels (an example is PM2000 [5]). As discussed in recent review articles [3, 6] and the references contained therein, NFAs manifest high tensile, creep and fatigue strengths, unique thermal stability and show a remarkable tolerance to neutron irradiation. The outstanding characteristics of NFAs derive primarily from the presence of a high density of nm-scale Y-Ti-O rich nanofeatures (NFs) that range in size from ≈ 1 to 50 nm. The NFs enhance SIA-vacancy recombination; and, perhaps most importantly, trap helium in small, high-pressure gas bubbles [7]. These bubbles reduce the amount of helium reaching grain boundaries, thus mitigating toughness loss at lower temperatures, and potential degradation of creep rupture properties at higher temperature. In principle, helium trapped in a high concentration of extremely small bubbles also reduces all other manifestations of radiation damage, including void swelling, that occur in other alloys [3, 6-8]. Another great advantage of having the NFs dispersed in the Fe matrix is that they impede dislocation climb and glide, and thus improve their strength and creep resistance. The high creep strength of these materials allows their use at high temperatures above the displacement damage regime. The effect of a high density of Y-Ti-O rich nano-clusters on the high temperature strength of ferritic alloys was studied in detail by Hoelzer, Miller et al [9] and it was shown that nano-clusters improved the high-temperature strength of these alloys significantly. These nano-features were found to be extremely stable with respect to temperature, and they were present in a high number density even after 24 hrs at 1300 °C in 12YWT, 14YWT and MA957 in atom-probe studies by Miller et al. [10].

NFAs are typically processed by ball milling pre-alloyed rapidly solidified metal and yttria (Y_2O_3) powders [3]. Proper milling effectively dissolves the Ti, Y and O solutes that then precipitate as NFs during hot consolidation by extrusion, or hot isostatic pressing (HIPing). Powder consolidation is usually followed by a series of deformation processing steps. Various studies have shown that there is not a single type of NF, but rather what might best be described as an NF zoo, even in a single alloy, like MA957 [3, 6]. The detailed characteristics of the NFs vary even more from alloy to alloy, since they are very sensitive to composition and processing variables. For example, the number density and volume fraction of NFs increase, while their sizes decrease, at higher consolidation temperatures [3, 6, 11]. Further, Ti is needed to form small NFs at higher consolidation temperatures [11]. Thus one critical objective is identifying the structure, composition and interface structures, that is the 'character', of various NFs. Such information is crucial to the development of a knowledge base for alloy optimization. A substantial body of work exists on the characterization of these NFs using atom probe tomography (APT) – see, e.g., [12-13]

It is the authors' view that the ability of NFs to trap and form fine scale He bubbles is expected to depend not only on their number densities and size distributions, but also on their interfacial and elastic properties. In particular, recent experiments and atomistic models have shown that the geometry and the atomic structure of interfaces play an important role in improving the radiation tolerance of materials [14-16]. It is crucial to understand the crystal structure, crystallography and interface properties of all nano-scale oxides in ODS-steels as opposed to focusing only on the 2-5 nm particles and ignoring everything else in the microstructure. It is conceivable that the 20 nm particles may have an interface structure that may be a stronger sink for defects than the 2-5 nm particles. The only way to know this is to understand in detail all the particles and then in future work, model the structure of the interfaces and their sink strength. Some recent TEM characterization of nano-scale precipitates in ferritic steels of somewhat different composition than that in the present work has been done by Klimiankou et al. [17-18], which demonstrates the effect of larger particles on inert gas entrapment. In this paper, the authors show that there are three types of NFs in a model Fe-14Cr-3W-0.4Ti-0.25Y_2O_3 alloy (called U14YWT) that was HIPed at 1150°C. The structure and chemistry of these three types of NFs are characterized using various TEM techniques, with particular focus on the 10-50 nm sized nano-feature class, which exhibits a hitherto unobserved crystal structure for such precipitates.

EXPERIMENTAL METHODS

Materials

U14YWT was prepared at UCSB by mechanically alloying atomized powders of Fe - 14 wt% Cr - 3 wt% W - 0.4 wt% Ti with 0.25 wt% Y_2O_3 in a ball mill attritor at ambient temperature for 10 hrs in a dry Ar atmosphere [11, 19]. The milled powder were then vacuum degassed and canned prior to hot isostatic pressing (HIPing) to full consolidation at 1150°C and 200 MPa for 3 h. This U14YWT is part of a much larger matrix of model alloys issued to study NFs and NF thermokinetics using a variety of characterization techniques [3, 11, 19].

Transmission Electron Microscopy (TEM)

In this work TEM specimens were prepared using a dual beam focused ion beam (FIB) FEI DB235™ instrument. Low energies down to 10 keV were used to perform final polishing of the sample, with very low currents (500 pA). In some instances, the FIB-ed sample was thinned further using a Gatan® PIPS™ precision ion mill at 2 keV. Subsequently, the samples were cleaned using a plasma cleaner with Ar gas.

The FIB-ed samples were then examined using an FEI Tecnai F30™ TEM operated at 300 kV. Energy dispersive X-ray spectroscopy (EDS) was used to measure the composition of the precipitates in the scanning transmission (STEM) mode. A relatively small spot size (no. 6) and a strong gun lens condition (no. 6) were maintained during STEM imaging and analysis. During collection of each spectrum, special care was taken to obtain enough counts so that the “peak to background ratio” was reasonably high for each of the relevant peaks. The collection times used were 30-60 s for each precipitate. The FEI™ software “TIA” was used to quantify the elements in EDS spectra. The background was calculated and subtracted automatically by the software. The uncertainties in the chemical composition of the precipitates presented in the tables are less than ± 5% of the value of the measured concentration of any given species.

High-resolution TEM (HRTEM) images were analyzed using Gatan® Digital Micrograph™ and NIH’s ImageJ™ software.

RESULTS

Three distinctly different kinds of features were observed, which could be categorized into the following classes: (a) large faceted, but irregular shaped features, 50-300nm in size; (b) intermediate sized 20-50 nm NFs with square center cross sections; and (c) small 2-5 nm NFs which appear to be round. Note, while we have classified the intermediate sized phases as NF in this paper, some literature restricts NF sizes to < 5-10 nm. It is the structure, chemistry and matrix-particle orientation relationship (OR) of the oxide phases, with special emphasis on the intermediate sized phase, that we focus on and present in this paper.

Large, faceted features (50-300nm)

The high angle annular dark field (HAADF) image in Fig. 1 shows a region of the FBI-sectioned TEM specimen. Many grains of various sizes are visible, ranging from 250nm-1mm, with a large number of dark particles distributed both inside the grains and on the grain boundaries. The dark contrast of these features suggests that they contain large amounts of oxygen, and therefore have a lower average Z than the Fe matrix. The presence of oxygen is also apparent in the EDS results presented below. Spot and EDS scan composition measurements were performed on some of the 100-300nm features, which were mostly located on the grain boundaries.

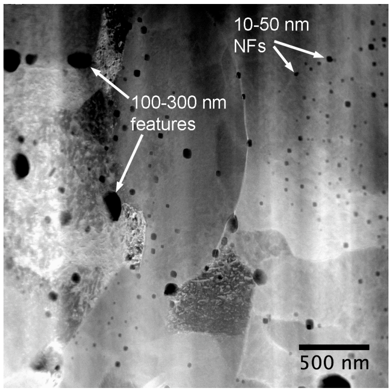

Fig. 1. HAADF STEM image showing large and intermediate sized particles.

The EDS spectrum from one of these large features, presented in Fig. 2(a), shows high intensities of the Ti(K), Cr(K) and O(K) peaks, along with a weak Fe(K) peak, that is likely due to a thin layer of Fe matrix above or below the particle. The chemical concentrations of different elements obtained from spot spectra for 7 such large features, presented in Table 1, show average compositions of ≈ 20 at. % Cr and Ti and, nominally, ≈ 60 at % O and trace quantities of Fe, W and Y.

Table 1. Chemical composition (in atomic %) of 7 large faceted particles in the 100-300 nm size showing the presence of almost equal amounts of Ti and Cr.

	1	2	3	4	5	6	7	Average
O(K)	48.1	61.6	53.9	65.8	61.32	62.67	65.89	59.90
Ti(K)	27.2	20.6	23.8	18.1	20.4	19.84	17.76	21.10
Cr(K)	24.2	17.6	21.9	15.9	18.11	14.97	16.19	18.41
Fe(K)	0.3	0.2	0.3	0.2	0.15	0.2	0.14	0.21
Y(K)	0	0	0	0	0	2.29	0	0.33
W(L)	0.06	0	0	0	0	0	0	0.01

The trace of a line EDS scan on one such feature is shown in Fig. 2(b), and the elemental profile of Fe is shown in Fig. 2(c), and those of Ti, Cr and O are shown in Fig. 2(d). The drastic drop in the Fe(K) peak intensity suggests that the particle occupies most of the thickness of the sample and that there is hardly any Fe inside the particle. Since the particle is about 140-160 nm wide in the direction of the trace, and since the shape of the particle is almost equiaxed, it may be assumed that the feature occupies most, if not all, of the thickness of the sample. Hence the X-ray peaks obtained from the region of the feature arise predominantly from the elements in the feature, and not from the matrix and any Fe in the EDX spectrum comes from a very thin layer of Fe matrix above or below the oxide. The intensities of the Ti(K) and Cr(K) peaks are almost equal inside the feature. Note that the Cr content of the particle is only slightly higher than the 14 % Cr in the FeCr matrix. However, if the feature did not contain Cr, some level of depletion would be observed.

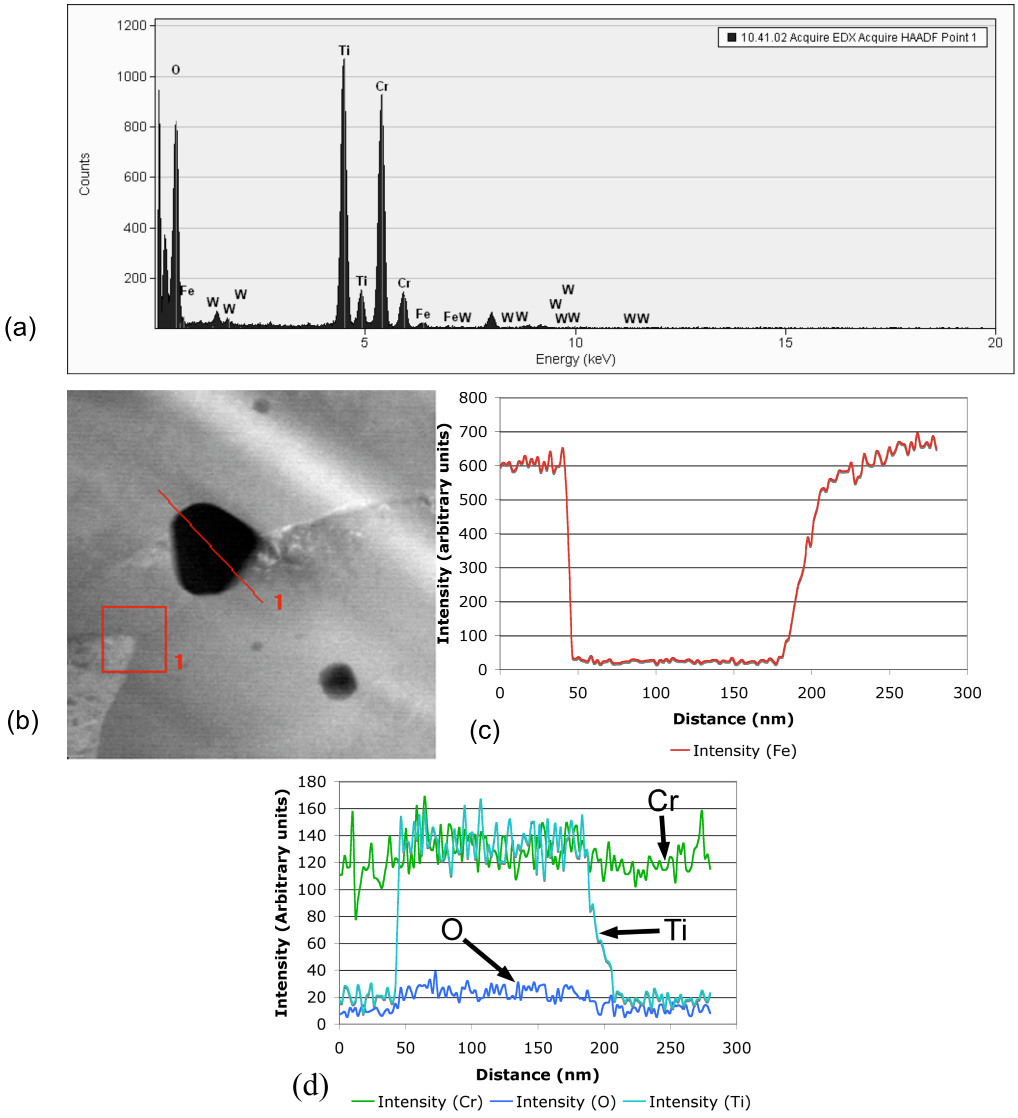

Fig. 2. (a) EDS spectrum collected from a spot in a large faceted particle showing mainly Ti, Cr and O peaks, apart from the Fe peak from the matrix, (b) A line spectrum

trace across one such particle, (c) The drift-corrected spectrum profile along the trace shown across the particle in (b) showing a drastic drop of the Fe intensity inside the particle, and (d) Almost equal intensities of Ti (K) and Cr(K) peaks and a rise in the O(K) intensity in the particle.

The structure of the large features was determined by BF TEM imaging and selected area diffraction. A BF TEM image of one feature is shown in Fig. 3(a), with the BCC Fe matrix on a [001] zone axis (ZA). The corresponding selected area diffraction pattern (SADP) is shown in Fig. 3(b). It is clear from the BF TEM image and the SADP that two of the major facets of the particle are parallel, or almost parallel, to {200} Fe (BCC) planes. The other facets are also parallel to BCC low index planes. The SADP in Fig. 3(b) also shows many spots from the precipitate, that were used to measure the d-spacing values shown in Table 2, along with those reported in the literature for a rhombohedral structure [20]. It is clear that there is reasonable agreement between the two sets of observations.

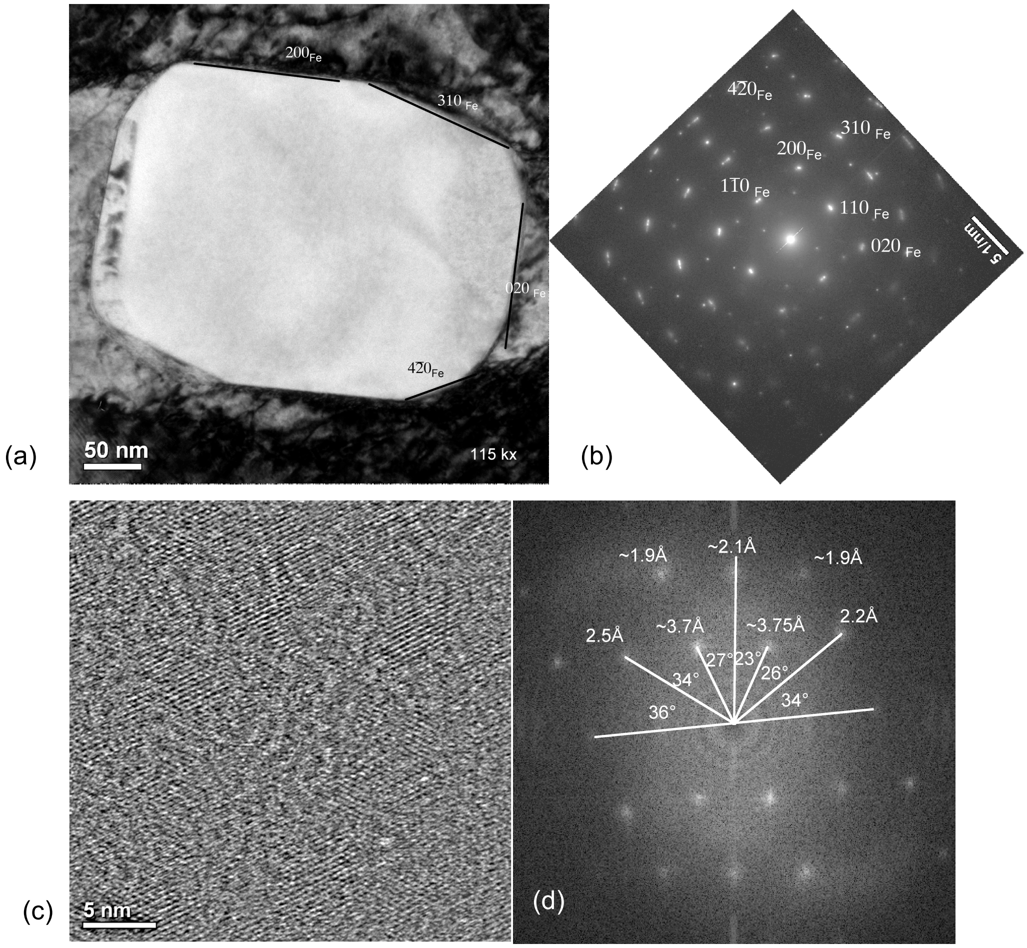

Fig. 3. (a) BF TEM image of a big faceted precipitate with the Fe matrix on a 001 zone axis, (b) Corresponding selected area diffraction pattern showing both matrix and precipitate spots, (c) HRTEM image of the particle shown in (a), and (d) FFT of the HRTEM image shown in (c) showing a few spots d-spacing equal to or close to $CrTiO_3$ as reported in the literature.

Table 2. *d-spacing values of different planes of $CrTiO_3$ as measured and as reported in the literature* [20]

	Measured (Å)	Reported in literature (Å)
1	3.7 - 3.8	3.67
2	2.0 - 2.2	2.2
3	1.9	1.835

An HRTEM image of the particle is shown in Fig. 3(c) and the corresponding fast Fourier transform (FFT) is presented in Fig. 3(d). The d-spacing values of the phase comprising the particle as measured from this FFT image agree with those measured from the SADP shown in Fig. 3(b). Therefore, the feature in Fig. 3(a) is consistent with rhombohedral $CrTiO_3$, although a precision measurement of lattice parameters was not performed.

Intermediate sized square NFs (10-50 nm)

Intermediate sized square-shaped NFs were also observed in the sample, as seen in the HAADF micrograph in Fig. 1. A higher magnification image of some similar particles is shown in Fig. 4(a). It is clearly visible in this image and in the images in Fig. 4(b) and 4(c), which show other ferrite grains, that these particles have a nominally square cross-section, and that they are morphologically oriented in the same direction inside any given grain. These precipitates will be referred to here as “large NFs”. The area fraction of these nominally square shaped large NFs varies from 1 to 4% from grain to grain, which is equivalent to a volume fraction of 0.15-0.8%, assuming a roughly cubic shape. The number density of these particles was found to vary between $2x10^{20}$ and $7x10^{20}$ NFs/ cubic m, and the surface area per unit volume was calculated to be in the vicinity of $8x10^5 – 2.4x10^6$ m^2/ m^3.

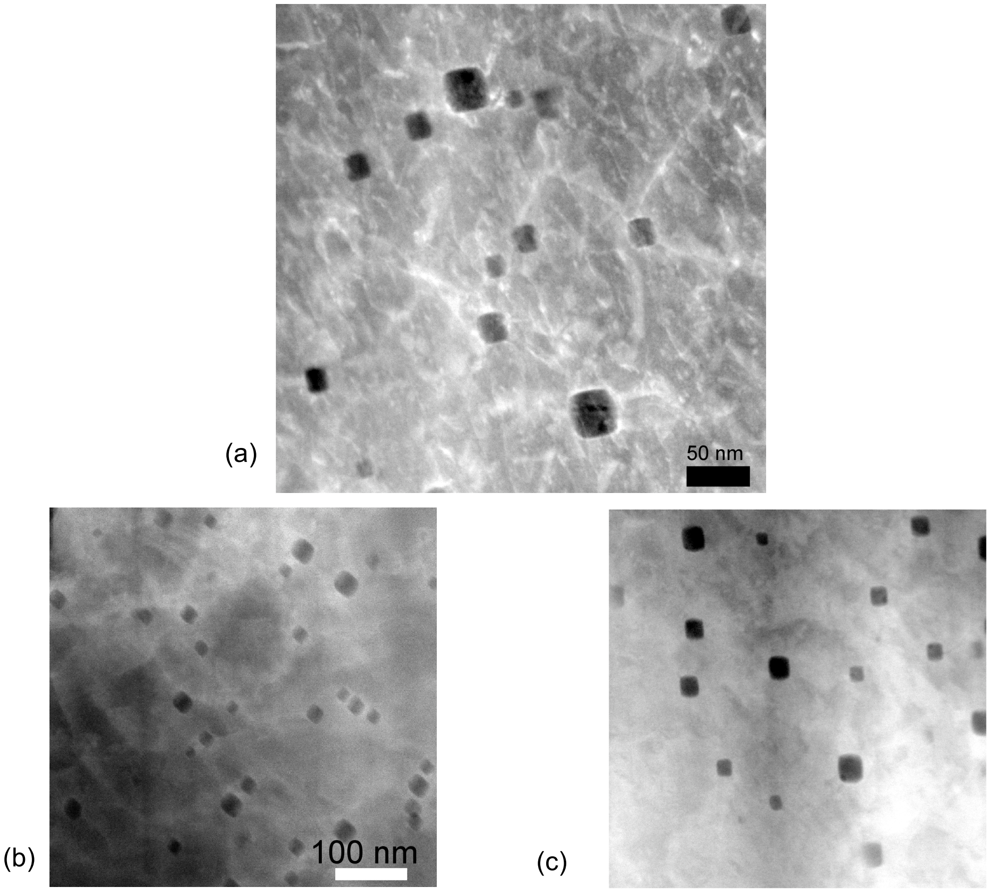

Fig. 4. (a) STEM HAADF image of 10-50 nm precipitates or “larger NFs” with a square shape in cross-section, mostly located on dislocations, (b) and (c) show similar precipitates or “nano-features” in other ferrite grains, all oriented with their facets parallel inside any given grain.

The STEM image in Fig. 5(a) shows one of the largest NFs in this class (indicated by arrow). There are four main facets which give the nano-feature an approximately square shape. The corners have smaller facets or are rounded, implying that these NFs are not strictly square, but are polygonal with a roughly square shape in their center plane. The EDS spectrum in Fig. 5(b) was collected from the particle showed in Fig. 5(a). The spectrum shows intense peaks for Y, Ti and O, along with weaker peaks from Fe and Cr; the latter arise most likely from matrix located above or below the NF, since the 50-60nm NF is probably smaller than the foil thickness in this area. A profile of the Fe-K and Cr-K peak intensities (Fig. 5(c)) shows a sharp drop for both Fe and Cr inside the NF, suggesting that any Cr signals arise from the matrix, unlike in the case of the larger particles, where the Cr intensity remains the same while the Fe intensity decreases. The Ti, Y and O intensities increase significantly inside the NF, while the small W intensity decreases to almost zero, as shown in Fig. 5(d). Other similar, but smaller, NFs also showed the same type of concentration profiles. Thus it can be stated with considerable certainty that these NFs are comprised mainly of Ti, Y and O. The HAADF image in Fig. 5(e) shows four such features, with sizes varying from ~25-60nm. The Y and Ti content, and the Y/Ti ratio are shown in Table 3.

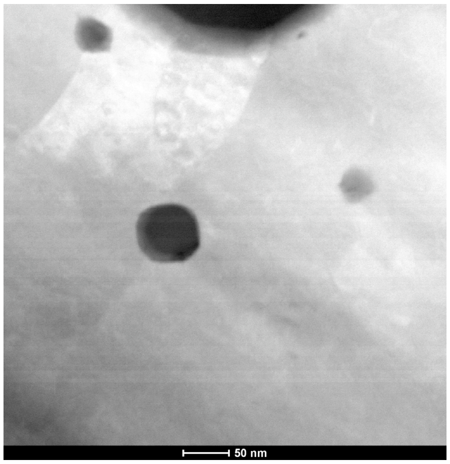
50 nm

(a)

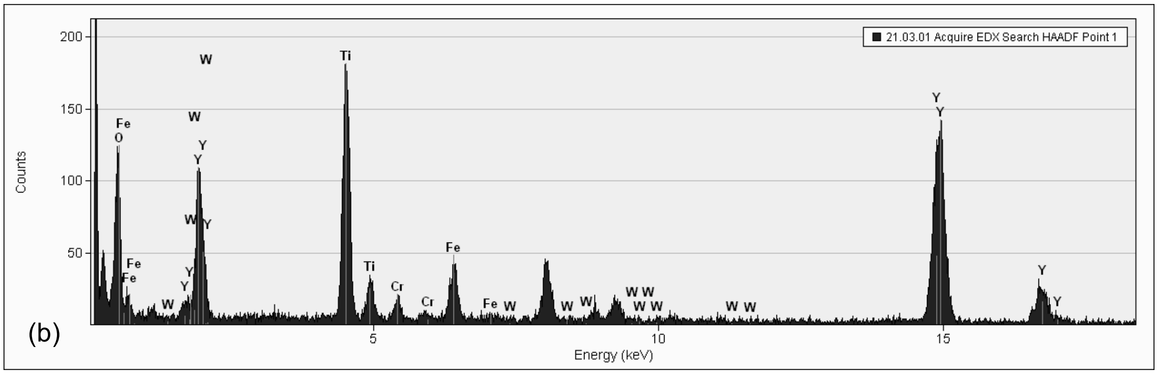
21.03.01 Acquire EDX Search HAADF Point 1
Counts
200
150
100
50
Energy (keV)
5
10
15
W
Ti
Y
Y
Fe
O
W
Y
Y
W
Y
Fe
Fe
Y
Y
W
Ti
Cr
Cr
Fe
Fe
W
W
W
W W
W W
W W
Y
Y

(b)

(c)

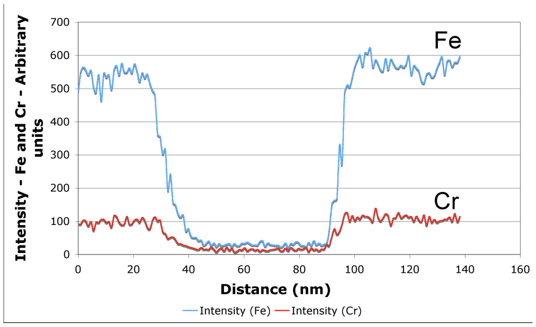
Intensity - Fe and Cr - Arbitrary units
700
600
500
400
300
200
100
0
0
20
40
60
80
100
120
140
160
Distance (nm)
Fe
Cr
Intensity (Fe)
Intensity (Cr)

(d)

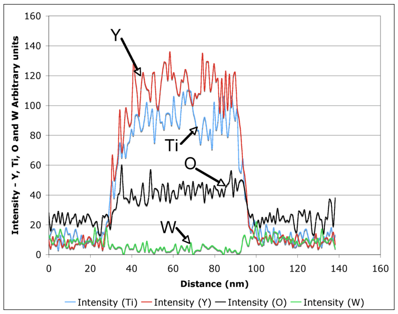
Intensity - Y, Ti, O and W Arbitrary units
160
140
120
100
80
60
40
20
0
0
20
40
60
80
100
120
140
160
Distance (nm)
Y
Ti
O
W
Intensity (Ti)
Intensity (Y)
Intensity (O)
Intensity (W)

(e)

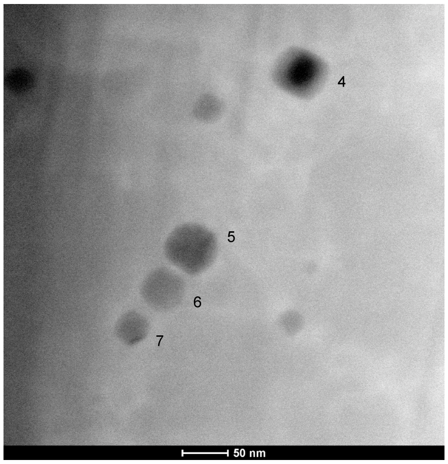
4
5
6
7
50 nm

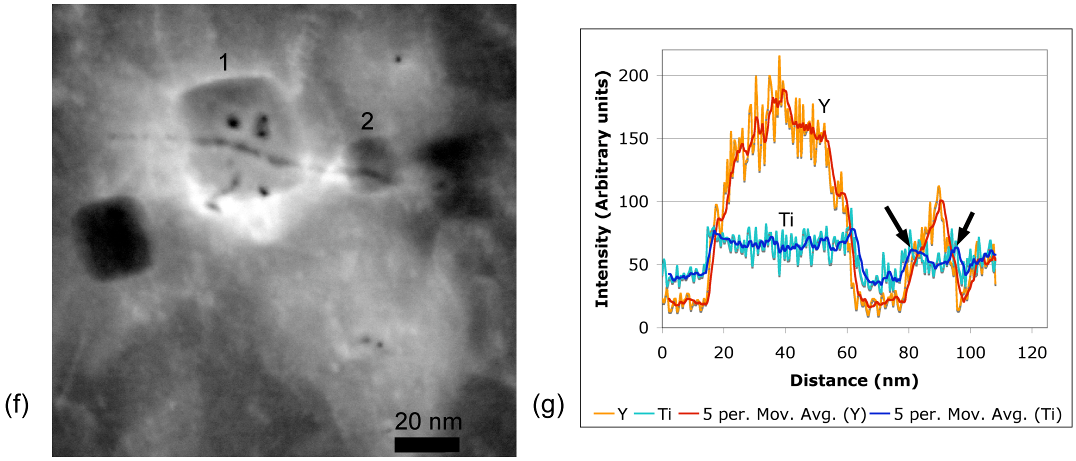

Fig. 5. (a) One of the larger square shaped particles - showing more facets near the corners, (b) EDX spectrum from the same particle, (c) Intensity profile for Fe and Cr across the NF shown in Fig. 5(a), showing sharp concentration drops reaching almost zero inside the NF for both elements, (d) Intensity profile for Ti, Y, O and W showing significant increases in concentration for Ti, Y and O, and a decrease in concentration for W inside the NF, (e) Four different "square" particles in the range of 25-60 nm, (f) two large NFs of different sizes with trace of EDS scan across them (the trace is not straight probably due to sample drift), (g) Ti and Y intensity profiles for particles 1 and 2.

Table 3. Y and Ti concentrations and Y/Ti ratio in intermediate size "square" features (or "large NFs") shown in Fig. 5(e).

	Particle 4	Particle 5	Particle 6	Particle 7
Ti (At. %)	0.6	4.8	3.1	6.3
Y (At. %)	1.1	4.6	2.9	3.9
Y/Ti	1.98	0.96	0.95	0.6

Thus it is clear that the Y/Ti ratio varies substantially from NF to NF. The larger NFs have higher Y/Ti ratio. This is true in general, as also illustrated by an EDS line scan across two NFs of different sizes (marked 1 and 2 in Fig. 5(f)), the Y and Ti intensity profiles for which are given in Fig. 5(g). However, there are some exceptions, such as the NF shown in Fig. 5(a).

It was found from various measurements performed on the micrographs such as those shown in Fig. 4 that these types of NFs with square cross-section have an average volume fraction of approximately 0.4% in the alloy. The density of these precipitates is close to 5 g/cm^3, and that of the matrix approximately 8 gm/cm^3. Assuming that the stoichiometry of the NFs is between Y_2TiO_5 and $Y_2Ti_2O_7$ (as seen from the EDS analysis) the fraction of total Y and Ti present in these NFs can be calculated.

According to these stoichiometries, the weight fraction of Ti in these precipitates is between 0.16 and 0.25, or ~0.2 on average. The total amount of Ti in the alloy is about 0.4 wt %. This will yield a value of approximately 12.5% of the total Ti residing in the square NFs. Similarly, the fraction of Y in the square NFs can be calculated by assuming an average weight fraction of Y in the square precipitates equal to 0.52 (0.58 for Y_2TiO_5 and 0.46 for $Y_2Ti_2O_7$). Since the total amount of Y in the alloy is about 0.2%, the fraction of total Y residing in the square NFs is about 0.65, assuming an average volume fraction of 0.4% for these NFs. The density of the Fe matrix was assumed to be 8 gm/ cm^3 and that of the oxides to be approximately 5 gm/ cm^3 in all of the calculations reported here.

A different region of the sample with similar “square” NFs is shown in Fig. 6(a), indicating the trace of the drift corrected spectrum profile taken from one of the NFs. The plot in Fig. 6(b) shows the profile of Ti, Y and O across the particle. It is clear that the concentration of Y is higher than that of Ti. The concentration of Ti at the edges seems to be slightly higher than that in the center of the NF (as indicated by the arrows). The same effect is seen in the concentration profiles of Fig. 5(g), to some extent (see arrows). This slight core-shell effect was seen in a number of the intermediate sized NFs.

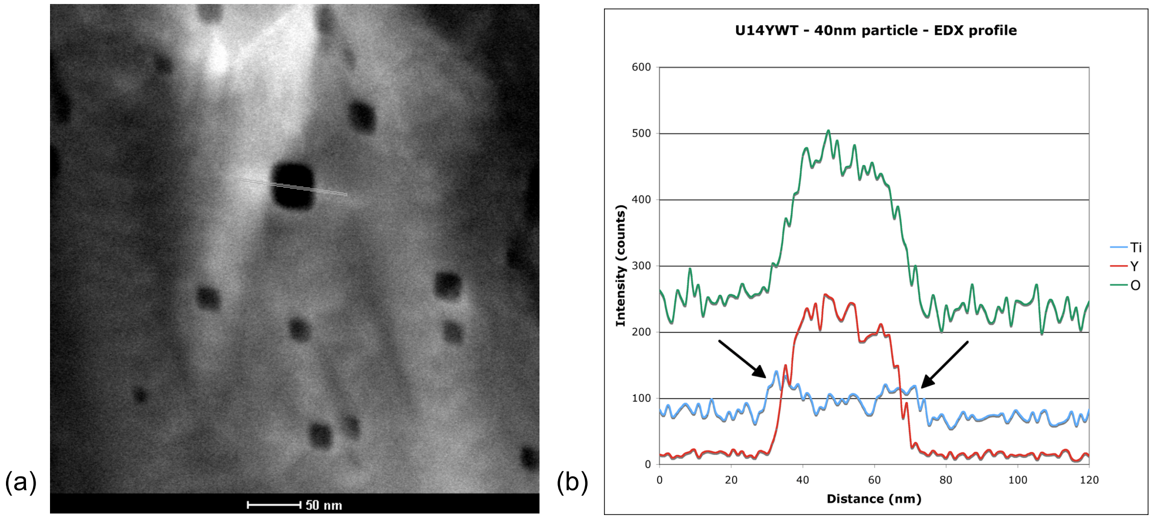

Fig. 6. (a) HAADF STEM image showing a particle across which a drift corrected spectrum profile was taken, (b) The spectrum profiles for Ti, Y and O, showing a high Y/Ti ratio, and a slightly higher Ti amount at the edges of the particle.

The structure of the intermediate sized NFs was investigated using high resolution transmission electron microscopy (HRTEM). An example is shown in Fig. 7(a) for a NF located at a low angle grain boundary in the ferrite (indicated by the arrow). The Y/Ti ratio of the particle was found to be 5/4. The HRTEM image of the particle and the surrounding matrix is shown in Fig. 7(b).

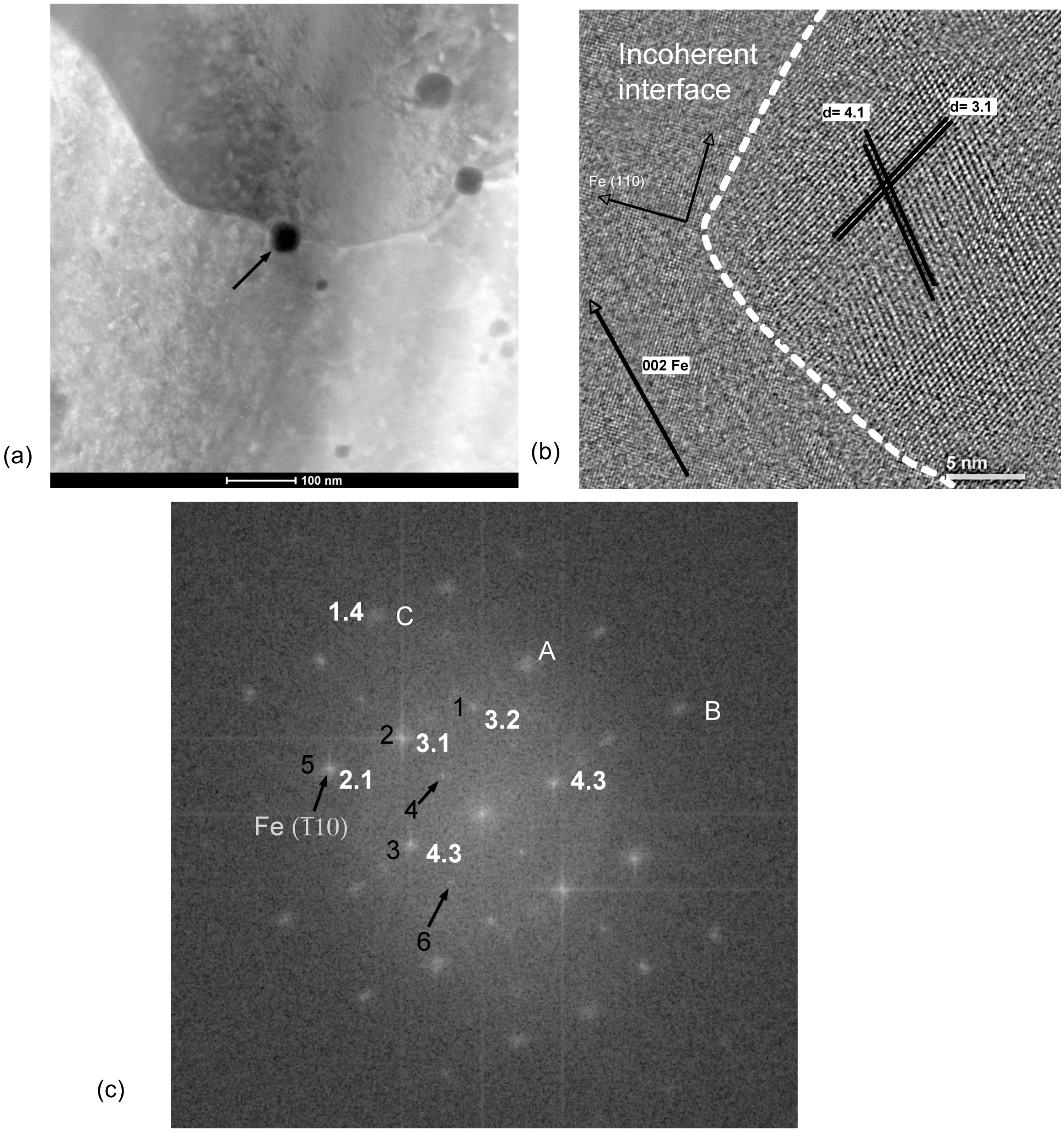

Fig. 7. (a) Particle at a small angle grain boundary, (b) HRTEM image of the "Square" precipitate indicated in (a), showing lattice fringes and the interface between the particle and the matrix, (c) Fast Fourier Transform (FFT) of the HRTEM image in (b) showing both BCC α Fe and precipitate spots.

The interface between the particle and the matrix is indicated by a dashed line. The Fast Fourier Transform (FFT) of this HRTEM image is shown in Fig. 7(c). The spots in the FFT image ware labeled 1 through 5 (black numbers) for the NF and A through C (white letters) for matrix, while the d spacings are shown in white numbers. These spots were analyzed in detail. The spot corresponding to a d-spacing of 2.1Å almost overlaps with the Fe BCC (110) spot. The lattice spacing values and the angles between the lattice planes are shown in Table 4.

Table 4. Measured d-spacing values and angles for the particle shown in Fig. 7.

Image	Spot (a)	d spacing of a (Å)	Spot b	d spacing of b (Å)	θ1 (deg)	θ4 (deg)	Angle between a and b (deg)
Square particle at GB	1	3.2	2	3.1	94.86	137.49	42.63
	2	3.1	3	4.3	137.49	205.11	67.62
	2	3.1	5	2.1	137.49	163.84	26.35
	1	3.2	3	4.3	94.86	205.11	110.25
	4	6.2	3	4.3	137.49	205.11	67.62

Visual examination showed that the d-spacing values and angles between the planes do not match those of any of the known Y-Ti-oxide. The structure of the NF was solved in the following manner. First it was assumed that the NF has a tetragonal structure. This assumption was based on the fact that the FFT pattern from the matrix seems to have 2 mirror planes, and that there is at least one known complex Y-Ti-oxide (Y_2TiO_5) that has a structure that is close to tetragonal. Subsequently, curves from the Hull-Davey chart were used to find the c/a ratio using the known d-spacing values. The c/a ratio was found to be approximately 0.6. The structure was then refined to make the d-spacing values and the angles match the experimentally observed values (from the FFT image) as closely as possible. It was found that the lattice parameters of a=11.6Å, b=12.2Å, and c=7.4Å gave the closest matching between the observed and the calculated d-spacing and angles. Based on these results the lattice was assumed to be face-centered orthorhombic. The corresponding calculated d-spacing values and angles are given in Table 5.

Table 5. Calculated d-spacing values and angles for orthorhombic structure and lattice parameters of a=11.6Å, b=12.2Å and c=7.4Å. The corresponding Miller indices are given in columns 1 and 2.

$h_1k_1l_1$	$h_2k_2l_2$	phi (deg)	d1 (Å)	Corresponding spot in FFT	d2 (Å)	Corresponding spot in FFT
0 -2 2	2 0 2	43.87	3.16	1	3.12	2
2 0 2	2 2 0	67.06	3.12	2	4.20	3
2 0 2	4 2 2	27.92	3.12	2	2.13	5
0 -2 2	2 2 0	110.94	3.16	1	4.20	3

As is clear from a comparison of Tables 4 and 5, there is very good agreement between the measured and calculated d spacing and angles. There are two additional pairs of very faint spots, numbered 4 and 6. These correspond to the precipitate **101** and **12`1** planes. Such spots can be caused by ordering in a direction perpendicular to these respective planes. This destroys the face-centering of the Bravais lattice and creates a “b centered” lattice.

A simulated diffraction pattern of the NF, using the calculated lattice parameters and a “b-centered” orthorhombic lattice, and that of the matrix, using known a Fe lattice parameters, are shown in Fig. 8 (a) and (b), respectively, reproducing the spots in the FFT (in Fig. 7(c)) as closely as possible. The simulated structure shows ordering on (202) and (24`2) planes. The spots 4 and 6 (corresponding to ±(101) and ±(12`1)) are reproduced at very low intensity, which may be the result of ordering, as was mentioned earlier.

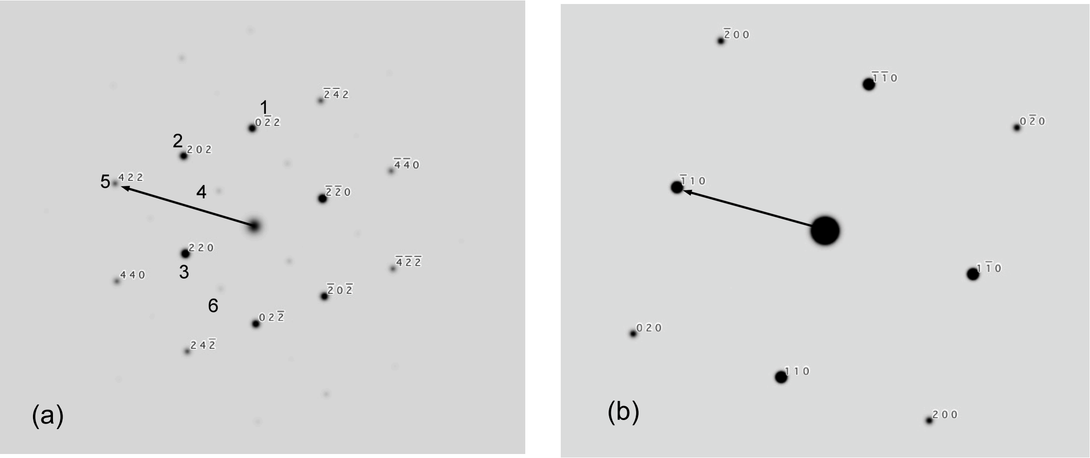

Fig. 8. Simulated diffraction patterns: (a) Precipitate with “**b**-centered” orthorhombic lattice oriented at zone axis $[1\bar{1}\bar{1}]$, (b) Matrix - α Fe oriented at zone axis $[001]$ - the orientation relationship is: (422)ppt || $(\bar{1}10)$Fe matrix; $[1\bar{1}\bar{1}]$ppt || $[001]$ Fe matrix.

The orientation relationship (OR) between the precipitate and the matrix was found to be: (422) ppt || ((`110) Fe Matrix and $[1\bar{1}\bar{1}]$ ppt || [001] Fe matrix.

The HRTEM image from another NF, taken from a different Fe BCC matrix zone axis, also showed fringes which had identical d-spacing values as the one discussed above. The lattice parameters of this structure do not match with those of any known complex Y-Ti-oxides, although they bear some resemblance to orthorhombic Y_2TiO_5, whose lattice parameters are slightly smaller for a (10.35Å) and b (11.25Å), and half for c, which is 3.7Å (see [21]).

The low index matching atomic planes of the precipitate and the matrix ({4 2 2}$_{\text{Precipitate}}$ and {`1 1 0}$_{\text{Fe BCC}}$ planes) are oblique to the interface planes. The lattice mismatch in the {`1 1 0 }$_{\text{Fe BCC Fe BCC}}$ direction is about 7%, and in the direction perpendicular to the plane of the figure it is about 3%, indicating that the interface is probably semi-coherent.

Close examination of the HRTEM image indicates that the interface between the particle and the Fe BCC matrix is irregular, and probably has steps. Such an interface may be developed parallel to some invariant line (of somewhat higher indices) between the two phases [22]. This may cause the formation of steps at the interface, with the terrace planes parallel to the matching low index crystallographic planes.

Small spherical shaped NFs (< 5nm)

The third type of feature in the U14YWT alloy HIP-ed at 1150°C was found to be extremely small, i.e. < 5nm in diameter, as shown in the HRTEM image in Fig. 9(a). The right hand side of the image shows numerous closely spaced spherical NFs, whereas the left hand side of the image shows very few features. This indicates that the NFs are distributed in an inhomogeneous manner inside the a ferrite grain. The average number density of the particles in the matrix, as calculated from this image (Fig. 9(a)), assuming a conservative sample thickness of 100 nm, was found to be ~2 x 10^{23} /m^3. Since the sample is likely to be thinner than 100 nm (since lattice fringes are clearly visible), the NF number density is likely to be higher than this in the grains where the particles are present. This number density is similar to estimates based on small angle neutron scattering (SANS), TEM and APT for similar NFAs [3, 6, 9, 11, 13, 19]. Fig. 9(b) shows an FFT diffraction pattern extracted from the HRTEM image in Fig. 9(a). The spots in the FFT image do not match the patterns for any known Y-Ti-oxides structures.

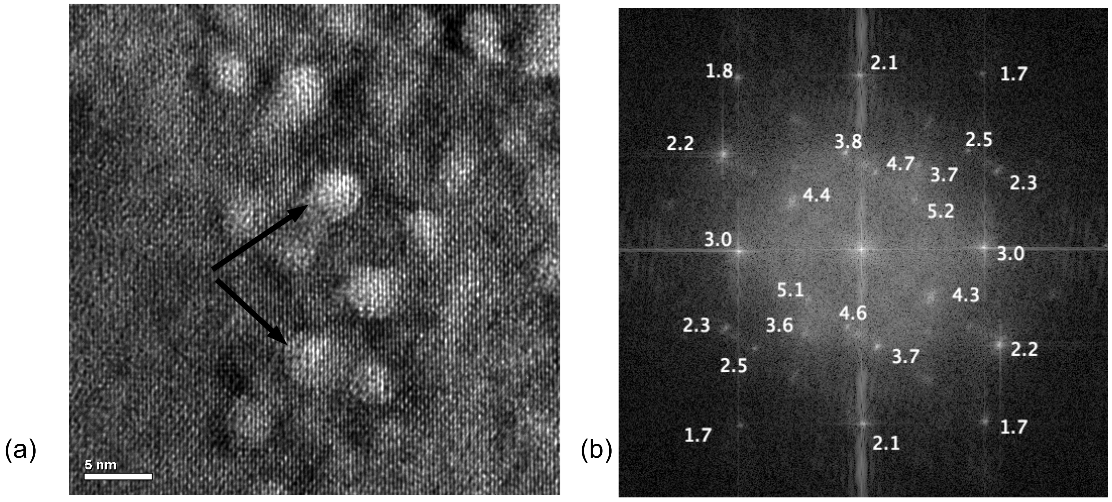

Fig. 9. (a) Extremely small NFs - 2-5nm in size, and spherical in shape as seen in an HRTEM image, (b) An FFT image extracted from HRTEM image in (a), showing reciprocal lattice spots from the NFs.

A U14YWT alloy HIP-ed at 850°C was also examined in the TEM. An HRTEM image, cleaned using a mask filter in the FFT, is shown in Fig. 10(a). The corresponding FFT diffraction pattern is shown in Fig. 10(b).

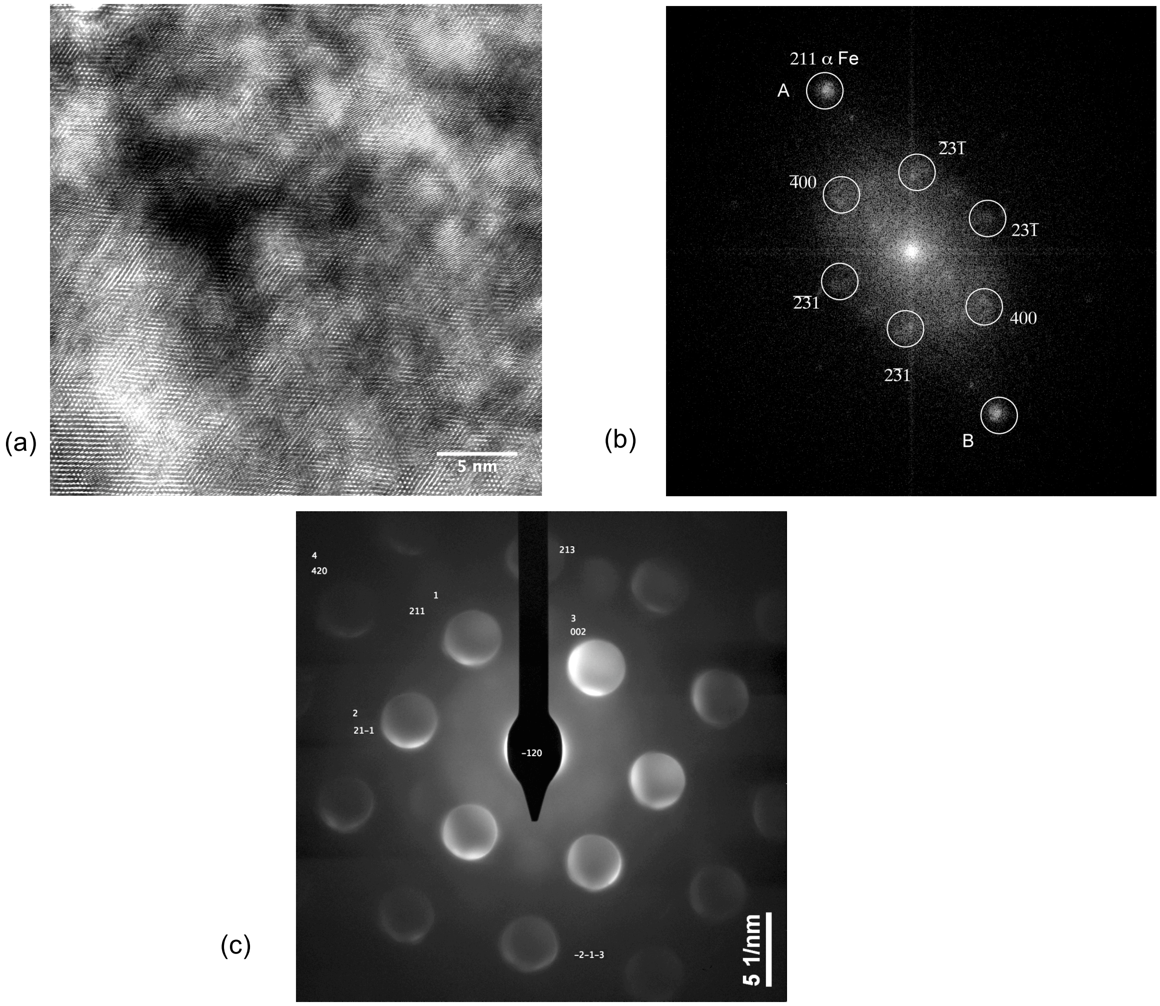

Fig. 10. (a) A cleaned HRTEM image from a U14YWT alloy sample HIP-ed at 850°C, (b) corresponding FFT pattern showing the spots from the Fe BCC matrix and the particles or nano-clusters, (c) Convergent beam electron diffraction pattern from Fe BCC grain whose HRTEM picture is shown in Fig. 10(a).

The spots marked A and B arise from the {211} a Fe planes. The six spots in a hexagonal arrangement are from the NFs, and are consistent with planes in a slightly distorted $Y_2Ti_2O_7$ structure. Using the convergent beam electron diffraction (CBED) pattern in Fig. 10(c), the orientation relationship (OR) between the particles and the matrix was determined to be:
$\{123\}$ ppt || $\{123\}$ α Fe and $[30\bar{1}]$ ppt || $[2\bar{1}0]$ α Fe.

Thus there seems to be a difference in the phase of the smallest size NFs found in the U14YWT samples HIP-ed at 1150°C and 850°C, respectively.

DISCUSSION

The microstructure of U14YWT alloy hot isostatic pressed (HIP-ed) at 1150°C was examined using TEM. Three types of features were observed, having different sizes and shapes.

The first type of features, the largest, were present in the size range of 50-300 nm, were irregular in shape, and had facets parallel to low index planes of the BCC iron matrix. They were found to be comprised of Cr, Ti and O, with a solute ratio of ≈ Cr:Ti:O = 1:1:3. Their crystal structure showed d-spacing values which were similar to those reported in literature for a rhombohedral $CrTiO_3$ structure. Due to their low number density, these features are not thought to be important for the radiation damage resistance of U14YWT. Indeed, they may have a slight detrimental effect on the properties of the alloy as they may remove a significant amount of Ti from the surrounding matrix, thus preventing the formation of the beneficial NFs.

The second type of feature, in the size range of 10-50 nm, were polyhedral, with faceted or rounded corners and an approximately square center section. These intermediate sized precipitates are classified here as "larger NFs". EDS showed the larger NFs were primarily composed of Y, Ti and O. The Y:Ti ratio varied from NF to NF in the range of <1:1 to ~2:1. The edges of these particles seem to have more Ti than at the center, suggesting a possible core-shell structure. Similar core shell structures have been observed previously in NFs present in other NFAs [23]. The larger NFs seemed to have slightly higher Y:Ti ratio. This observation may suggest that for the larger NFs, there is greater opportunity to reach an equilibrium composition, which may have a high Y:Ti ratio. Similar variations in Y:Ti ratio with size have also been observed in a sample of MA-957 alloy steel, although only up to a size range of ~15-20 nm, after which the authors reported a roughly constant Y:Ti ratio [24].

The structure of these larger NFs was examined using high-resolution TEM. A detailed examination of HRTEM micrographs and their FFT images suggested an orthorhombic phase, with the lattice being centered on one of the faces. The lattice parameters were found to be a= 11.6Å, b= 12.2Å and c= 7.4Å. The two larger parameters, a and b, were close to the lattice parameters of orthorhombic $Y_2Ti_2O_5$, and the third parameter, c, was found to be double that of the c edge of Y_2TiO_5. The spots in the FFT pattern of the HRTEM image suggested that there was ordering on two oblique planes. These larger NFs do not have a structure that is identical to any of the known Y-Ti-oxides, although it is somewhat similar to the orthorhombic Y_2TiO_5 phase. They also exhibit a variable, non-stoichiometric composition. These observations suggest that the larger NFs are not at equilibrium, but belong to a metastable transition phase. The high- resolution TEM images suggested that the interface between these particles and the Fe BCC matrix was irregular, and possibly stepped. The interface was observed to be semi-coherent, which may act as good sinks for defects and help in the trapping of He, thus preventing the formation of large bubbles in the neighboring matrix. These NFs are different from those reported in other studies by Hoelzer, Miller et al. [9, 13] in that they have a nominally square cross-section, are quite well distributed in space for their size range, and their structure is not identical to any known Y-Ti-oxide.

These NFs appear in very high number densities ($2x10^{20}$ – $7x10^{20}$ / m^3), and thus provide significant surface area per unit volume for He entrapment. The ability of larger NFs (similar in size as reported here) to trap inert gases such as Ar is exemplified by the existence of cavities filled by Ar decorating the interface between the matrix and the particle in the work of Klimiankou, et al. [18] The average distance between these particles is ~90-100 nm. Such small distances between these NFs can result in significant increase in strength by providing resistance to dislocation motion. Thus, although these NFs are larger than the 2-5nm NFs generally thought to be the primary reason for enhanced radiation resistance and strength, they are present in substantially small sizes and number densities to affect the properties of the alloy significantly. Moreover, their presence also diminishes the concentration of available solute elements for the precipitation of the smaller NFs, and as much as ~12-15% of Ti and ~ 60-70% of Y may reside in these square NFs. Therefore, it is of extreme interest to the NFA community to understand if these larger particles can compensate for the lower concentration of the 2-5 nm NFs.

A third type of small NFs, less than 5nm in diameter, were distributed in the Fe BCC matrix inhomogeneously. Some of the grains showed a high number density of these precipitates, while some others did not have detectable numbers. The number density of these particles was estimated to be of the order of $2x10^{23}$ particles/m^3 in the regions in which they were observed. This number is close to that estimated by SANS and 3-DAP in the same 14YWT alloy and in similar alloys. High-resolution TEM (HRTEM) images and corresponding FFT images were not consistent with the structure of known Y-Ti-oxides. This was found to be in contrast to the extremely tiny clusters that were found in the U14YWT alloy HIP-ed at 850°C, which may be $Y_2Ti_2O_7$. The exact nature of the small NFs (<5 nm) needs to be investigated further using extraction of these precipitates from the alloy using a carbon replica method [25-26].

The inhomogeneous distribution of the small NFs (<5nm) and the significant number of the larger NFs (5-10nm) makes the understanding of the effects of the larger NFs on the properties of these steels important for the development of these alloys.

ACKNOWLEDGEMENTS

The corresponding author dhriti1@gmail.com is at the Institute of Materials Engineering, ANSTO, NSW, Australia, 2234. The authors would like to thank Dr. Longzhou Ma at UNLV for his kind permission to use the TEM at the Harry Reid Environmental Center when needed. The many helpful discussions with Prof. J. P. Hirth are also gratefully acknowledged. This TEM work at LANL was funded by Los Alamos National Laboratory LDRD. The alloy development and characterization studies carried out at UCSB were supported by the DOE Offices of Fusion Energy Sciences and Nuclear Energy.

REFERENCES

[1] S. J. Zinkle, Busby, J. T., "Structural Materials for Fission and Fusion Energy," *Mater. Today* 2009, 12:12.

[2] M. I. Hoffert, Caldeira, K., Benford, G., Criswell, D. R., Green, C., Herzog, H., Jain, A.K., Kheshgi, H. S., Lackner, K.S., Lewis, J. S., Lightfoot, H. D., Manheimer, W, Mankins, J. C., Mauel, M. E., Perkins, L. J., Schlesinger, M. E., Volk, T., Wigley, T. M. L., "Advanced Technology Paths to Global Climate Stability: Energy for a Greenhouse Planet," *Science* 2002, 298:981.

[3] Odette, G. R., Alinger, M. J., Wirth, B. D., "Recent Developments in Irradiation-Resistant Steels," *Annu. Rev. Mater. Res.* 2008, 471.

[4] Mansur, L. K., "Theory and Experimental Background on Dimensional Changes in Irradiated Alloys," *J. Nucl. Mater.* 1994, 216:97.

[5] Czyrska-Filemonowicz, A., Dubiel, B., "Mechanically Alloyed, Ferritic Oxide Dispersion Strengthened Alloys: Structure and Properties," *J. Mater. Process. Tech.* 1997, 64:53.

[6] Odette, G. R., Hoelzer, D. T., "Recent Progress in Developing Irradiation Tolerant Nanostructured Ferritic Alloys: Transforming Helium Accumulation from a Liability to an Asset," JOM Journal of the Minerals, Metals and Materials Society 2010, In Press.

[7] Yamamoto, T., Odette, G. R., Miao, P., Edwards, D.J., Kurtz, R.J., "Helium Effects on Microstructural Evolution in Tempered Martensitic Steels: In situ Helium Implanter Studies in HFIR," *J. Nucl. Mater.* 2009, 386-388:338.

[8] Odette, G. R., Miao, P., Edwards, D. J., "Helium Transport, Fate and Management in Nanostructured Ferritic Alloys: In Situ Helium Implanter Studies," *J. Nucl. Mater.* 2010, accepted for publication.

[9] Hoelzer, D. T, Bentley, J., Sokolov, M. A., Miller, M.K., Odette, G. R., Alinger, M.J., "Influence of Particle Dispersions on the High-Temperature Strength of Ferritic Alloys," *J. Nucl. Mater.* 2007, 367-370:166.

[10] Miller, M. K., Hoelzer, D. T., Kenik, E. A., Russell, K. F., "Stability of Ferritic MA/ODS Alloys at High Temperatures," *Intermetallics* 2005, 13:387.

[11] Alinger, M. J., Odette, G. R., Hoelzer, D. T., "On the Role of Alloy Composition and Processing Parameters in Nanocluster Formation and Dispersion Strengthening in Nanostuctured Ferritic Alloys," *Acta Mater.* 2009, 57:392.

[12] Miller, M. K., Hoelzer, D. T., Kenik, E. A., Russell, K. F., "Nanometer Scale Precipitation in Ferritic MA/ODS Alloy MA957," *J. Nucl. Mater.* 2004, 329-333:338.

[13] Miller, M. K., Russell, K. F., Hoezler, D. T., "Characterization of Precipitates in MA/ODS Ferritic Steels," *J. Nucl. Mater.* 2006, 351:261.

[14] Bai, X-M., Voter, A. F., Hoagland, R. G., Nastasi, M., Uberuaga, B. P., "Efficient Annealing of Radiation Damage Near Grain Boundaries via Interstitial Emission," *Science*, 327:1631.

[15] Demkowicz, M. J., Hoagland, R. G., Hirth, J. P., "Interface Structure and Radiation Damage Resistance in Cu-Nb Multilayer Nanocomposites," *Phy. Rev. Lett.* 2008, 100:136102.

[16] Misra, A., Demkowicz, M., Zhang, X., Hoagland, R., "The Radiation Damage Tolerance of Ultra-High Strength Nanolayered Composites," *JOM J. Minerals, Metals and Mater. Soc.* 2007, 59:62.

[17] Klimiankou, M., Lindau, R. M. A., "TEM Characterization of Structure and Composition of Nanosized ODS Particles in Reduced Activation Ferritic-Martensitic Steels," *J. Nucl. Mater.* 2004, 329-333:347.

[18] Klimiankou, M., Lindau, R. M. A., "Energy-Filtered TEM Imaging and EELS Study of ODS Particles and Argon-Filled Cavities in Ferritic-Martensitic Steels," *Micron* 2005, 36:1.

[19] Alinger, M. J., Materials Engineering, vol. Ph. D. Santa Barbara: University of California, Santa Barbara, 2004.

[20] Vasyutinski, N., "Ryseva," *Russ. J. Inorg. Chem.* 1978, 23:621.

[21] Mumme, W. G., Wadsley, A. D., "The Structure of Orthorhombie Y2TiO5, an Example of Mixed Seven and Fivefold Coordination," *Acta Crystallogr.* 1968, B24:1327.

[22] Furuhara, T., Howe, J. M., Aaronson, H. I., "Interphase Boundary Structures of Intragranular Proeutectoid Alpha-Plates in a Hypoeutectoid Ti-Cr Alloy," *Acta Metall. Mater.* 1991, 39:2873.

[23] Marquis, E. A., "Core/Shell Structures of Oxygen-Rich Nanofeatures in Oxide-Dispersion Strengthened Fe--Cr Alloys," *Appl. Phy. Lett.* 2008, 93:181904.

[24] Sakasegawa, H., Chaffron, L., Legendre, F., Boulanger, L., Cozzika, T., Brocq, M., de Carlan, Y., "Correlation Between Chemical Composition and Size of Very Small Oxide Particles in the MA957 ODS Ferritic Alloy," *J. Nucl. Mater.* 2009, 384:115.

[25] Czyrska-Filemonowicz, A., Gorczyca, S. S. K., "Extraction Double-Replica Technique for Electron Microscopy Studies of Precipitates," *Prakt. Metallogr.* 1992, 29:35.

[26] Egeland, G. W., Zhang, H., Wang, H., Dai, Y., "Precipitate Analysis of 9-12 % Cr Ferritic/Martensitic and ODS Steels Using the Carbon Replica Technique," International Conference on Fusion Reactor Materials - ICFRM-13. Nice, France, 2007.

1.3 Transmission Electron Microscopy Characterization of the Structure and Composition of the Nanofeatures in Nanostructured Ferritic Alloy MA957 — Y. Wu, E. Haney, N. Cunningham and G. R. Odette *(Univ. of California Santa Barbara)*

OBJECTIVE

The objective of this work is to characterize the number density, size distribution, structure and compositions of nanofeatures (NF) in nanostructured ferritic alloys (NFA), with emphasis on the features with diameters less than 5 nm.

SUMMARY

Bright field transmission electron microscopy (TEM), high resolution TEM (HRTEM), scanning TEM (STEM) and energy dispersive X-ray (EDX) spectroscopy were combined to comprehensively characterize the Ti-Y-O enriched nano-scale features (NF) in a nanostructured ferritic alloy (NFA), MA957. The characterization included the NF number densities, size distributions, volume fractions, crystal structures and compositions. In foil measurements were complemented by studies of NF on extraction replica foils. The conditions examined included: two heats of extruded MA957; one of these heats following long-term thermal aging at 1000°C for 19.53 kh; and two friction-stir-weld variants. The study revealed the presence of diffracting complex oxide phases that varied somewhat with the feature size. However, the smallest features, with diameters (d) < 5 nm, were found to be consistent with cubic pyrochlore $Y_2Ti_2O_7$ complex oxides with average Y/Ti ratios of ≈ 1. Long-term thermal aging coarsened the NF, while friction stir welding had relatively little effect on their number density and size distribution.

BACKGROUND

This report addresses critical issues related to the development of a potentially transformational class of materials that we call NFA that are needed for advanced nuclear fission and fusion energy systems [1]. NFA derive from roots in oxide dispersion strengthened (ODS) steels, like PM2000, that contain coarser scale oxides [2-4]. NFA manifest a combination of outstanding high temperature strength, unique thermal stability and remarkable irradiation tolerance. These outstanding characteristics derive from the presence of an ultrahigh density of Y-Ti-O rich nano-scale features (NF). The multifunctional NF impede dislocation climb and glide, enhance SIA-vacancy recombination and, perhaps most importantly, trap He in very small, high-pressure gas bubbles [2,3,5]. The bubbles reduce the amount of He reaching grain boundaries, thus avoiding severe fracture toughness loss at lower irradiation temperatures, and potential degradation of creep rupture properties at higher temperatures. In principle, He trapped in a high number density of small bubbles also mitigates many other manifestations of irradiation effects, including void swelling that is an issue at intermediate temperatures [2,3].

NFA are typically processed by ball milling elemental or pre-alloyed rapidly solidified metallic powders with yttria (Y_2O_3) powders [2-4]. Typical NFA compositions are $\approx$ 14Cr, 0.2Y, 0.15O, 0.4Ti, 3.0W (wt.%). Proper milling effectively dissolves the Ti, Y and O. These solutes then precipitate as NF during hot consolidation [2,6]. As expected for precipitation processes, the NF number densities decrease with increasing consolidation temperatures. Further, Ti is needed to form NF at higher temperatures [6]. While they form rapidly, the NF are extremely thermally stable [3,7-9]. Powder consolidation is usually followed by a series of deformation processing-fabrication treatments.

While their roots were established long ago, NFA remain in the very early stages of development. One important challenge is determining the detailed characteristics of the NF, including the: number densities, size distributions, volume fractions, crystal structures and compositions. However, the detailed nature of the NF has not been clearly established. In part, this is because different characterization methods have not provided consistent results.

There are at least 6 known Y-Ti-O phases in the X-ray diffraction database, as shown in Table 1. With one exception the Y/Ti ratios of these oxides are greater than or equal to 1 and the O/(Ti+Y) ratios are greater than 1. Atom probe tomography (APT) studies have been interpreted to suggest that the NF are highly non-stoichiometric coherent transition phases [7-11], perhaps akin to G-P zones, possibly with complex core shell structures [12,13]. The APT Y/Ti ratios typically range from about 0.25 to 0.5, while the corresponding O/(Ti+Y) ratios are less than 1. Further, standard APT reconstruction algorithms indicate that the NF contains large quantities of Fe and Cr.

Table 1. Known Y-Ti-O complex oxides.

	Y-Ti-O	Crystal system	a (Å)	b (Å)	c (Å)	Reference code
1	Y_2TiO_5	orthorhombic	10.35	3.70	11.25	01-076-0787
2	Y_2TiO_5	hexagonal	3.61	3.61	11.84	00027-0981
3	$Y_2Ti_2O_7$	Cubic	10.09	10.09	10.09	01-072-0302
4	$YTiO_{2.085}$	Cubic	10.18	10.18	10.18	01-085-0001
5	$YTiO_3$	orthorhombic	5.33	5.62	7.60	01-070-2297
6	YTi_2O_6	orthorhombic	7.41	10.81	5.13	00-047-1786

In contrast, most previous TEM studies have indicated that the NF are complex oxides, primarily cubic pyrochlore $Y_2Ti_2O_7$. For example, scanning transmission electron microscopy (STEM) energy dispersive X-ray (EDX) measurements on NF extracted from NFA MA957, reported by Sakasegawa et al., indicate that the NF are non-stiochiometric $Y_2Ti_2O_7$, with Y/Ti < 1.0 for precipitates in the larger size range from up to 15 nm and Y/Ti ≈ 0.5 for the smallest pyrochlore features [14]. At largest sizes, from ≈ 15 to 35 nm, the oxides are closer to stiochiometric, with Y/Ti ≈ 1.0. Yamashita et al. also found non-stiochiometric $Y_2Ti_2O_7$, but generally with a range of Y/Ti slightly greater than 1 [15,16]. Klimiankou et al. found near stoichiometric $Y_2Ti_2O_7$ in a 9Cr NFA using electron energy loss spectroscopy (EELS), HRTEM-fast Fourier transform (FFT) power spectra indexing and energy filtered TEM (EFTEM) methods [17,18].

Early x-ray diffraction (XRD) studies by Okuda and Fujiwara also indicated the presence of $Y_2Ti_2O_7$ in a 14Cr model NFA [19]. This observation has been confirmed recently by Sasasegawa et al. based on XRD measurements on nano-pore filtered oxides extracted from a 9 Cr martensitic alloy [20]. Alinger et al. reported small angle neutron scattering (SANS) data on model NFA that were generally consistent with a mix of stoichiometric and/or non-stoichiometric oxides [5]. The SANS data also suggested that the range of

NF compositions strongly depend on the on the details of the alloy composition and processing conditions; the latter involved either hot isostatic pressing (HIPing) or powder annealing, over a range of temperatures (primarily from 850 to 1150°C) and with different time-temperature histories. Ohnuma et al. used a clever combination of SANS and small angle X-ray scattering (SAXS) to measure the composition and atom density of small NF in a 9Cr alloy, which were found to be consistent with $Y_2Ti_2O_7$ [21].

In fewer cases Y_2TiO_5 complex oxides have been reported, including one example for an NFA with lower alloy Ti contents [16], as well as in this work. Recently, Bhattacharyya et al. found a new phase in a model NFA following HIPing at 1150˚C for features in the size range from 10~50 nm [23]. HRTEM-FFT indexing showed this phase to be a probable variant of orthorhombic Y_2TiO_5, with Y/Ti ratios measured by EDX between 1 and 2. In addition, HRTEM-FFT indexing showed that small, < 5 nm $Y_2Ti_2O_7$ oxides form in NFA with the same alloy composition following HIPing at 850˚C. Studies by Ohtsuka et al. show the strong influence of the Y-Ti-O alloy composition on the structure, composition, number density and size distributions of NF [23,24]. More generally, variations in alloy compositions and processing conditions result in differences in the NF populations, suggesting that they can be manipulated to provide an optimal balance of mechanical properties and irradiation tolerance.

The previous studies described above have primarily involved characterization of larger NF with diameters (d) > 5 nm. Here we report on a detailed TEM study of a commercial vendor NFA, MA957, that extend the characterization NF to those with d < 5 nm. The MA957 was produced by INCO in the early 1980's for possible application in liquid metal breeder reactors [25]. The focus on MA957 is motivated by its role as a reference material in a wide variety of studies, using various characterization methods to examine the alloy's baseline properties and micro-nanostructures, as well as the corresponding effects of processing, joining, thermal aging and neutron or charged particle irradiations.

EXPERIMENTAL METHODS

Materials

TEM studies were carried out on 5 different MA957 conditions. Two base heats of INCO MA957 were examined in this study: a) a US heat of MA957 (US MA957) obtained from Pacific Northwest National Laboratory in the form of as extruded 25 mm diameter rods; and, b) a French heat of MA957 (FR MA957) obtained from the CEA Saclay via Oak Ridge National Laboratory. The US MA957 was also examined after: a) long term high temperature aging at 1000°C for ≈ 19.53 kh (LTTA); b) friction stir welding (FSW); and c) FSW plus annealing at 1150°C for 1 h (FSW-A). The nominal composition of MA957 is 14.9 Cr, 1.1 Ti, 0.17 Mo, 0.13 Y and 0.19 O from Y_2O_3 and ≈ 0.88 O overall, bal Fe (at.%), along with trace levels of impurity elements such as Al, Mn, Si and C. The main difference between the composition of MA957 and more recent NFA products is that the former contains Mo instead of W, and MA957 has a much higher Ti content. The base alloys were consolidated at approximately 1150°C. The FR MA957 was further processed by gun drilling and hot extrusion to form 65 mm outer diameter tubing, with a wall thickness of 9 mm. Additional processing details are not available. The LTTA of US-MA957 was carried out in a sealed tube with a He atmosphere at 1000°C. MA957 coupons were wrapped in high Cr stainless steel foil during aging to reduce the loss of this element. Approximately two millimeters of the sample was removed to avoid near surface effects. Sectioned plates of US-MA957 with dimensions of 100 × 17 × 2 mm^3 were butt-FSW in the long dimension direction at a tool spindle speed of 130-160 rpm and travel speed of 150-200 mm/min [26]. Material from the middle of the FSW zone was characterized. The FSW material was also annealed at 1150°C for 1 h (FSW-A). The basic microstructures and properties of these alloys have been described elsewhere [27,28].

TEM

The NF were characterized both in thin TEM foils, on extraction replicas, and in one case as bulk extractions in filters. The extractions were carried out two different methods. In the first case, the polished (0.3 μm alumina finished) surface of the MA957 was electrochemically etched with a solution of 1% tetra methyl ammonium chloride-10% acetyl acetone-methanol at a potential of ≈ 6 V [15]. The etched surface was then coated with a 10-20 nm carbon film. The carbon film containing NF was subsequently removed by a second electrochemical etching step and captured on a TEM grid. This method yields both isolated and a few clustered NF on the carbon extraction replica foils. The second method was to first C-coat the polished surface (without etching) and then to remove the C film by a single electrochemical etching process. This method yielded larger coagulated clusters of small NF in some cases. The first extraction method is useful for determining the size distributions on the NF, typically using high angle annular dark field (HAADF) imaging, as well as possible NF associations with each other and with other phases. However, the extractions do not provide reliable estimates of the NF number densities (N), in part due to the complex topology of the etched surfaces. The conventionally extracted particles were also examined using HRTEM and EDX to characterize the structure and composition of the NF, respectively. The second extraction method is useful for increasing the signal for both EDX and selected area diffraction (SAD) measurements on large clusters of small NF. In the case of the FR MA957 neither extraction method produced NF that could be reliably used for EDX. In this case, the two-step extraction was carried out on somewhat roughened surfaces to produce higher areal densities of NF consistent with EDX measurements. In addition 50 nm pore size filters containing NF removed from bulk extraction solutions, that were then flash burned and fabricated into electron transparent TEM specimens, were successfully used for EDX studies of the FR MA957.

There is of course an issue concerning the effect of the extraction process on the character of the NF. We believe that this is not a significant issue for the oxides themselves since they are stable under the non-acidic etching, and the their characteristics generally resemble those observed in foil. However, this does not address the question of possible segregation of elements like Ti or O to the oxide interfaces, the termination composition of the interface or the stability of the very smallest NF even at subunit cell sizes. These important questions will be addressed in future research. What is reported here is what is observed within the limitations of the various techniques.

Thin TEM foils were prepared by either a lift-out technique using a FEI Helios-focused ion beam (FIB) tool or by twin jet electro-polishing. We focus here on the FIBed specimens, since they are far superior to electro-polished samples, mainly because of their reduced magnetic mass. The final thickness of the FIBed foils was between 30 and 70 nm. A final, low energy Ga beam (2kVand 5.5pA) was used to remove the higher energy ion damage to achieve high quality samples. The HAADF studies were performed using an FEI TITAN at 300 kV. The in-foil studies involved conventional bright field diffraction contrast imaging and phase contrast HRTEM imaging that were performed on either an FEI TITAN at 300 kV or an FEI T20 TEM/EDX at 200 kV. EDX spectra were recorded on an FEI T20 in STEM mode with the stage tilted to 10˚, at a spot size of 3 or 4, and condenser aperture of 70 μm, which is the optimal experimental condition for measuring the composition of the small NF. Analysis of the HRTEM images was carried out by FFT power spectrum diffraction pattern indexing. The lattice spacing and inter-planar angles were measured by using Image J and Adobe Photoshop 6.0. The NF number densities were determined from the in foil micrographs. The foil thickness was measured by convergent beam electron diffraction. The size distributions of the NF were measured on both the conventional extractions and in foil specimens.

RESULTS

NF Number Densities, Size Distributions, Volume Fractions and Morphologies.

Figure 1 show examples of bright field (BF) in-foil TEM micrographs for the US (a) and French (b) MA957 NFA. Polyhedral NF are observed over a wide range of sizes and are qualitatively similar in both cases. The NF appears to be somewhat coarser in the US-M957, which also contains a higher dislocation density in this micrograph. The NF images are sharper in the FR MA957, but this is probably associated with the specific imaging conditions, rather than actual physical differences. Figure 2 shows the NF in the LTTA (1000°C for ≈ 19.53 kh) condition. While some small NF is still observed, coarsening is clearly observed after LLTA, and there is a large increase in the number of larger precipitates (> 10 nm). Figure 3 shows BF in-foil TEM images of NF in the FSW (a) and FSW-A (b).

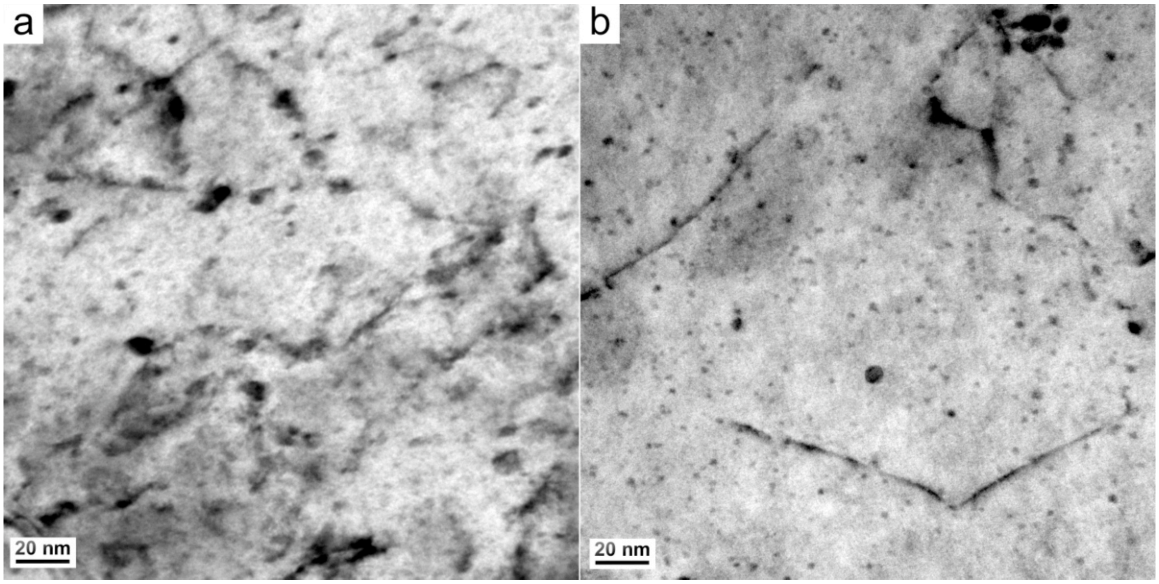

Figure 1. BF in-foil TEM images showing NF in US MA957 (a) and French MA957 (b).

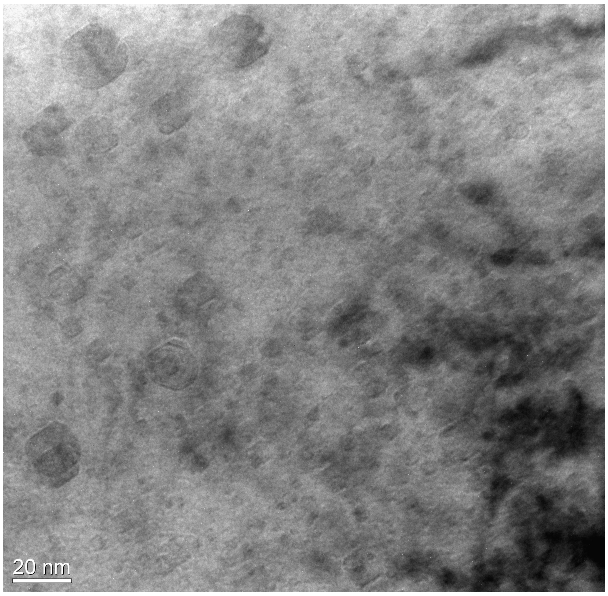

Figure 2. A BF in-foil TEM image showing NF in long-term thermal aging (LTTA) US MA957.

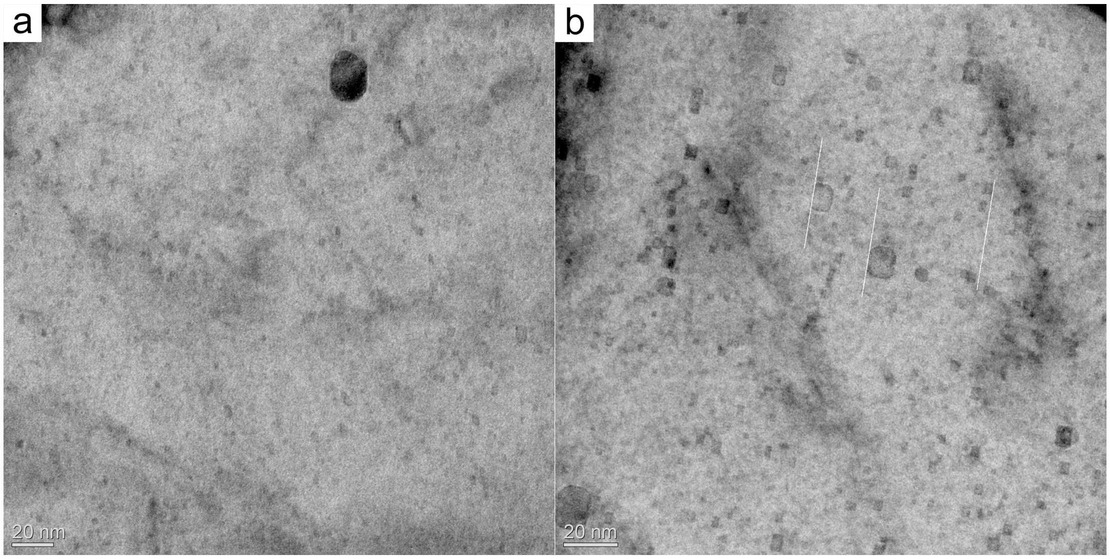

Figure 3. BF in-foil TEM images of NF in the FSW (a) and FSW-A (b) conditions.

Due to favorable imaging condition for the FSW-A sample, the NF are especially visible as truncated cubic polyhedral shapes, many with similar orientations with respect to the ferrite matrix. The NF is clearly visible down to ≈ 1 nm. The image was recorded near the <001> zone axis of the ferrite matrix, and the white dashed lines are the corresponding (100) planes. The NF number densities, N, were determined from the in-foil micrographs and are summarized in Table 2. The value of N is highest in the FR MA957 and lowest in the LTTA condition. The apparent N is nominally somewhat larger in the FSW-A condition compared to the as-extruded alloy.

Table 2. The number density and average diameter of the NF with d<10 nm in the five different MA957 conditions.

N, <d>	US MA957	French MA957	FSW	FSW-A	LTTA
N (10^{23}/m^3)	1.3	3.8	1.3	2.2	0.5
<d> (nm)	3.4	2.8	2.8	2.4	4.8

Figures 4 shows an example of a HAADF image of the conventional NF extractions from the FR MA957 that appear with white contrast owing to their larger average nuclear charge Z compared to the C foil. The HAADF imaging was useful in measuring the NF size distributions in the various MA957 conditions. The size distributions for the US and French-MA957 for both the in-foil and extracted NF are shown in Figure 4a and 4b. A comparison of the in foil NF size distributions for FR and US MA957 is shown in Figure 4c. In both cases, but particularly for US-MA957, the distribution is shifted to slightly larger sizes. In part this is believed to be due to agglomeration of the smaller extracted particles. The in-foil NF N = $1.3 \times 10^{23}/m^3$ and <d> = 3.4 nm for the US-MA957, versus N = $3.8 \times 10^{23}/m^3$ and <d> = 2.8 nm for the French-MA957. The corresponding average volume fractions are 0.40% and 0.61%, respectively.

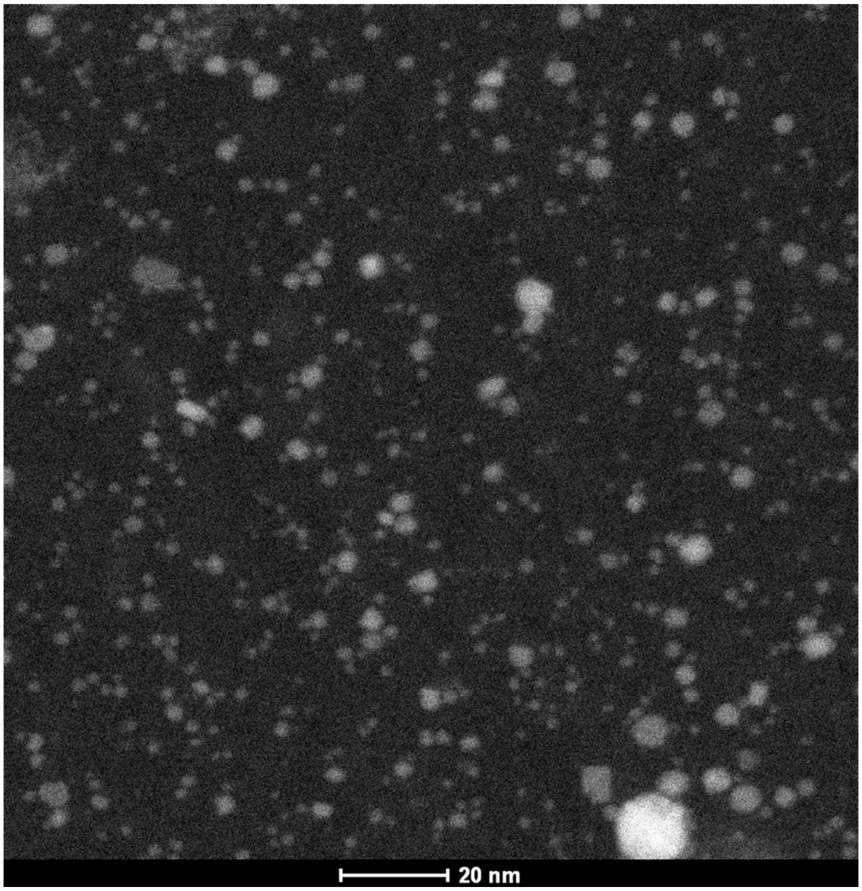

Figure 4. HAADF images of replica samples of French MA957.

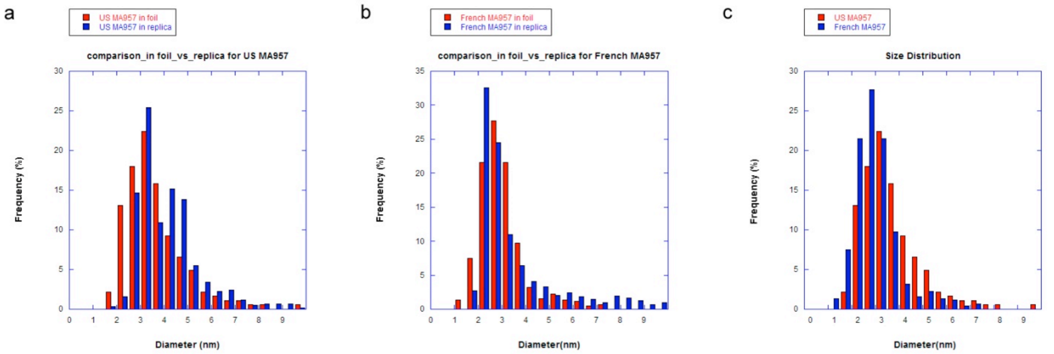

Figure 5. Comparison of in foil versus extraction replica NF size distributions in US MA957 (a) and French MA957 (b); in foil US MA957 and French MA957 NF size distributions (c).

Figure 6 shows the in-foil NF size distribution for the US-MA957 in the as extruded and LTTA condition. Significant coarsening is evident, with an increase in the average diameter from <d> = 3.4 to 4.8 nm, accompanied by a reduction in N from ≈ 1.3×10^{23} to $0.5 \times 10^{23}/m^3$. Figure 7 shows the corresponding effects of FSW (a) and FSW-A (b) on the in foil NF size distributions in US-MA957. The N and <d> for the FSW are $1.3 \times 10^{23}/m^3$ and 2.8 nm, respectively, compared to the same nominal N and slightly larger <d> = 3.4 nm in the as-extruded condition. The apparent N = $2.2 \times 10^{23}/m^3$ is larger in the FSW-A condition and the <d> = 2.4 nm is slightly smaller. This possible refinement may suggest some dissolution of the solutes during severe deformation and re-precipitation upon annealing. The small differences in NF sizes measured by TEM are consistent with independent APT and SANS data [28]. However, the latter two methods suggest reductions in N by 10% (APT) to 50% (SANS, but method this is less reliable in this case) in the FSW condition and a 50% reduction in the APT N for the US MA957 FSW-A condition.

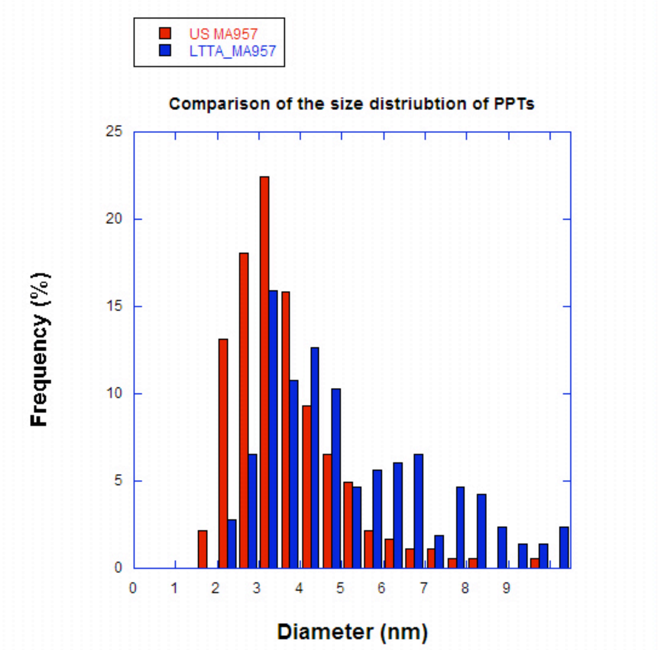

Figure 6. Comparison of the NF size distributions in the as extruded and LTTA US MA957.

It is important to put the apparent similarities and differences in the various MA957 conditions cited above in perspective. Specifically the NF populations can vary significantly over length scales of tens of nm to µm and there are limitations in all the characterization methods. Thus the most robust conclusions are that the NF are qualitatively similar in all cases, with discrete phase polyhedral morphologies from <d> ≈ 1 to > 10 nm. The NF in the US MA-957 may be slightly coarser (larger <d> and smaller N) than in the French-MA957. The NF are only moderately affected, but perhaps slightly refined and redistributed, in the FSW and FSW-A conditions. However, LTTA results in significant coarsening, as reflected in a significantly larger <d> and smaller N.

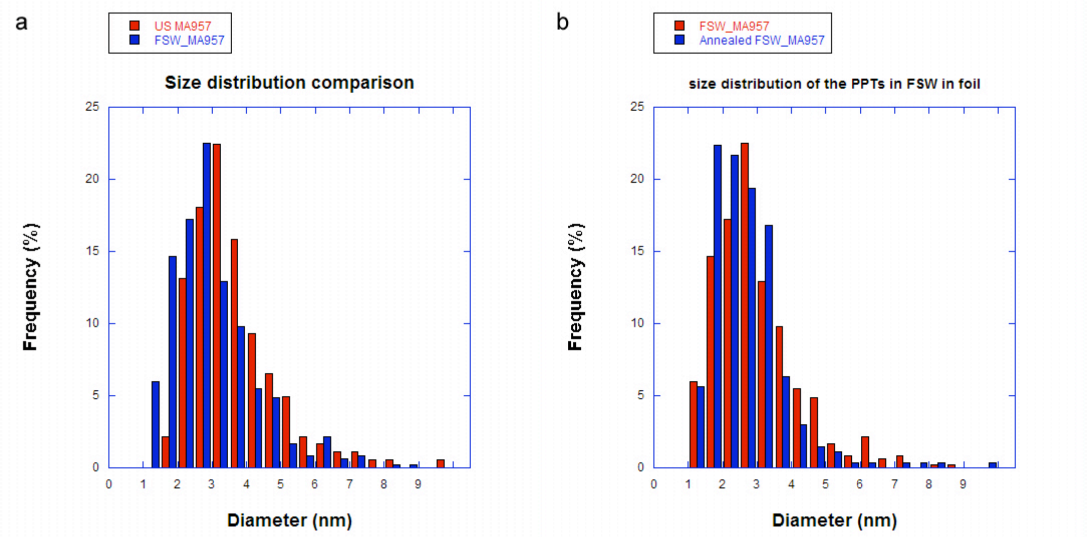

Figure 7. Comparison of the NF size distributions in the as extruded and FSW US MA957 (a); comparison of the NF size distributions in the FSW MA957 and FSW-A US MA957 (b).

The Structure and Composition of the NF in the French and US-MA957

Figure 8 shows an HRTEM image (a) of a rather large feature (d ≈ 12 nm) in the US MA957 along with the corresponding FFT power spectrum diffraction pattern (b). Table 3 shows the corresponding measured inter-planar distances and angles. These results are not consistent with either cubic $Y_2Ti_2O_7$ or hexagonal Y_2TiO_5 or YTi_2O_6. However, the diffraction data are much more consistent with orthorhombic Y_2TiO_5 <1 -15 4> or $YTiO_3$ <2 1 -2>. An even larger ≈ 20 nm feature shown in Figure 8c was not found to be consistent with any known Y-Ti oxide phase. As shown below, EDX results the features in the size range above ≈ 5 nm show Y/Ti ratios from ≈ 1.0 to 2.0. Figure 9 shows an HTREM images (a,c) and corresponding diffraction patterns (b,d) for slightly smaller ≈ 5 to 6 nm NF in the FR MA957. As shown in Table 4a the inter-planar spacing and angles are reasonably consistent with the $Y_2Ti_2O_7$ <011> (b) and <001> (d) zone axes. Similarly, a HRTEM image of a small precipitate was indexed as $Y_2Ti_2O_7$ with a <245> zone axis, as shown in Table 4b. Table 5 summarizes the results of the HRTEM FFT structure analysis of individual NF. While a large number of NF (d < 10 nm) were examined only 7 could be individually identified as possible orthorhombic Y_2TiO_5 phases in the US MA-957, and two Y_2TiO_5 plus 4 $Y_2Ti_2O_7$ NF in the FR MA957.

Figure 10 shows an example EDX spectrum for one of the smaller (d < 10 nm) extracted oxides from the US MA957, indicating that it is predominately composed of Y, Ti and O, with an average Y/Ti/O ratio of 22/16/62. Table 5 also summarizes the average Y/Ti/O compositions from EDX measurements for the US and FR MA957 for the smaller individual extracted oxides. The number of oxides measured is given in brackets in the second column. The average Y/Ti(≈ 1.4) ratio is higher in the US-MA957. The Y/Ti is lower in the French-MA957 (≈ 1.2), and is closer to stoichiometric $Y_2Ti_2O_7$. Note these compositions do not, in general, suggest that there is a mixture of $Y_2Ti_2O_7$ and Y_2TiO_5 phases, since the compositions vary from stoichiometric values for the individual oxides. In-foil EDX on the three oxides in the FSW and annealed MA957, shown in Figure 11, with d ≈ 13.4, 9.2 and 5.2 nm, have Y/Ti ratios of 2, 0.9 and 0.8, respectively. The largest oxide is compositionally consistent with Y_2TiO_5, while the latter are more likely slightly non-stoichiometric $Y_2Ti_2O_7$.

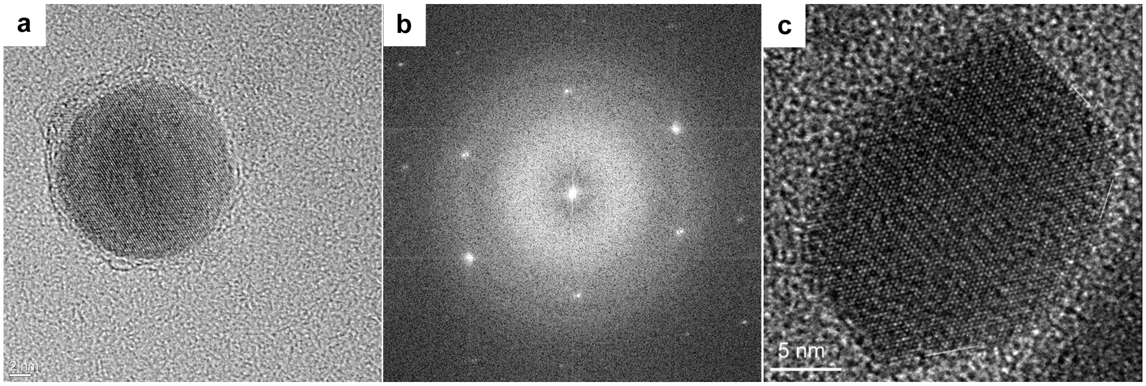

Figure 8. A HRTEM lattice image of a large feature in US MA957 (a) and the corresponding FFT power spectrum, (b) HRTEM lattice image of a large unidentified precipitate, and (c).

Table 3 measured and calculated inter-planar distances (d) and angles (a) in Fig. 8 and possible indexing.

d (Å), a	d_1	d_2	d_3	a_{12}	a_{13}	a_{23}
Measured	2.55	2.15	2.20	61.5°	66.7°	51.8°
Y_2TiO_5(o)	2.52 {401}	2.09 {313}	2.18 {1-1-4}	62.2°	67.6°	50.2°
$YTiO_3$(o)	2.50 {-120}	2.09{202}	2.18 {122}	62.3°	67.3°	50.4°

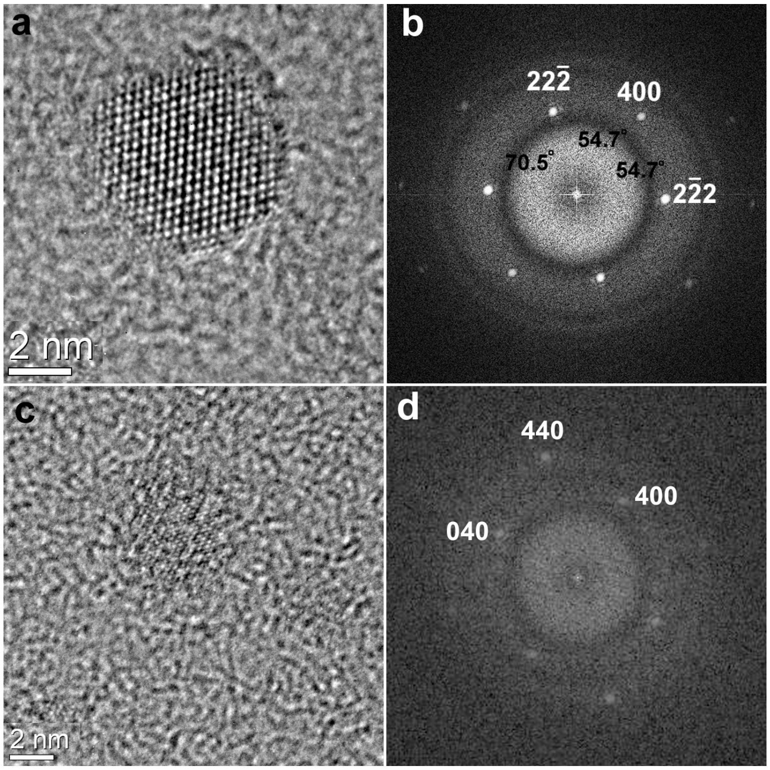

Figure 9. HRTEM lattice images of small NF in French MA957 (a, c) and the corresponding FFT power spectra (b, d).

Table 4a. Measured and calculated inter-planar distances (d) and angles (a) for Fig.9a and possible indexing.

d (Å), a	d_1{2-22}	d_2{400}	d_3{22-2}	a_{12}	a_{23}	a_{31}
Measured	2.96	2.60	3.09	53.4°	55.6°	71.0°
$Y_2Ti_2O_7$	2.90	2.52	2.90	54.7°	54.7°	70.5°

Table 4b. Measured and calculated inter-planar distances (d) and angles (a) for Fig.9c and possible indexing.

d (Å), a	d_1{400}	d_2{440}	d_3{040}	a_{12}	a_{13}
measured	2.52	1.78	2.52	45.15°	90°
$Y_2Ti_2O_7$	2.65	1.87	2.65	45°	90°

Table 5. Summary of HRTEM and EDX results from individual NF (d < 10 nm).

MA957	<Y/Ti/O (#)	Phase				
		Unknown	Not Indexed	Pos. Y_2TiO_5	Pos. $Y_2Ti_2O_7$*	Pos. $Y_2Ti_2O_7$
FR	23/19/58 (27)	4	17	0	1	4
US	21/15/64 (12)	3	61	2	5	6

* Only one set of planes

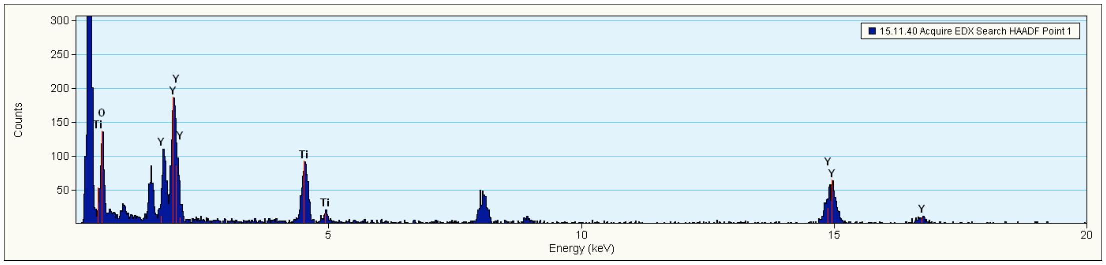

Figure 10. An example of an EDX spectrum for a small (d ≈ 10 nm) NF.

HRTEM and EDX characterization of the structure of individual NF in the range of d < 5 nm is more difficult. Thus we have used the second replica extraction procedure to produce higher local densities or aggregated clusters of NF that were characterized by HRTEM, selected area diffraction (SAD) and EDX. Figure 12a shows an example of high local densities of polyhedral NF extracted from US MA957. Figure 12b shows a SAD pattern taken for the group of small particles. In this case the SAD has been calibrated to a GaN standard shown in Figure 12c. Table 6 shows that the SAD rings indicate NF d-spacings that are highly consistent with $Y_2Ti_2O_7$. HRTEM FFT power spectra on groups of these oxides yield similar results.

Table 6. Summary of d spacing's measured from the SAD ring pattern shown in Fig. 12(b).

Compound	hkl	Measured	Calculated
GaN Standard	100	2.763	2.763
$Y_2Ti_2O_7$	222	2.926	2.91
$Y_2Ti_2O_7$	400	2.563	2.52
$Y_2Ti_2O_7$	440	1.798	1.78
$Y_2Ti_2O_7$	622	1.540	1.52

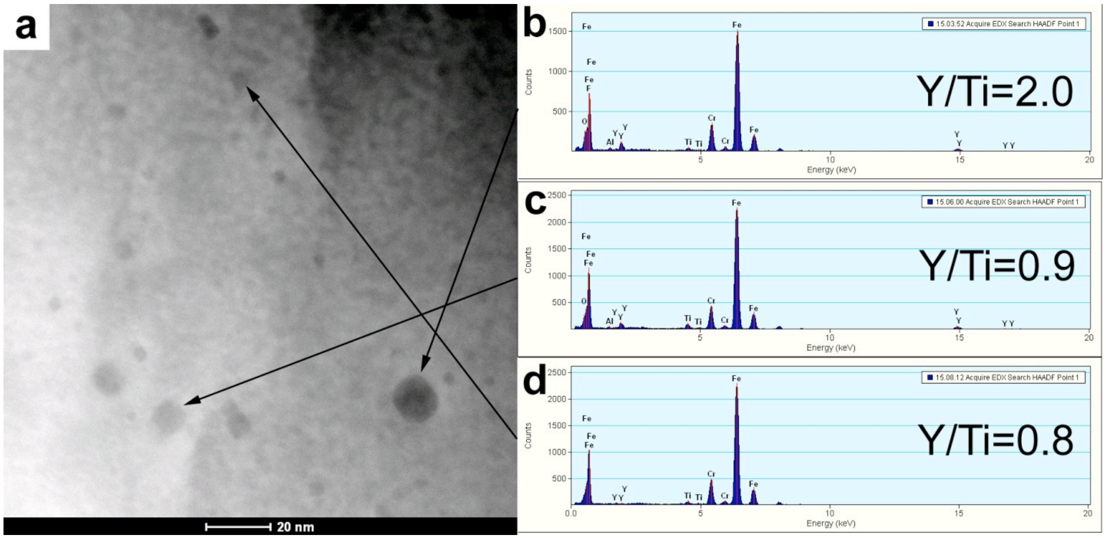

Figure 11. A HAADF image of FSW-A US MA957 (a) and corresponding EDX on the three indicated NF (b, c, d).

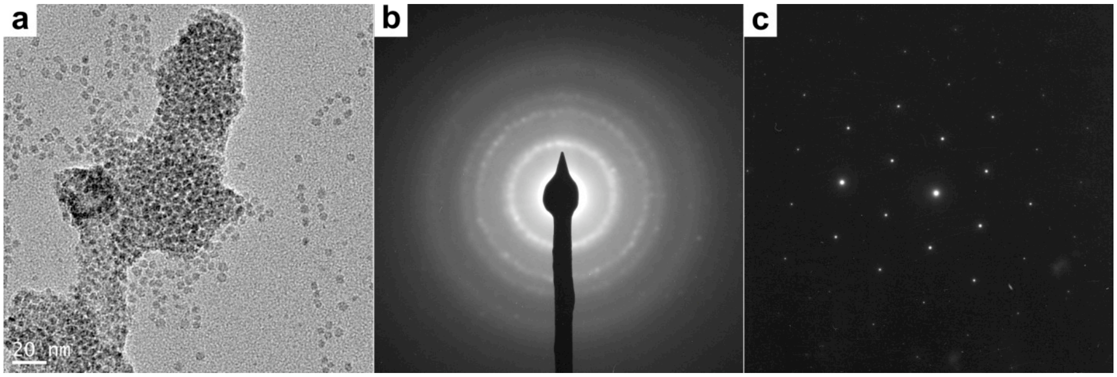

Figure 12. An example of high local densities of polyhedral NF extracted from US MA957 by the second replica method (a); a SAD pattern taken for the clump of particles (b); the SAD has been calibrated to a GaN standard (c).

Figure 13a shows a cluster of oxides and Figure 13b the corresponding EDX measurements. The aggregate compositions are 15.5% Y (L), 15.4% Ti (K), 1.1% Cr (K) and 68% O (K). These values are very close to the composition of $Y_2Ti_2O_7$ 18.2% Y, 18.2% Ti and 63.6% O. EDX of the small precipitates in the FR MA957 were carried out on both rough surface two-step extractions and the filtered bulk extractions. The EDX Y/Ti ratio also averages ≈ 1 in these cases.

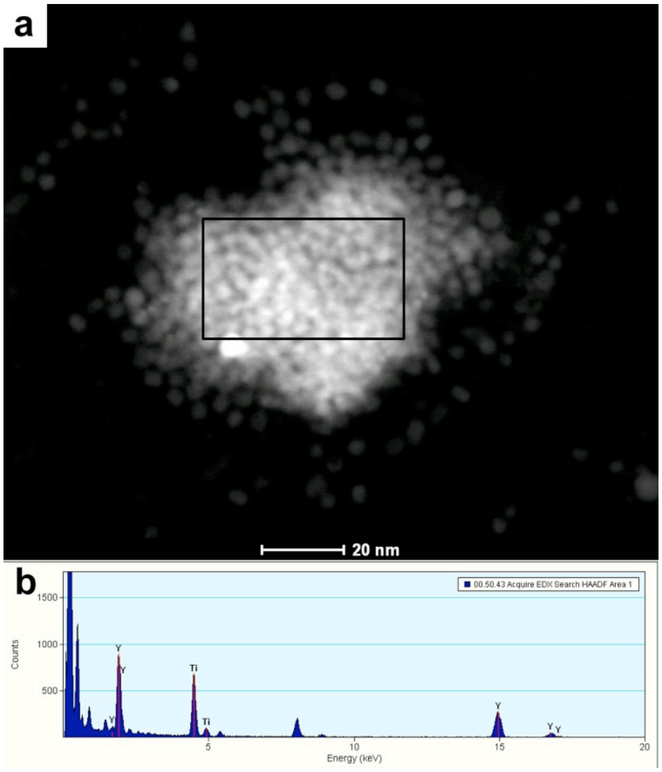

Figure 13. A HAADF image of a cluster of small NF (a); andm the corresponding EDX spectrum (b).

DISCUSSION, SUMMARY AND CONCLUSIONS

The sizes (d) and number densities (N) of the NF appear to be generally similar in the FR and US MA957 heats. TEM indicates that the FSW and FSW-A conditions are also similar to one another and to the parent as extruded US MA957. However, it is noted that the in foil estimates of the N for US-MA957 found here are somewhat lower than previously reported [28]. Further, SANS and APT data suggest that there is a more significant decrease in N in the FSW and, especially, the FSW-A conditions than indicated by the current TEM data. LTTA at 1000°C for 19.53 kh coarsens the NF with a significant increase in <d> and decrease in N, consistent with trends observed in APT and SANS studies [29].

The HRTEM-FFT, SAD and EDX data indicate that the smallest (d < 5 nm) NF in MA957 are cubic pyrochlore $Y_2Ti_2O_7$ complex oxides, broadly consistent with most previous TEM and XRD observations of larger precipitates in similar alloys. BF TEM suggests that the NF have an orientation relationship (OR) with the (100) planes in the Fe-Cr ferrite matrix. Work is continuing to establish the full OR, including the corresponding oxide interface planes and directions.

Notably, the TEM results are inconsistent with interpretation of AP data that suggest that the NF are far from equilibrium, perhaps coherent, transition phase solute clusters with much lower Y/Ti and O/(Ti + Y) ratios as well as very high Fe and Cr contents even in the center of small NF. Thus, we believe that the conclusion regarding their being an APT Fe-Cr content artifact is robust. However, the observations reported here do not address the possibility that solutes segregated to the NF interfaces, perhaps forming a $Y_2Ti_2O_7$ oxide and a Ti and O enriched shell.

REFERENCES

1. S. J. Zinkle and J. T. Busby, *Mater. Today* **12**, 12-11 (2009).
2. G. R. Odette, M. J. Alinger, and B. D. Wirth, *Annu. Rev. Mater. Res.* **38**, 471 (2008).
3. G. R. Odette and D. T. Hoelzer, *JOM* **62**, 84 (2010).
4. G. R. Odette, P. Miao, D. J. Edwards et al., “Helium Transport, Fate and Management in Nanostructured Ferritic Alloys: In Situ Helium Implanter Studies,” *J. Nucl. Mater.* (2010) in press.
5. M. J. Alinger, G. R. Odette and D. T. Hoelzer, *Acta Mater.* **57**, 392 (2009).
6. N. J. Cunningham, G. R. Odette and E. Stergar, Fusion Materials Semiannual Progress Report for the Period Ending December 31, 2010, DOE-ER-0313/49 (2011) 1.
7. M. K. Miller, D. T. Hoelzer, E. A. Kenik, and K. F. Russell. *J. Nucl. Mater.* **329**, 338 (2004).
8. M. K. Miller, D. T. Hoelzer, E. A. Kenik, and K. F. Russell, *Intermetallics* **387**, 133–134 (2005).
9. M. K. Miller, K. F. Russell, and D. T. Hoelzer, *J. Nucl. Mater.* **351**, 261 (2006).
10. M. K. Miller, E. A. Kenik, K. F. Russell, L. Heatherly, D. T. Hoelzer, and P. J. Maziasz, *Mater. Sci. Eng. A* **353**, 140 (2003).
11. P. Pareige, M. K. Miller, R. E. Stoller, D. T. Hoelzer, E. Cadel, and B. Radiquet, *J. Nucl. Mater.* **360**, 136-43 (2007).
12. E. A. Marquis, *Appl. Phys. Lett.* **93**, 181904 (2008).

13. C. A. Williams, E. A. Marquis, A. Cerezo and G. D. W. Smith, *J. Nucl. Mater.* **400**, 37 (2010).
14. H. Sakasegawa, L. Chaffron, F. Legendre, L. Boulanger, T. Cozzika, M. Brocq, and Y. de Carlan, *J. Nucl. Mater.* **384**, 115 (2009).
15. S. Yamashita, S. Ohtsuka, N. Akasaka, S. Ukai, and S. Ohnuki, Phil. Mag. Lett, **84**, 525 (2004).
16. S. Yamashita, N. Akasaka, and S. Ohnuki, *J. Nucl. Mater.* **329**, 377 (2004).
17. M. Klimiankou, R. Lindau, and A. Möslang, *J. Nucl. Mater.* **329**, 347 (2004).
18. M. Klimiankou, R. Lindau, and A. Möslang, *Micron*, **36**, 1 (2005).
19. T. Okuda and M. Fujiwara, *J. Mater. Sci. Letts.* **14**, 1600 (1995).
20. H. Sakasegawa, M. Tamura, S. Ohtsuka, S. Ukai, H. Tanigawa, A. Kohyama, M. Fujiwara, J. Alloys and Compounds **452**, 2 (2008).
21. M. Ohnuma, J. Suzuki, S. Ohtsuka, S.-W. Kim, T. Kaito, M. Inoue, H. Kitazawa, Acta Materialia **57**, 5571 (2009).
22. D. Bhattacharyya, P. Dickerson, G. R. Odette, S. A. Maloy, A. Misra, and M. A. Nastasi, this report.
23. S. Ohtsuka, S. Ukai, M. Fujiwara, T. Kaito, and T. Narita, *J. Nucl. Mater.* **329**, 372 (2004).
24. S. Ohtsuka, S. Ukai, M. Fujiwara, T. Kaito, and T. Narita, *J. Phys. Chem. of Solids* **66**, 571 (2005).
25. J. J. Fisher, “Dispersion Strengthened Ferritic Alloy for Use in Liquid-Metal Fast Breeder Reactors,” U.S. Patent No. 4,075,010 (1978).
26. J. Bernath and J. Gould, Report on Development of Candidate Joining Technology for MA957 Sheet, Edison Welding Institute, Columbus, OH, USA, March 2005.
27. P. Miao, G. R. Odette, T. Yamamoto, M. Alinger, and D. Klingensmith, *J. Nucl. Mater.* **377**, 59 (2008).
28. A. Etienne, N. J. Cunningham, Y. Wu and G. R. Odette, Mater. Sci. and Tech. 724, 27-4 (2011).

1.4 Inter-Laboratory Atom Probe Tomography Characterization Study of the Nanofeatures and the Bulk and Matrix Compositions of US MA957 — N. J. Cunningham, G. R. Odette (Univ. California Santa Barbara), E. Stergar (University of Leoben),[1] E. A. Marquis (Oxford University),[2] A. Etienne, C. Hatzoglou, B. Radiguet and P. Pareige (University of Rouen)

OBJECTIVE

The objective of this work was to carry out an inter-laboratory comparison of the nano-features (NF) and bulk and matrix compositions of a reference nano-structured ferritic alloy (NFA) characterized by atom probe tomography (APT) at four institutions. The reference NFA was an as-extruded heat of US MA957.

SUMMARY

APT studies were carried out at the University of California Santa Barbara (UCSB), University of Leoben (UL) in Austria, Oxford University (OU) in England and University of Rouen (UR) in France. The tools used at UCSB, OU and LU were all Cameca (previously Imago) HR3000X-HR Local Electrode Atom Probes (LEAPs), while the fourth instrument at Rouen was a Camaca Laser Assisted Wide Angle Tomographic Atom Probe (LAWATAP). The measurements reported by the various APT groups are in remarkable agreement with one another. The bulk average compositions (at.%) for Fe, Cr, Ti, Y and O are: 83.6±0.39, 14.8±0.46, 0.771±0.059, 0.064±0.022 and 0.273±0.031, respectively. The corresponding matrix Fe, Cr, Ti, Y and O are, respectively: 84.1±0.283, 14.7±0.212, 0.636±0.021, 0.017±0.001 and 0.109±0.020. The average NF compositions, based only on their Y, Ti and O contents (at.%), are 13.9±0.92 Y, 41.6±3.34 Ti and 45.4±4.77 O, respectively. The corresponding average NF number density (N) and average diameter (<d>) are: 5.1±1.06x10^{23}/m^3 and 2.72±0.56 nm, respectively.

PROGRESS AND STATUS

Experimental Methods

Data was collected using a range of experimental conditions. Similarities and differences in the various APT methods are briefly summarized here, but will be discussed in much greater detail in future publications. The compositions of the matrix and overall bulk were evaluated, along with the composition, number density (N) and diameters of the NF; the mean diameter is reported here, <d>. Not all of these measurements are available from all the participating institutions at this time, so this should be considered to be a preliminary report. The data analysis is continuing along with some additional APT measurements. In total, volume equivalent to ≈ 500x10^6 atoms were probed in this study.

Samples at UCSB were prepared by either electropolishing or using an FEI Helios 600 focused ion beam (FIB) instrument, while all samples prepared RU and LU were electropolished. LEAP measurements at all three institutions were performed in voltage or laser mode with a 200 to 250 kHz pulse rate and 0.5 to 1% target evaporation ratio. The analysis conditions at UCSB ranged from 0.05 to 0.5 nJ laser pulse energy, temperatures between 33 and 70 K and a 20 to 25% pulse fraction. All the samples at LU were run in laser pulsing mode at energies between 0.1

---

[1] Current institution, University of California, Santa Barbara and Berkeley

[2] Current institution, University of Michigan

and 0.3 nJ and temperature between 33 and 58 K. At Oxford samples were run in either voltage mode (25°K and 15%) or in laser pulsing, typically at 40-50°K and 0.4 nJ to minimize the Fe*/Fe^{2+} ratio. LAWATAP measurements at UR used a laser pulse rate of 100 kHz, at a laser power of either 0.14 or 0.19 nJ at 50 K. In the later case, the laser energies were set to get a laser pulse equivalent to a voltage pulse fraction of 20%. It should be noted that the laser spot size is larger in the LAWATAP, hence the corresponding energy density is significantly lower than in the laser LEAP measurements.

The LEAP data were analyzed using the IVAS software package, while the LAWATAP results were analyzed with the GRM 3D Data Software developed by the Group of the Physics of Materials (GPM) at UR. In all the IVAS reconstructions, the NFs were identified and their compositions were determined using the maximum separation distance method for the solute ions of interest, Y, Ti and O, including their ionic forms like TiO and YO [1]. All these solute ions in a cluster were used to determine the radius of gyration (l_g), which is related to an estimated physical spherical radius as $r_{sphere} = 1.29l_g$ [2,3]. At OU the clusters were identified using the TIO and YO molecular species. Cluster compositions were measured with a $L= d_{max}$ and $e = d_{max}/2$. The cluster compositions were calculated after removing all of the Fe atoms and other elements proportionately to the matrix composition. At UR cluster atoms were identified by using a grid to divide the analyzed volume into small cubes, first calculating the concentration of solutes in each cube, and then assigning a concentration value to each ion using linear interpolation based on its proximity to the center of the surrounding cube volumes. Atoms at concentrations greater than a specified limit were considered to be in the cluster. The NF number density was calculated using the total number of ranged atoms in the measured volume. NFs on the edge of the volume were counted as one-half.

The mass spectrum for MA957 has many overlapping and interfering peaks. In order to obtain better estimates of composition, where possible the natural isotope abundance and the ion counts in the most isolated peaks were used to establish the contributions from the same element with overlapping peaks. Large post-peak tails, especially from Fe^{+2} isotopes, overlap the peaks for Y^{+3} and some TiO^{+2}. The numbers of ions in these smaller peaks were found by subtracting off the post peak Fe^{+2} tail.

Results

Table 1 summarizes the bulk composition measurements for the key matrix and solute elements Fe, Cr, Ti, Y, O and Mo. The numbers for the various labs are the un-weighted averages of the individual APT measurements that collectively result in the total of the number of ions collected that are also shown in the Table. The overall averages of the different labs are: 83.6±0.39 Fe, 14.8±0.46 Cr, 0.771±0.059 Ti, 0.064±0.022 Y, 0.273±0.032 O, and 0.158±0.016 Mo. The standard deviations (SD) are relatively small in all cases. Table 2 summarizes the matrix compositions, defined, as the solute atoms not included in the NF clusters. The averages are 84.1±0.283 Fe, 14.7±0.212 Cr, 0.636±0.021 Ti, 0.017±0.001 Y, 0.109±0.020 O and 0.143±0.017 Mo. The matrix composition SD are again all relatively small.

Table 1. APT bulk average compositions of MA957 (at%).

Lab	Fe	Cr	Ti	Y	O	Mo	10^6 ions
UCSB	83.4	14.8	0.831	0.054	0.296	0.143	57.1
Rouen	83.3	15.2	0.771	0.049	0.287	0.155	32.6
Leoben	84.0	14.3	0.713	0.089	0.236	0.174	70.0
Av	83.6	14.8	0.771	0.064	0.273	0.158	-
SD	0.39	0.46	0.059	0.022	0.032	0.016	-

Table 2. APT matrix average compositions of MA957 (at%).

Lab	Fe	Cr	Ti	Y	O	Mo	10^6 ions
UCSB	84.0	14.8	0.651	0.017	0.092	0.108	9.7
Rouen	83.9	15.0	0.636	0.015	0.123	0.162	32.6
Oxford	84.4	14.5	0.622	0.019	0.114	0.160	TBD
Av	84.1	14.7	0.636	0.017	0.109	0.143	-
SD	0.283	0.212	0.021	0.001	0.020	0.037	-

Based on standard analysis the NF nominally contains large quantities of matrix Fe and Cr. For reasons that will be discussed in detail in future publications, and which are also the subject of a growing literature [for example see 4,5] the large quantities of NF Fe and, at least to a significant extent Cr, are believed to be artifacts of the APT method. These artifacts are primarily associated with so-called trajectory aberrations that artificially insert matrix ions into the NF volume in the case of features that have a lower evaporation potential than the bulk ferrite phase [6,7]. Thus we focus here on the Y, Ti and O ions that are the ingredients of the complex oxides like $Y_2Ti_2O_7$ that are known to form the core of NF in NFA [6]. The average NF compositions for the various labs are shown in Table 3. The overall average solute values are: 13.9±0.81 Y, 41.9±3.19 Ti and 44.2±4.65 O. Thus the compositions of the NF are also very similar in all cases. The corresponding average Y/Ti ratio is 0.33 and the average (Y+TI)/O ratio is 1.24. Notably these values are inconsistent with known Y-Ti-O complex oxides, like cubic pyrochlore $Y_2Ti_2O_7$ and orthorhombic Y_2TiO_5.

Table 4 shows that the various APT measurements NF N and <d> are also in reasonably good agreement with one another. The overall averages are N = $5.1\pm1.06\text{x}10^{23}/\text{m}^3$ and <d> = 2.72±0.56 nm. The only apparent systematic difference is that the <d> is significantly larger in the case of the LAWATAP (RU) results, with <d> =3.36 nm, compared to the average of 2.38 for the LEAP measurements at UCSB and LU.

Table 3. APT NF Y-Ti-O solute compositions (%).

Lab	Y	Ti	0	10^6 at
UCSB	14.4	45.6	39.9	57.1
Rouen	14.3	40.7	45.0	32.6
Leoben	14.4	44.0	42.0	65
Oxford	12.5	37.3	52.2	NA
Aver	13.9	41.9	44.8	-
SD	0.81	3.19	4.65	-

Table 4. APT NF number densities (N) and average diameters (<d>).

Lab	N ($10^{23}/m^3$)	<d> (nm)	# Clust
UCSB	3.9	1.18	805
Rouen	6.6	1.68	404
Leoben	5.7	1.21	823
Oxford	4.4	-	TBD
Aver	5.1	1.36	
SD	1.06	0.28	-

ANALYSIS AND DISCUSSION

A detailed analysis and interpretation of these results will be presented in a future publication. However, it is useful to briefly examine the implications of these observations. First, APT measurements clearly can be very precise, and overall do not seem to be highly dependent on the individual laboratory where they are carried out. However, being precise does not necessarily translate to being accurate if the technique implicitly shares common limitations, anomalies and artifacts. For example it is now established by TEM, in the size range where the two techniques overlap, that the NF in MA957 consist of the pyrochlore $Y_2Ti_2O_7$ complex oxide, with a Y/Ti ratio ≈ 1, rather than the 0.33 observed in APT [6]. The (Ti+Y)/O ratio is harder to establish with TEM but is lower for $Y_2Ti_2O_7$ at ≈ 0.57 than observed by APT at ≈ 1.24. Discussion of the limitations that might lead to these apparent discrepancies are beyond the scope of this short report. However, we will further analyze the results to probe possible explanations of APT observations and to gain additional insight.

Table 5 shows the nominal overall chemical composition of the MA957 along with the average APT bulk and matrix compositions. The bulk compositions of Y, Ti, O and C are significantly lower than the nominal alloy chemistry. This may be due to the sequestering of these elements in a low number density of coarse phases, such that the probability of encountering them in APT study is very low. Alternatively, the APT may undercount some of these elements. Table 5 also shows the difference between the APT bulk and matrix compositions. The differences are small except in the case of Y, Ti and O, consistent with the fact that these elements are associated with the phase separated NF. The fraction of these solutes that are presumably associated with the NF is 0.23, 0.75 and 0.61 of the bulk composition for Ti, Y and O, respectively. Table 6 summarizes the estimated NF solute contents based on the atomic fraction differences (%), consisting of 0.143 Ti, 0.049 Y and 0.17 O, respectively. Table 7 summarizes various estimates of the NF volume fraction (f_{nf}) in various ways. In the first case, the f_{nf} is estimated to simply be the sum of the Y, Ti and O differences between the bulk and matrix, which is f_{nf} ≈ 0.36%. In the second case it is assumed that the Y, Ti and O reside in a stoichiometric $Y_2Ti_2O_7$ oxides with a density of 4.98 g/cm^3, based on the Y estimated to be in the NF, giving $f_{nf} \approx 0.28\%$. The two other estimates of f_{nf} are based on the Ti and O NF $Y_2Ti_2O_7$ contents, resulting in $f_{nf} \approx 0.81$ and 0.16%, respectively. These estimates of f_{nf} are somewhat lower than SANS measurements with $f_{nf} \approx 0.92 \pm 0.08$, except for the estimate based on Ti. Table 8 compares the estimated NF Y/Ti and (Y+Ti)/O ratios based on both direct evaluations of the clusters and the solute atomic balance estimates. The agreement is remarkably good, although the two evaluations are not completely independent of one other.

Table 5. Averages solute location and differences including some trace elements (%).

Loc	Fe	Cr	Ti	Y	O	Mo	Mn	Si	C	Al
Chem	83	14.3	1.12	0.128	0.79	0.17	0.065	0.059	0.073	0.183
Bulk	83.6	14.8	0.779	0.065	0.281	0.157	0.066	0.069	0.006	0.038
Matr	84.1	14.7	0.636	0.017	0.109	0.143	0.057	0.076	0.005	0.022
Diff	-0.50	0.031	0.143	0.049	0.172	0.014	0.009	-0.006	0.001	0.016
Dif/Av	-0.01	0.00	0.18	0.75	0.61	0.09	0.14	-0.09	0.17	0.42

Table 6. Y, Ti, O solute balances estimates of f_{nf} (%).

Location/Solute	Ti	Y	O
Bulk	0.779	0.065	0.281
Matrix	0.636	0.017	0.109
Estimated in NF	0.143	0.049	0.172

Table 7. Solute balance estimates of NF volume fractions (f_{nf}) and solute ratios.

f_{nf}(%), Y/Ti, (Y+Ti)/O	
f_{nf} from Y+Ti+O	0.36
f_{nf} from $Y_2Ti_2O_7$ and Y	0.28
f_{nf} from $Y_2Ti_2O_7$ and Ti	0.81
f_{nf} from $Y_2Ti_2O_7$ and O	0.16

Table 8. Comparison of NF Y/Ti and (Y+Ti)/O ratios from APT evaluations (DE) of the clusters and atomic mass balance estimates (MB).

Ratios	Clusters	Atomic Balances
Y/Ti	0.33	0.34
(Y+Ti)/O	1.24	1.12

CONCLUSIONS

An inter-laboratory round robin APT study of the bulk, matrix and NF compositions of a US heat of MA957 showed that the results found by the four participants are generally in excellent agreement with one another. The agreement is also good for the number densities of the NF. There is a more significant difference in the LAWATAP evaluation of the average NF diameter, which is significantly larger than observed in the LEAP measurements. This difference could come from the tools used for the data analysis. Some LEAP data will be analyzed with the GPM 3D Software to clarify this point. Solute atom fraction based estimates of the NF volume fractions are reasonable but somewhat lower than the estimates based on SANS. However, direct APT evaluation of the NF composition is in good agreement with indirect estimates based on the differences between bulk and matrix Y, Ti and O contents. Both indicate an Y/Ti ratio of ≈ 0.33±0.01 and a (Y+Ti)/O ≈ 1.18±0.06.

FUTURE WORK

The data analysis will be completed and a few additional measurements will be carried as needed. A paper on these results will be prepared for journal publication. This paper will be expanded to discuss APT issues, anomalies and artifacts.

REFERENCES

1. D. Vaumousse, Cerezo, A., Warren, P. J., *Ultarmicroscopy* **95**, 215 (2003).
2. M. K. Miller, *Atom Probe Tomography: Analysis at the Atomic Level*, Kluwer Academic/Plenum Publishers, New York (2000).
3. R. P. Kolli, and Seidman, D.N., *Microsc. Microanal.* **13**, 272 (2007).
4. E. A. Marquis, *Appl. Phys. Lett.* **93** (2008).
5. C. A. Williams, Marquis, E. A., Cerezo, A., and Smith, G. D. W., J. *Nucl. Mater.* **400**, 37-45 (2010).
6. M. K. Miller, Hetherington, M. G., “Local Magnification Effects in the Atom Probe,” Surf. Sci. **246**, 442 (1991).
7. A. Morley, Sha, G., Hirosawa, S., Cerezo, A., Smith, G. D. W., “Determining the Composition of Small Features in Atom Probe: BCC Cu-Rich Precipitates in an Fe-Rich Matrix. Ultramicroscopy 109, 535 (2009).
8. Y. Wu, Haney, E. M., Cunningham, N., Odette, G. R., DOE Fusion Reactor Materials Program Semiannual Progress Report for the Period Ending June 30, 2011, DOE/ER-0313/50 2011 (this report).

1.5 The Effect of Bulk Oxygen Concentration on the Micro-nanostructure and Strength of a 14Cr Nanostructured Ferritic Alloy

— Y. Wu, N. J. Cunningham, A. Etienne,[1] E. Haney, G. R. Odette (University of California Santa Barbara), E. Stergar (Leoben University),[2] D. T. Hoelzer (Oak Ridge National Laboratory), B. D. Wirth (University of California Berkeley[3]) and S. A. Maloy (Los Alamos National Laboratory)

OBJECTIVE

The objective is to evaluate the effect of bulk O on the microstructure, nanofeatures and hardness of nanostructured ferritic alloys (NFA) that otherwise have a generally similar compositions and processing paths.

SUMMARY

The effects of bulk O variations on the characteristics of the grain structure, nanofeatures (NFs) and microhardness of nanostructured ferritic alloys (NFA) were investigated. The grain structures were characterized by optical metallography and transmission electron microscopy (TEM). The NFs were characterized by TEM, atom probe tomography (APT) and small angle neutron scattering (SANS). Based on bulk chemical analysis of the milled powders, the O content ranged from 0.065 to 0.249 (wt.%). The variations in O resulted from differences in the milling conditions. The low O powders (OW3) were milled with a procedure that minimized contamination, while the high O powders (OW1), that initially had a low O content in the as atomized condition, were contaminated with both N and O during milling. The intermediate O powders (OW4) minimized this contamination while increasing O with additions of FeO during milling. The three powder batches were all consolidated by hot isostatic pressing (HIPing) at 1150°C and 200 MPa. All the consolidated alloys had bimodal distributions of grain sizes, that were characterized by the two average large and small sizes ($d_{s,l}$) and the relative fraction of the small grains (f_s). The NFs were Y-Ti-O enriched phases characterized by their number density (N), size distributions and average diameter (<d>), composition (especially the Y/Ti ratio) and phase structure (not evaluated in this study). Both the large and small grain sizes decreased with increasing O contents, while the fraction of small grains increased. The size of the NFs decreased and their number density increased with increasing O. TEM energy dispersive x-ray (EDX) studies indicated the low O alloy contained fewer and coarser features compared to alloys with higher O. TEM showed that the low O features were much more highly enriched in Y compared to Ti, including a majority that contained no Ti. However, APT showed that NFs in the low O alloy with $\langle d \rangle \approx 5$ nm had Y/Ti ratios < 1 that is only slightly larger than found in the other cases. The Vickers microhardness (H_v) of the alloys increased significantly with increasing O, reflecting both the effects of differences in the grain size and scale dispersion strengthening features. The H_v increased systematically with the volume fraction of NFs measured by SANS.

---

[1] Current institution Rouen University

[2] Current institution University of California Santa Barbara and Berkeley

[3] Current institution University of Tennessee Knoxville

PROGRESS AND STATUS

Ohtsuka, Ukai and their co-workers have shown that the O content of 9 Cr steels, that are transformable analogs to NFAs, has a strong effect on both their micro-nanostructures and properties [1-3]. This is in part attributed to an O effect on the composition and scale of the dispersion strengthening oxides and in part due to the effect of O on the fraction of ferrite versus martensite in the normalized and tempered alloys. Decreasing O was reported to lead to oxides richer in Y and to a decrease in the fraction of the ferrite phase where the NFs preferentially form.

This work is part of a collaborative program to develop a larger best practice heat of 14Cr NFA [4]. The alloys in this study were fabricated from atomized Fe-14Cr-0.4Ti-0.2Y powders. The addition of Y was intended to explore the possibility of minimizing, or eliminating, the milling step normally used to mix Y_2O_3 into solid solution. However, it was found that the Y phase separates during atomization and that extensive milling is still needed prior to consolidation, in this case by HIPing at 1150°C and 200 MPa. The main focus of this work has been on the powders with low O. The first milling procedure that was used added O and N to the powders as a contaminant (OW1). An improved milling procedure reduced the contamination (OW3). However, as described below, the low O in this alloy resulted in low hardness and coarser grain and NF structures. Thus more O was added to the initially low O powders by milling them with FeO (OW4). Examining the micro-nanostructure and hardness of the three alloys provides an opportunity to assess the effects of O in a non-transformable fully ferritic 14Cr alloy.

EXPERIMENTAL PROCEDURES

The experimental procedures are only very briefly outlined here. Full details will be provided in future reports and publications. The as atomized alloy powders described above were provided by ATI Powder Metals, along with their bulk chemical compositions. Milling was carried out for 40h in a dry Ar atmosphere using a Zoz Simolayer CM-01 attritor mill at UC Berkeley (OW1 and 3) and in a CM-08 attritor mill at Oak Ridge National Laboratory (OW4). The grain structures were characterized by optical metallography and TEM. The NFs were characterized by TEM, APT and SANS. The Vickers microhardness of the alloys was measured at a 500 g load. The compositions of the powders used in this study are shown in Table 1. OW1 and OW4 alloys used the -100/+325 mesh L2311 powder, while OW3 used the -325 mesh L2314 powder. Table 2 shows the O and N contents of the three powders after milling.

Table 1. ATI powder compositions (wt%).

Batch	Mesh	Alloy	Fe	Cr	W	Ti	Y	Al+Si	O	N	C
L2311	-100/+325	OW1, 4	Bal	14.0	3.0	0.35	0.21	0.045	0.014	0.002	0.006
L2314	-325	OW3	Bal	14.0	3.0	0.36	0.21	0.045	0.034	0.002	0.005

Table 2: N and O wt% in the milled powders used for OW1, OW3 and OW4 HIP alloys (wt.%).

Alloy	N	O
OW1	0.190	0.249
OW3	0.016	0.065
OW4	0.013	0.127

RESULTS

As shown in Figure 1, all the NFA had bimodal grain structure with large grains up to tens of μm or, and small grains d < 1 μm. Table 3 summarizes the grain structures, characterized by the two average large and small sizes ($d_{s,l}$) and relative fraction of the small grains (f_s). The d_l increase and the f_s decrease systematically with decreasing O. The highest O OW1 alloy has the smallest d_l. However, systematic ordering of d_s is not observed in the intermediate and low O alloys.

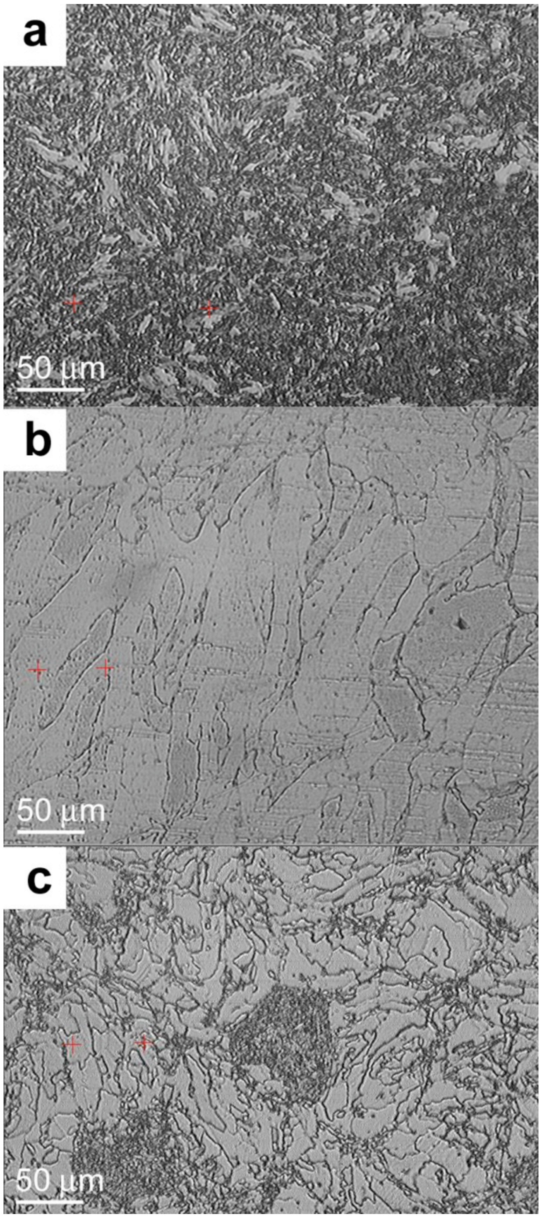

Figure 1. Optical micrographs of etched (a) OW1, (b) OW3, and (c) OW4.

Table 3. The average large and small grain sizes ($d_{s,l}$) and relative fraction of the small grains (f_s) in OW1, OW3 and OW4.

Alloy	d_l (µm)	d_s (nm)	f_s (%)
OW1	9.4	151	70
OW3	23.3	323	2
OW4	11.3	582	10

TEM micrographs showing the NFs in OW1, OW3 and OW4 are shown in Figure 2. Figure 3 compares the corresponding size distributions. The size and concentration of the NFs in low O, OW3 are <d> ≈ 4.7 nm and N ≈ $6.2\times10^{22}/m^3$, respectively, while those in intermediate O, OW4 are <d> ≈ 2.4 nm and $2.8\times10^{23}/m^3$. The NFs in high O, OW 1 are only slightly coarser compared to those in OW4 with <d> ≈ 3.4 nm and N ≈ $1.2\times10^{23}/m^3$.

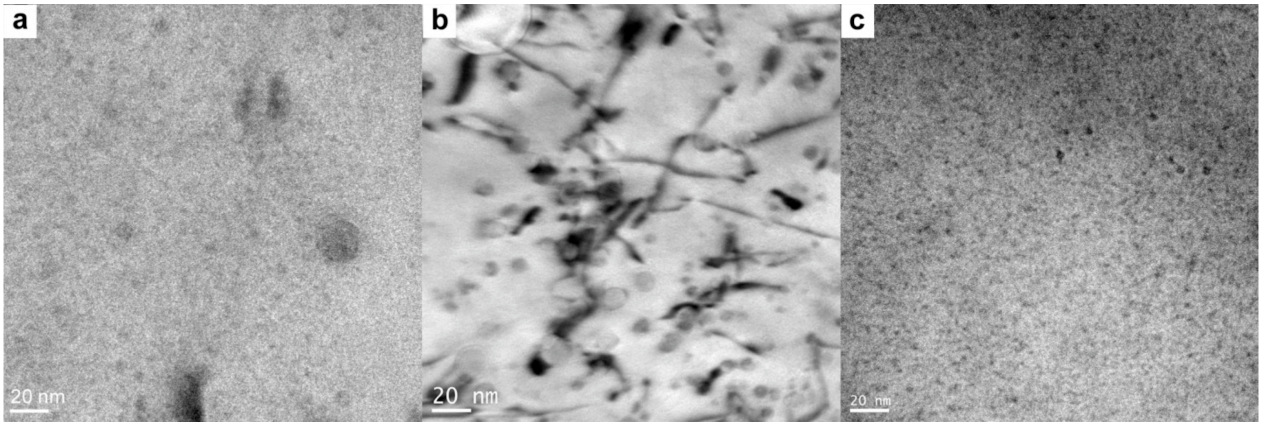

Figure 2. TEM micrographs of the NFs in OW1 (a), OW3 (b) and OW4 (c).

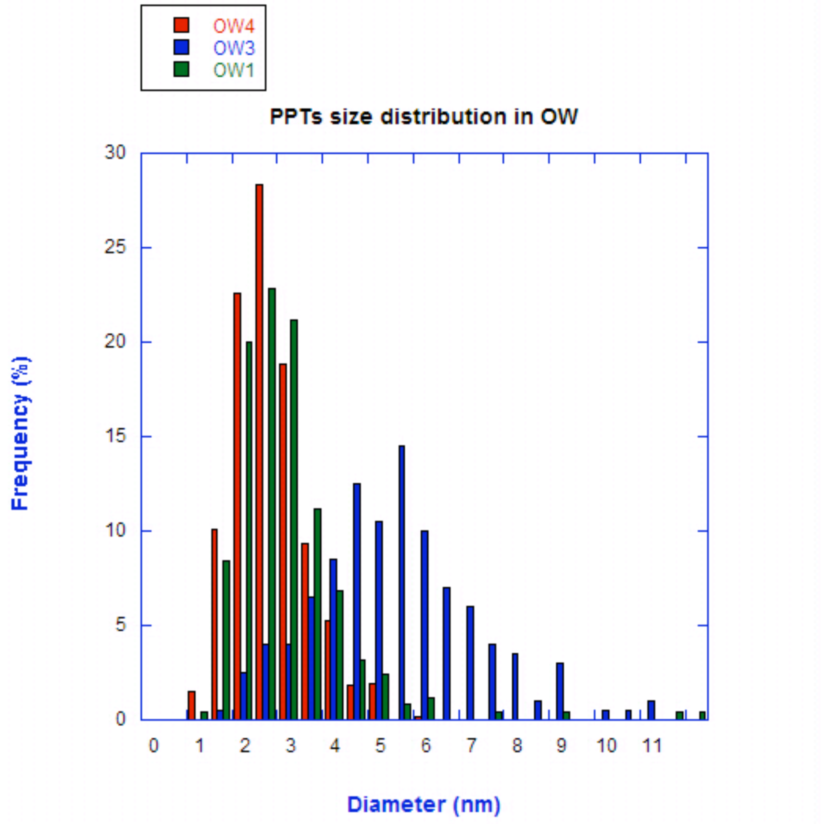

Figure 3. The size distributions of the NFs in OW1, OW3 and OW4 measured by bright field TEM.

EDX was also used to estimate the compositions of NFs extracted on C foils. Figure 4 shows EDX measurements on individual precipitates in OW3, while Figure 5 shows the EDX spectrum for a broad area containing many smaller NFs in OW4. In the low O, OW3 alloy, 15 out of the 20 precipitates observed were Y-rich and contained no Ti (average diameter ≈ 7.0 nm), while 1 had a Y/Ti ratio between 1 and 2 (diameter ≈12.0 nm) and 4 had ratios between 2 and 10 averaging 4.6 (average diameter ≈ 6.0 nm). In contrast the average Y/Ti ratio in the medium O, OW4, was 0.5 and 1.2 (d<5 nm), 2.3 (5<d<10 nm) in the high O, OW1.

Table 3. The NF N and <d> measured by TEM.

Alloy	<d> (nm)	N ($10^{23}/m^3$)
OW1	3.4	1.2
OW3	4.7	0.6
OW4	2.4	2.8

Figure 6 shows examples NFs found in the APT studies of OW1, OW3 and OW4. The corresponding N and <d> are summarized in Table 4. In OW3 <d> = 5.8 nm and N = $6.0\times10^{22}/m^3$. This is in contrast to the smaller diameters of 1.7 nm and 2.5 nm and higher number densities of $2.9\times10^{23}/m^3$ and $9.6\times10^{23}/m^3$ for OW1 and OW4, respectively. The Y/Ti/O ratios for OW1, OW3, and OW4 were 23/37/41, 22/31/46, and 11/42/47 respectively. OW3 has the highest Y/Ti ratio, but it is still less than 1.

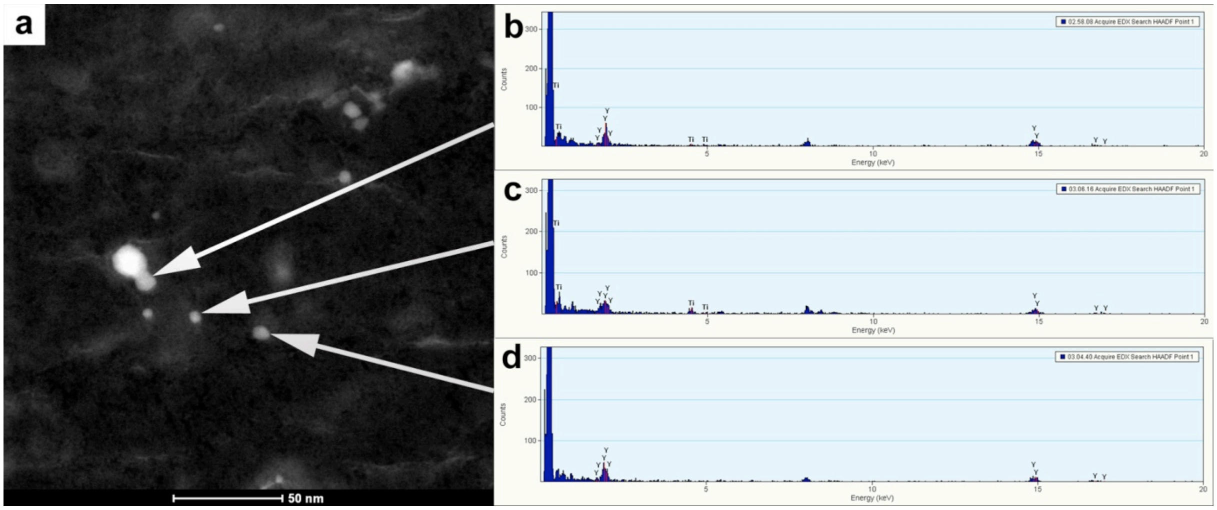

Figure 4. STEM image of an extraction replica sample from OW3 (a); EDX spectra from the PPTs marked by the arrows (b)-(d).

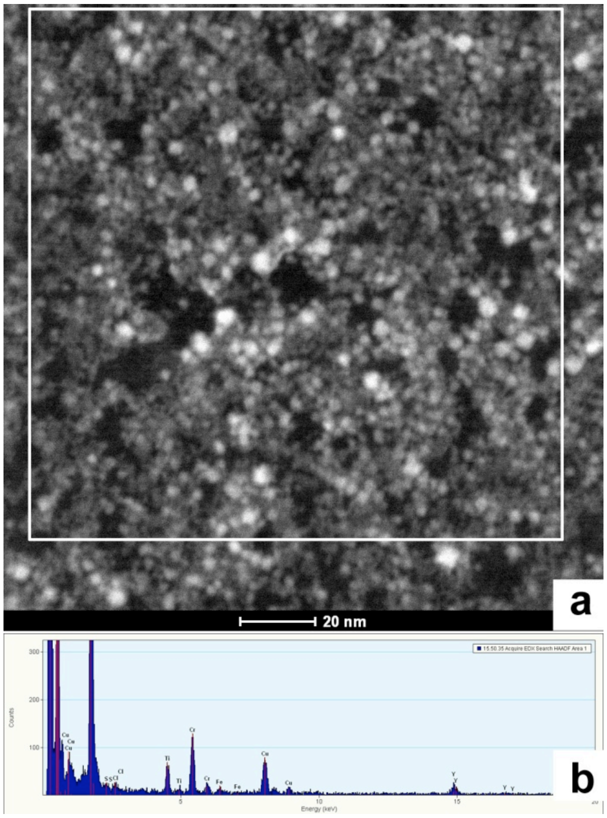

Figure 5. STEM image of an extraction replica sample from OW4 (a); EDX spectrum of the square area in (a) is shown in (b).

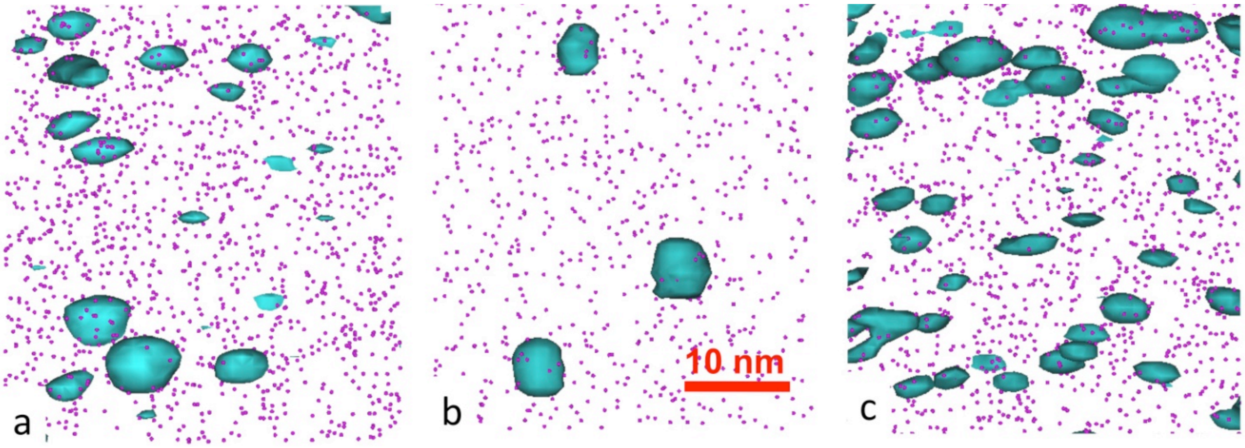

Figure 6. 20 nm thick Atom maps with Cr ions and Y-Ti-O isoconcentration surfaces (4.0%) for (a) OW1, (b) OW3, and (c) OW4.

Table 4. The NF number density (N) and average diameter (<d>) measured by APT.

Alloy	<d> (nm)	N ($10^{23}/m^3$)
OW1	1.7	2.9
OW3	5.8	0.7
OW4	2.5	9.6

SANS was performed on OW1, OW3, and on an L2314 powder attritor milled with FeO and annealed for 3 h at 1150ºC, which is expected to be representative of OW4. OW1 and the OW4 surrogate FeO milled and annealed powder had smaller <d> = 2.8 nm, while low O, OW3 had larger <d> = 5.4 nm. High O, OW1 had N = $1.1\times10^{24}/m^3$, while the intermediate O, OW4 surrogate FeO milled and annealed powder had N = $7.1\times10^{23}/m^3$. Consistent with the TEM and APT results, the low O, OW3 had the lowest N =$5.2\times10^{22}/m^3$. The nominal NF volume fractions for the OW1, OW3 and OW4 surrogate and OW3 were 1.2, 0.8 and 0.4% respectively.

Table 5. The NF N and <d> measured by SANS.

Alloy	<d> (nm)	N ($10^{23}/m^3$)	f
OW1	2.8	11	1.2
OW3	5.4	0.5	0.4
OW4*	2.8	7.1	0.8

*Powder milled with FeO and annealed.

DISCUSSION

A summary of the NF sizes and number densities for the three techniques is shown in Table 6, along with the APT Y/Ti/O ratios and microhardness values. Figure 7 shows the average N and <d> for the three techniques as a function of the alloy O content. The NF characteristics are similar at the intermediate and high O levels, but as noted previously, the NF are larger and much fewer in number in case of the lowest O. Figure 8 shows that the microhardness increases with O. Table 6 also shows the microhardness (H_v) and the NF volume fraction (f) measured by SANS. Notably, as shown in Figure 9, H_v increases in direct proportion to the $\sqrt{f}$.

Table 6. Summary of the N and <d> in OW1, OW3 and OW4 measured by TEM, APT and SANS.

Technique	OW1	OW3	OW4
O (wt.%)	0.249	0.065	0.127
TEM d (nm)	3.4	4.7	2.4
APT d (nm)	1.7	5.8	2.5
SANS d (nm)	2.8	5.4	2.8*
TEM N (10^{23} m^{-3})	1.2	0.6	2.8
APT N (10^{23} m^{-3})	2.9	0.7	9.6
SANS N (10^{23} m^{-3})	11	0.5	7.1*
SANS f (%)	1.2	0.4	0.8
APT Y/Ti/O	23/37/41	22/31/46	11/42/47
Microhardness (kg/mm^2)	443±12	252±7	368±4

**Equivalent milled and annealed powder*

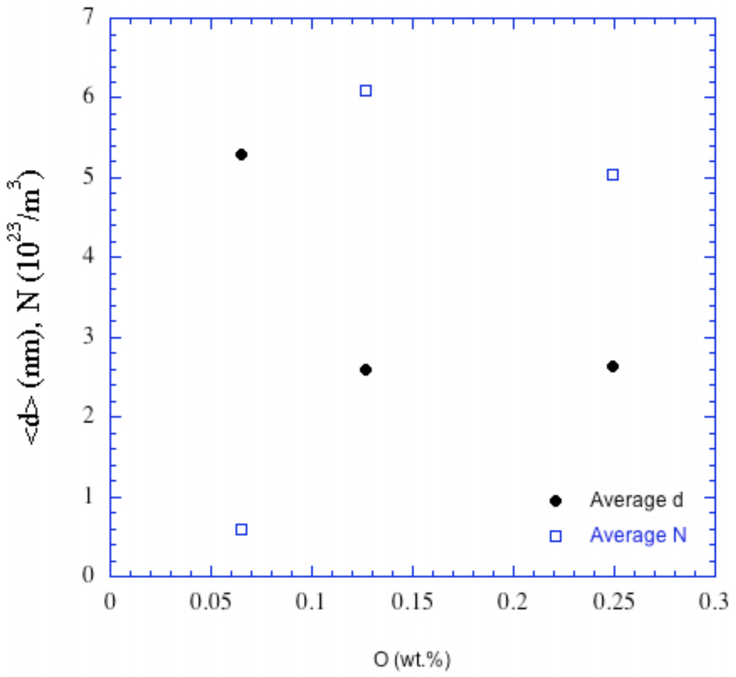

Figure 7. The average of <d> and N for TEM, APT and SANS vs O content.

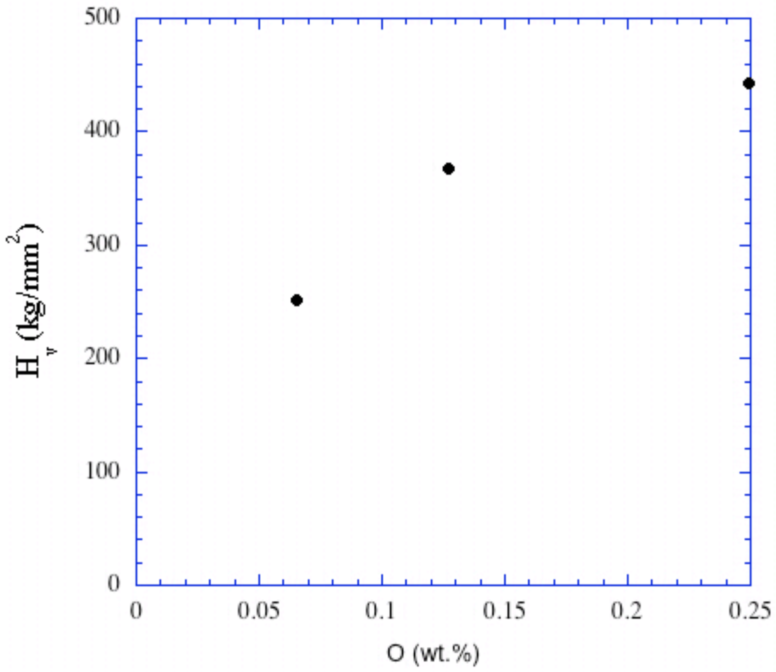

Figure 8. The alloy H_v versus O content.

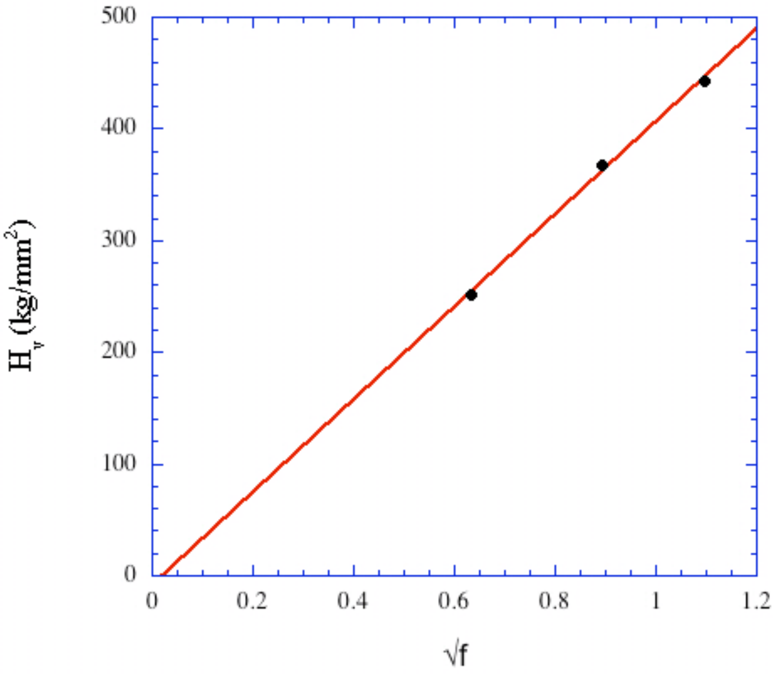

Figure 9. The alloy H_v versus the square root of the NF volume fraction (√f) measured by SANS.

FUTURE WORK

A journal paper will be prepared describing these results and submitted for publication.

ACKNOWLEDGEMENT

This work was carried out as part of a multi-laboratory collaboration, led by S. Maloy (LANL) between LANL, UCSB and ORNL that was supported by the DOE Office of Nuclear Energy Fuel Cycle R&D Program. The research at UCSB and UC Berkeley was supported by subcontracts from LANL as well as a NERI grant at UCSB. A smaller contribution to this research was also made by the DOE Office of Fusion Energy.

REFERENCES

1. S. Ohtsuka, S. Ukai, M. Fujiwara, T. Kaito, T. Narita, *J. Nucl. Mater.* **329**, 372 (2004).
2. S. Ohtsuka, S. Ukai, M. Fujiwara, T. Kaito, T. Narita, *J. Phys. Chem. of Solids* **66**, 571 (2005).
3. S. Ukai, S. Ohtsuka, *Energy Materials* **2**, 26 (2007).
4. S. Maloy et al., “Final Report on Improved Processing and Fabrication of Advanced, adiation-tolerant ODS Steels,” LANL report LA-UR-11-10289, 2/28/11.

1.6 Effects of Neutron Irradiation on Hardness Properties of Friction Stir Processed ODS Ferritic Steel — Sanghoon Noh (Kyoto University), M. A. Sokolov (Oak Ridge National Laboratory), Ryuta Kasada, Akihiko Kimura (Kyoto University) and Takuya Nagasaka (National Institute for Fusion Science)

OBJECTIVE

The effects of neutron irradiation were investigated on a friction stir processed ODS steel. To investigate the neutron irradiation behavior in the joint area, the hardness measurements as post irradiation experiment (PIE) were carried out on the cross section using a micro Vickers hardness tester.

SUMMARY

Oxide dispersion strengthened ferritic steels (ODS-FS) have been considered as one of the most promising structural materials for advanced nuclear systems such as fusion reactors and next generation fission reactors, because of its excellent elevated temperature strength, corrosion and radiation resistance. Especially, irradiation resistance is a critical issue for the high performance of ODS-FS. In this study, effects of the irradiation on hardness properties of friction stir processed (FSP) ODS-FS were investigated. FSP technique was employed on ODS-FS. A plate specimen was cut out from the cross section and irradiated to 1.2 dpa at 573K in the High Flux Isotope Reactor (HFIR). To investigate the effect of neutron irradiation on processed area, the hardness distributions were evaluated on the cross section. Hardness of FSP ODS-FS was various with each microstructure after irradiation to 1.2 dpa at 573K. The increase of Vickers hardness was significant in the stirred zone and heat affected zone. Base material exhibited the lowest hardening about 38HV. Since nano-oxide particles in stirred zone showed identical mean diameter and number density, it is considered that hardening differences between stirred zone and base material is due to differences in initial dislocation density.

PROGRESS AND SATATUS

Experimental

ODS-FS used in this study is Fe-15Cr-4Al-0.7Y_2O_3 ODS ferritic steel. Chemical compositions are shown in Table 1. The ODS-FS were fabricated by mechanical alloying and hot-extrusion process. An ODS-FS rod was machined to the dimension of 115 mm length × 20 mm width × 8 mm thickness, of which the longitudinal direction (L-direction) was parallel to the extruded direction, was friction stir processed in the air at room temperature. The material of the rotating tool used in this study is a polycrystalline cubic boron nitride (PCBN). The rotating tool is plunged into the plate and moved along bonding direction. The ODS-FS was friction stir processed at a tool traveling speed of 50mm/min and tool rotating speed of 800rpm. Consequently, the process was done parallel to the extruded direction. Detailed fabrication and processing condition are described in previous paper [1]. A plate specimen was cut out from the cross section and irradiated to 1.2 dpa at 573K in the High Flux Isotope Reactor (HFIR). To investigate the effect of neutron irradiation on processed area, the hardness distributions were evaluated on the cross section using a micro Vickers hardness tester with 200gf for 10s at room temperature in a regular interval of 0.5 mm.

Fig. 1. Cross sectional optical micrograph of friction stir processed ODS-FS.

Table 1. Chemical compositions of ODS ferritic steel.

Fe	C	Si	Mn	P	Cr	W	Al	Ti	Y_2O_3
Bal.	0.018	0.02	0.02	<0.005	15.39	0.28	3.78	0.1	0.7

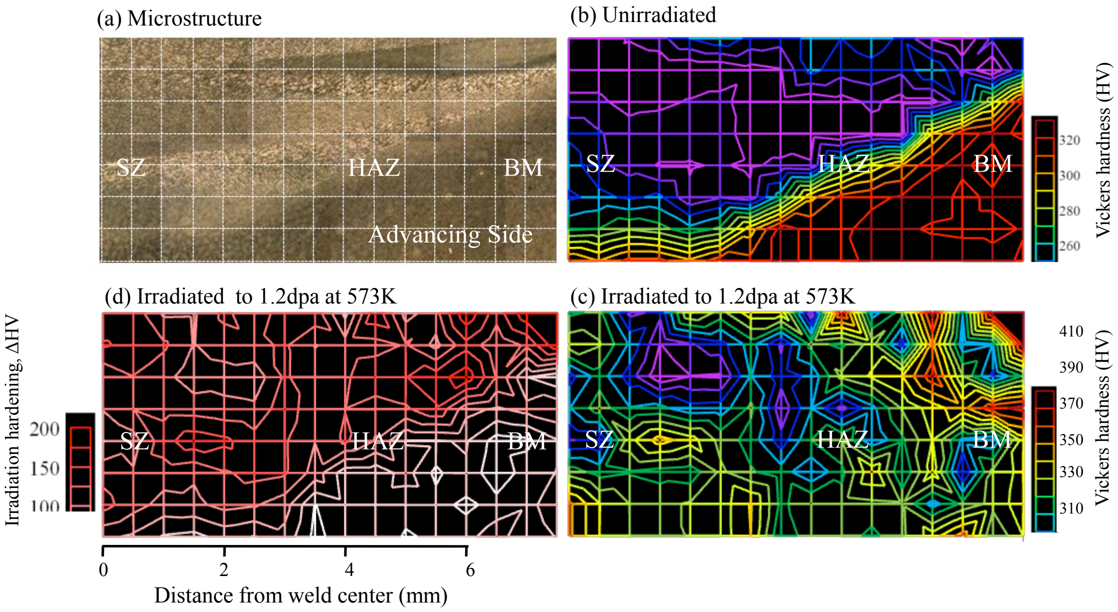

Fig. 2 Irradiation hardening of friction stir processed ODS ferritic steel

TEST RESULTS

Optical micrograph of friction stir processed ODS-FS on transverse cross section is shown in Fig. 1. Two distinct zones can be clearly identified as base material (BM) and stirred zone (SZ). The SZ exhibits a symmetric basin-shape with about 3mm depth at bottom and significantly spreading toward the upper surface. In Fig. 2, the hardness distribution on the transverse cross section is illustrated as a color level map. Each cross line indicates the measured point of hardness and its color shows the hardness level. The variable colored distribution area is well corresponding with the changes in the microstructure developed during friction stir process, that is, changing colored area matches with the geometries of rotating pin and shoulder. As seen in Fig. 2(b), boundary area between SZ and BM is limited to very narrow area that can be defined as a heat affected zone (HAZ). SZ around the weld center shows lower hardness of 210 ± 12 HV than that of 316 ± 6 HV of base material. The hardness distribution of tool advancing side after neutron irradiation in HFIR to 1.2 dpa at 573K is illustrated in Fig. 2(c, d). After irradiation, hardness distribution changed randomly from 310 to 420 HV, but degrees of irradiation hardening was clearly occurred in each microstructure. In Fig. 3, irradiation hardening of each microstructure SZ, HAZ and BM is illustrated. The irradiation hardening in BM is not so high about 38HV, compared with those in SZ showed about 120HV. This means that microstructural difference results different irradiation hardening at 572K. S. Noh et al. reported that nano-oxide particles in SZ were uniformly distributed and reserved with same mean particle size and number density with BM [1]. More detailed microstructural observation is essentially required, however, it can be assumed that this is because of dislocation density difference between BM and SZ developed during the friction stir process.

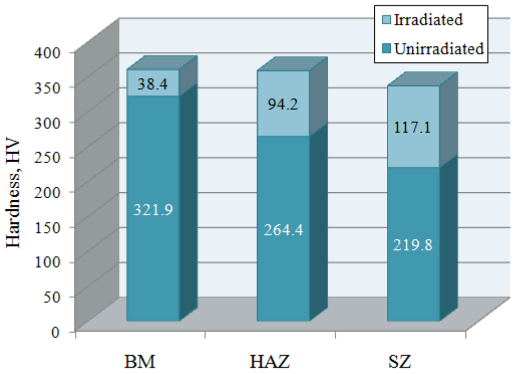

Fig. 3. Irradiation hardening of each microstructure.

Meanwhile, the dislocation density of metal is closely related to the thermal history during the processing. The maximum temperature of the work piece by frictional heat can be examined with some FSW parameters by Arbegast and Hartley [2]. They measured the average maximum temperature for a relationship between maximum welding temperature (T, °C) and FSW parameters (ω, v; tool rotation speed (rpm), traveling speed (mm/min)) and it can be expressed by, where the exponent *α* was

$$\frac{T}{T_m} = K\left(\frac{\omega^2}{\nu \times 10^4}\right)^{\alpha} \tag{2.1}$$

reported to be in the 0.06 in steels, the constant *K* is 0.65 in steels, and T_m is the melting point, 1513°C of this ODS-FS. Thus, the maximum temperature of the ODS-FS estimated during the process is estimated to be about 1305°C. Compared with tool traveling speed of Al alloy, 50mm/min on ODS-FS is very slow in this study, so the workpiece could be heated up to high temperature, 1305°C in several minutes. Consequently, it is considered that dislocation recovery occurred in the SZ and dislocation density was reduced during friction stir process. This could explain the result of irradiation hardening difference between SZ and BM after HFIR irradiation.

REFERENCES

[1] S. Noh, R. Kasada, A. Kimura, S. H. C. Park, S. Hirano, Microstructure and mechanical properties of friction stir processed ODS ferritic steels, Journal of Nuclear Materials, In Press (2011).

[2] W.J. Arbegast, P. J. Hartley, in: Proceedings of the Fifth International Conference on Trends inWelding Research 541 (1998).

1.7 Joining of 14YWT and F82H by Friction Stir Welding — D. T. Hoelzer, M. A. Sokolov and Z. Feng, ORNL

OBJECTIVE

The objective of this work was to investigate the feasibility of joining specimens of the advanced ODS 14YWT alloy with each other and with F82H by friction stir welding.

SUMMARY

A sample was prepared for the initial joining study using friction stir welding (FSW) that consisted of 4 specimens of the advanced oxide dispersion strengthened (ODS) 14YWT-SM6 ferritic alloy, 15 mm long, 6 mm wide and 2.86 mm thick each, that were spot welded in a corresponding slot that was machined in an F82H plate. The FSW run was successfully performed on the sample using a polycrystalline boron nitride tool (PCBN) that resulted in joints showing good bonding between specimens of 14YWT-SM6 and between 14YWT-SM6 and F82H. The joints were characterized by light microscopy and SEM analysis and were observed to be relatively narrow in width. However, porosity was observed in the thermomechanically affected zone (TMAZ) of 14YWT-SM6 on the advancing side of the FSW joint and at the interface between F82H and 14YWT-SM6. Further refinements in the FSW process will be required to minimize defects including porosity.

PROGRESS AND STATUS

Introduction

Friction stir welding (FSW) is an innovative solid-state joining technique that was invented in 1991 [1]. The basic concept of FSW involves plunging a specially designed tool rotating at high speeds into the seam between work pieces and joins them by solid-state mixing as the tool travels along the seam. Heat is produced by friction from contact between the rotating tool and work pieces that allows material to flow around the tool during the translation of the rotating tool. As the tool travels along the seam to be joined, a cavity forms at the rear but is filled with material redistributed by the rotating tool to form the weld. The redistribution process causes the material to experiences extreme levels of plastic deformation and thermal exposure that can have a significant effect on microstructural changes in weld zone. A recent review of the friction stir welding and related friction stir processing methods has been published [2].

The FSW technique was originally developed for the Al industry. However, since the FSW technique is based on the solid state joining concept, it has recently been applied to joining high performance alloys that typically are produced with complex microstructures. Oxide dispersion strengthened (ODS) ferritic alloys (FA; >12Cr) and tempered martensitic steels (TMS; <12Cr with C) represent a class of complex high performance materials that are produced by the mechanical alloying method to utilize a dispersion of thermally stable oxide particles to greatly improve the strength and creep properties at elevated temperatures. Although there have been a limited number of FSW studies that have been conducted on ODS alloys in the recent past, these studies demonstrated that joints could be produced with INCO MA957 FA [3,4], INCO MA956 [5,6], ODS Eurofer 97 TMS [7] and Plansee PM2000 FA [8]. However, further research focusing on improvements in the FSW conditions and microstructural characterization is needed in order to improve the joints that are produced in ODS FA and TMS.

Recent advances in understanding the MA process have led to development of the advanced ODS 14YWT ferritic alloy, or Nanostructured Ferritic Alloy (NFA), during the past 10 years. The salient characteristics of 14YWT consist of a high number density of 2-4 nm dia. Ti-, Y-, and O-enriched particles, or nanoclusters (NC), and nano-size (<500 nm) grains that provide high strength up to 800ºC [9]. Numerous small heats of 14YWT have been produced with similar NC dispersion and grain size characteristics. The purpose of this study was to investigate the feasibility of joining specimens of 14YWT by FSW without degrading the highly tailored microstructure. In addition, the study also focused on joining dissimilar materials of 14YWT to F82H. The 14YWT used in this study was from the 14YWT-SM6 heat that was produced in 2005. This heat was primarily used in the doctoral research project of McClintock [10]. The objective of this project was to investigate the tensile and fracture toughness properties of 14YWT-SM6 before and after exposure to neutron irradiation at HFIR to a dose of ~1.35 dpa at 300ºC. A significant highlight obtained in this study was the discovery that the 14YWT-SM6 heat possessed a fracture toughness transition temperature of -150ºC and upper shelf energy of ~150-175 MPa·m$^{0.5}$ that did not change after neutron irradiation [11, 12].

Procedure

The specimens used in the friction stir welding experiments were prepared from material of 14YWT, 14WT and F82H. The 14YWT was from the SM6 heat that was produced in 2005. The nominal composition of the 14YWT-SM6 heat was Fe-14Cr-3W-0.4Ti + 0.3Y_2O_3 (all values in wt. %). The 14WT was from the SM3 heat that was also produced in 2005. The 14WT-SM3 heat was a reference heat to 14YWT-SM6 since it was ball milled with no Y_2O_3, so the nominal composition was similar to 14YWT-SM6 but contained no Y. It was planned to use the 14WT specimens in the trial FSW attempt to help elucidate any changes in the FSW parameters that may be required to make before attempting the experiment with the 14YWT-SM6 specimens. Both the 14YWT-SM6 and 14WT-SM3 heats were 0.8 kg in mass and were processed with similar conditions, i.e. ball milling time of 40 h and extruded at 850ºC. The F82H plate used in this experiment was supplied to ORNL by JAEA.

A total of 4 specimens were produced from the 14TYWT-SM6 and 14WT-SM3 heats. These specimens were cut from the end of broken dual notch bend bar specimens that were used in three point bend tests in the unirradiated condition. A dual notch bend bar specimen that was fabricated from 14YWT-SM6 prior to the three point bend test is shown in Figure 1. The fracture surfaces of the tested specimens were preserved.

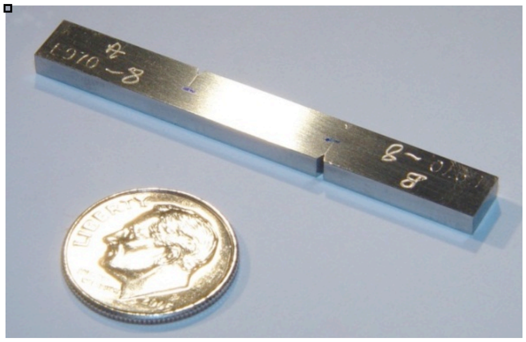

Figure 1. A dual notch bend bar specimen that was used to prepare specimens of 14YWT and 14WT to be used in the friction stir welding experiment.

The preparation of 2 samples used in the FSW study consisted of embedding 4 specimens of the NFA 14YWT and the reference 14WT (ball milled with no Y_2O_3) within several plates of F82H. First, a 12 x 30 mm^2 slot was cut by Electro Discharge Machining (EDM) in a plate of F82H that was 63 mm long, 25 mm wide and 2.86 mm thick. A total of 4 specimens of 14YWT and 14WT were cut from the ends of dual notch bend bar specimens that had been tested. The dimensions of these specimens were 15 mm long, 6 mm wide and 2.86 mm thick. The 4 specimens were then arranged in the 12 x 30 mm^2 slot that was cut from the F82H plate. Next, a 30 mm long, 25 mm wide and 2.86 mm plate of F82H was placed next to the plate containing the slot holding the 4 specimens of 14YWT and 14WT in place. Two additional plates of F82H possessing the same dimensions described previously were used as backing plates. Finally, spot welds were used on butt joints holding the 14YWT and 14WT specimens in the slotted F82H plate and between the plates of F82H as shown in Figure 2. For both samples, the extrusion direction of the 14YWT-SM6 and 14WT-SM3 specimens lies parallel to the long axis of the bend bar specimens. Therefore, the traveling direction of the rotating tool during FSW was parallel to the extrusion direction of these specimens, i.e. from left to right in Figure 2.

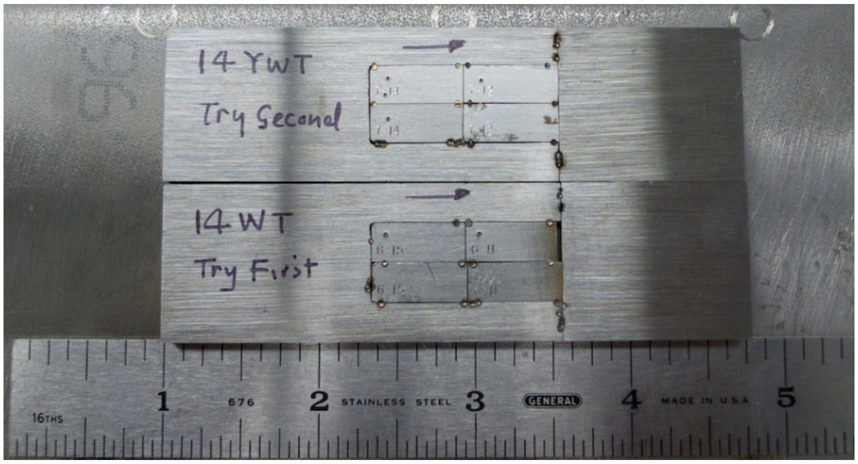

Figure 2. Digital image showing the 4 spot welded specimens of 14YWT-SM6 and 14WT-SM3 embedded in the slots that were cut in the F82H plates.

Operation of three independent axes with adjustable, adaptable pin tools for on-the-fly mode switching between fixed, adjustable, and self-reacting welding modes. It can also handle computer controlled operation and key process parameter monitoring and is capable of making non-linear, variable-thickness, and double-curvature welds. The friction stir welding experiments were conducted using a pin tool fabricated from Polycrystalline Cubic Boron Nitride (PCBN). After the FSW runs were performed on the 2 samples, 3 specimens were cut from the FSW zones and mounted and polished for microstructural characterization. The location of the 3 specimens is shown in Figure 3. One specimen was cut at the leading edge of the bend bar fracture toughness specimens and the next 2 specimens were cut at the 0.25L (L = 30 mm) and 0.50L positions.

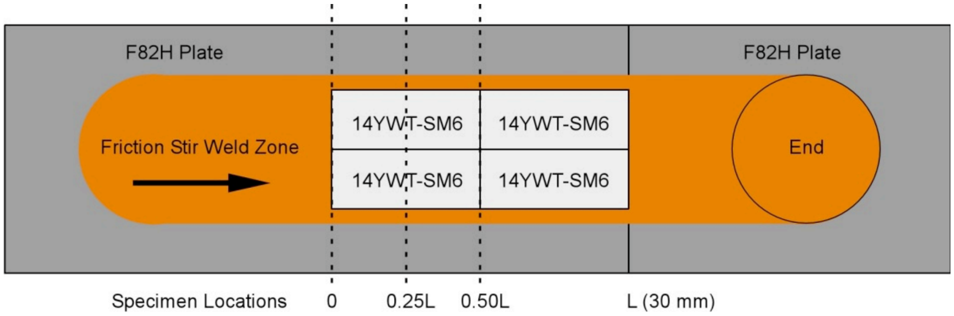

Figure 3. Schematic showing the location of specimens cut from the FSW zone and mounted for metallography and SEM analysis.

RESULTS AND DISCUSSION

Friction Stir Welding Experiment

The initial FSW run was performed on the 14WT-SM3/F82H sample and was then followed by the FSW run on the 14YWT-SM6/F82H sample. Digital images depicting the friction stir welding process on the 2 samples is shown in Figure 4. The PCBN tool making initial contact with the 14WT-SM3/F82H sample to start the joining process is shown in Figure 4a. The completed FSW runs that were performed on both samples are shown in Figure 4b. The results show that mixing by FSW occurred over areas in both samples that included material from the F82H plate and the bend bar fracture toughness specimens of 14WT-SM3 and 14YWT-SM6, as was shown in Figure 2. In addition, it should be pointed out that the PCBN pin tool did not fracture during each of the 2 FSW runs.

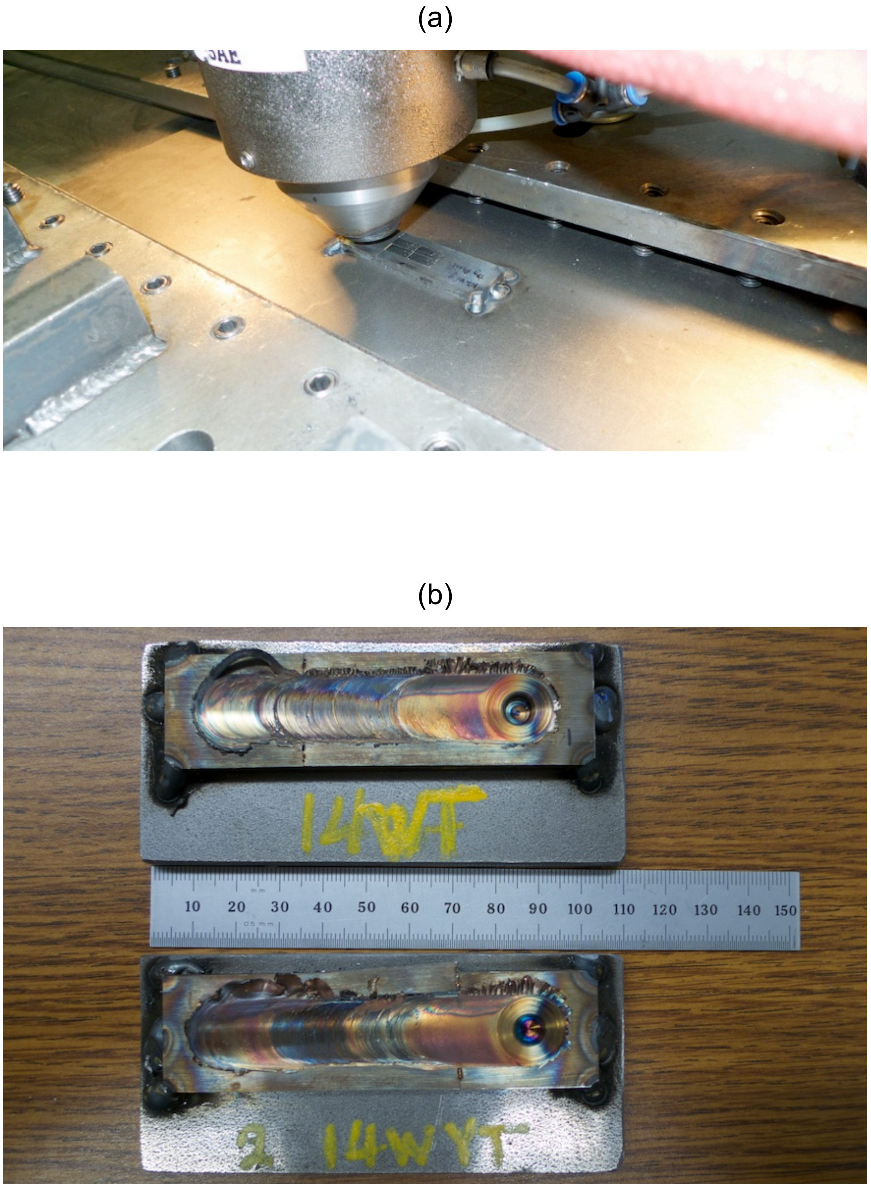

Figure 4. Digital images showing (a) contract between PCBN tool and the initial 14WT-SM3/F82H sample and (b) the completed friction stir welds of the 14WT-SM3/F82H and 14YWT-SM6/F82H samples.

Microstructural Characterization

The preliminary microstructural study of the F82H/14YWT-SM6 sample was conducted on the specimen that was cut at the 0.25L location. The microstructure of the specimen viewed in cross section by light microscopy is shown in Figure 5. This specimen was polished and etched to reveal the F82H plate located on the bottom and right side. The chemical etch had little effect on 14YWT-SM6, which appears mostly shiny due to the high (14%Cr) content combined with the nano-size grain structure. Etching was able to reveal the interface between the thermomechanically affected zone (TMAZ) and heat affected zone (HAZ) on the advancing side of the FSW joint of 14YWT-SM6. However, no discernable interfaces were observed near the center of the weld nugget between 2 bend bar specimens of 14YWT-SM6 or on the retreating side of the FSW joint. An interface was observed between the TMAZ of the F82H plate and 14YWT-SM6 specimens. These results indicated that good bonding occurred between the bend bar specimens of 14YWT-SM6 and between F82H and 14YWT-SM6 in the initial FSW attempt. On the other hand, several large pores were present in the lower side of the TMAZ of 14YWT-SM6 on the advancing side, which indicated that the FSW process conditions still need to be refined.

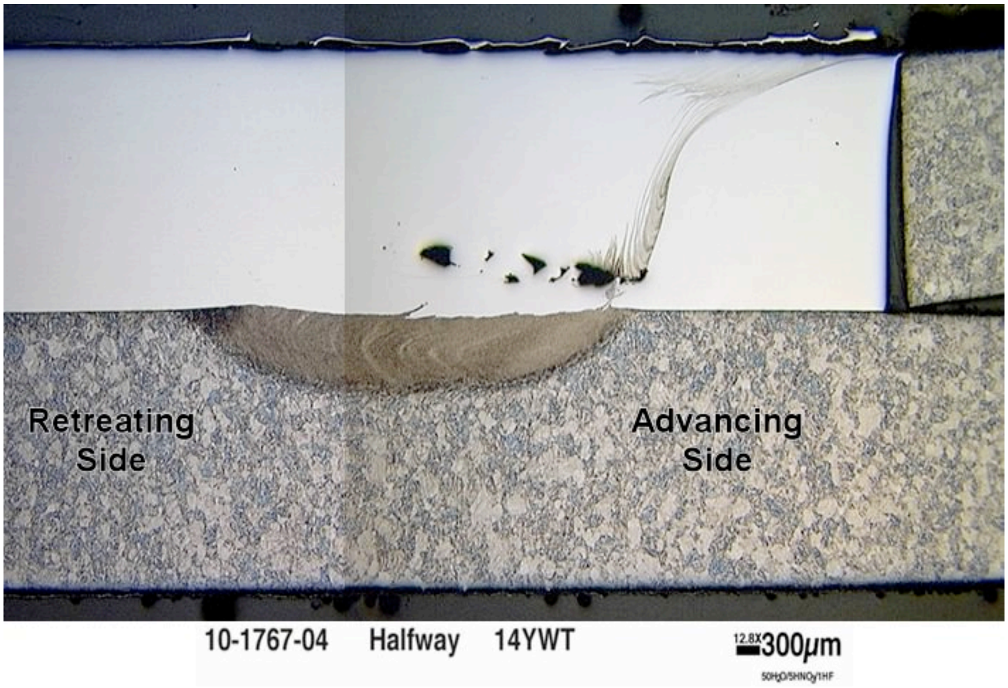

Figure 5. Light micrograph showing the cross sectional view of the FSW joint located at the 0.25L (L=30 mm) position.

SEM analysis was performed on the same specimen (0.25L) of the F82H/14YWT-SM6 sample that was shown in Figure 5. However, the mounted specimen was re-polished, with a final polish using colloidal silica and no subsequent etching. This procedure was required in order to image the nano-size grains present in 14YWT-SM6 using secondary electrons (SE) and back scattered electrons (BSE).

The microstructures representative of F82H and 14YWT-SM6 in the unaffected region and/or HAZ are shown in Figure 6. The microstructure of F82H consisted of large prior austenite grain boundaries with fully martensitic lath structure as shown in Figure 6a. The microstructure of 14YWT-SM6 shown in Figure 6b consisted of <500 nm size grains that are nearly equiaxed in shape since the orientation of the polished specimen in normal to the extrusion axis.

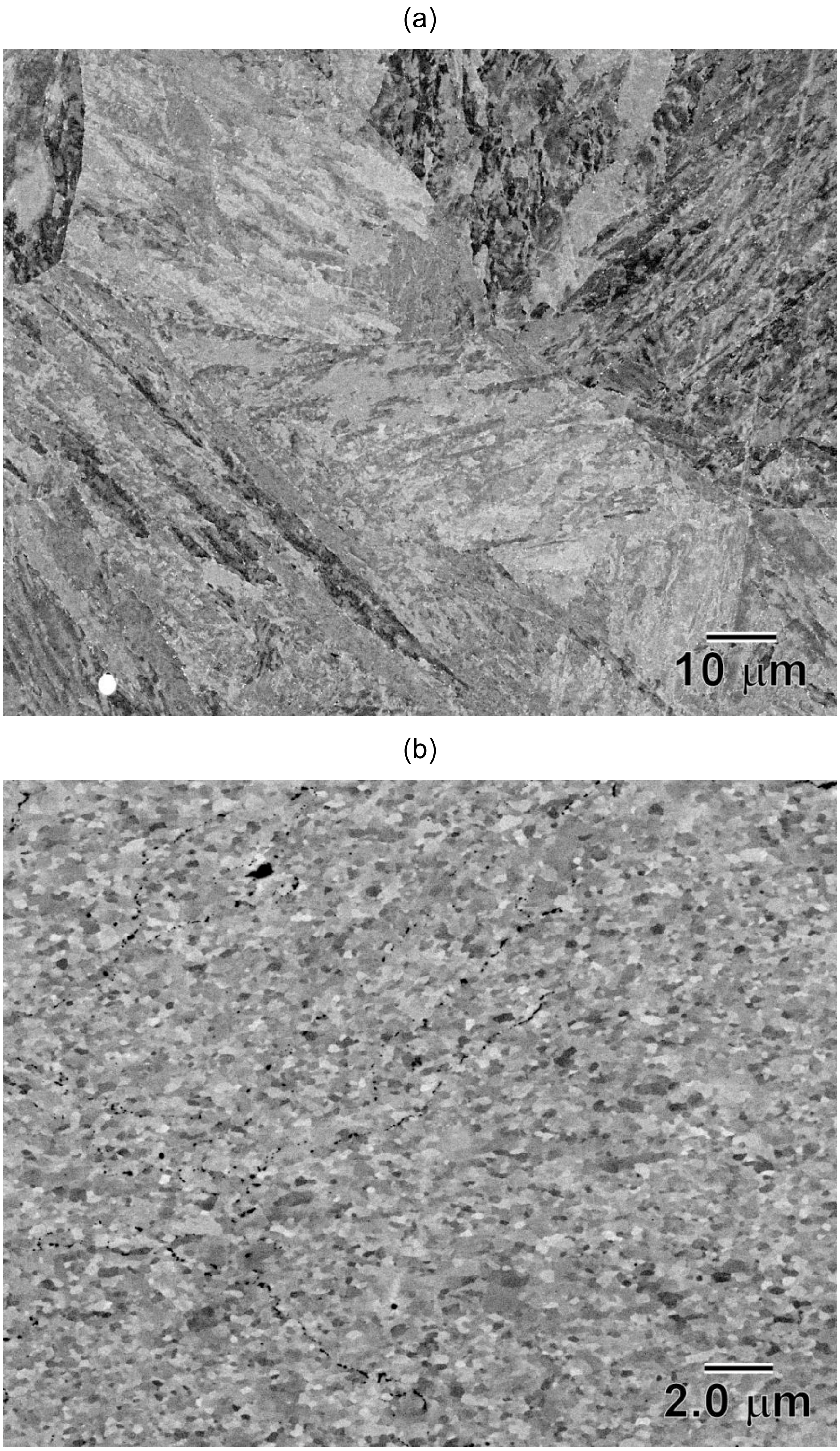

Figure 6. SEM backscattered electron micrographs showing the representative microstructures of (a) F82H and (b) 14YWT-SM6 in the unaffected or heat affected zones.

(a)

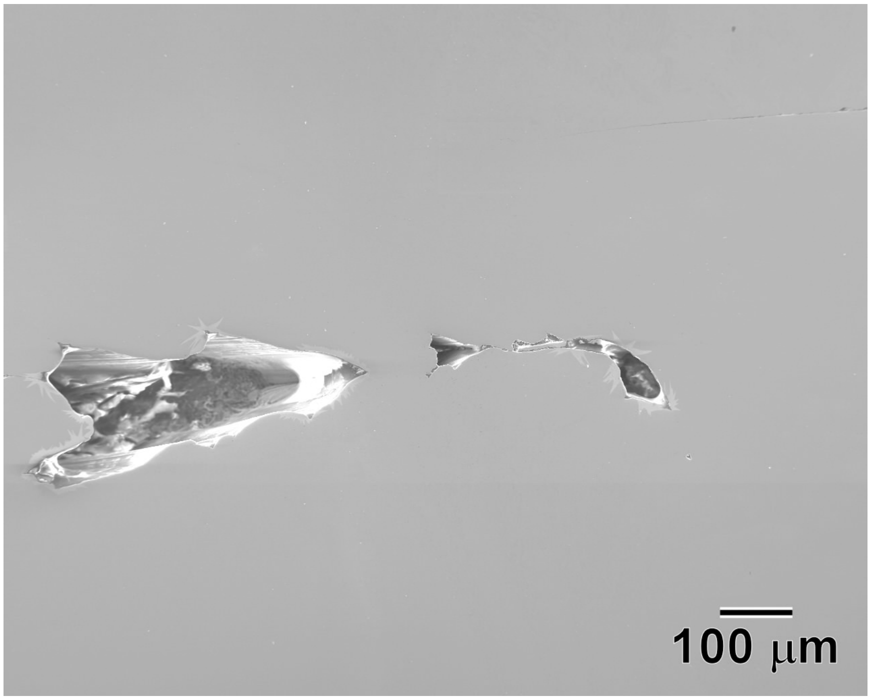

(b)

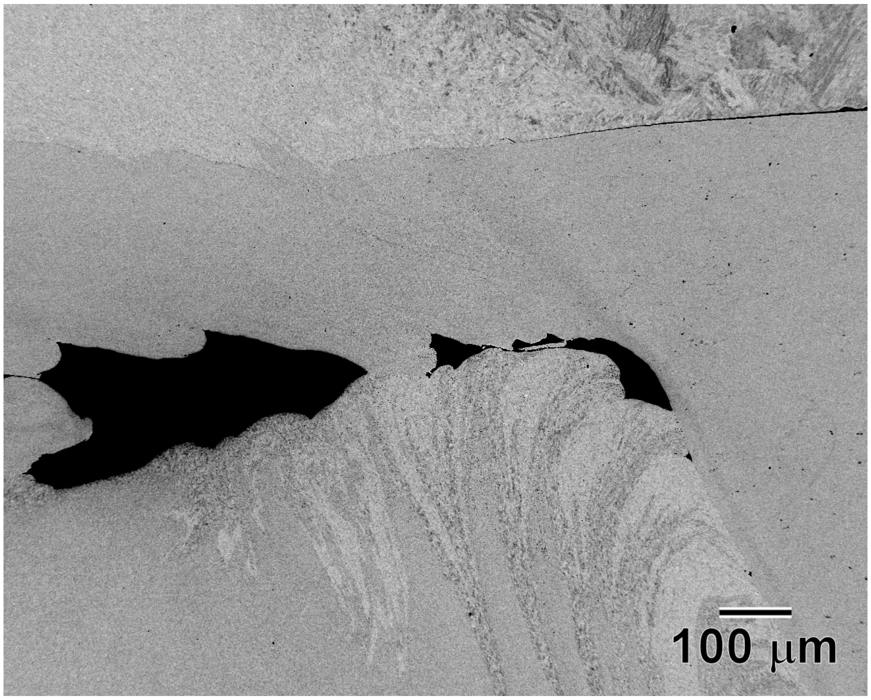

Figure 7. SEM micrographs showing the microstructure of F82H (top) and 14YWT-SM6 (bottom) near the large cavities that formed on the advancing side of the FSW zone. (a) secondary electron micrograph and (b) backscattered electron micrograph.

The microstructure that was observed by SEM near the large pores on the advancing side of the F82H/14YWT-SM6 specimen is shown in Figure 7 at a low magnification. The SE image in Figure 7a showed virtually no interfaces in the weld nugget and HAZ regions while the BSE image in Figure 7b revealed interfaces between F82H and 14YWT-SM6 in the top section of the weld nugget and between the TMAZ and HAZ of both F82H and 14YWT-SM6. The narrow gap between the unwelded F82H plate and 14YWT-SM6 specimen in the upper right region of the micrographs was observed to terminate at the weld zone. The BSE image in Figure 7b showed an extensive mixing pattern in the TMAZ located below the pores in 14YWT-SM6. This region pertained to the etched region observed above the pores by light microscopy in Figure 5. The BSE image also revealed a nonlinear interface between F82H and 14YWT-SM6 that provided evidence that mixing occurred between the two materials. The BSE image also indicated that considerable refinement in the microstructure occurred in the FSW nugget of F82H.

Coupled SE and BSE images of the interface observed between the TMAZ and HAZ of 14YWT-SM6 from the same location of the microstructure are shown at progressively higher magnifications in Figures 8 and 9, respectively. The bottom of the large pore located near the interface was included in these images to act as a reference point. The SE images observed in Figures 8a and 9a are sensitive to topographical features and revealed porosity in the TMAZ of 14YWT-SM6. The size and distribution of the pores were non-uniform, but were much smaller than the large pores present in the TMAZ. The BSE images shown in Figures 8b and 9b are sensitive to channeling effects related to grain orientation and allowed a more clear image of the grain size compared to the SE images. The BSE images showed that the interface region separating the TMAZ from the HAZ of 14YWT-SM6 was relatively narrow. The results indicated that FSW increased the grain size in the TMAZ by a factor of 2 to 4 times the size observed in the HAZ. This result implied that elevated temperatures greater than 1000ºC must have occurred during FSW based on results obtained from TMT processing of 14YWT that showed no increase in grain size after annealing at 1000ºC for 1 h. The analysis showed no correlation between the smaller pores and grain boundaries in the TMAZ. Although not fully understood, similar development of porosity has typically been observed on the advancing side of the FSZ joints in other studies [2].

The joint observed between F82H and 14YWT-SM6 in the weld nugget is shown in a set of coupled SE and BSE images recorded at progressively higher magnifications in Figures 10 and 11, respectively. At the lowest magnification shown in Figure 10, the SE and BSE images showed that good bonding occurred during FSW resulting in an interface between F82H and 14YWT-SM6. The BSE image in Figure 10b revealed that the interface was nonlinear due to mechanical mixing of the microstructures between F82H and 14YWT-SM6. However, no discernable grain structure can be observed in either F82H or 14YWT-SM6 at the low magnification. At the higher magnification shown in Figure 11, extensive porosity was observed to have developed at the interface between F82H and 14YWT-SM6 during FSW. The analysis indicated that the size and distribution of the pores was non-uniform and that there was no correlation between these pores and the grain boundaries in the TMAZ of F82H and 14YWT-SM6. It should be noted that the white features observed by SE in Figure 11a are colloidal silica particles used for the final polishing of the specimen that were not completed removed during cleaning. The BSE image in Figure 11b showed that the interface region separating the TMAZ of F82H and 14YWT-SM6 was relatively narrow. However, the FSW decreased the grain size in the TMAZ of F82H that resulted in equiaxed morphology and modified martensitic lath structure. In the TMAZ of 14YWT-SM6, the FSW increased the grain size and appeared to have slightly elongated the grains with an orientation relative to the interface. Additional SE and BSE images were recorded along the joint between F82H and 14YWt-SM6 and the results showed that porosity was present along the entire joint. The origin of the porosity may be related to the narrow gap that existed between the F82H plate and the bend bar specimens of 14YWT-SM6 that was mixed and redistributed into pores during the solid state mechanical mixing.

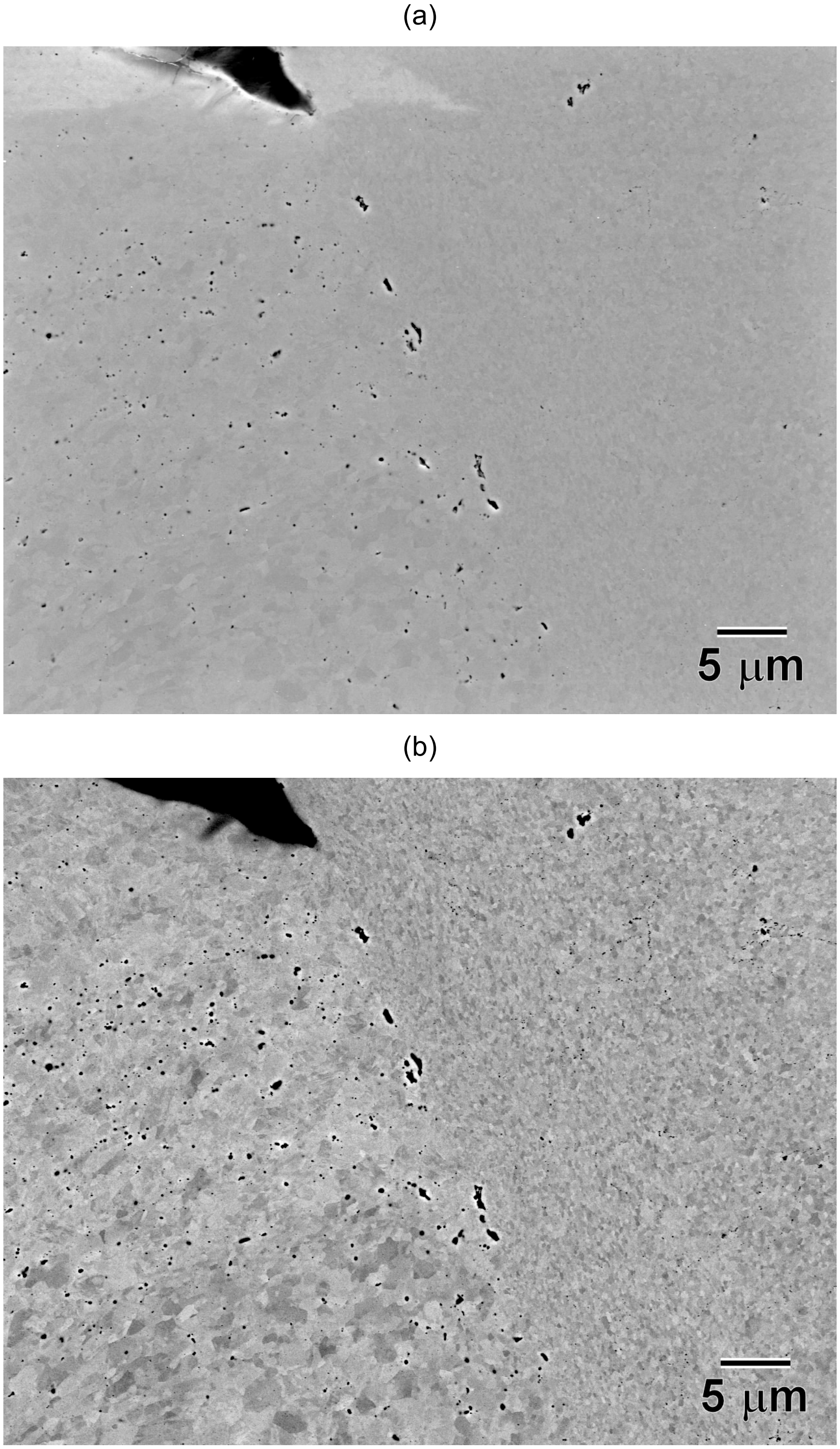

Figure 8. SEM micrographs of the joint between the FSW zone (left) and unaffected microstructure (right) of 14YWT-SM6. (a) Secondary electron micrograph and (b) backscattered electron micrograph.

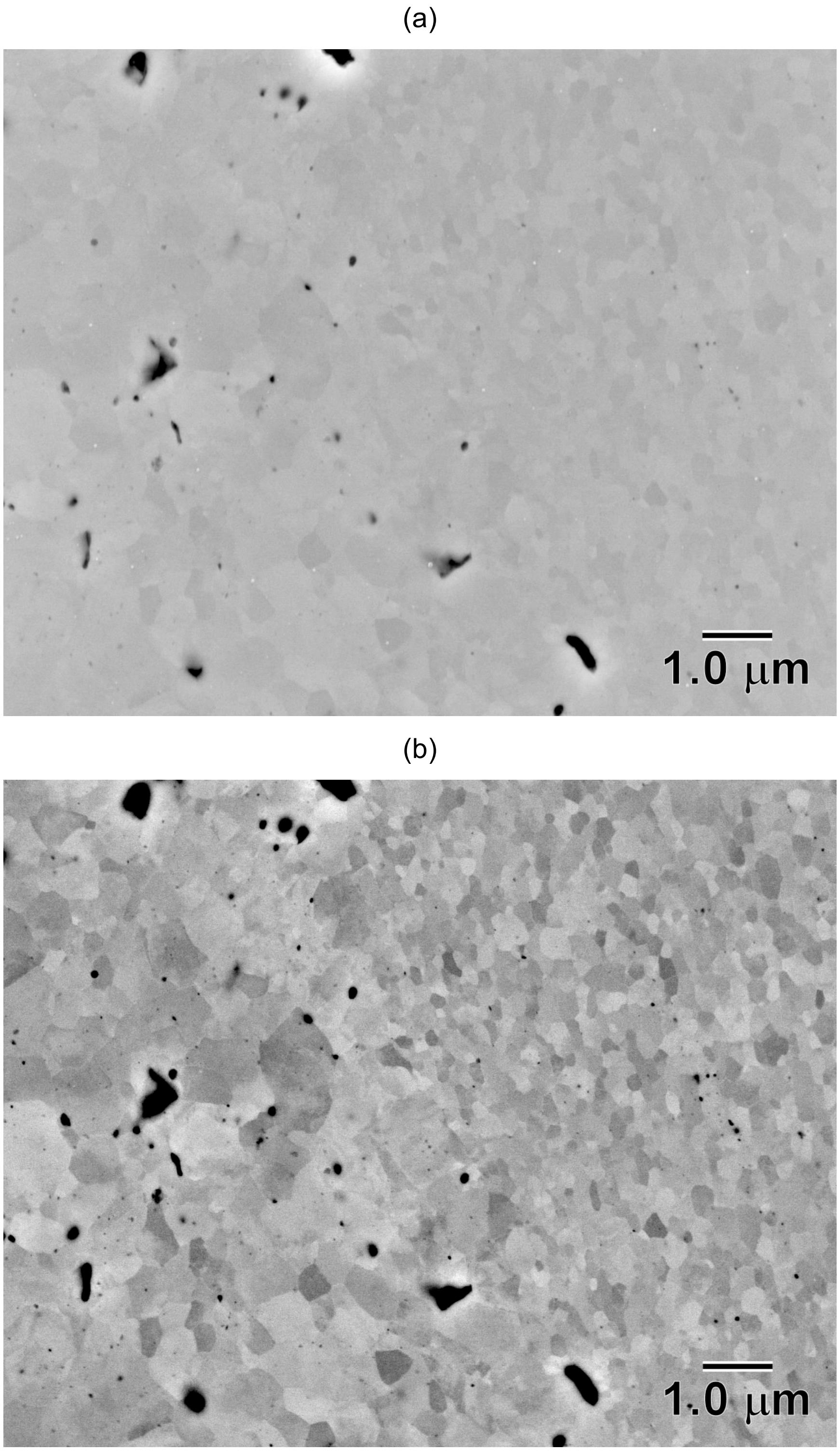

Figure 9. High magnification SEM micrographs of the joint between the FSW zone (left) and unaffected microstructure (right) of 14YWT-SM6. (a) Secondary electron micrograph and (b) backscattered electron micrograph.

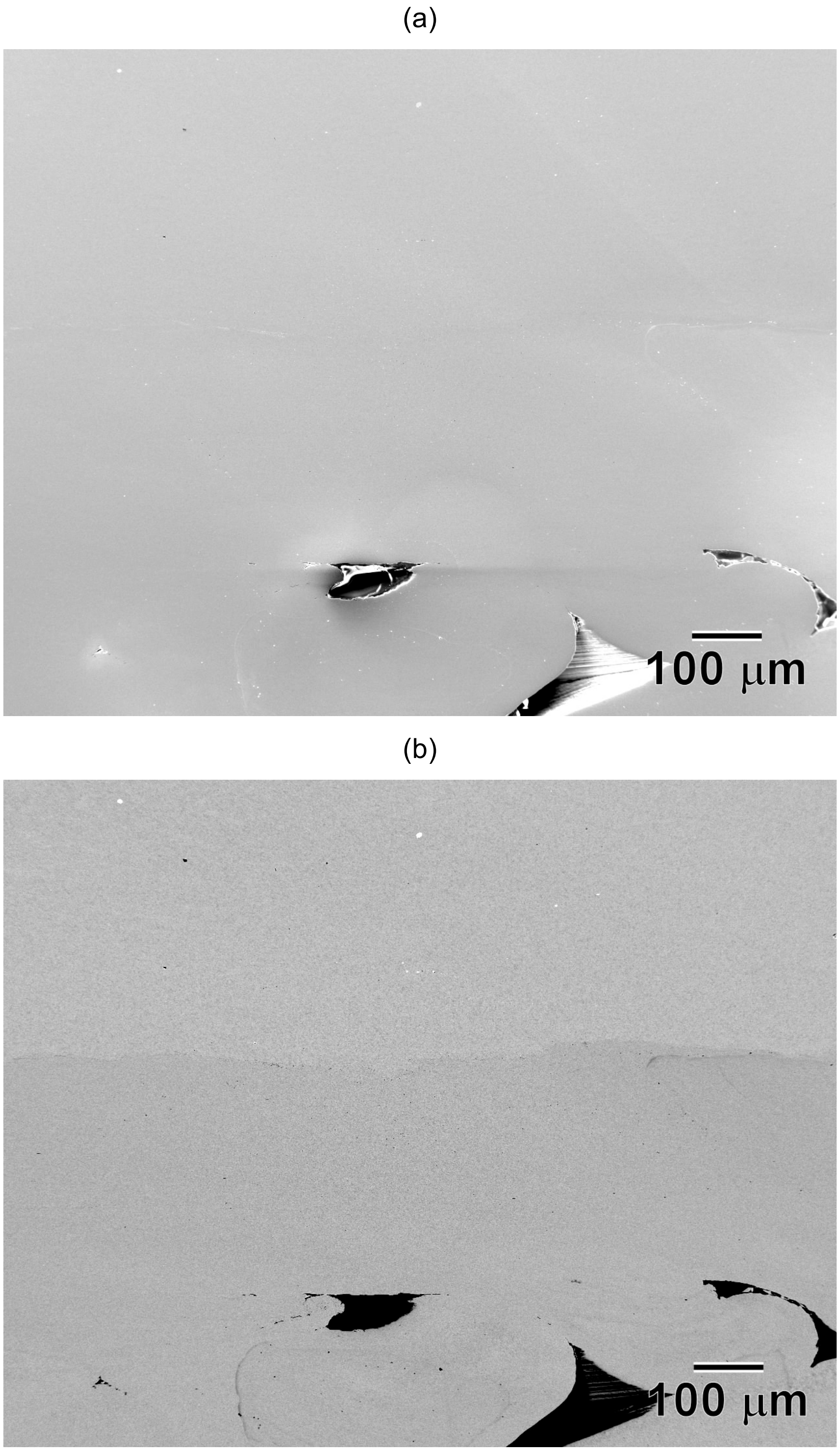

Figure 10. SEM micrographs showing the joint between the FSW zones of F82H (top) and 14YWT-SM6 (bottom) and the large cavities in the FSW zone of 14YWT-SM6. (a) Secondary electron micrograph and (b) backscattered electron micrograph.

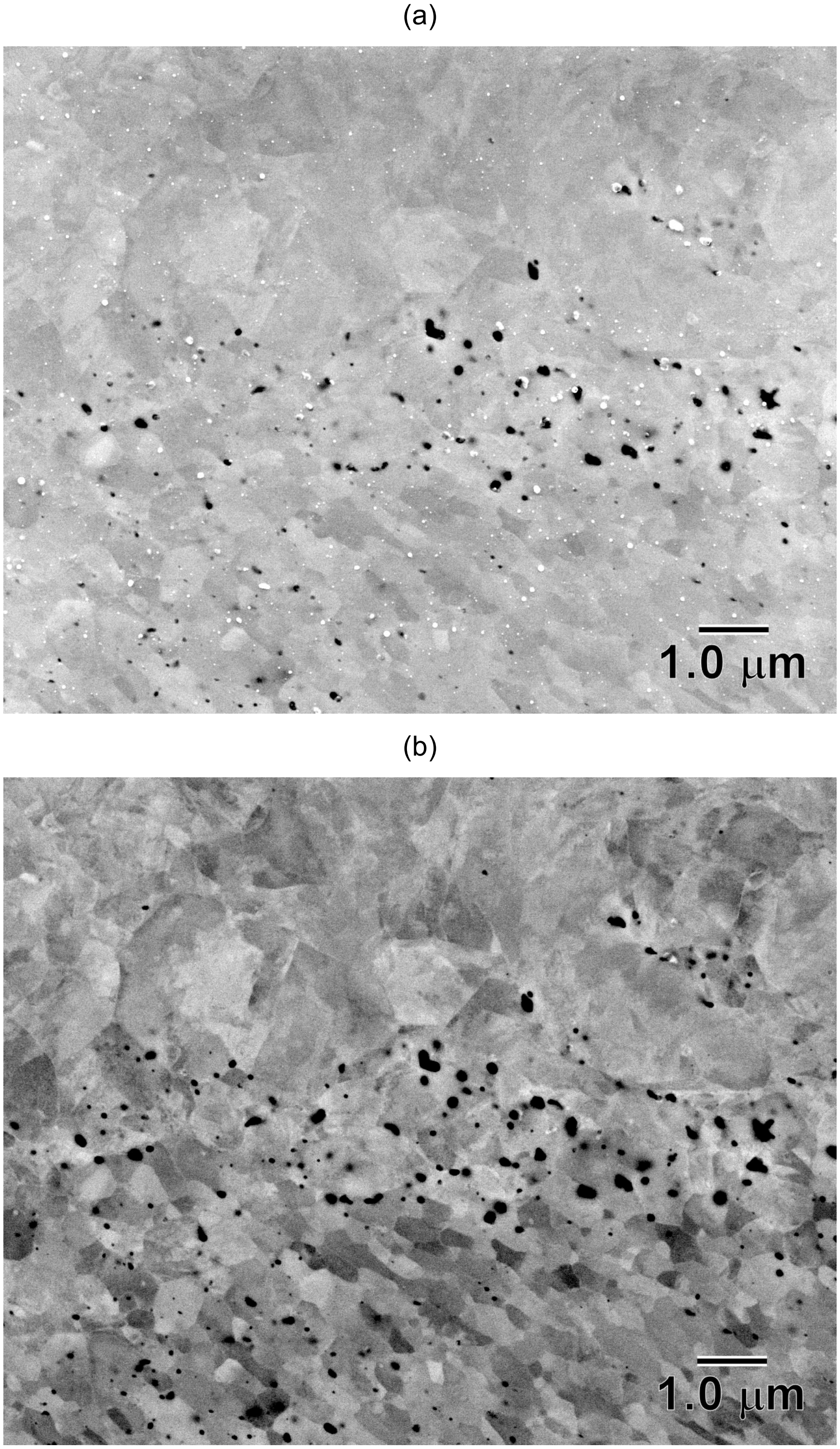

Figure 11. SEM micrographs of the joint between the FSW zones of F82H (top) and 14YWT-SM6 (bottom). (a) Secondary electron micrograph and (b) backscattered electron micrograph.

No results have been obtained on the microstructural characterization of the interfaces between the TMAZ and HAZ on the retreating side of the 14YWT-SM6 specimen or near the center where the joint between 2 bend bar specimens of 14YWT-SM6 is present. These regions will be characterized in the near future.

CONCLUSION

The initial attempt to join bend bar specimens of the advanced ODS 14YWT-SM6 alloy to each other and 14YWT-SM6 specimens to F82H plate was successfully obtained by friction stir welding. The joints were characterized by light microscopy and SEM analysis showed overall good bonding between TMAZ and HAZ of 14YWT-SM6 and between F82H and 14YWT-SM6. The interfaces were observed to be relatively narrow in width. However, porosity was observed in the TMAZ of 14YWT-SM6 on the advancing side of the FSW joint and at the interface between F82H and 14YWT-SM6. Further refinements in the FSW process will be required to minimize defects including porosity.

FUTURE WORK

The next procedure for characterization of the FSW joints present in the F82H/14YWT-SM6 sample will involve the preparation of TEM specimens using the lift-out procedure from strategic locations in the polished specimen and thinning by the Focused Ion Beam (FIB) method. The purpose of the TEM analysis will be to investigate the effect that FSW had on the size and distribution (spatial and number density) of the Ti-, Y- and O-enriched nanoclusters present in 14YWT-SM6 and to study the mixing characteristics of the microstructures between F82H and 14YWT-SM6 at the interface.

REFERENCES

[1] W. M. Thomas, E. D Nicholas, J. C. Needham, M. G. Murch, P. Templesmith and C. J. Dawes, G. B. Patent Application No. 9125978.8, 1991.
[2] R. S. Mishra and Z. Y. Ma, *Mater. Sci. Eng. R* **50** (2005) 1-78.
[3] S. M. Howard, B. K. Jasthi, W. J. Arbegast, G. J. Grant, S. Koduri, D. R. Herling and D. S. Gelles, DOE/ER-0313/37, 2004, 55-60.
[4] P. Miao, G. R. Odette, J. Gould, J. Bernath, R. Miller, M. Alinger, and C. Zanis, *J. Nucl. Mater.* **367–370** (2007) 1197-1202.
[5] Z. Feng and W. Ren, **Initial Development in Joining of ODS Alloys Using Friction Stir Welding**, ORNL/GEN4/LTR-06-021, (2006).
[6] Z. Feng and W. Ren, 2007 ASME PVP Conference, paper number PVP200726663.
[7] G. J. Grant, D. S. Gelles, R. J. Steel and R. Lindau, DOE/ER-0313/38 (2005) 47-53.
[8] F. Legendre, S. Poissonnet, P. Bonnaillie, L. Boulanger and L. Forest, *J. Nucl. Mater.* **386-388** (2009) 537-539.
[9] D. T. Hoelzer, J. Bentley, M. A. Sokolov, M. K. Miller, G. R. Odette and M. J. Alinger, *J. Nucl. Mater.* **367-370** (2007) 166-172.
[10] D. A. McClintock, Ph.D. Dissertation, Univ. of Texas, Austin (2008).
[11] D. A. McClintock, D. T. Hoelzer, M. A. Sokolov and R. K. Nanstad, *J. Nucl. Mater.* **386–388** (2009) 307–311.
[12] D. A. McClintock, M. A. Sokolov, D. T. Hoelzer and R. K. Nanstad, *J. Nucl. Mater.* **392** (2009) P353–359.

2.1 Tensile Properties of Unidirectional CVI SIC/SIC Minicomposites with a Multilayer interphase and Near-Stoichiometric SIC Fibers — K. Ozawa,* Y. Katoh, L.L. Snead (Oak Ridge National Laboratory), T. Nozawa, H. Tanigawa (Japan Atomic Energy Agency)

OBJECTIVE

The tensile behaviors of unirradiated unidirectional single tow SiC/SiC minicomposites are reported. Identical materials are to be irradiated in HFIR to investigating the effects of high-dose neutron irradiation on fiber/matrix interfacial properties, under the DOE-JAEA Phase VI Collaboration Project.

SUMMARY

Tensile properties of unidirectional single tow SiC/SiC minicomposites reinforced with Hi-Nicalon™ Type-S and Tyranno™-SA3 were evaluated. The interphase structure was pyrolytic carbon (PyC) / SiC multilayer and the thickness of the innermost PyC layer was varied (~70, ~240 and ~1150 nm). Only the Hi-Nicalon Type-S minicomposites with ~240 and ~1150 nm-thick PyC interphases exhibited the pseudo-ductile behavior; others reinforced with Tyranno-SA3 and the Hi-Nicalon Type-S composite with 70 nm-thick PyC interphase underwent brittle to near-brittle fracture behavior. The brittle failure behavior for those composites was attributed primarily to the quite low fiber volume fraction (5-10%). The Hi-Nicalon Type-S minicomposites with ~240 nm-thick PyC interphase exhibited ultimate tensile strength equivalent to 79-104% of the fiber bundle strength but only 70-85% of the strength for the ~1150 nm interphase for a given gauge length. Based on the analysis of the hysteresis loops recorded during the tensile loading and unloading sequences, the sliding stress estimated for the ~1150 nm-thick interphase appeared to be about 0.7 times that of the ~240 nm-thick interphase. This shows that both composites satisfied the global load sharing condition, but the composite with the thicker interphase could not achieve its fiber bundle strength, probably due to the lower interfacial sliding stress.

PROGRESS AND STATUS

Introduction

Silicon carbide (SiC) -based ceramics and composites (SiC/SiC) are considered for applications in various components of fusion and advanced fission reactor systems and fuel assemblies, due primarily to their superior irradiation performance and thermo-physical, -chemical, and -mechanical properties [1, 2]. Continuous SiC-fiber, SiC-matrix composites are of particular importance for applications which require reliability, toughness, and near-net shape fabrication.

One focus of irradiation studies of SiC/SiC composites in the past few decades has been determination of the fundamental response of the materials produced with various constituent options and processing routes. Through this effort, composites containing near-stoichiometric SiC fibers and high crystalline SiC matrices produced by chemical vapor infiltration (CVI) or nano-infiltration and transient eutectic-phase (NITE) processes are found to possess acceptable

---

* Present affiliation: Fusion Structural Materials Development Group, Fusion Research and Development Directorate, Japan Atomic Energy Agency (JAEA), Japan.

irradiation stability. However, a design scheme for the optimum interphase for radiation service remains unresolved due primarily to the lack of understanding of the irradiation effects on the fiber/matrix interfacial properties.

The minicomposite, which is a composite uni-directionally reinforced with a single fiber tow, is an appropriate geometry for evaluating the interfacial properties [3]. The general advantages of the minicomposite approach are as follows: 1) due to its simple uni-directional (UD) fiber architecture, the in-situ fiber strength and interfacial properties can be determined in relatively simple ways [4, 5], and 2) a large number of specimens can be fabricated at low cost in a relatively short time. Moreover, the very small volume of the minicomposite samples is attractive for irradiation studies due to the very high per-unit-volume cost of irradiation and the radiological concerns associated with the evaluation of irradiated material.

Based on the following background, a procedure for evaluating mechanical properties of the SiC/SiC minicomposite samples has been established at Oak Ridge National Laboratory, with the specific consideration of minimizing the personnel exposure during testing of the radiological samples. In the course of the test procedure development, CVI SiC matrix minicomposite samples with single PyC interphase, reinforced with four different near-stoichiometric SiC fibers were evaluated in the unirradiated condition [6]. In this study, the tensile properties of the SiC/SiC minicomposites with PyC/SiC multilayered interphase structure are reported. These materials will be irradiated starting this year under the DOE-JAEA Phase VI Project to investigate the effects of neutron irradiation on F/M interphase microstructure and mechanical properties [7].

EXPERIMENTAL

Materials

Table I describes the minicomposites, and scanning electron micrographs of polished cross sections for each minicomposite are shown in Figure 1. In brief, six types of UD single-tow minicomposites reinforced with two different SiC fibers were prepared in this study. Hi-Nicalon™ Type-S (TypeS) or Tyranno™-SA3 (SA3) fibers were used as reinforcements. The UD minicomposites were fabricated by the CVI process at Hyper-Therm High-Temperature Composites, Inc. (Huntington Beach, California). The fiber/matrix (F/M) interphase consists of five SiC/PyC layer sequences; nominal structure is fiber/e nm PyC/1000 nm SiC/20 nm PyC/1000 nm SiC/20 nm PyC/1000 nm SiC/20 nm PyC/1000 nm SiC/20 nm PyC/matrix, where e is the thickness of the innermost PyC interphase. Three different thickness of e was prepared. Total thickness of the interphase should be 4150-5230 nm Hereafter, the IDs indicated in Table I (TypeS-70, -240, -1150 for Hi-Nicalon Type-S (UD) fiber reinforced CVI matrix minicomposites with e = 70, 240, 1150 nm, and SA3-70, -230, -1000 for Tyranno-SA3 minicomposites with e = 70, 240, 1150 nm) are used.

Table I. Properties of minicomposites used in this study. Nominal mechanical properties of SiC fibers are also listed as supplied by their manufactures.

ID	Fiber	e [nm]	Matrix	r_f [μm]	N [-]	V_f [%]	σ_f [GPa]	E_f [GPa]	ϵ_f [%]
TypeS-70	Hi-Nicalon Type-S	70	CVI	6	500	5-6	2.6	420	0.6
TypeS-240	Hi-Nicalon Type-S	240	CVI	6	500	5-6	2.6	420	0.6
TypeS-1150	Hi-Nicalon Type-S	1150	CVI	6	500	5-10	2.8	420	0.6
SA3-70	Tyranno-SA3	70	CVI	3.75	1600	5-9	2.8	409	0.7
SA3-230	Tyranno-SA3	230	CVI	3.75	1600	5-7	2.8	409	0.7
SA3-1000	TyrannoSA-3	1000	CVI	3.75	1600	5-9	2.8	409	0.7

Table I notations are based on: multilayer structure is fiber/ e nm PyC /1000 nm SiC /20 nm PyC/1000 nm SiC/20 nm PyC/1000 nm SiC /20 nm PyC/1000 nm SiC/20 nm PyC/matrix. e = the thickness of the most inner PyC layer, r_f = the fiber radius, N = the number of filaments in a tow, V_f the fiber volume fraction, σ_f = the single fiber strength at 25 mm, E_f = the Young's modulus of a fiber, and ϵ_f = the fiber elongation.

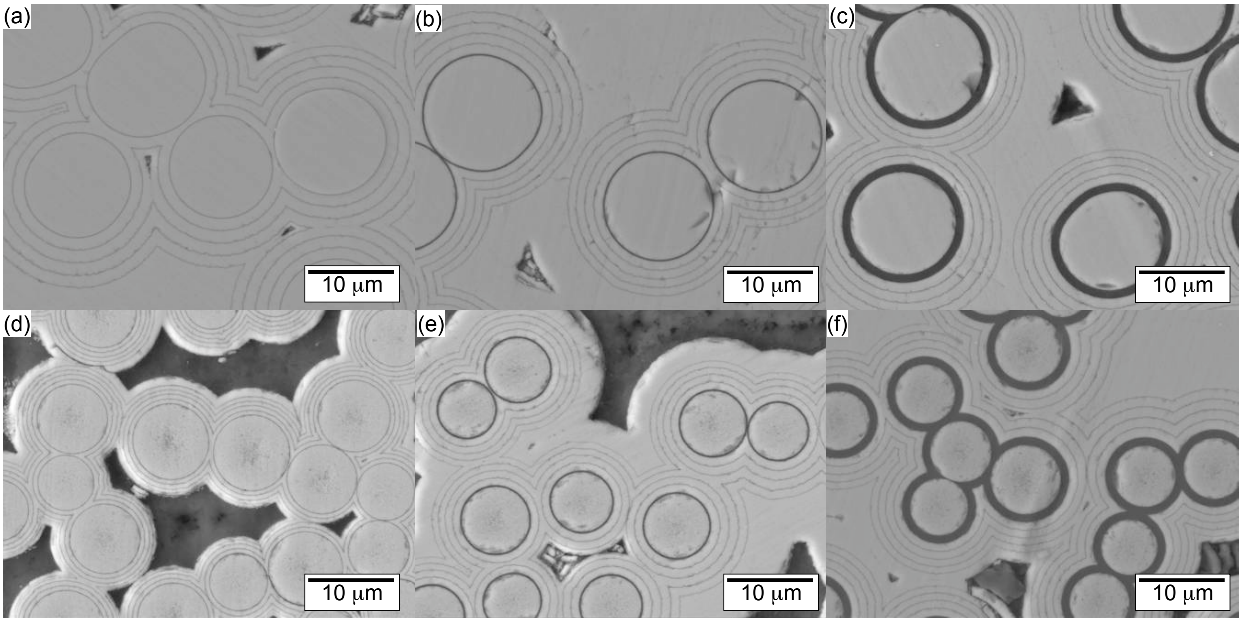

Figure 1. Scanning electron micrographs of polished cross sections of (a) TypeS-70, (b) TypeS-240, (c) TypeS-1150, (d) SA3-70, (e) SA-230 and (f) SA-1000 minicomposites.

Cross sectional area of the minicomposite ($S_\mathrm{c} = S_\mathrm{f} + S_\mathrm{i} + S_\mathrm{m}$) and fiber volume fraction (V_f) were calculated from the mass of the fiber bundle, PyC and minicomposite;

$$V_\mathrm{f} = \frac{S_\mathrm{f}}{S_\mathrm{f}+S_\mathrm{i}+S_\mathrm{m}} = \frac{\pi r_\mathrm{f}^2 N}{\pi r_\mathrm{f}^2 N + \pi\left((r_\mathrm{f}+e)^2 - r_\mathrm{f}^2\right)N + \frac{M_\mathrm{c} - (M_\mathrm{f} + M_\mathrm{i})}{L d_\mathrm{m}}} \quad (1)$$

where S_j is the cross sectional area, r_f the fiber radius, N the number of filaments in a tow, M_j the mass, L the specimen length, and d_j the density. Subscripts f, i, m and c denote fiber, interphase, matrix and composite respectively. M_f and M_i are obtained from $M_\mathrm{f} = S_\mathrm{f} N L d_\mathrm{f}$ and $M_\mathrm{i} = S_\mathrm{i} N L d_\mathrm{i}$. In the calculation, it was assumed that the innermost PyC layer was perfectly deposited around each fiber and that the effect of other four thin PyC layers on mass and density can be ignored. The parameters used in the V_f calculation were listed in Table II. It is noted that all composites in this study have a quite low V_f (only 5-10%).

Table II. The values used in the analysis for fiber volume fraction and ultimate tensile stress.

Symbol	Description	Fiber type	Value	Unit	Ref.
d_f	Density of SiC fiber	(Hi-Nicalon Type-S)	2.98	g/cm^3	[8, 9]
		(Tyranno-SA3)	3.1	g/cm^3	[8, 9]
d_m	Density of SiC matrix		3.21	g/cm^3	[10]
d_i	Density of PyC layer		1.91	g/cm^3	[11]
σ_1	Fiber bundle strength at L_1	(Hi-Nicalon Type-S)	2477	MPa	[8, 9]
		(Tyranno-SA3)	2412	MPa	[8, 9]
L_1	Fiber gauge length		25	mm	[8, 9]
m	Weibull modulus	(Hi-Nicalon Type-S)	6.4	-	[8]
		(Tyranno-SA3)	8.2	-	[8]

Tensile Tests

The test apparatus and specimen preparation are described elsewhere [6]. Tensile tests were conducted using an electromechanical testing machine (Insight 10, MTS Systems Co., Eden Prairie, Minnesota) with a load capacity of 1000 N. Strain was measured by a pair of linear variable differential transducers, LVDTs (Lucas Schaevitz GCA-121-125, Hampton, Virginia). We adopted an alignment system similar to the one used in single fiber tensile testing standardized in ASTM C 1557 in order to assure specimen alignment. The pair of aluminum tabs was fastened to both sides of a minicomposite sample using an epoxy adhesive dispersed by a syringe. The specimen to be glued was fixed in a V-notched fixture with flathead screws for assuring specimen alignment. This fixture including the specimen was cured at 110°C for more than 3 hours in an air furnace in order to develop the adhesive’s maximum bonding strength. The gauge length of the specimens is 18 mm, defined by the distance between the inner ends of the aluminum tabs. The specimen was clamped into the simple V-notched fixtures with flathead screws. A guide rail was used to confirm specimen alignment and to avoid damaging the specimen during handling.

The tests were conducted at ambient conditions under crosshead displacement control at 0.05 mm/min. Unloading/reloading cyclic tensile tests were conducted to evaluate interfacial properties. Prior to the tensile tests, compliance of the grip assembly was determined using a set of tungsten wires with varied gauge lengths, and the system compliance of 4.32 × 10^{-2} μm/N was obtained. Tensile strain (ϵ) is determined by the following equation, $\epsilon = (\Delta L - C_S P)/L_0$, where ΔL the average crosshead displacement recorded by LVDTs, C_S the system compliance, P the applied load, and L_0 the gauge length. The minicomposite tensile stress (σ) is simply defined as $\sigma = P/S_c$. The proportional limit stress (PLS) was defined as the stress at 0.5% deviation from the extrapolated fit of the slope by the least squares method for the initial loading.

The ultimate tensile strength of the minicomposite (UTS, σ_{UTS}) was converted to the fiber-averaged UTS ($\sigma_{\mathrm{U,f}}$) using the equation, $\sigma_{\mathrm{U,f}} = \sigma_{\mathrm{UTS}}/V_{\mathrm{f}}$. This was compared with the fiber bundle strength (σ_{bundle}) in order to know the interaction between effective UTS on fibers and interfacial sliding stress (τ). σ_{bundle} at given length was calculated from the following equation based on the weakest-link theory, assuming that fracture origins of a same fiber is spatially distributed strictly within a volume three-dimensionally [12, 13];

$$\frac{\sigma_1}{\sigma_2} = \left(\frac{V_2}{V_1}\right)^{1/m} = \left(\frac{L_2}{L_1}\right)^{1/m} \tag{2}$$

where σ_j, V_j, L_j, and m are the fiber bundle strength, the volume of the fiber bundle, the gauge length at the condition *j* (= 1 or 2), and the Weibull shape parameter, respectively. The fiber characteristic values reported by Sauder *et al.* [8, 9] were used as a reference shown in Table II.

RESULTS AND DISCUSSION

Tensile Stress-Strain Responses

Representative tensile stress-tensile strain curves are shown in Figure 2 for all six materials. Also, the results of the mechanical properties evaluation are listed in Table III. The TypeS-70, SA3-70 and -1150 composites exhibited brittle behavior with no fiber pull-out observed on the fracture surfaces by optical microscope observation. The SA3-1000 composites have instable fracture behavior; includes both brittle and pseudo-ductile, but fiber pull-out was not confirmed. Only the TypeS-240 and -1150 composites exhibited pseudo-ductile fracture with significant fiber pull-out. Both composites showed significant drop of tensile stress just after their proportional limit (Figure 2 (b, c)). As shown in Figure 3, the Type-S minicomposite with thicker e (-1150) had larger tensile elongation (0.5-0.75% vs. 0.2-0.6% of the TypeS-240) and smaller normalized tensile strength to the fiber bundle strength at given gauge length (70-85% vs. 79-104 % of the TypeS-240). For all six composites, the matrix crack spacing ($\bar{d}$) could not be measured even though the methods by Murakami boiling etching solution and by a crack measurement using replica films were tried.

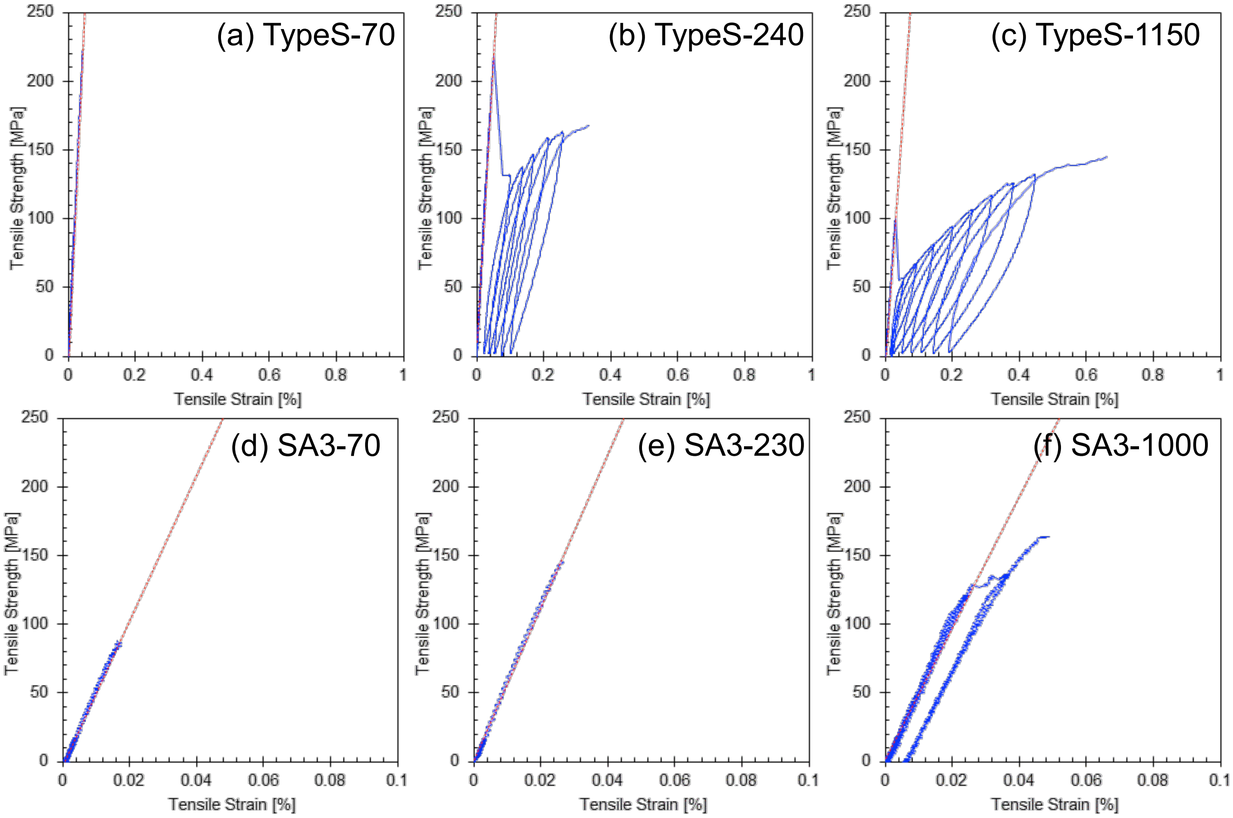

Figure 2. Representative tensile stress-strain curves for (a) TypeS-70, (b) TypeS-240, (c) TypeS-1150, (d) SA3-70, (e) SA3-230 and (f) SA3-1000 minicomposites. Note that the tensile strain axis is different for the Type S and SA3 minicomposites.

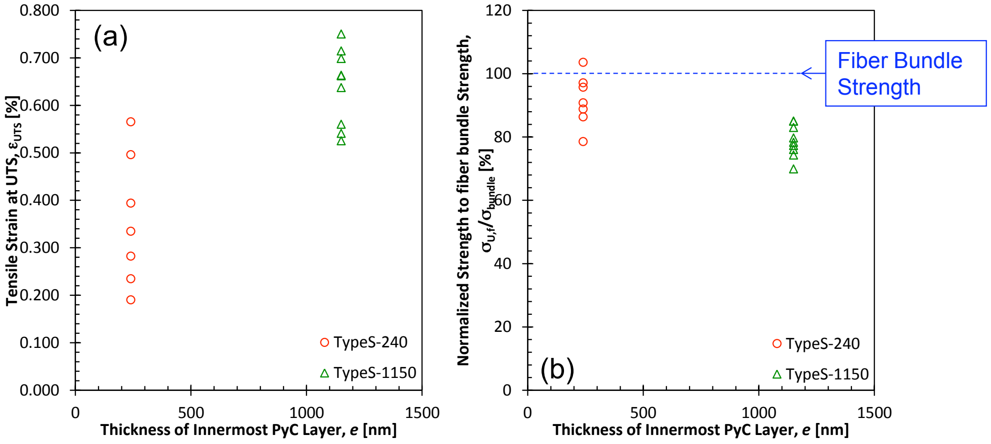

Figure 3. (a) Tensile strain at UTS, and (b) strength normalized to fiber bundle strength of the TypeS-240 and -1150 composites.

Table III. Tensile properties of the minicomposites. Numbers in parenthesis show one standard deviation.

ID	Fiber	e [nm]	Matrix	Fracture Behavior	σ_{PLS} [MPa]	σ_{UTS} [MPa]	ϵ_{UTS} [%]	$\sigma_{\mathrm{U,f}}/\sigma_{\mathrm{bundle}}$ [%]	#
TypeS-70	Hi-Nicalon Type-S	70	CVI	Brittle	-	164 (80)	0.044 (0.024)	-	3
TypeS-240	Hi-Nicalon Type-S	240	CVI	Pseudo-Ductile	106 (55)	136 (18)	0.357 (0.137)	92 (8)	7
TypeS-1150	Hi-Nicalon Type-S	1150	CVI	Pseudo-Ductile	99 (54)	141 (27)	0.639 (0.080)	79 (5)	9
SA3-70	Tyranno-SA3	70	CVI	Brittle	-	71 (23)	0.013 (0.005)	-	2
SA3-230	Tyranno-SA3	230	CVI	Brittle	-	146 (-)	0.026 (-)	-	1
SA3-1000	Tyranno-SA3	1000	CVI	Brittle	-	199 (42)	0.045 (0.014)	-	4
				Pseudo-Ductile	130 (27)	205 (33)	0.065 (0.012)	-	5

σ_{PLS} = the proportional limit stress of a minicomposite, σ_{UTS} = the ultimate tensile strength of a minicomposite, ϵ_{UTS} = the tensile strain at UTS, $\sigma_{\mathrm{U,f}}/\sigma_{\mathrm{bundle}}$ = normalized strength to fiber bundle strength, and # = the number of valid tests.

The reasons that almost half of the composites exhibited brittle behavior and that the TypeS-240 and -1150 showed discontinuity in their strain-stress curves at their proportional limit can be reasonably explained by the quite low fiber volume fraction (V_{f}), although the potential effects of PyC/SiC multilayered interphase structure (4150-5230 nm in total) and fiber surface roughness can also be considered. Under such low V_{f} condition, cracks could not detect the F/M interphases, and then penetrate the F/M interphase. As a result the composites exhibited brittle behavior with flat fractured surfaces. Based on a simple calculation according to the classical Aveston-Cooper-Kelly theory [14] (the theory by Budiansky *et al.* [15] is suitable for non-slipping interphase, but the ACK theory was chosen due to calculation simplicity), more than 20% fiber volume fraction is estimated as necessary for these minicomposites to exhibit “multiple” fracture [16], which is the behavior of a composite’s pseudo-ductility when the fibers will not fail and load transferred to them when the matrix breaks, leading to multiple cracking of the matrix. However the V_{f} of the minicomposites this study (5-10%) is much smaller than the critical V_{f} for the “multiple” fracture from the theory. As a result of the preliminary optical microscope observation, any sign of “multiple” fractures (pull-out, matrix crack spacing, etc.) could not be measured this time.

The reason of the discontinuity in TypeS-240, -1150 at their proportional limit in their strain-stress curve is also due to the quite low V_{f}. It was confirmed that very thick CVI-SiC matrix (around 200-300 μm) was deposited around the fibers, shown in Figure 4. It is reported by Morscher [17] that such thick “sheath” deposition makes it difficult to measure the fiber pull-out length and matrix crack spacing ($\bar{d}$), i.e. to evaluate interfacial sliding stress (τ) directly. Additionally, this sheath also makes the proportional limit stress more scattered and unsuitable, because the minicomposites without cracks behaves as if they are monolithic material until crack initiates.

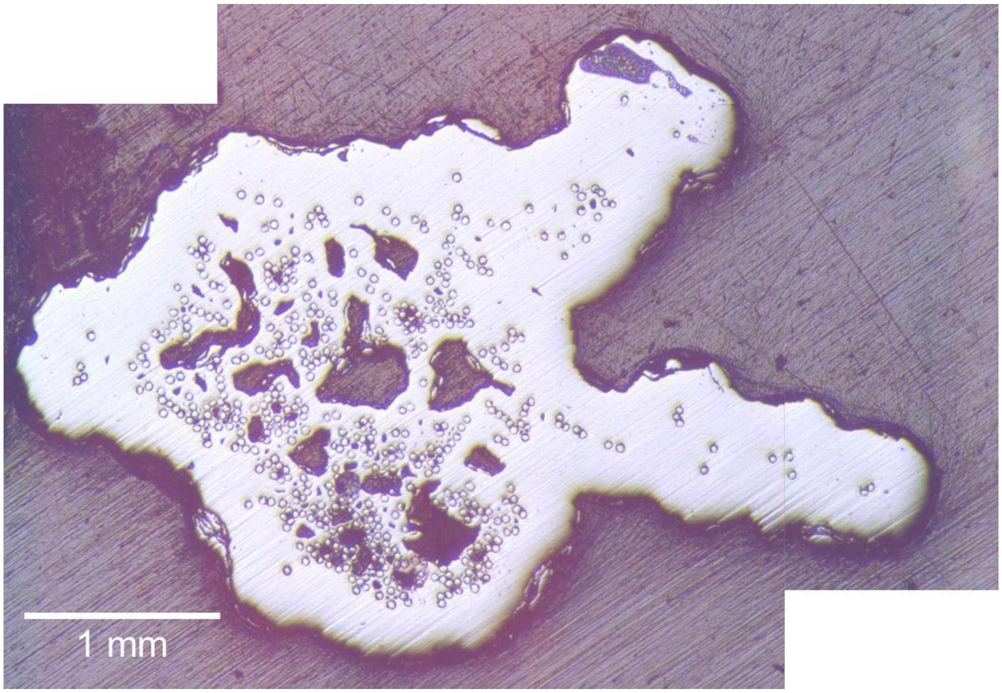

Figure 4. Optical micrograph of cross section of the TypeS-1150 minicomposite with thick CVI coating.

Hysteresis Loop Analysis

In order to know the relationship between τ and in-situ fiber strength, the hysteresis loop analysis was found to be a good tool. Since the $\bar{d}$ could not be experimentally detected due to quite low V_f, (i.e. thick "sheath" coating), τ cannot be obtained quantitatively. However, it can be qualitatively estimated from the hysteresis loop analysis, by the following method of Katoh *et al.* [18]. Maximum hysteresis loop width ($\delta\epsilon_\mathrm{max}$) is expressed as follows [19],

$$\delta\epsilon_\mathrm{max} = \frac{b_2(1-a_1V_\mathrm{f})^2\sigma_\mathrm{p}^2}{8V_\mathrm{f}^2\tau E_\mathrm{m}} \cdot \frac{r_\mathrm{f}}{\bar{d}} \tag{3}$$

, where σ_p is the peak stress, E_i the Young's modulus, $\bar{d}$ the mean matrix crack spacing distance, and a_1, b_2 the Hutchinson-Jensen parameters given by [20],

$$a_1 = \frac{E_\mathrm{f}}{E_\mathrm{c}} \tag{4}$$

$$b_2 = \frac{(1+\nu)E_\mathrm{m}[E_\mathrm{f}+(1-2\nu)E_\mathrm{c}]}{E_\mathrm{f}[(1+\nu)E_\mathrm{f}+(1-\nu)E_\mathrm{c}]} \tag{5}$$

with ν being Poisson's ratio, assumed to be same and isotropic in fiber and matrix ($\nu_{\mathrm{f}} = \nu_{\mathrm{m}} = \nu$). Also, the matrix damage parameter ($\mathcal{D}$) is defined as [21],

$$\mathcal{D} = \frac{E_c - E^*}{E^*} = \mathcal{B}\frac{r_{\mathrm{f}}}{\bar{d}}\sigma_{\mathrm{p}}^2 \tag{6}$$

where E^* is the elastic unloading modulus at peak stress, and $\mathcal{B}$ a constant. Using this equation, Equation (3) can be rewritten, with K constant, as;

$$\delta\epsilon_{\mathrm{max}} = \frac{K}{\tau}\cdot\mathcal{D}\sigma_{\mathrm{p}}^2 \tag{7}$$

Equation (7) indicates that τ can be estimated qualitatively from the slope of a $\delta\epsilon_{\mathrm{max}} - \mathcal{D}\sigma_{\mathrm{p}}^2$ plot. Figure 5 shows this analytical result for the TypeS-240 and TypeS-1150 minicomposites. $\delta\epsilon_{\mathrm{max}}$ was measured at half of peak stress of each cycle. According to the hysteresis loop analysis, τ of the TypeS-1150 composites is about 0.7 times as the TypeS-240 composites.

The tensile properties of a UD composite system are strongly affected by the Weibull modulus (m), the characteristic strength (σ_0) of the fibers, and the interfacial sliding stress (τ). Under the assumption of global load sharing (GLS) theory [22], the fiber-averaged UTS ($\sigma_{\mathrm{U,f}}^{\mathrm{GLS}}$) in a unidirectional composite system is expressed as follows:

$$\sigma_{\mathrm{U,f}}^{\mathrm{GLS}} = \left(\frac{\sigma_0^m \tau L_0}{r_{\mathrm{f}}}\right)^{\frac{1}{m+1}} \left[\frac{2(m+1)}{(m+2)m}\right]^{\frac{1}{m+1}} \left(\frac{m+1}{m+2}\right) \tag{8}$$

with the in-situ fiber bundle strength ($\sigma_{\mathrm{U,f}}^{\mathrm{GLS}}$), Weibull mean strength (σ_0), the Weibull modulus(m), the gauge length (L_0), and the interfacial sliding stress (τ). Roughly interpreting this equation, $\sigma_{\mathrm{U,f}}^{\mathrm{GLS}}$ is dependent on only τ. Hence, it is considered that both composites satisfy the global load sharing condition suggested by Curtin [22], but the TypeS-1150 could not achieve its fiber bundle strength compared with the TypeS-240, probably due to the lower interfacial sliding stress.

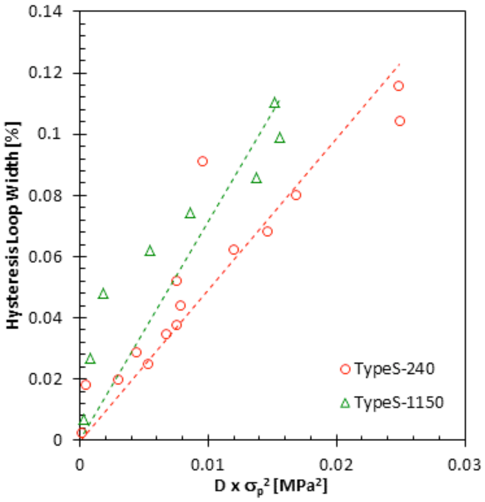

Figure 5. Hysteresis loop width plots against the $\mathcal{D}\sigma_p^2$ values of the TypeS-240 and -1150 minicomposites. It is noted that steeper slope indicates lower τ.

ACKNOWLEDGEMENT

This research was sponsored by the Office of Fusion Energy Sciences, US Department of Energy under contract DE-AC05-00OR22725 with UT-Battelle, LLC.

REFERENCES

[1] T. Nozawa, T. Hinoki, A. Hasegawa, A. Kohyama, Y. Katoh, L. L. Snead, C. H. Henager Jr, J. B. J. Hegeman, *J. Nucl. Mater.* **386-388** (2009) 622.
[2] Y. Katoh, L. L. Snead, C. H. Henager Jr., A. Hasegawa, A. Kohyama, B. Riccardi, H. Hegeman,
J. Nucl. Mater. **367-370** (2007) 659.
[3] R. Naslain, J. Lamon, R. Pailler, X. Bourrat, A. Guette, F. Langlais, Composites *Part A: Appl. Sci. Manuf.* **30** (1999) 537.
[4] J. Lamon, F. Rebillat, A. G. Evans, *J. Am. Ceram. Soc.* **78** (1995) 401.
[5] E. Vagaggini, J.-M. Domergue, A. G. Evans, *J. Am. Ceram. Soc.* **78** (1995) 2709.
[6] K. Ozawa, Y. Katoh, E. Lara-Curzio, L. L. Snead, T. Nozawa, *Ceram. Eng. Sci. Proc.* **31** (2010) 208.
[7] T. Nozawa, K. Ozawa, H. Tanigawa, Y. Katoh, L. L. Snead, R. E. Stoller, Research Plan and Status of High-Dose Rabbit Irradiation Experiment for Silicon Carbide Composites, in these reports.
[8] C. Sauder, A. Brusson, J. Lamon, *Ceram. Eng. Sci. Proc.* **29** (2008) 91.
[9] C. Sauder, A. Brusson, J. Lamon, *Int. J. Appl. Ceram. Technol.* **7** (2010) 291.
[10] From the manufacturer's catalogue,
http://www.dow.com/assets/attachments/business/gt/advanced_ceramics/cvd_silicon_carbide/tds/cvd_silicon_carbide.pdf
[11] Estimated from the PyC oxidation rate of the same minicomposites. C. H. Kim, Y. Katoh, "Active and passive oxidation of CVD-SiC under HTGR operating condition," presented at the

35th International Conference and Exposition on Advanced Ceramics and Composites, (2011).
[12] J. B. Watchman, **Mechanical Properties of Ceramics**, John Wiley & Sons Inc., New York, 1996.
[13] ASTM C 1239-07.
[14] J. Aveston, G. A. Cooper, A. Kelly, The Properties of Fibre Composites: Conference Proceedings, National Physical Laboratory, 4 November (1971) 15.
[15] B. Budiansky, J. W. Hutchinson, A. G. Evans, *J. Mech. Phys. Solids* **34** (1986) 167.
[16] J. Aveston, A. Kelly, *J. Mater. Sci.* **8** (1973) 352.
[17] G. N. Morscher, J. Martinez-Fernandez, *J. Am. Ceram. Soc.* **82** (1999) 145.
[18] Y. Katoh, L. L. Snead, T. Nozawa, S. Kondo, J. T. Busby, *J. Nucl. Mater.* **403** (2010) 48.
[19] A. G. Evans, J. M. Domergue, E. Vagaggini, *J. Am. Ceram. Soc.* **77** (1994) 1425.
[20] J. W. Hutchinson, H. M. Jensen, *Mech. Mater.* **9** (1990) 139.
[21] M. Y. He, B. X. Wu, A. G. Evans, J. W. Hutchinson, *Mech. Mater.* **18** (1994) 213.
[22] W. A. Curtin, B. K. Ahn, N. Takeda, *Acta Materialia* **46** (1998) 3409.

2.2 Low Activation Joining of SiC/SiC Composites for Fusion Applications

— C. H. Henager, Jr., R. J. Kurtz (Pacific Northwest National Laboratory[1], Richland, WA 99336, USA), and M. Ferraris, (Politecnico di Torino, Torino, Italy)

OBJECTIVE

This work discusses the latest developments in TiC + Si displacement reaction joining at PNNL based on mechanical property test results from miniature torsion joints tested at Politecnico di Torino.

SUMMARY

The use of SiC composites in fusion environments likely requires joining of plates using reactive joining or brazing. One promising reactive joining method uses solid-state displacement reactions between Si and TiC to produce Ti_3SiC_2 + SiC. We continue to explore the processing envelope for this joint for the TITAN collaboration in order to produce optimal joints to undergo irradiation studies in HFIR. The TITAN collaboration has designed miniature torsion joints for preparation, testing, and irradiation in HFIR. PNNL synthesized 40 miniature torsion joints and several were tested for shear strength prior to irradiation testing in HFIR. The resulting tests indicated that 1) joint fixture alignment problems cause joint strengths to be lower than optimal, 2) that non-planar torsion test failures may limit the effectiveness of the miniature specimen design, and 3) that several joints that were well aligned had high shear strengths and promising mechanical properties. In summary, it appears that high joint strengths cause non-planar shear fracture and complicate strength analysis for miniature torsion specimens.

PROGRESS AND STATUS

Introduction

SiC is an excellent material for fusion reactor environments, including first wall plasma facing materials and breeder-blanket modules. It is low-activation, temperature-resistant, and radiation damage tolerant compared to most materials. In the form of woven or braided composites with high-strength SiC fibers it has the requisite mechanical, thermal, and electrical properties to be a useful and versatile material system for fusion applications, especially since microstructural tailoring during processing allows control over the physical properties of interest [1-6]. However, it is difficult to mechanically join large sections of such materials using conventional fasteners so the analog of welding is being pursued for these ceramic materials [2, 4-15]. Such methods include metallic brazes [8, 16], glass ceramics [7, 17], preceramic polymers [15], and displacement reactions [2, 6]. This paper reports on the current status of SiC and SiC-composite joining for fusion applications based on displacement reactions between Si and TiC. This has been used to produce bulk composite material consisting of SiC-Ti_3SiC_2, with small amounts of TiC determined by the phase equilibria conditions [18].

---

[1] PNNL is operated for the U.S. Department of Energy by Battelle Memorial Institute under Contract DE-AC06-76RLO 1830.

EXPERIMENTAL PROCEDURES

Joints are made using a tape calendaring process using organic binders and plasticizers together with a mixture of TiC and Si powders, with 99.99% purity, average diameters less than 45 μm, and a TiC:Si ratio of 3:2. The flexible tapes were 200 μm thick and were cut to a disk shape and applied between two CVD SiC miniature torsion specimens as shown in Figure 1. Two batches of specimens were prepared for this study, with the first batch using torsion samples with different dimensions as indicated in Figure 1. In both cases, the green joints were placed within a graphite fixture shown in Figure 2 that allows for alignment of the torsion joints and for applied compressive force during heating in an inert gas furnace enclosure. Joints were formed by heating the torsion coupons in argon to 1698K at 10K/min and holding for 2 hours at 40 MPa applied pressure. The resulting joints were dense and approximately 15 μm thick. They were prepared for optical and scanning electron microscopy using standard ceramographic cutting, grinding, and polishing methods.

The joints were sent to Prof. M. Ferraris of Politecnico di Torino, Torino, Italy for testing as part of the TITAN collaboration. The joints are tested in torsion using a test fixture as shown in Figure 3. The hourglass specimens are held in place using the square top and bottom specimen shapes with the joint joining the two half specimens as shown in Figure 1 along the circular center region. The test places the joint in pure shear and presumably tests the shear strength more accurately than other tests, such as notched shear tests with problematic bending moments and stress concentrations.

RESULTS

Figure 1 shows the torsion specimen drawing and a fabricated joint at PNNL prior to any testing. Figure 2 shows the joints placed into the graphite alignment fixture prior to processing in argon at 1698K for 2 hours. Some slight misalignment can be observed in some of the processed joints as shown in Figure 3. An improved graphite alignment fixture has been designed based on these initial processing results.

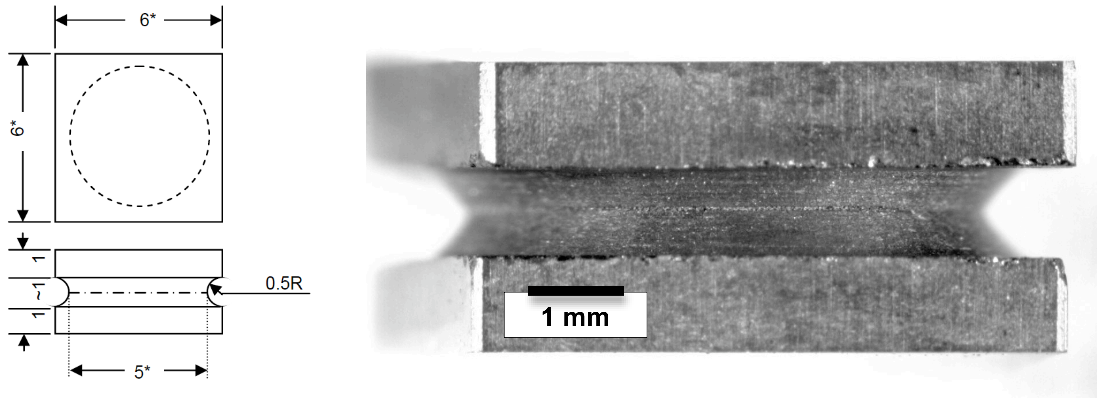

(a) (b)

Figure 1. (a) Drawing of miniature torsion joining specimen for HFIR irradiation. Dimensions are shown in mm in (a). Shown in (b) is a photomicrograph of a PNNL fabricated torsion specimen. The joint line is visible along the specimen horizontal centerline.

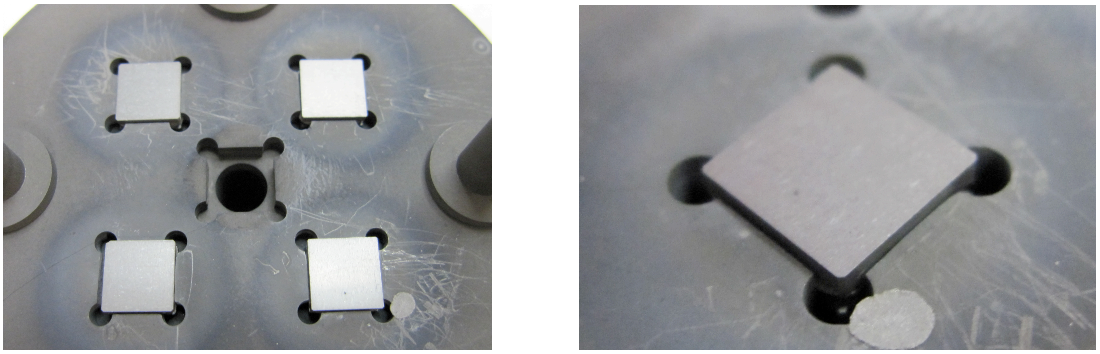

(a) (b)

Figure 2. (a) Photomicrograph of graphite joining fixtures with 4 torsion joints ready for processing. The central hole in this photo allows an alumina-sheathed thermocouple to be placed close to the joints during processing. Shown in (b) is a close-up photomicrograph of a single joint held in place prior to processing. The torsion joints are 6-mm square and slightly less than 3-mm in height.

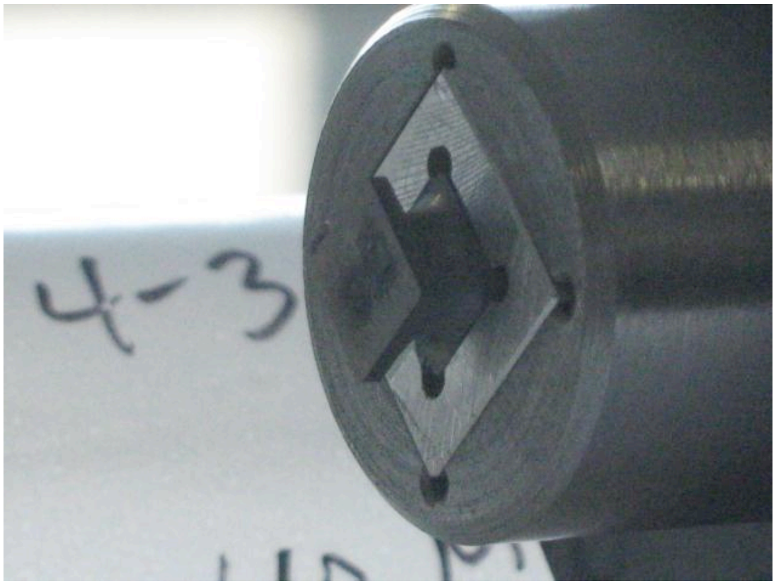

Figure 3. PNNL joint specimen 4-3 in the torsion test holder at Politecnico di Torino prior to testing. This particular specimen was one of the first batch that was taller, thus, it was almost 4-mm in height compared to 3-mm height shown in Figure 1.

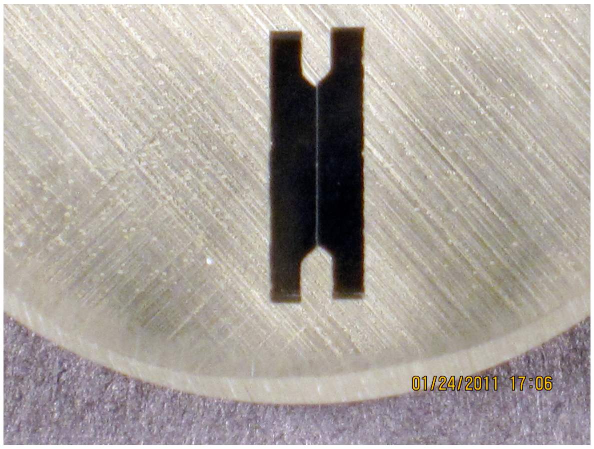

Figure 4. Sectioned 3-mm high joint mounted in epoxy for joint photomicrography and for checking joint alignment. The joint specimen can be seen to be slightly misaligned in this photo.

Several joints of both the 4-mm high and 3-mm high specimens were tested in Torino and the results of the 4-mm high specimen tests are shown in Figure 5. Two trends were observed after this more complete round of testing. One trend is that proper joint alignment and pressure application is required for this reaction joining process to obtain high strengths in the torsion measurement. The second is that most of the joined specimens fractured outside of the plane of the joint and, thus, do not give an accurate shear strength measurement. One joint that fractured mainly within the plane of the joint was specimen 1-3, which had the highest measured joint strength (See Figure 6). Other weaker joints were apparently measured accurately, such as specimen 6-1, which was measured at 3 MPa shear strength since it was not processed completely as shown in Figure 7. The remainder of the specimens fractured outside of the plane of the joint, either partly or completely, several of which are shown in Figure 8. These cannot be relied upon to give reliable data using this test specimen geometry. However, it may be that these joints exceed the shear strength of CVD SiC and planar joint failure cannot be expected to obtain.

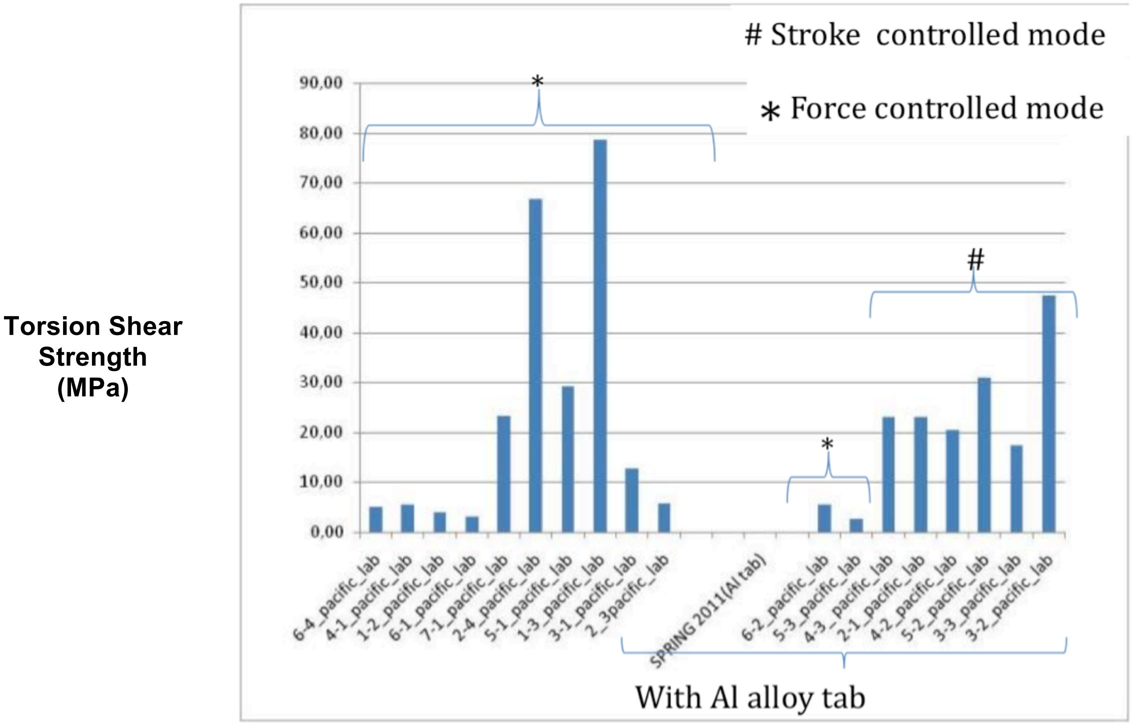

Figure 5. Bar graph of joint strengths measured in MPa of torsion shear strength. The only high-strength specimen that fractured within the joint plane was Specimen 1-3, the one with the highest measured shear strength. Many of the specimens exhibiting low joint strengths were processed incompletely due to fixture alignment problems and did not receive the full applied joining pressure.

Several of the fractured joints were examined at Politecnico via SEM. Specimen 6-1, a low strength joint (3 MPa) fractured along the torsion joint in shear as shown in Figure 7. Fractography reveals that this joint was weak due to poor bonding to the CVD SiC surface and due to the porosity of the joint. However, joint 1-3, which was a high strength joint (79 MPa) is imaged in Figure 6. A mostly planar fracture in the joint region is observed that deviates from planarity at some point during fracture. Images at higher magnifications reveal that surface damage to the CVD SiC has occurred due to strong joint bonding. Both joint alignment and proper processing are observed to play a role in joint strength in these preliminary torsion shear tests. However, the lack of planar fractures for many joints that were processed correctly and that presumably had high strengths suggests that the miniature torsion specimen design needs to be modified to account for this. This will be the subject of future research and development.

Some of the basis for the miniature torsion specimen design has been the use of epoxy joints between steel and SiC torsion specimens where the joint failure was definitely observed between the joining specimens in the plane of the joint as shown in Figure 9. Torsion strength data was obtained for at least 10 specimens for each of these materials and conditions and the data is shown in Figure 10. It is very consistent strength data and shows the advantages of this method when the joints are of moderate strength. One goal of the future test development will be to maintain the joint design overall so that the existing fixtures can be used but to explore ways to reduce the joint area. One suggestion is the drill a hole in the center of the joined specimens so that the joined area changes from a circular region to an annulus with reduced joined area.

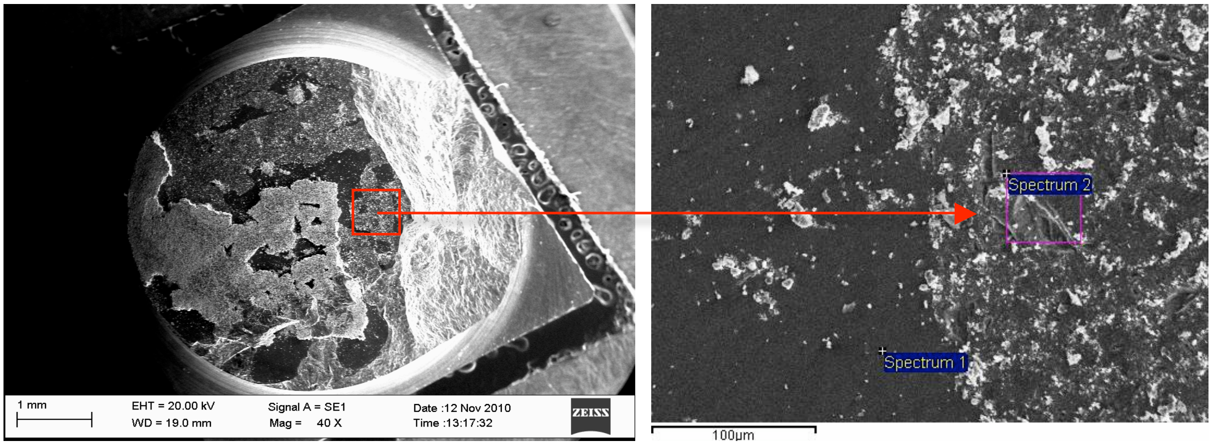

(a) (b)

Figure 6. SEM micrograph in (a) reveals mostly planar fracture surface for specimen 1-3, which exhibited 80 MPa shear strength. The photo in (b) indicates that regions of severe surface damage in the CVD SiC can be observed where the fracture path was presumably located at the joint/SiC interface.

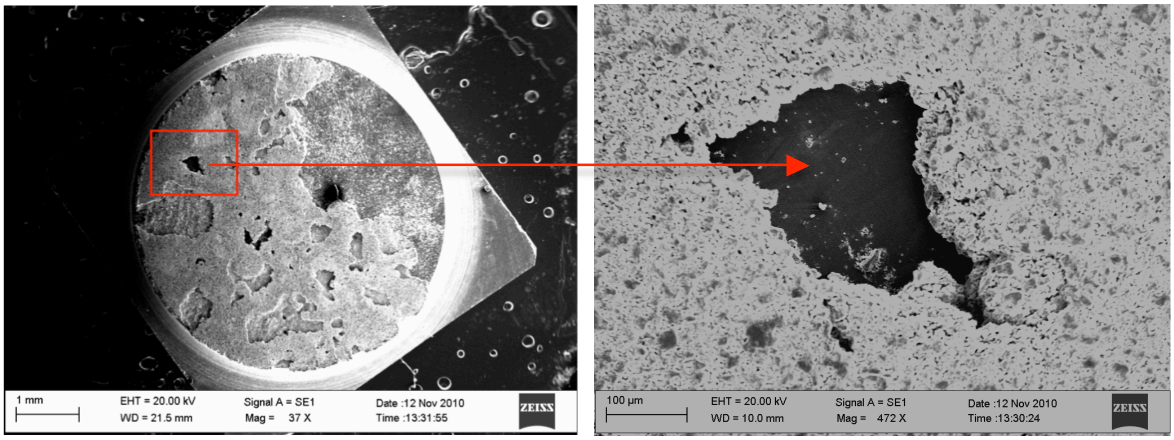

(a) (b)

Figure 7. SEM micrograph in (a) reveals a planar fracture surface for specimen 6-1, which had a 3 MPa shear strength. The photo in (b) reveals regions of unbonded SiC and porous joint material, which is evidence of a poorly processed joint due to low joining pressure.

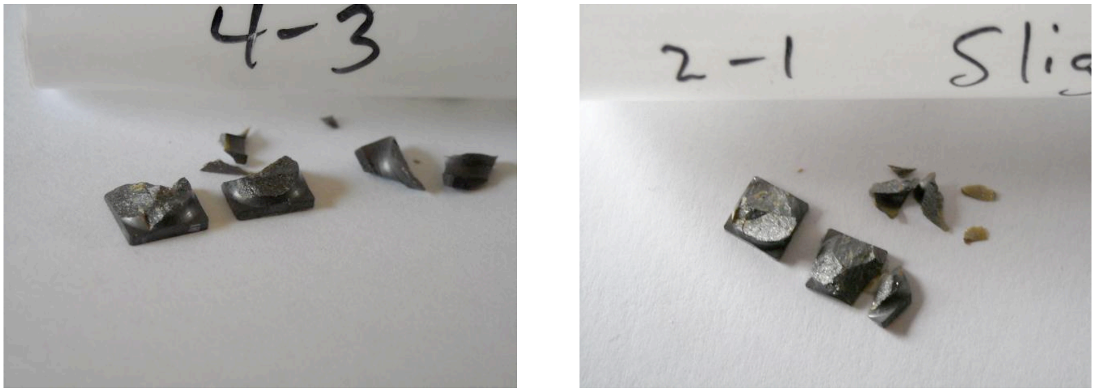

Figure 8. Photographs of fractured specimens exhibiting non-planar fracture from torsion testing. These fractures do not provide accurate shear strength data even though they suggest that the joints are strong.

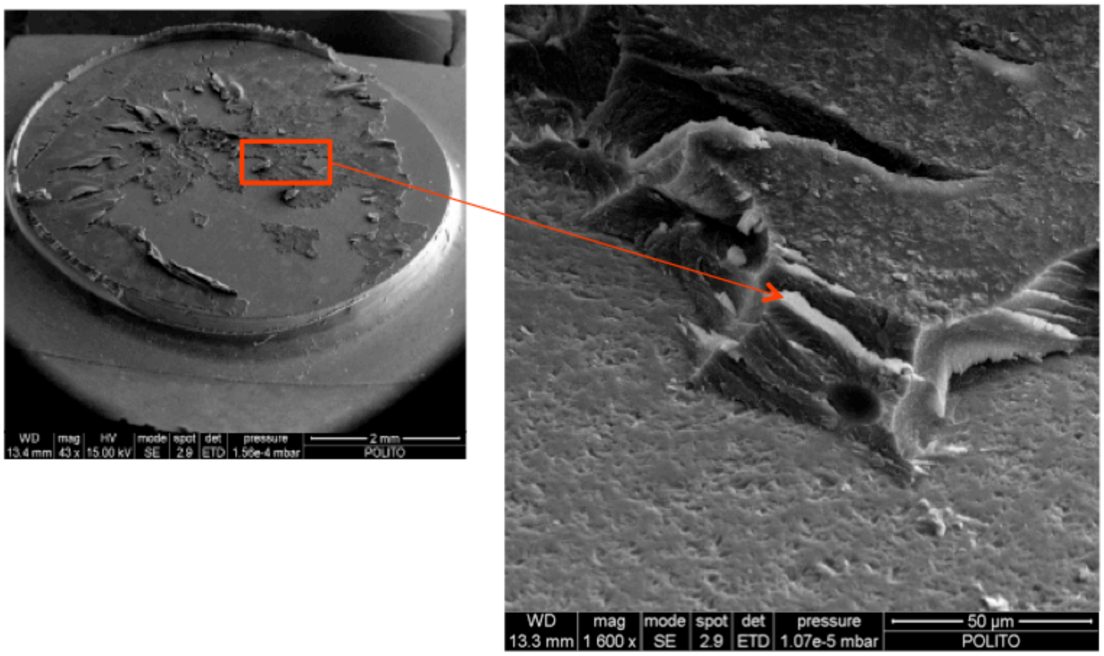

Figure 9. SiC/epoxy joint showing the in-plane fracture path and surface fracture morphology after torsion strength testing at Politecnico di Torino.

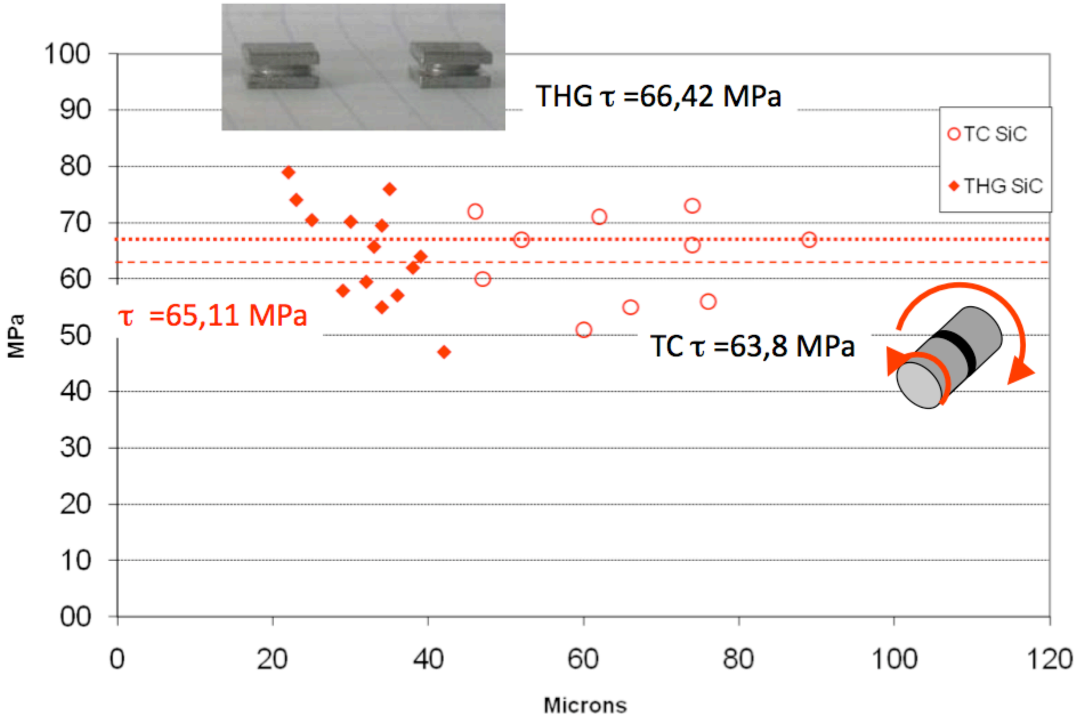

Figure 10. Comparison of two torsion test methods with epoxy joints using torsion strength data obtained at Politecnico di Torino. A torsion cylinder test (TC) is compared to the torsion hourglass (THG) specimen referred to in this report as the miniature torsion test. The results are consistent and comparable.

REFERENCES

1. Katoh, Y., L. L. Snead, C. H. Henager Jr, A. Hasegawa, A. Kohyama, B. Riccardi, and H. Hegeman, "Current status and critical issues for development of SiC composites for fusion applications," *J. Nucl. Mater.* **367-370 A** (2007) 659-671.
2. Henager, C. H., J. Y. Shin, Y. Blum, L. A. Giannuzzi, B. W. Kempshall, and S. M. Schwarz, "Coatings and joining for SiC and SiC-composites for nuclear energy systems," *J. Nucl. Mater.* **367-370** (2007) 1139-43.
3. Yvon, P. and F. Carre, "Structural materials challenges for advanced reactor systems," *J. Nucl. Mater.* **385** (2009) 217-222.
4. Nozawa, T., T. Hinoki, A. Hasegawa, A. Kohyama, Y. Katoh, L. L. Snead, C. H. Henager Jr, and J. B. J. Hegeman, "Recent advances and issues in development of silicon carbide composites for fusion applications," *J. Nucl. Mater.* **386-388** (2009) 622-627.
5. Jung, H.-C., Y.-H. Park, J.-S. Park, T. Hinoki, and A. Kohyama, "RD of joining technology for SiC components with channel," *J. Nucl. Mater.* **386-388** (2009) 847-851.
6. Henager, C. H. J. and R. J. Kurtz, "Low-activation joining of SiC/SiC composites for fusion applications," *J. Nucl. Mater.* **in press** (2011).
7. Ferraris, M., P. Appendino, V. Casalegno, F. Smeacetto, and M. Salvo, "Joining of ceramic matrix composites for fusion application," *Adv. Sci. Technol.* **33** (2003) 141-152.
8. Riccardi, B., C. A. Nannetti, T. Petrisor, and M. Sacchetti, "Low activation brazing materials and techniques for SiCf/ SiC composites," *J. Nucl. Mater.* **307-311** (2002) 1237-1241.

9. Jones, R., H. L. Giancarli, A. Hasegawa, Y. Katoh, A. Kohyama, B. Riccardi, L. L. Snead, and W. J. Weber, "Promise and challenges of SiC_f/SiC composites for fusion energy applications," *J. Nucl. Mater.* **307-311 (**2002) 1057-1072.
10. Bruce, R. L., S. K. Guharay, F. Mako, W. Sherwood, and E. Lara-Curzio, "Polymer-derived SiCf/SiCm composite fabrication and microwave joining for fusion energy applications," IEEE/NPSS Symposium on Fusion Engineering, **(**2002) 1078-8891.
11. Zucchetti, M., M. Ferraris, and M. Salvo, "Safety aspects of joints and coatings for plasma facing components with composite structures," *Fusion Eng. Des.* **58-59 (**2001) 939-943.
12. Raffray, A. R., R. Jones, G. Aiello, M. Billone, L. Giancarli, H. Golfier, A. Hasegawa, Y. Katoh, A. Kohyama, S. Nishio, B. Riccardi, and M. S. Tillack, "Design and material issues for high performance SiC_f/SiC-based fusion power cores," *Fusion Eng. Des.* **55 (**2001) 55-95.
13. Lewinsohn, C. A., R. H. Jones, T. Nozawa, M. Kotani, Y. Katoh, A. Kohyama, and M. Singh, *"Silicon carbide based joining materials for fusion energy and other high-temperature, structural applications," Ceram. Engr. Sci. Proc.* **22 (**2001) 621-625.
14. Lewinsohn, C. A., M. Singh, T. Shibayama, T. Hinoki, M. Ando, Y. Katoh, and A. Kohyama. *Joining of silicon carbide composites for fusion energy applications*. 2000. Colorado Springs, CO, USA: Elsevier.
15. Colombo, P., B. Riccardi, A. Donato, and G. Scarinci, "Joining of SiC/SiC_f ceramic matrix composites for fusion reactor blanket applications," *J. Nucl. Mater.* **278 (**2000) 127-135.
16. Riccardi, B., C. A. Nannetti, T. Petrisor, J. Woltersdorf, E. Pippel, S. Libera, and L. Pilloni, *Issues of low activation brazing of* SiC_f*/SiC composites by using alloys without free silicon,* 2004. Kyoto, Japan: Elsevier, Amsterdam, Netherlands.
17. Katoh, Y., M. Kotani, A. Kohyama, M. Montorsi, M. Salvo, and M. Ferraris, "Microstructure and mechanical properties of low-activation glass-ceramic joining and coating for SiC/SiC composites," *J. Nucl. Mater.* **283-287 (**2000) 1262-6.
18. Radhakrishnan, R., C. H. Henager, Jr., J. L. Brimhall, and S. B. Bhaduri, "Synthesis of Ti_3SiC_2/SiC and $TiSi_2$/SiC composites using displacement reactions in the Ti-Si-C system," *Scr. Mater.* **34 (**1996) 1809-1814.

3.1 THERMOMECHANICAL DAMAGE OF TUNGSTEN UNDER TRANSIENT PLASMA HEAT LOADS — T. Crosby and N. M. Ghoniem (University of California, Los Angeles)[1]

OBJECTIVE

The objective of this work is the development of a computational model to determine the relation between the thermo-mechanical loading conditions and the onset of damage and failure of tungsten surfaces.

SUMMARY

Tungsten is a primary candidate for plasma facing components (PFCs) in fusion energy systems because of its superior thermophysical properties. International efforts are focused on the development of tungsten surfaces that can intercept ionized atoms and high heat flux in the divertor region of magnetic fusion confinement devices. Designing a robust interface between thermonuclear plasma and the heat sink material in the divertor remains a major challenge to the success of future fusion power reactors. In this report, we present a multiphysics computational model to determine the extent of thermomechanical damage in tungsten under type-I edge localized modes (ELMs). The model is formulated in a finite element framework, and is based on a multiphysics approach that combines elastoplastic mechanical analysis and thermal heat conduction. The model is coupled with a reaction-diffusion model of material swelling and grain boundary degradation due to helium bubbles resulting from the plasma flux. Contact cohesive elements are used to model grain boundary sliding and fracture. The present results establish the connection between plastic deformation and the onset of material damage.

PROGRESS AND STATUS

Introduction

In nuclear fusion reactors, plasma facing components (PFC) (e.g. divertor) are subjected to high fluxes of energetic neutrons, hydrogen and helium ions. The impingement of these energetic atom fluxes leads to rapid and transient surface heating. Bombardment by helium isotopes leads to helium-induced damage accompanying micro-structural evolution, such as material swelling and the formation of blisters [1], dislocation loops and helium holes or bubbles [2]. Several recent experiments (see references [3] and [4]) have shown that the damage in the surface region and inside the material degrades the thermo-physical properties as well as the optical reflectivity of tungsten.

The divertor in fusion reactors are subjected to transient plasma events characterized with high thermal energy for a short time. One of these transient events is the Edge Localized Mode (ELM) which is a highly nonlinear magneto-hydrodynamic event and which is accompanied by a periodic expulsion of particles and high thermal energy (3-10% of the core thermal energy). ELM energies deposited at the divertor plates a substantial fraction of the total plasma energy content. Typical values for ELM energy

---

[1] Formatted from the original paper "**THERMOMECHANICAL DAMAGE OF TUNGSTEN UNDER PLASMA HEAT LOADS**", T.Crosby and N.M. Ghoniem, to be published in "Journal of ASTM International"

densities are 0.1-0.5 (MJ/m^2) for JET and 1-5 (MJ/m^2) for ITER. The duration of the ELM events are relatively short, 0.1-1 ms, causing material damage like melting, ejection of clusters and droplets and release of hydrogen isotopes. ELM events have also long-term effects such as degradation of thermo-physical properties due to cyclic heat loading [5], [6].

Experimental observations of cracks developing in tungsten subjected to transient heat loads exist in the literature, for example the results of experimental observations shown in Fig. 1, [7, 8].

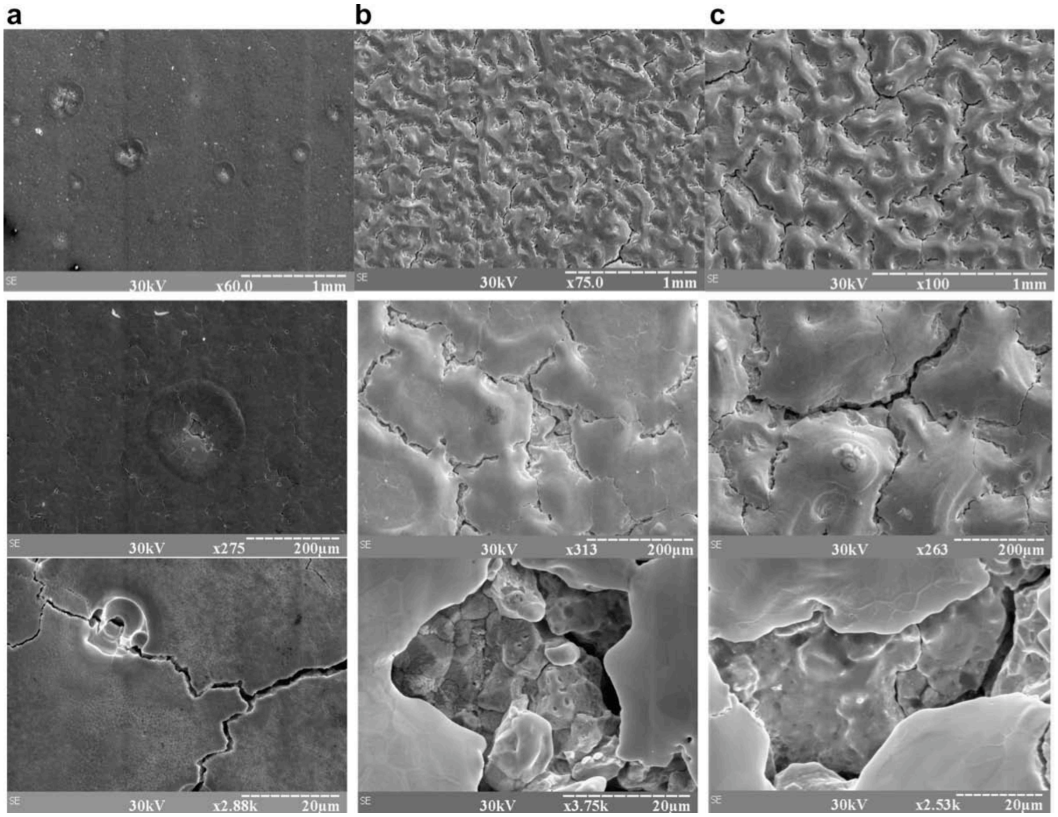

Figure 1. SEM images of the tungsten surface after 100 (a), 210 (b) and 350 (c) pulses (Q = 0.75 MJ/m^2) with different magnification [8].

Components (PFC) because it has good thermo-physical properties, a high melting point, a low sputtering rate, and a low tritium inventory [9]. Models that describe and study the change in tungsten structure and the damage that takes place as a result of its interaction with the plasma edge are critical in determining the limits for its operating conditions in environments with extreme heat flux. Recent experiments have shown that under helium and hydrogen ion bombardment conditions, some near-surface grains are ejected from the bulk to the surface region [10]. The main objective of this report is to develop a computational model for the development of thermo-mechanical damage in W under energetic ion bombardment conditions.

Coupled Thermal and Mechanical Models

In Tokomak-type plasma applications, such as in JET and ITER, the divertor is subjected to transient high heat loads that propagate inside the divertor material by heat conduction. This is described with the heat conduction equation given by:

$$\rho c_p \frac{\partial T}{\partial t} + \nabla\cdot(-k\nabla T) = Q - \rho c_p \mathbf{u}\cdot\nabla T \tag{1}$$

where Q is a heat source, and k is the thermal conductivity.

To simulate transient conditions of the plasma, the tungsten surface is subjected to a heat flux of the from:

$$-\mathbf{n}\cdot\mathbf{q} = q_0 + h(T_\infty - T)$$

(2)

where q_0 is the inward heat flux normal to the boundary and $\mathbf{q}$ is the total heat flux vector :

$$\mathbf{q} = -k\nabla T + \rho c_p \mathbf{u} T \tag{3}$$

In order to perform thermo-mechanical analysis, a boundary value problem (BVP) is formulated for an elastic material response. The BVP is constructed by substituting the constitutive equation for linear elasticity:

$$\sigma_{ij} = C_{ijkl}\epsilon^e_{kl} \tag{4}$$

into the strong form of the equilibrium equation:

$$\sigma_{ij,j} + f_i = 0 \tag{5}$$

The total strain is the sum of elastic, plastic and thermal strains, i.e.:

$$\epsilon_{ij} = \epsilon^e_{ij} + \epsilon^p_{ij} + \epsilon^\theta_{ij} = \frac{1}{2}\left(u_{i,j} + u_{j,i}\right) \tag{6}$$

where σ is the symmetric stress tensor and f is body force, ϵ^e is the elastic strain tensor, and ϵ^θ is the strain tensor due to thermal expansion.

$$\begin{cases} \sigma_{ij} n_j = t_i \text{ on } \partial\beta_t \\ u_i = \bar{u}_i \text{ on } \partial\beta_u \end{cases} \quad s.t. \quad \partial\beta_u \cup \partial\beta_t = \beta \,, \qquad \partial\beta_u \cap \partial\beta_t = \varnothing \tag{7}$$

Damage Crack Formation Model

Grain boundary sliding and motion result in stress concentrations along grain boundaries, which are generally weak regions in the material susceptible to crack initiation and propagation. We consider here a crack equilibrium model to describe crack damage formation along weak grain boundaries. From force equilibrium on the crack faces and using a stress equation for the field similar to that of a dislocation, an expression for the equilibrium crack length is found to be [12]:

$$2L = \frac{F^2(1-\nu^2)}{\pi\mu E} \tag{8}$$

As a simple constitutive damage model, we take the grain boundary thermally induced forces in the crack surface to be simply proportional to the internal strain at the grain boundary during the transient:

$$F = \nabla\cdot(\mathbf{C}:(\epsilon^{\gamma} + \epsilon^{\theta})) \tag{9}$$

The thermal force exhibits spatial and time dependence, as a result of the spatial dependence and time dependence of the temperature field and locality of grain boundaries.

COMPUTATIONAL MODEL

A multiphysics computational model has been developed within a finite element framework in order to investigate the synergistic effects of transient high heat loads and helium ion irradiation. The implementation of the model utilizes the capabilities of the COMSOL multiphysics platform in which a transient heat conduction analysis, coupled with a large deformation quasi-static elastic structural mechanics analysis with contact elements along the grain boundaries were solved in a segregated fashion. The simulated model is a 10 mm x 10 mm, two-dimensional block, which was divided into a random distribution of grains using an algorithm based on the Voronoi diagram as shown in Fig. 2.

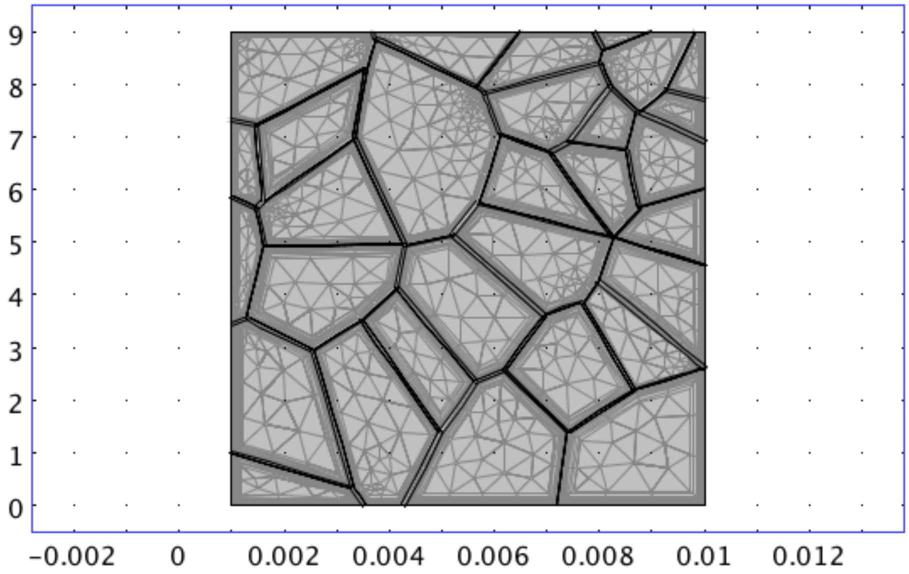

Figure 2. Initial configuration of the random distribution of grains with boundary layer mesh [mm].

The grain boundaries were replaced with cohesive contact elements to better simulate sliding and opening between the grains, as a result of He bubble formation along grain boundaries causing the grains to open up and form micro-cracks. A boundary layer mesh was utilized along the grain boundaries, as can be seen in the figure.

Thermal boundary condition were prescribed as an inward heat flux, q_0, on the left side. The heat flux pulse was taken to be 10 x 10^3, 2 x 10^3, 1 x 10^3 (MW/m^2), for the duration of 0.1,0.5 and 1 ms, respectively, as shown schematically in Fig [3]. These heat flux profiles are similar to conditions expected in ITER during ELM transient heat loads. A convective heat flux boundary condition was applied on the other side of the W plate, representing helium cooling. The mechanical boundary conditions were taken as free surface on the left side, while the right side was fixed. Periodic boundary condition for both the displacement and the temperature field were used on the top and bottom boundaries of the model. The simulation duration was taken to be 0.1 s, with time steps of 0.1 ms using a segregated solver that combines transient thermal analysis with the quasi-static mechanical analysis.

RESULTS

The high heat flux applied to the surface of tungsten cause the temperature on the surface of the material and inside it to increase causing thermal expansion and contraction during the thermal transient, forcing the grains to slide relative to each other. This relative motion between the grains leads to their separation between them, forming inter-granular micro-cracks. The cracks propagate inside the material forming networks of cracks of different resolutions, which can be categorized into primary (relatively larger) cracks, and secondary (relatively smaller) cracks. Typical results at the end of the simulation that show the onset of cracks of different sizes are shown in Figs. 4, 5, and 6, as well as contour plot for the plastic strain in Figs. 7, 8, and 9.

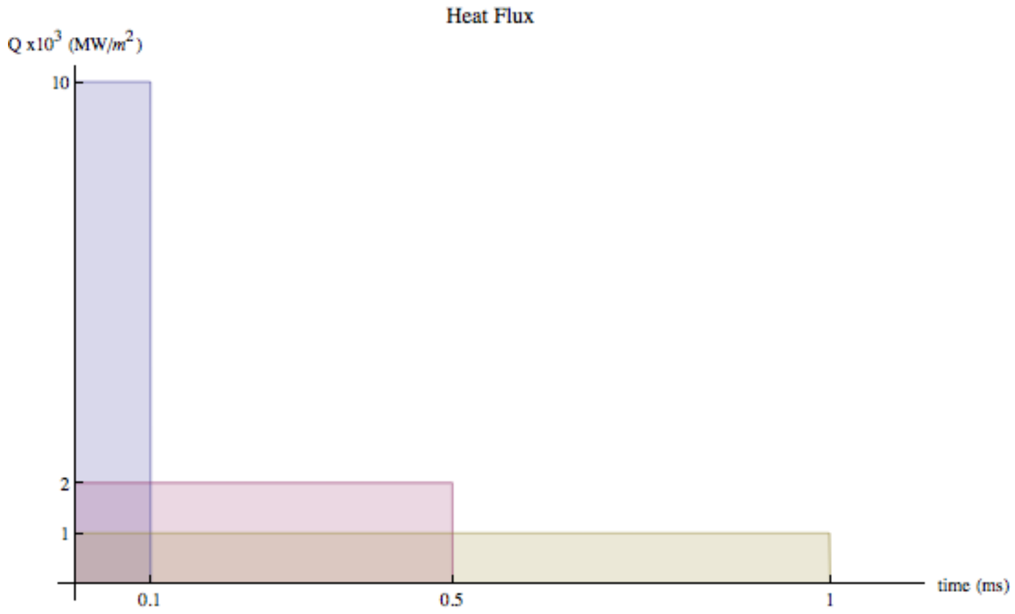

Figure 3. Incident heat flux profile: values of the heat flux (MW/m^2) vs. duration of application (ms) for the three cases considered.

It's noted that the temperature rises to very high values exceeding the melting point for the case when the heat flux is 1 x10^4 (MW/m^2). Our model doesn't directly address the ensuing evaporation of W from the surface in such severe conditions, as experimentally observed, for example in references [11] and [12]. The temperature of the surface at the end of the simulation is shown in Fig [10].

We note the difference in the distribution and in the size of cracks for the different applied heat fluxes. Thus, we see from the results that the cracks have larger sizes for the case when the heat flux is 1 x10^4 (MW/m^2), but they closer to the surface, while for the case when the heat flux is 1 x10^3 (MW/m^2), the cracks are smaller in size and formed at deeper distances from the surface of tungsten. This is due to the difference in transient heat transport for the different heat fluxes profiles.

Another aspect of the tungsten surface damage is grain ejection, which has been experimentally observed in tungsten subjected to He irradiation [10]. When the W surface is subjected to He and D^+ bombardment at high temperature, helium and vacancies diffuse to the grain boundaries forming grain boundary bubbles. When the surface is subsequently subjected to a transient heat load, He bubbles grow and expand rapidly along grain boundaries, causing substantial pressure on grain faces. When the pressure exceed a critical value greater than the cohesive forces on grain boundaries, causing the grains to completely separate resulting in the phenomenon called grain ejection.

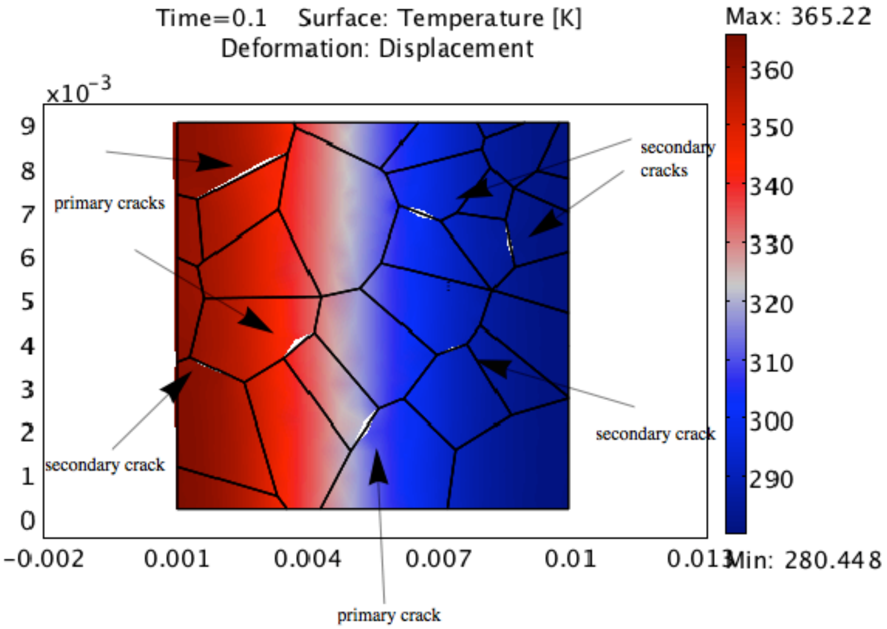

Figure 4. Temperature and damage distribution in [K] and tungsten grain boundary damage due to differential thermal expansion/contraction and crack formation when subjected to Q = 1x10^3 (MW/m^2).

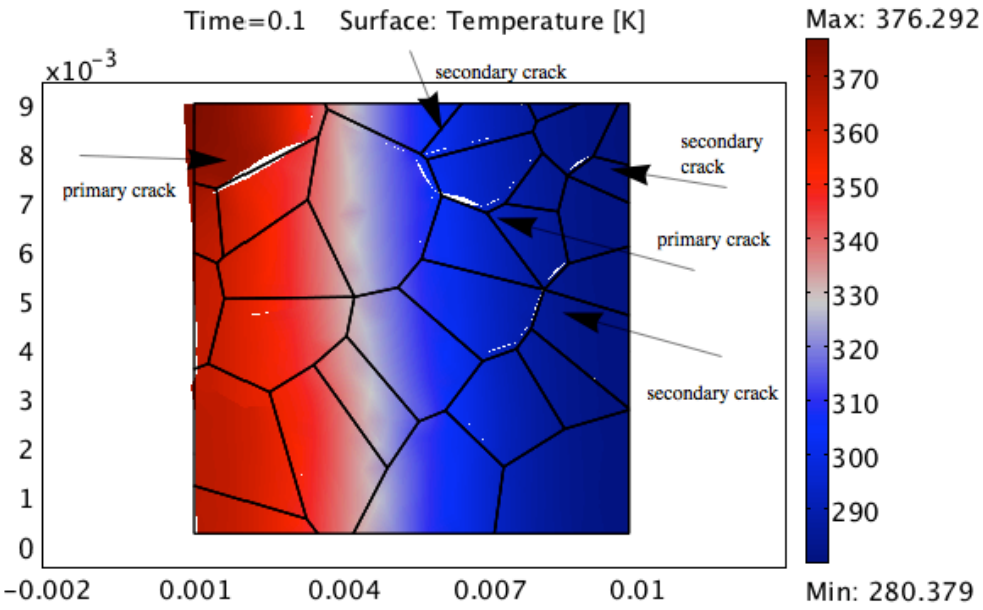

Figure 5. Temperature and damage distribution in [K] and tungsten grain boundary damage due to differential thermal expansion/contraction and crack formation when subjected to Q = 2x10^3 (MW/m^2).

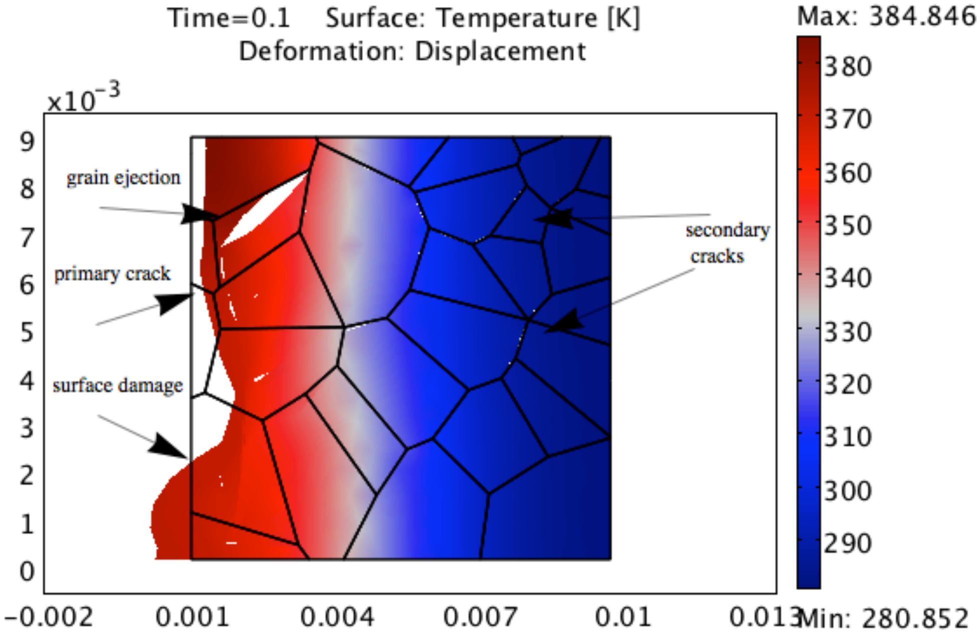

Figure 6. Temperature and damage distribution in [K] and tungsten grain boundary damage due to differential thermal expansion/contraction and crack formation when subjected to Q = 10x10^3 (MW/m^2).

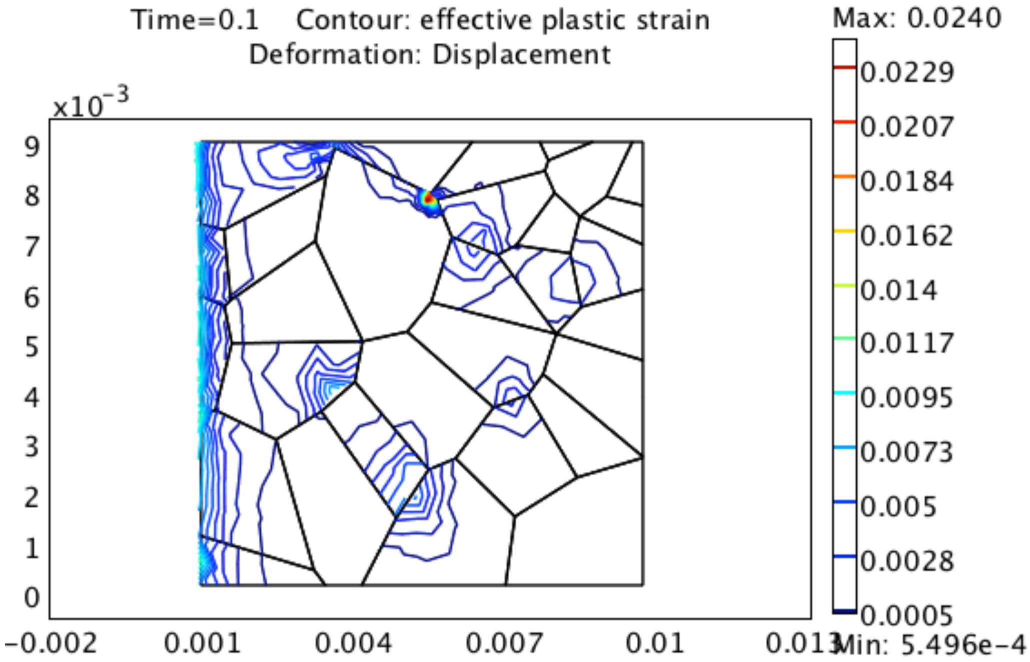

Figure 7. Contour plots of the effective plastic strain (Dimensionless) Q = 1x10^3 (MW/m^2).

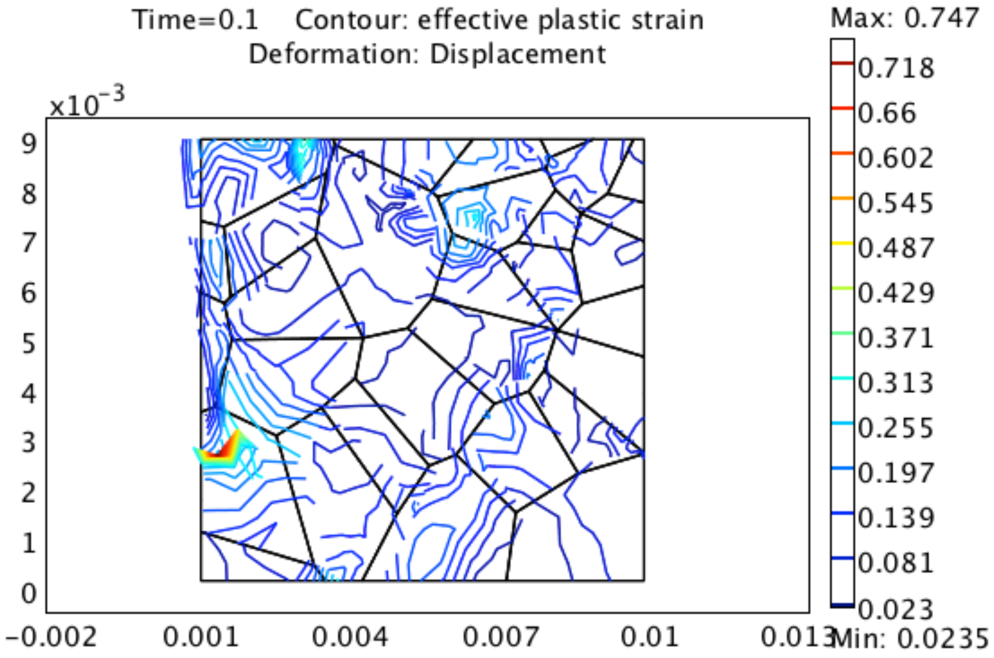

Figure 8. Contour plots of the effective plastic strain (Dimensionless) Q = 2x10^3 (MW/m^2).

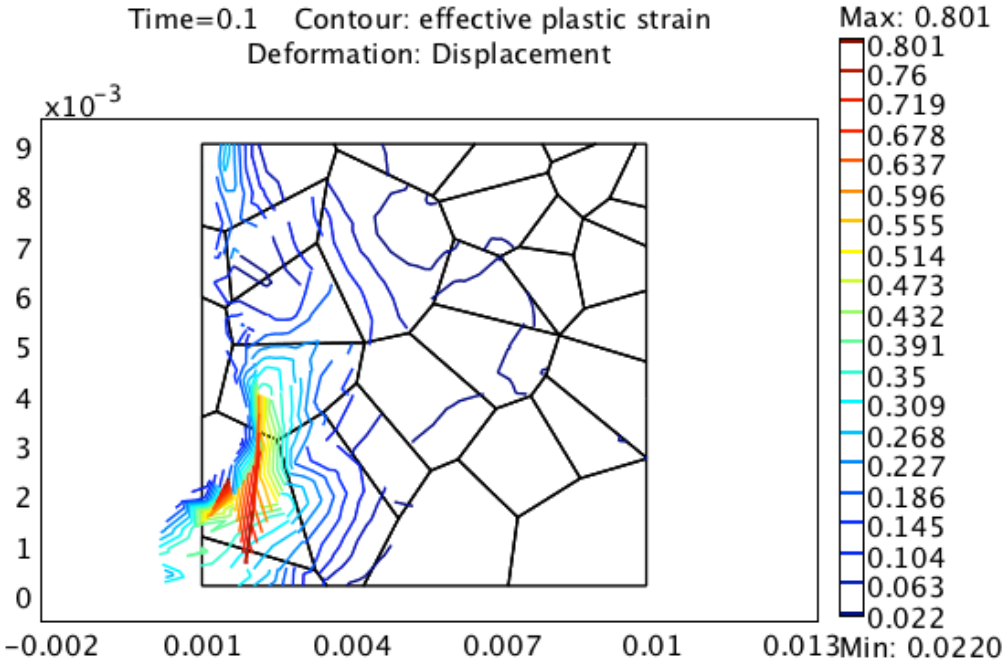

Figure 9. Contour plots of the effective plastic strain (Dimensionless) Q = 10x10^3 (MW/m^2).

3.2 Development of Mo-Re Alloys — M.A. Sokolov and E.K. Ohriner (Oak Ridge National Laboratory)

OBJECTIVE

Mo-Re alloys are attractive in high-temperature reactor applications due to their good thermal properties and high strength at elevated temperatures. The objective of this research is to evaluate Mo-Re alloys that are expected to be tolerant to irradiation and viable for use in high temperature reactor environments. This work is also expected to add to the scientific understanding of Re-bearing refractory alloys.

SUMMARY

Most previous work on Mo-Re alloys focused on 5-13 or 41-47wt% Re, leaving large gaps in the understanding of the influence of Re in improving properties of Mo and W alloys. Previous studies on these alloys focused on tensile and smooth bar bend tests, whereas fracture toughness data are needed to evaluate suitability for structural applications. The scarce existing fracture toughness data shows poor toughness for up to 5 wt% Re and very high toughness for 41-47 wt% Re, with no data for intermediate Re contents. Preparation of Mo-15 wt.% Re and Mo-25 wt.% Re alloys is in progress. The materials are prepared by vacuum arc remelting (VAR) of pure molybdenum with a Mo-Re master alloy.

PROGRESS AND STATUS

Introduction

Nearly 40 years ago, studies found that molybdenum alloyed with rhenium resulted in improved ductility and fabricability over unalloyed Mo. This “rhenium effect” [1-6] has been observed in group VI-A refractory metals (W and Mo especially) and results in improved strength, creep resistance, and low temperature ductility. Early studies suggested the improved low-temperature ductility was associated with enhancement of mechanical twinning [2,6]. Alternative explanations include solid solution softening (decreased resistance to dislocation glide), and reduction of oxygen content along grain boundaries, due to increased interstitial oxygen solubility [7].

Dilute Mo-Re alloys (<18 wt% Re) have been studied and reported to have maximum tensile ductility at 11-13 wt% Re in room temperature tests [8-9]. However, in a subsequent critical review of the data, Wadsworth et al. [7] found that many of these claims were not conclusive due to inadequately controlled C and O impurity levels. As a result, the improved performance of Mo-Re with Re contents from 10-30 wt% Re alloys is largely unproven. However, more concentrated Mo-Re alloys (with 40-50 wt% Re) are used extensively in industries ranging from medicine to defense. In particular, two alloys (with 41 and 47.5 wt% Re) have been commercially available since the 1960’s. These alloys are more expensive and dense than unalloyed Mo, but possess better ductility, strength, thermal properties, and fabricability.

A major concern for Mo-based alloys is their low fracture toughness even at temperatures above the ductile-to-brittle transition temperature. The limited available data for Mo and Mo alloys [10-11] suggest that the unirradiated fracture toughness of Mo alloys containing < 5% solute additions is less than 30 MPa√m up to at least 450ºC, with a typical value at 230ºC of ~20 MPa√m. Additions of 1 to 2 volume percent of dispersed oxide particles or Re solute produces a slight increase in the fracture toughness and a shift in the DBTT to lower temperatures, although the effect on fracture toughness is small. Fracture toughness for concentrated Mo-Re alloys has been measured only recently by Sokolov for Mo-41Re and Mo-47.5Re over a range of temperatures [12]. It was shown that the fracture toughness values for the Mo-41Re and Mo-47.5Re are a factor of 5-10 higher than TZM (Mo with Zr and Ti additions) and Mo-5Re alloys. This drastic improvement over unalloyed Mo and dilute Mo alloys creates further incentive for investigating the Re effect in Mo and W alloys.

Another key factor in assessing potential materials for reactor applications is the material performance under neutron irradiation. Studies of the effects of neutron irradiation at high fluence on Mo–Re alloys ($\sim 20 \times 10^{21}$ n/m^2, E>0.1 MeV) at temperatures of 373 to 800°C report dramatically decreased ductility following irradiation [13-14], leading to the belief that the minimum operating temperature for Mo-Re alloys to avoid low temperature radiation embrittlement is ~830ºC. However, in a very recent study by Busby et al. [15], Mo-41Re and Mo-47.5Re were irradiated at even higher temperatures to investigate the suitability of Mo-Re alloys for high temperature reactor applications. Instead of improving ductility with increasing irradiation temperature, a relatively low maximum in ductility was observed for Mo-41Re around 950ºC which rapidly degrades at even higher temperatures. The ductility of Mo-47.5Re reaches a maximum after irradiation at only 800ºC. Further, the fracture surfaces were found to be increasing intergranular with increasing temperature, indicating that a different embrittlement mechanism is responsible.

The degradation of concentrated Mo-Re alloys at temperatures above 800ºC is likely due to radiation-induced precipitation (RIP). Radiation-induced precipitation of both σ and χ phases has been reported in several studies [16-19] and could be the result of radiation-induced segregation (RIS). Predictions of RIS in Mo-Re [20] indicate that Re will become enriched at defect sinks such as grain boundaries and dislocations (network or dislocation loops). For concentrated alloys, only a small amount of local Re enrichment is required to enter a regime where precipitation will occur. Precipitation could also result from radiation-induced transmutation [21]. Both ^{185}Re and ^{187}Re have large (n,γ) thermal energy cross-sections which lead to significant transmutation of Re to Os, although the rates of transmutation will depend on the neutron energy spectrum. Osmium has a lower solubility limit in Mo than Re and could form Mo_3Os at relatively low doses in a high-Re alloy, leading to embrittlement. Mo-Re-Os precipitates may also be possible.

Thus, while the recent work by Busby et al. indicates that highly concentrated alloys such as Mo-41Re and Mo-47.5Re may not be suitable for high temperature reactor environments, the very high fracture toughness values measured by Sokolov provides motivation to continue to look at Mo-Re alloys. Reducing the Re content from the commercially available Mo-41Re and Mo-47.5Re to more moderate 15 and 25wt% Re may considerably improve the alloys performance under irradiation while retaining good ductility and fracture toughness. In addition, this study could provide fundamental information on the impact of Re content and C and O concentrations in Mo and W alloys, filling a key gap in understanding the “Re-effect”. For example, while Mo alloys are not of interest to fusion energy programs due to issues with waste disposal, W-Re alloys don’t have this problem and are of interest because of their lower sputtering rates by the plasma relative to other candidate materials for this application. As a result, an improved understanding of the “Re effect” applied to W-Re alloys could also allow this class of materials to be utilized for fusion reactor applications.

Alloy Preparation

Preparation of Mo-15 wt.% Re and Mo-25 wt.% Re alloys is in progress. The materials were prepared by vacuum arc remelting (VAR) of pure molybdenum with a Mo-Re master alloy of either 41% or 52% Re. The materials are alloyed to contain about 80 ppm carbon in the melted product. The master alloy was prepared by electron beam melting of sintered powder compacts. The electrode assembly within the VAR furnace is shown in Figure 1. The Mo-15% Re following melting is shown in Figure 2 along with the remaining unmelted portion of the electrode. It is planned to extrude the melted ingots to sheet bar during August 2011 and hot roll to sheet material for testing.

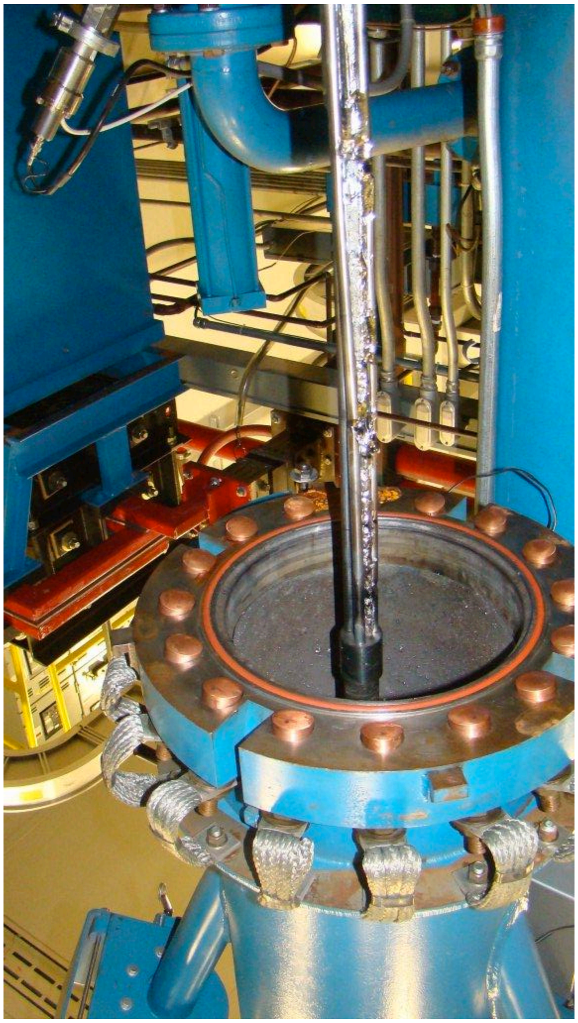

Figure 1. Electrode assembly for Mo-25% Re alloy consisting of Mo rods and EB melted Mo-Re master alloy bars.

Figure 2. Vacuum arc remelted ingot of Mo-15% Re alloy on molybdenum pad with remaining unmelted portion of the electrode consisting of Mo rods and EB melted Mo-Re master alloy bars.

REFERENCES

[1] G. A. Geach and J. E. Hughes, “The Alloys of Rhenium with Molybdenum or with Tungsten and Having Good High Temperature Properties,” 2nd Plansee Seminar, ed. F. Benesovsky (Pergamon: London: 1956).

[2] R. I. Jaffee, C. T. Sims and J .J. Harwood, “The Effect of Rhenium on the Fabricability and Ductility of Molybdenum and Tungsten,” 3rd Plansee Seminar, ed. F. Benesovsky (Springer-Verlag:Vienna: 1959).

[3] D. J. Maykuth, F. C. Holden and R. I. Jaffee, "The Workability and Mechanical Properties of Tungsten- and Molybdenum-Base Alloys Containing Rhenium," Electrochemical Society Symp. Rhenium, ed. B. W. Gonser (Elsevier: New York: 1962) pp. 125.

[4] C. T. Sims and R. I. Jaffee, *Trans. ASM* **52** (1960) 929.

[5] J. G. Booth, R. I. Jaffee, and E. I. Salkovitz, "The Mechanisms of the Rhenium-Alloying Effect in Group VI-A Metals." 5th Plansee Seminar, ed. F. Benesovsky (Springer-Verlag:Vienna: 1959).

[6] A. Lawley and R. Maddin, "Tensile Behavior of Zone Melted Molybdenum-Rhenium Single Crystals," *Trans. TMS-AIME* **224** (1962) 573-583.

[7] J. Wadsworth, T. G. Nieh, and J. J. Stephens, "Dilute Mo-Re Alloys - A Critical Evaluation of Their Comparative Mechanical Properties," *Scr. Metall.* **20**, Pergamon, Ltd., (1986), 637-42.

[8] L. B. Lundberg, E. K. Ohriner, S. M. Tuominen, and E. P. Whelan, "Solution Softening in Molybdenum Rhenium Alloys," *Physical Metallurgy Technology of Molybdenum and Its Alloys*, AMAX, Greenwich, CT (1985) pp. 71-79.

[9] W. D. Klopp and W. R. Witzke, "Mechanical Properties of Electron-Beam Melted Molybdenum and Dilute Molybdenum-Rhenium Alloys," NASA TM X-2576, 1972.

[10] H. A. Jehn and K. K. Schulze, "High-Temperature Gas-Metal Reactions of Mo and Its Alloys," in K. H. Miska et al. (eds.), *Physical Metallurgy and Technology of Molybdenum and Its Alloys*, AMAX Specialty Metals., Greenwich, CT, 1985, pp. 107-117.

[11] B. V. Cockeram, "Measuring the Fracture Toughness of Molybdenum-0.5% Titanium-0.1% Zirconium and Oxide Dispersion-Strengthened Molybdenum Alloys Using Standard and Subsized Bend Specimens," *Metall. Mater. Trans*. *A* **33** (2002) 3685-3707.

[12] M. A. Sokolov, "Fracture Toughness Characterization of Two Mo-Re Alloys," ORNL/LTR/NR-JIMO/04-16, 2004.

[13] S. A. Fabritsiev and A. S. Pokrovsky, "The Effect of Rhenium on the Radiation Damage Resistivity of Mo-Re Alloys," *J. Nucl. Mater.* **252** (1998) 216-227.

[14] A. Hasegawa, K. Ueda, M. Satou and K. Abe "Neutron Irradiation Embrittlement of Molybdenum Rhenium Alloys and Their Improvement by Heat Treatment," *J. of Nucl. Mater.* **258-263**, Part 1, October 1998, 902-906.

[15] J. T. Busby, K. J. Leonard, and S. J. Zinkle, "Effects of Neutron Irradiation on Refractory Metal Alloys," ORNL/LTR/NR-PROM/05-38, 2005.

[16] Y. Nemoto, A. Hasegawa, M. Satou, K. Abe and Y. Hiraoka, "Microstructural Development and Radiation Hardening of Neutron Irradiated Mo–Re Alloys," *J. of Nucl. Mater.* **324**, Issue 1, 1 January 2004, 62-70.

[17] F. A. Garner, L. R. Greenwood, and D. J. Edwards, "The Influence of Starting State on Neutron Induced Density Changes Observed in Nb-1Zr and Mo-41Re at High Exposures," *J. of Nucl. Mater.* 212-215 (1994) 426-430.

[18] R. A. Erck and L. E. Rehn, "Chi-Phase Precipitation in Ion-Irradiated Molybdenum-Rhenium Alloys," *Phil. Mag. A* **62**, 1 (1990), p. 29-51.

[19] G. A. Cottrell, “Sigma Phase Formation in Irradiated W, Ta, and Mo in a Fusion Power Plant,” *J. Nucl. Mater.* **334** (2004) 166-168.

[20] R. A. Erck and L. E. Rehn, “Kinetics of Radiation-Induced Segregation in Mo-Re Alloys,” *J. Nucl. Mater.* **168** (1989) 208-219.

[21] L. R. Greenwood and F. A. Garner, “Transmutation of Mo, Re, W, Hf, and V in Various Irradiation Test Facilities and STARFIRE,” *J. Nucl. Mater.* **212-215** (1994) 635-639.

4.1 EFFECTS OF NEUTRON IRRADIATION ON HARDNESS OF W-ODS FERRITIC STEEL JOINTS

— Sanghoon Noh (Kyoto University), M. A. Sokolov (Oak Ridge National Laboratory), Ryuta Kasada, Akihiko Kimura (Kyoto University) and Takuya Nagasaka (National Institute for Fusion Science)

OBJECTIVE

The effects of neutron irradiation on VPS-W coated ODS steel joints were investigated. The neutron irradiation effects in the joint area were evaluated by post irradiation hardness measurements on the cross section using a micro Vickers hardness tester.

SUMMARY

In present study, the effects of neutron irradiation on the hardness of W-coated ODS steels were investigated. Vacuum plasma spraying (VPS) technique was employed to fabricate W layer on the surface of substrates. Substrate materials were K1-, K4-ODS ferritic steels and F82H steel, which are 3mm thick plates. Tungsten powder of 99.9% high purity was used for VPS process. The powders were sprayed by the plasma jet of argon and hydrogen mixture to the surface of substrates pre-annealed at 773K. VPS-W coated specimens were irradiated at 723K to 4.5, 9.6 dpa in the High Flux Isotope Reactor (HFIR), respectively. To investigate the effect of neutron irradiation on joint area, the hardness distributions were evaluated on the cross section using a micro Vickers hardness tester. Microstructure analysis revealed that W was successfully coated on each substrate by VPS process, in spite of mismatch of the CTE between these materials. The hardness of W was significantly varied from 260 to 480Hv because inhomogeneous cooling rate during the process. After irradiations, irradiation hardening was occurred in the VPS-W, while substrate materials did not.

PROGRESS AND STATUS

Experimental

The substrate materials were F82H (IAE HEAT) steel, two kinds of oxide dispersion strengthened (ODS) ferritic steels. The thickness of the substrates were 3-8 mm. W powder was temporarily melted and sprayed on the substrate by a plasma jet of argon and hydrogen mixture in a vacuum chamber. The substrate temperature was annealed at around 773K during the process. The resulting thickness of the W coatings was about 0.1 mm or 0.7 mm. Schematics of VPS process are illustrated in Fig. 1. Microstructure was observed by field-emission type scanning electron microscope (FE-SEM). VPS process is described in previous study [1]. W coated substrates for the neutron irradiation were machined with a dimension of 8(L)×3.8(H)×0.5(t) mm, so coated interface is located on the cross section.

Neutron irradiation was conducted in the high flux isotope reactor (HFIR) at 723K to 4.5 and 9.6 dpa in the capsule ID T9C1 and T9C2, respectively. After irradiation, hardness measurement across the coated interface was carried out using a micro Vickers hardness tester with 100gf for 10s at room temperature in a regular interval of 200 μm in the hot cell. Chemical composition and specimen description are summarized in Table 1.

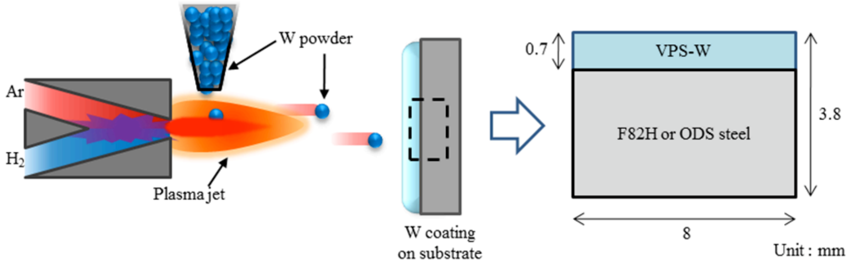

Fig. 1. Schematic of VPS process.

Table 1. Chemical composition and process description.

ID.	Materials	Dimension	Capsule ID	History	Irr. Cond.
KFW4	W-F82H(Fe-8Cr-2W-0.1C)	4x8x0.5t (mm^3)	-	VPS at 773K	As received
K1C4	W-K1(Fe-19Cr-0.3W-0.35Y_2O_3)				
K4S4	W-K4(Fe-19Cr-4Al-2W-0.35 Y_2O_3)				
KFW1	W-F82H(Fe-8Cr-2W-0.1C)		T9C1		4.5dpa@723K
KFW2	W-F82H(Fe-8Cr-2W-0.1C)		T9C2		9.6dpa@723K
K1C1	W-K1(Fe-19Cr-0.3W-0.35 Y_2O_3)		T9C1		4.5dpa@723K
K1C2	W-K1(Fe-19Cr-0.3W-0.35 Y_2O_3)		T9C2		9.6dpa@723K
K4S1	W-K4(Fe-19Cr-4Al-2W-0.35 Y_2O_3)		T9C1		4.5dpa@723K
K4S2	W-K4(Fe-19Cr-4Al-2W-0.35 Y_2O_3)		T9C2		9.6dpa@723K

TEST RESULTS

The hardness profiles for VPS-W coated specimens as received are shown in Fig. 2.

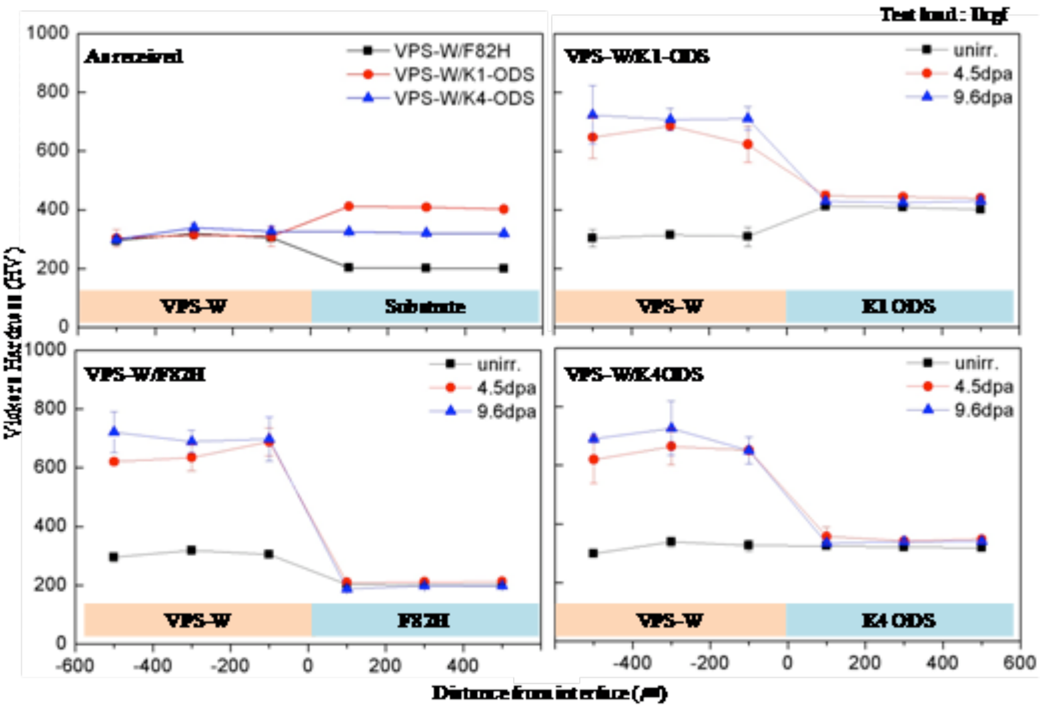

Fig. 2. Hardness distributions of VPS-W coated materials before/after HFIR irradiation.

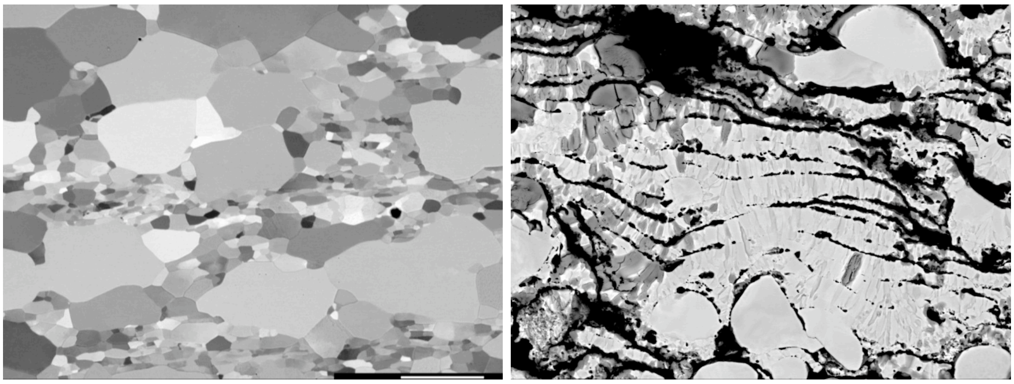

Fig. 3. Microstructures of bulk W (Left) and VPS-W (Right).

VPS-W has hardness values from 260 to 480HV. It is due to inhomogeneous solidification and cooling rate resulting closed pores during VPS process as shown in Fig. 3. Nagasaka et al. reported the VPS-W had lower measured density than that of bulk tungsten fabricated by powder sintering and hot rolling [1]. Hardness of substrates shows different distributions due to their different chemical composition. K1 ODS steel has highest hardness about 400HV and hardness of K4 ODS steel was lowered to 320HV because of Al addition, finally F82H steel showed lowest, about 220HV. However, each substrate showed uniform hardness distribution. In substrates, irradiation hardening is not occurred in increase of dose rate. Neutron irradiation defects of steels are easily diffused because annealing rate is faster than defect forming rate on irradiation at 500 °C. After neutron irradiation, degrees of hardening of VPS-W are also not so higher even with increase of dose rate. This is because dose rate which effects on hardening of pure W may be saturated on 4.5 dpa and it is reported that hardening rate is experimentally saturating between 1 and 10 dpa in HFIR [2]. It is known that hardening mechanism of pure W is mainly caused by void formation, and the saturation of the hardening effect was probably due to void lattice formation [3]. The relation between irradiation hardening and dose rate is shown in Fig. 4. While bulk W fabricated powder-sintering method shows significant hardening rate about 530HV, VPS-W was not so high, about 360HV.

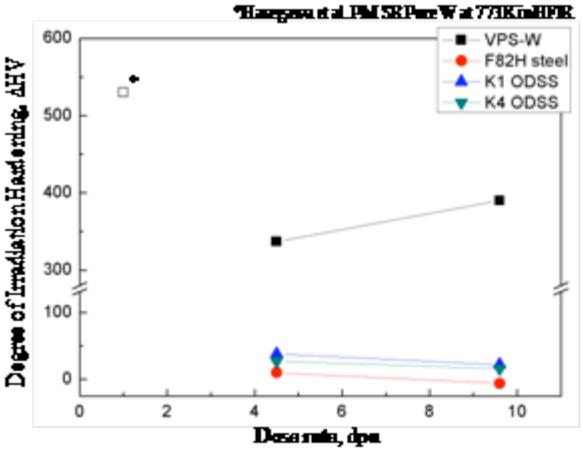

Fig. 4. Irradiation hardening of each material.

REFERENCES

[1] T. Nagasaka, R. Kasada, A. Kimura, Y. Ueda, T. Muroga, *Fusion Sci. Tech.* **56**, 1053-1057 (2009).

[2] A. Hasegawa, T. Tanno, S. Nogami, M. Satou, *Journal of Nuclear Materials*, in press (2010).

[3] T. Tanno, A. Hasegawa, J. C. He, M. Fujiwara, S. Nogami, M. Satou, T. Shishido and K. Abe, *Mater. Trans.* **48**, 2399–2402 (2007).

COMPATIBILITY OF MATERIALS EXPOSED TO ISOTHERMAL Pb-Li – B. A. Pint and K. A. Unocic (Oak Ridge National Laboratory, USA)

OBJECTIVE

One proposed U.S. test blanket module (TBM) for ITER uses ferritic-martensitic alloys with both eutectic Pb-Li and He coolants at ~475°C. In order for this blanket concept to operate at higher temperatures (~700°C) for a DEMO-type reactor, several Pb-Li compatibility issues need to be addressed. Some of the issues currently being investigated are the behavior of dispersion strengthened Fe-Cr alloys compared to conventional wrought material, the performance of Al-rich coatings to inhibit corrosion and dissimilar material interaction between SiC and ferritic steel.

SUMMARY

Characterization of wrought and oxide dispersion strengthened (ODS) Fe-Cr alloys after exposure to Pb-Li in isothermal capsule experiments is in progress. Oxide precipitates appear to coarsen near the surface perhaps due to the loss of metallic substrate. To further investigate the performance of Al-rich coatings, a time series of exposures in Pb-Li is being conducted and results are compared to observations for uncoated Fe-Cr specimens. Measurement of the Al profile after 500h suggests that there is an initial Al loss from the coating on exposure. Dissimilar metal experiments with SiC capsules and Fe and SiC specimens have been completed and the mass change data suggests a large difference in behavior for the Fe specimens after 1000h at 700°C. Unfortunately, the SiC specimens chipped during loading/unloading resulting in unreliable mass change data.

PROGRESS AND STATUS

Introduction

A current focus of the U.S. fusion materials program is to address issues associated with the dual coolant Pb-Li (DCLL) blanket concept[1] for a test blanket module (TBM) for ITER and enhanced concepts for a DEMO-type fusion reactor. A DCLL blanket has both He and eutectic Pb-17 at.%Li coolants and uses reduced activation ferritic-martensitic (FM) steel as the structural material with a SiC/SiC composite flow channel insert (FCI). Thus, recent U.S. compatibility research has examined issues with Pb-Li.[2-8] Compared to Li,[9] a wider range of materials can be compatible with Pb-Li because of the low activity of Li.[10] In particular, SiC readily dissolves in Li, but not Pb-17Li.[2,4,11] However, like Pb, Pb-Li dissolves Fe, Cr and especially Ni from many conventional alloys above 500°C.[12,13] This is not a concern for a DCLL TBM operating at <500°C. However, a DCLL blanket for a commercial reactor would be more attractive with a higher maximum operating temperature, perhaps >600°C if ODS ferritic steels[14] were used. Even at 550°C, a recent study of Eurofer 97 (Fe-Cr-W) showed a very high dissolution rate in flowing Pb-Li.[13] Therefore, preliminary Pb-Li compatibility capsule experiments are being conducted at 500°-700°C in order to investigate several concepts before flowing Pb-Li compatibility tests are conducted. Recent capsule experiments have investigated (1) the compatibility of ODS ferritic steels compared to conventional wrought FM steels, (2) the effectiveness of Al-rich coatings to inhibit dissolution, (3) the effect of Fe and Ni impurities in the Pb-Li on the amount of dissolution, and (4) potential dissimilar material effects between Fe and SiC. To address the first two topics, characterization of ODS and wrought FeCr alloys exposed to Pb-Li is presented here as well as a time series of coated specimens. For the fourth topic, the capsule experiments have been completed and the mass change data suggests that a change in the amount of dissolution occurred at 700°C.

Experimental Procedure

Static capsule tests were performed using Mo capsules and type 304 stainless steel (SS) outer capsules to protect the inner capsule from oxidation. The dissimilar materials capsules had an inner chemical vapor deposited (CVD) SiC capsule. Since this capsule cannot be sealed, it is placed inside a Mo capsule and held shut by a Mo wire welded into the Mo capsule lid that is welded shut. A similar SS capsule was used to protect the Mo capsule in these experiments. For the Mo capsules, the specimens were ~1.5 mm thick and 4-5 cm^2 in surface area with a 600 grit surface finish and were held with 1 mm diameter Mo wire. (Mo can be considered to be essentially inert under these conditions.) For the SiC capsules, a CVD SiC spacer is used to hold a specimen that is ~1.5 mm thick and 2-3 cm^2 in surface area. The representative FM steel used in prior work was Grade 92 (Fe-9Cr-2W) and two ODS alloys also were evaluated, one from ORNL (14YWT) and the other (ODM401) from Dour Metal sro. All of the alloy compositions are shown in Table 1. For coated specimens, the coupons were polished to a 0.3μm alumina finish and cleaned ultrasonically in acetone and alcohol. Aluminizing was performed in a laboratory-scale CVD reactor consisting of an inductively heated alumina tube with flowing H_2 carrying the $AlCl_x$ vapor. The reactor has been described in detail elsewhere.[15] For the dissimilar metal experiments, unalloyed Fe specimens were used to simplify the experiment and the CVD SiC specimen was high-purity material from Rohm & Haas. For the Mo capsule results reported here, the capsules were loaded with 125g of Pb-Li in an Ar-filled glove box. For the smaller CVD SiC capsules, only 20g of Pb-Li was used. To avoid recent issues with variable Li composition in the current commercial batch of Pb-Li,[7] this material was cast at ORNL and chemical analysis showed a Li content of 16.5at.%Li in one stick and 15.9% in a second stick that was used for the current series of coated specimens in Mo capsules. The Mo and SS capsules were welded shut in a glove box to prevent the uptake of impurities during the isothermal exposure. After exposure, residual Pb-Li on the specimen surface was removed by soaking in a 1:1:1 mixture of acetic acid, hydrogen peroxide and ethanol for up to 72 h. Mass change was measured with a Mettler-Toledo balance with an accuracy of 0.01 mg/cm^2. Characterization included x-ray diffraction (XRD), x-ray photoelectron spectroscopy (XPS), scanning electron microscopy (SEM) equipped with energy dispersive x-ray (EDX) analysis and electron microprobe analysis (EPMA) equipped with wavelength dispersive x-ray analysis.

Results and Discussion

Figure 1 shows the mass change data for both ODS alloys and aluminized alloy 401 after 1,000h at 700°C that was reported previously.[8] (A prior report outlined that it was not possible to aluminize the 14YWT alloy,[16] likely due to the high N content and small grain size in this batch.) Both P92 and the ODS alloys showed a similar mass loss which is not particularly surprising since Fe and Cr are thought to dissolve in Pb-Li at a similar rate. Figure 2 shows cross-sections of the bare alloys after exposure at 700°C. The Gr.92 specimen showed some areas with a flat surface and some rougher areas as shown in Figure 3a. Prior work has suggested that the native oxide on the steel may inhibit dissolution while it remains in

Table 1. Alloy chemical compositions (atomic% or ppma) determined by inductively coupled plasma analysis and combustion analysis.

Material	Fe	Ni	Cr	Al	O	C	N	S	Other
14YWT	83.3	0.03	14.1	0.04	6000	3000	5170	69	0.59W,0.12Y 0.28Ti,0.08Si
401	82.6	0.12	14.8	0.12	6560	610	1770	89	0.17Mo,0.13Y 1.2Ti,0.08Si
Gr.92 (9Cr-2W)	87.2	0.1	9.9	0.02	80	5120	2330	87	0.55W, 0.46Mn 0.30Mo,0.32Si

< indicates below the detectability limit of <0.01% or <0.001% for interstitials

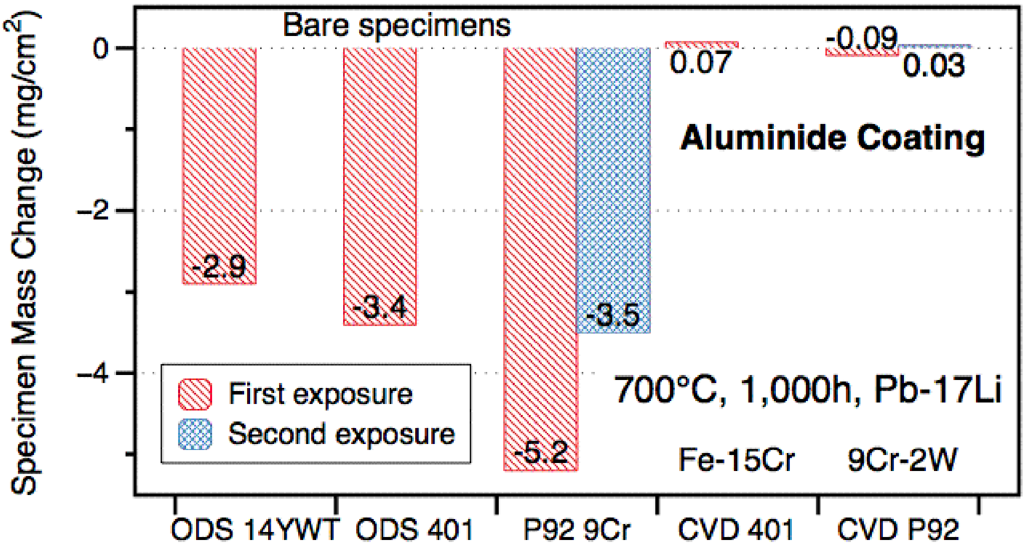

Figure 1. Mass change results after exposure for 1,000h at 700°C in Pb-Li for both wrought and ODS FeCr alloys and with and without CVD aluminide coatings.

place.[13] Areas like Figure 2a show Cr depletion, while the flat areas show no Cr depletion as shown in Figure 3. Also shown in Figure 3, the Cr depletion is minimal after exposure of Gr.92 at 600°C. The ODS alloys showed large oxide particles and some void formation near the surface after 1,000h exposures, Figure 2b-2c. This behavior increased after a 5,000h exposure of 14YWT at 700°C, Figure 2d. The higher

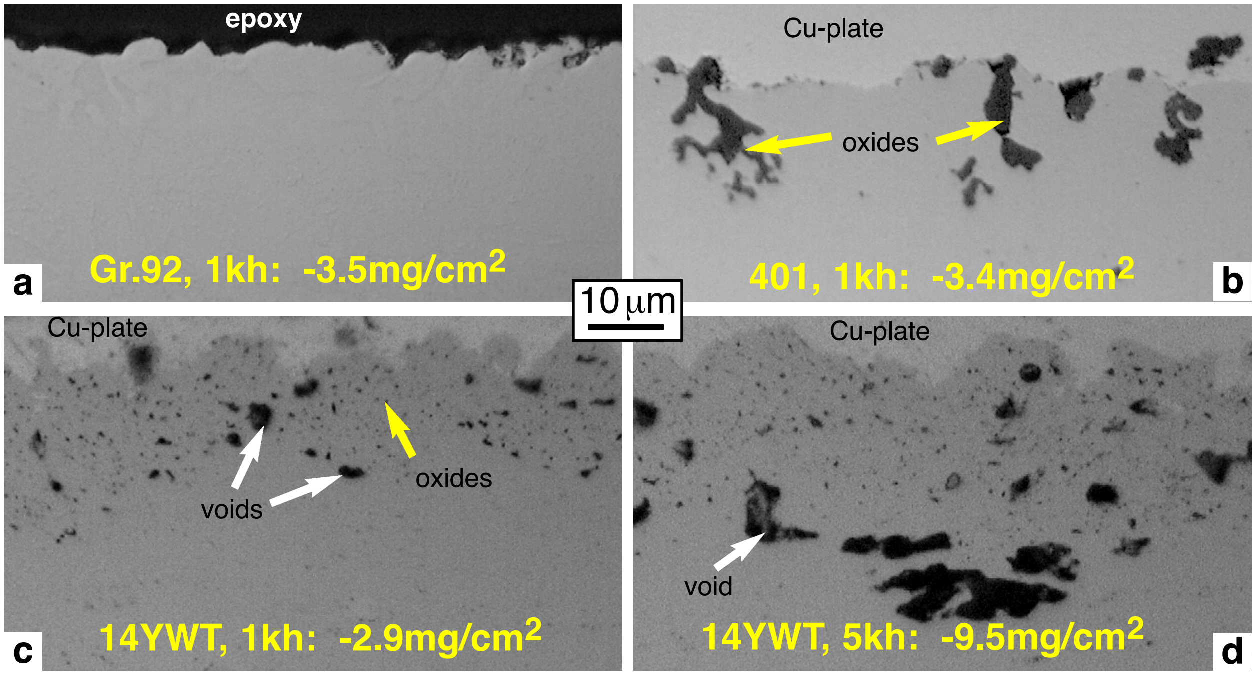

Figure 2. Light microscopy of FeCr alloys exposed to Pb-Li at 700°C (a) Gr.92 for 1,000h, (b) 401 for 1,000h, and 14YWT for (c) 1,000h and (d) 5,000h.

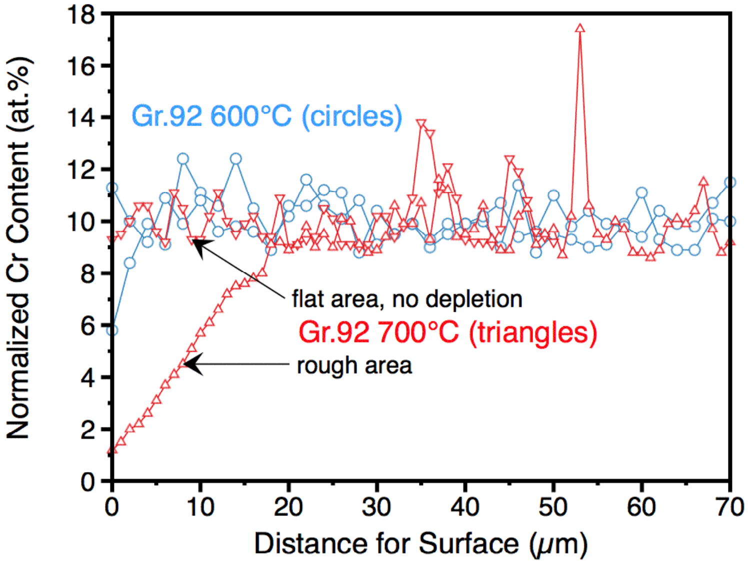

Figure 3. EPMA Cr composition profiles from Gr.92 specimens exposed for 1,000h in Pb-Li at 600° and 700°C.

Cr content in the ODS alloys may have contributed to the different behavior. However, Figure 1 shows that with the same CVD coating procedure, the ODS 401 substrate showed a similar reduction in mass loss as coated Gr.92. Figure 4 shows a cross-section of the coated 401 specimen after exposure to Pb-Li. None of the large oxide particles are present in this cross-section as in the uncoated specimen, Figure 2b.

While these coatings appear to be effective in 1,000h capsule tests, one issue that has arisen is the high Al loss from the coating observed after exposure at 700°C.[5] To further investigate coating performance, two sets of experiments are being conducted. For the first experiment, a single aluminized Gr.92 specimen was sectioned so that the same coating could be studied at three stages: as-coated, after pre-oxidation and after exposure to Pb-Li. The as-coated and pre-oxidized Al profiles were presented previously showing little difference after 2h at 800°C.[8] The third piece has been exposed for 1,000h at 700°C and is currently being mounted for microprobe analysis. For the second experiments, coated Gr.92 specimens were exposed to Pb-Li at 700°C for different times. Figure 5 shows the current results including the mass change of uncoated specimens for comparison in Figure 5a. A mass loss was measured after

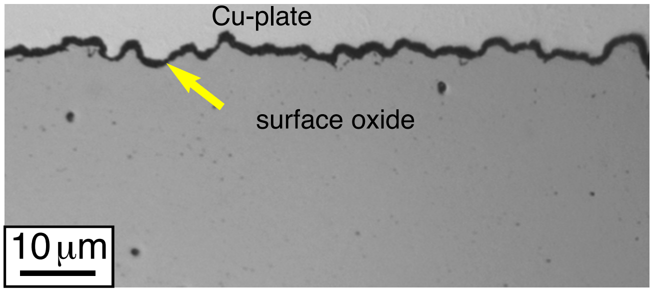

Figure 4. Light microscopy of polished cross-section of aluminized 401 exposed to Pb-Li at 700°C for 1,000h. A thin oxide is present at the surface which shows some roughness.

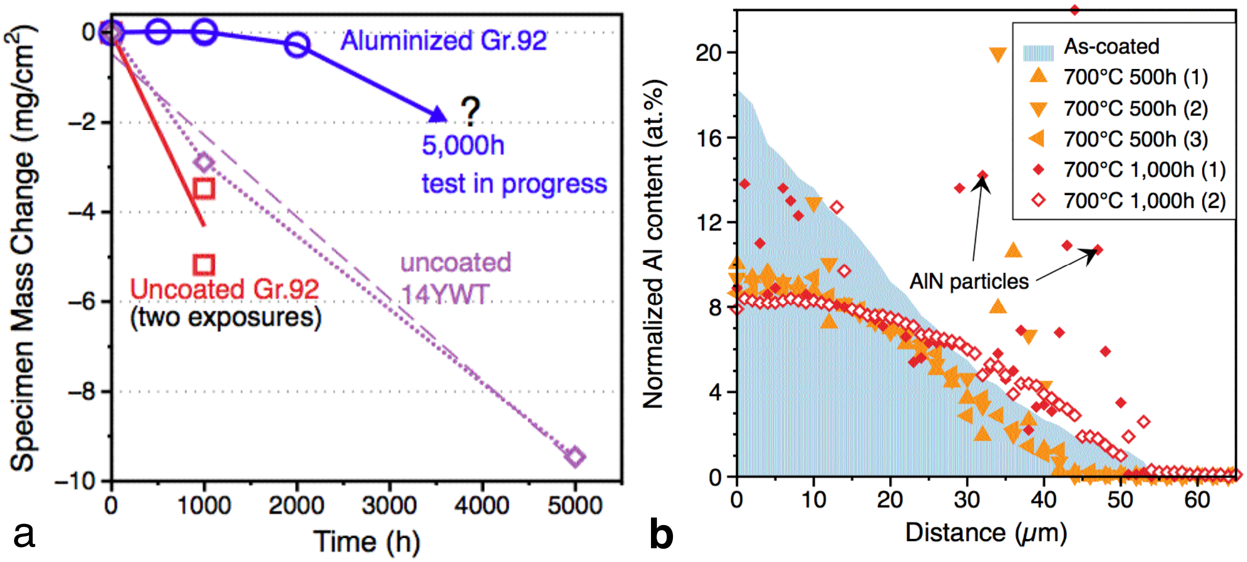

Figure 5. (a) Specimen mass change as a function of exposure time in Pb-Li at 700°C (b) Normalized Al content by EPMA as a function of depth for coated Gr.92 specimens after exposure for 500h and 1,000h at 700°C in Pb-Li. Typical as-coated Al profile is shown in shaded area.

the 2,000h coating exposure and the specimen appeared shiny suggesting there was no surface oxide (as in Figure 4). This specimen is now being characterized. The 5,000h exposure will be complete in September. For the 500h exposure, the Al loss is shown in Figure 5b and is compared with Al profiles from a typical as-received specimen (shaded area) and the previous 1000h exposure. The profiles suggest that little additional Al was lost from the coating between 500 and 1000h. However, during the initial 500h exposure, a significant loss in Al occurred dropping the surface Al content from ~18at% to ~10%.

The final area is the dissimilar material experiments comparing the behavior of Fe and SiC specimens in Pb-Li with mild steel and SiC capsules. The Fe capsule mass changes were presented previously[7] and are included in Figure 6 with the new results from SiC capsules. Unfortunately, the SiC specimen with a SiC holder resulted in some specimen chipping during loading and/or unloading that resulted in some mass losses unrelated to the Pb-Li reaction. The most striking observation is that there was a major difference in the mass change of the Fe specimen at 700°C between the two types of capsules. A large mass loss was observed with the steel capsule and a much smaller loss with the SiC capsule. The mass loss due to dissolution of Fe in the Pb-Li is not unexpected. The decrease in mass loss with the SiC capsule may be due to C uptake from the CVD SiC capsule as FeC_x is thermodynamically more stable than SiC. The specimens are now being characterized. One difference between the two capsule experiments is the specimen surface area to Pb-Li volume ratio. In the SiC capsule the ratio is 1.5 (2.7 cm^2 vs. 1.8 cm^3) while in the Fe capsule it is 0.5 for just the specimen (5 cm^2 vs. 11 cm^3). However, if the capsule wall also is considered (as it also may dissolve) the ratio is 2.5 because of the large surface area of the capsule in contact with ~11cm^3 of Pb-Li. Nevertheless, this difference does not appear sufficient to explain the large change in mass between the two experiments. This mechanism may not be a concern for <500°C operation but needs to be evaluated for higher temperature systems, especially with a temperature gradient. The characterization of the current specimens should give some indication of the extent of the dissimilar material reaction.

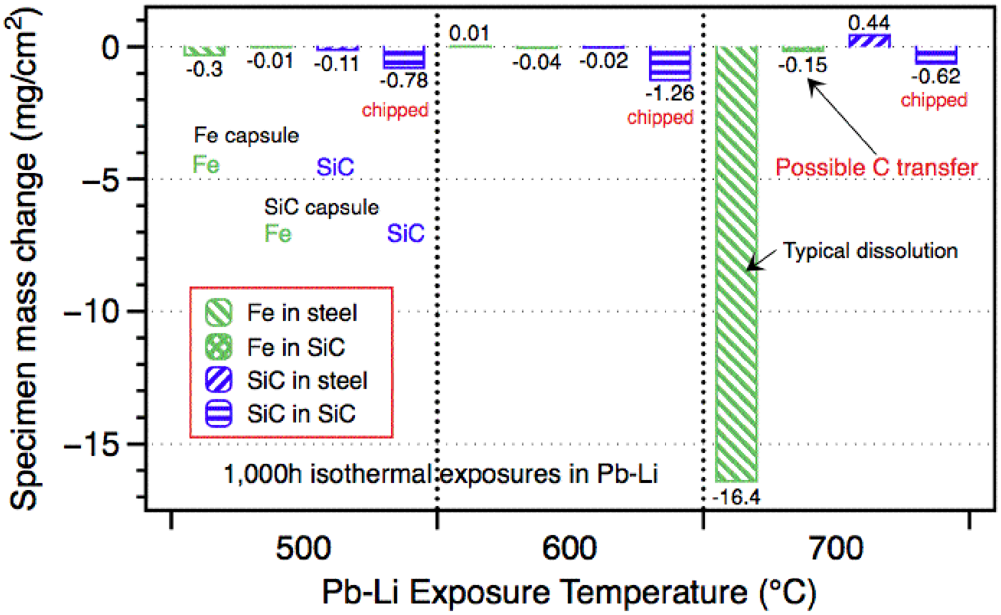

Figure 6. Specimen mass change from a series of capsule experiments with carbon steel or CVD SiC capsules and Fe and CVD SiC specimens exposed to Pb-Li for 1,000 h at each temperature.

References

[1] M. Abdou, D. Sze, C. Wong, M. Sawan, A. Ying, N. B. Morley and S. Malang, Fus. Sci. Tech., 47 (2005) 475.
[2] B. A. Pint, Fus. Sci. Tech. 52 (2007) 829.
[3] B. A. Pint and K. L. More, J. Nucl. Mater. 376 (2008) 108.
[4] B. A. Pint, Mater. Sci. Forum, 595-598 (2008) 549.
[5] B. A. Pint, J. Nucl. Mater., in press.
[6] B. A. Pint and K. A. Unocic, DOE/ER-0313/47 (2009) 82.
[7] B. A. Pint, DOE/ER-0313/48 (2010) 102.
[8] B. A. Pint, DOE/ER-0313/49 (2011) 54.
[9] J. E. Battles, Intern. Mater. Rev. 34 (1989) 1.
[10] P. Hubberstey, J. Nucl. Mater. 247 (1997) 208.
[11] T. Yoneoka, S. Tanaka and T. Terai, Mater. Trans. 42 (2001) 1019.
[12] O. K. Chopra, D. L. Smith, P. F. Tortorelli, J. H. DeVan and D. K. Sze, Fusion Technol., 8 (1985) 1956.
[13] J. Konys, W. Krauss, J. Novotny, H. Steiner, Z. Voss and O. Wedemeyer, J. Nucl. Mater. 386-88 (2009) 678.
[14] S. Ukai and M. Fujiwara, J. Nucl. Mater. 307 (2002) 749.
[15] Y. Zhang, B. A. Pint, K. M. Cooley and J. A. Haynes, Surf. Coat. Tech. 202 (2008) 3839.
[16] A. Vande Put and B. A. Pint, DOE/ER-0313/48 (2010) 110.

ADDITIONAL CHARACTERIZATION OF V-4Cr-4Ti EXPOSED TO FLOWING Li – B. A. Pint and K. A. Unocic (Oak Ridge National Laboratory)

OBJECTIVE

Characterize specimens exposed to flowing Li in a thermal gradient to evaluate the effects on V-4Cr-4Ti and a multi-layer electrically-insulating coating needed to reduce the magneto hydrodynamic (MHD) force in the first wall of a lithium cooled blanket.

SUMMARY

In order to further understand the behavior of specimens exposed in the loop, microstructural characterization is being performed on the V-4Cr-4Ti tensile specimens that showed dynamic strain aging at 500°C. Initial results are presented. Also, further characterization on the dual layer MHD coatings is planned.

PROGRESS AND STATUS

Introduction

Previous reports[1,2] presented 500°C tensile behavior of V-4Cr-4Ti after various exposures including flowing Li in a thermal convection loop with a peak temperature of 700°C for 2,355h.[3] The results were unusual and more characterization was warranted which is now being undertaken. Also, the dual layer (Y_2O_3/V) MHD coatings deposited by physical vapor deposition that were exposed in the loop were not fully characterized because a method was not apparent to evaluate the electrical resistivity without damaging the coatings. Using focused ion beam milling may now provide an opportunity to study those coatings.

Experimental Procedure

Details of the thermal convection loop exposure have been presented previously.[3] The specimens consisted of miniature tensile specimens (type SS-3: 25 x 4 x 0.9mm), tab specimens and specimens with a dual layer MHD coating linked in a chain held together with V-4Cr-4Ti wire. The tensile specimens were annealed for 1h at 1050°C prior to exposure in Li. The exposure temperature for each specimen is estimated by using a linear extrapolation of the temperatures measured at the top and bottom of the each leg.[3] Tensile testing was conducted at 500°C in a vacuum with a base pressure of 10^{-6}Pa (10^{-8}Torr) and a strain rate of $10^{-3}s^{-1}$. Initial microstructural characterization is being performed, first consisting of scanning electron microscopy (SEM) of the fracture surfaces and metallographic cross-sections of the tensile specimens. Additional characterization of the microstructure (e.g. hardness profiles and transmission electron microscopy (TEM)) will be conducted as warranted.

Results and Discussion

Figure 1 shows a summary of fracture surfaces and deformation regions of the tensile specimens fractured at 500°C in vacuum. All of the specimens show some ductile behavior. The as-received specimen showed the most ductility, Figure 1a. (In general, all of the specimens showed an increase in ultimate tensile stress (UTS) compared to the unexposed specimens and some decrease in ductility.) The specimen exposed to isothermal Li at 800°C for 1,000h (Figure 1b) and the specimen from the top of the hot leg (highest temperature, ~627°C, Figure 1d) show a 45° orientation of the fracture surface suggesting a change in the deformation mechanism near the maximum shear stress. To evaluate the operating mechanism and grain orientations, electron backscatter diffraction in the SEM and TEM will be used. The initial characterization

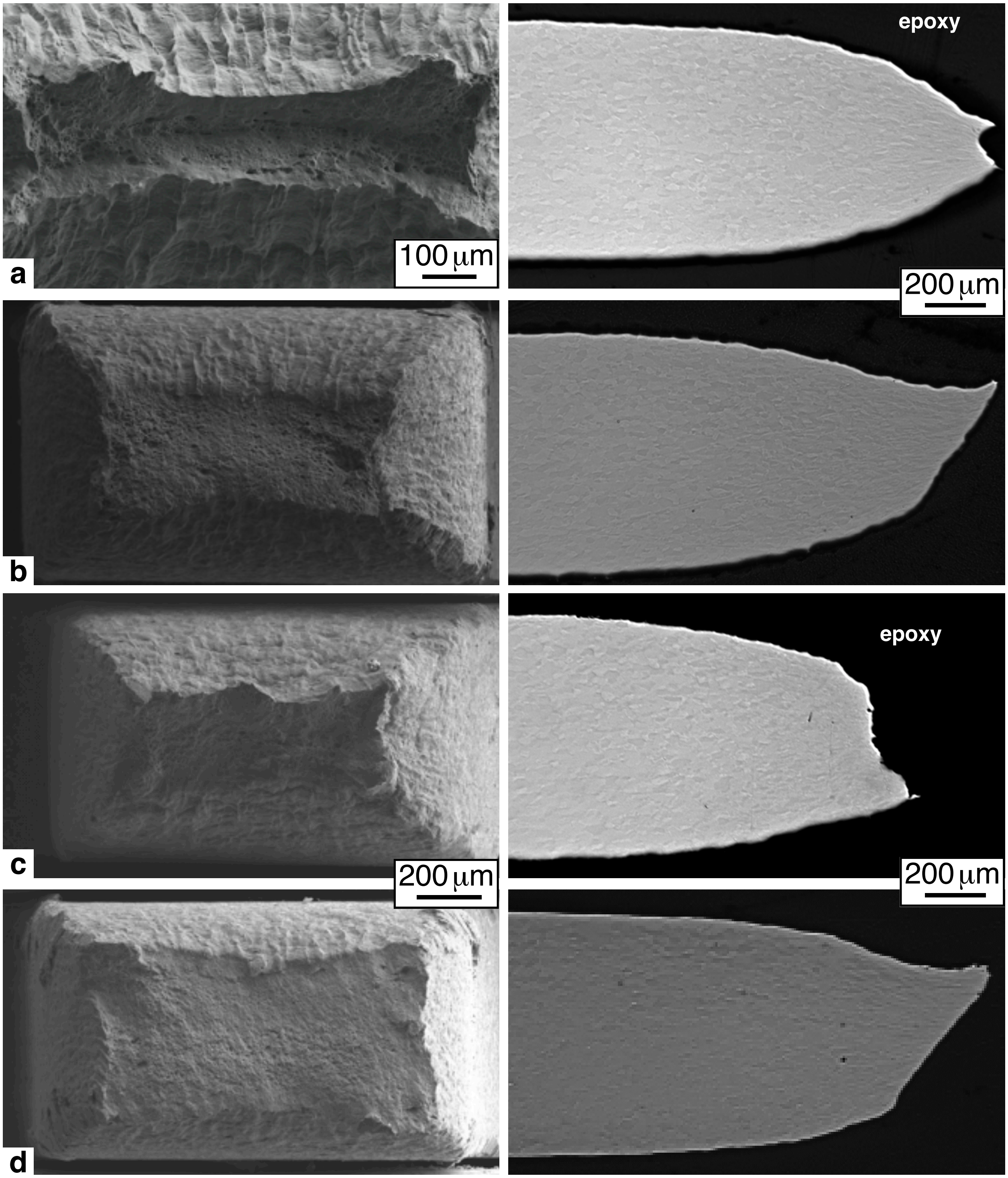

Figure 1. SEM of fracture surface and light microscopy of cross sections for V-4Cr-4Ti tensile specimens tested at 500°C: (a) as-received, (b) 800°C isothermal capsule exposure in Li, (c) cold leg, ~516°C and (d) hot leg, ~627°C. All of these specimens showed dynamic strain ageing at 500°C.

of the tab (spacer) V-4Cr-4Ti specimens in the loop showed precipitate coarsening and depletion near the surface. However, the initial evaluation of these specimens did not reveal similar behavior in these specimens. As each specimen was too small to perform a chemical analysis, V-4Cr-4Ti tab and tube wall specimens were used to measure chemistry changes. These analyses consistently showed a decrease in the O content and an increase in the C and N contents.[1, 3-5] These changes in interstitial content are expected based on Li thermodynamics of gettering O, but low affinity, compared to vanadium, for C and N. One goal of the characterization is to determine if these composition changes are uniform or if there is a gradient within the material and if location in the loop affected the microstructure. Ultimately, a better understanding of the precipitate evolution during exposure in the loop should explain the variations observed in the dynamic strain aging behavior during 500°C tensile testing and the differences observed between these specimens and those exposed to static Li in an Ar-filled glove box.[6]

References

[1] B. A. Pint, DOE/ER-0313/45 (2008) 11.
[2] B. A. Pint, DOE/ER-0313/46 (2009) 1.
[3] B. A. Pint, et al., J. Nucl. Mater. 386-388 (2009) 712.
[4] B. A. Pint, et al., DOE/ER-0313/43 (2007) 2.
[5] B. A. Pint, DOE/ER-0313/44 (2008) 10.
[6] M. M. Li, D. T. Hoelzer and M. L. Grossbeck, J. Nucl. Mater. 392 (2009) 364.

6.1 First-Principles Investigation of the Influence of Alloying Elements on the Elastic and Mechanical Properties of Tungsten — G. D. Samolyuk, Y. N. Osetskiy, and R. E. Stoller (Oak Ridge National Laboratory)

OBJECTIVE

The objective of this research is to support possible approaches to the design of ductile tungsten alloys through the use of relevant *ab initio* electronic structure calculations.

SUMMARY

The properties of ½<111> screw dislocations in $W_{1-x}Tm_x$ alloys with different transition metal, Tm, concentrations within the local density approximation of density functional theory was investigated. The electronic structure of alloys was described within the virtual crystal approximation. It was demonstrated that alloying of W with transition metals from group VIII modifies the properties of screw dislocation similar to the effect of alloying with Re. Specifically, the alloying changes the dislocation core from symmetric to asymmetric and reduces the value of the Peierls barrier and Peierls stress. These modifications are caused by filling of d-electron states of W.

PROGRESS AND STATUS

Introduction

Alloys of W with Re have been studied extensively using both experiment [1, 2] and theory [3, 4, 5]. Adding Re has the effect of ductility improvement of the tungsten. In [5] it was demonstrated using first principles calculations that addition of Re to tungsten modifies the symmetry properties of ½<111> screw dislocations and reduces the value of the Peierls barrier. In the present research we investigate the properties of screw dislocations in binary $W_{1-x}Tm_x$ using first-principles electronic structure calculations for a set of transition metals (Tm). This result will be used in a future search for alloying elements causing changes in tungsten alloys properties similar to the effects of Re.

Formalism

We calculated the electronic structure within the local density approximation of density functional theory (DFT) using the quantum espresso package [6]. The plane wave energy cut off at 42 Ry allows accuracy 0.2 mRy/atom. The alloying was modeled using the virtual crystal approximation (VCA). As a realization of VCA for the pseudo potential method we used the scheme proposed in Ref. [7]. A periodic quadrupole arrangement of ½<111> screw dislocation was used to describe the core structure and Peierls barrier. Two dislocations with opposite Burgers vectors were placed in a super cell containing 135 atoms with lattice vectors $\boldsymbol{b}_1=(9\boldsymbol{u}_1+5\boldsymbol{u}_2+\boldsymbol{u}_3)/2$, $\boldsymbol{b}_2=5\boldsymbol{u}_2$ and $\boldsymbol{b}_3=\boldsymbol{u}_3$, where vectors $\boldsymbol{u}_1$=<112>, $\boldsymbol{u}_2$=<110> and $\boldsymbol{u}_3$=<111>/2. The BZ summations were carried out over a 1x2x8 BZ grid with Gaussian boarding of 0.02 Ry. It was demonstrated that summation over 1x1x3 BZ grid used in our previous calculation in not accurate enough. The Peierls barrier in $W_{1-x}Tm_x$ was obtained by moving a ½<111> dislocation from easy to hard core configurations.

RESULTS

The applicability of the virtual crystal approximation to $W_{1-x}Re_x$ binary alloys was verified in our previous research, see [9]. Also it was demonstrated that the so-called rigid band approximation can be applied. Thus, all dilute tungsten based alloys with the same number of electrons per atom (*e*/*a*) have the same elastic constants. The concentration of different alloying elements which give the same (*e*/*a*) value can be calculated through the simple expression

$$x = \frac{(e/a)}{Z - Z_W}, \tag{1}$$

where Z is the number of valence electrons of the alloying transition metal atom and Z_W of tungsten. As it was demonstrated in our previous reports [9], the d band filling by addition of electrons from the VIII group transition metal, the lattice parameter decreases and elastic anisotropy $A = C_{44}/C'$ increase [9]. The obtained result agrees with experiment [10]. Also the C' and A values demonstrate very close dependence on concentration if they are plotted as a function of (*e*/*a*), the number of electrons per atom. This similarity supports conclusion that the main effect of alloying W with transition metals with larger number of *d* electrons is related to *d* band filling.

The calculated structure of the easy core configuration of a 1/2<111> dislocation is shown on Fig. 1 for pure W, $W_{0.75}Re_{0.25}$ and $W_{0.88}Fe_{0.12}$, where concentrations of transition metals were chosen to give the same (*e*/*a*) value. The circles on Fig. 1 represent W atoms looking in the <111> direction and the structure of dislocation is illustrated by differential displacement maps [11]. It should be mentioned that for tungsten alloys with other Tm with the same (*e*/*a*) value the core configurations are the same as for Re and Fe alloys but are not shown here. As was demonstrated in [5] for W a symmetric core is obtained, i.e. the dislocation expands equally along the six <112> directions.

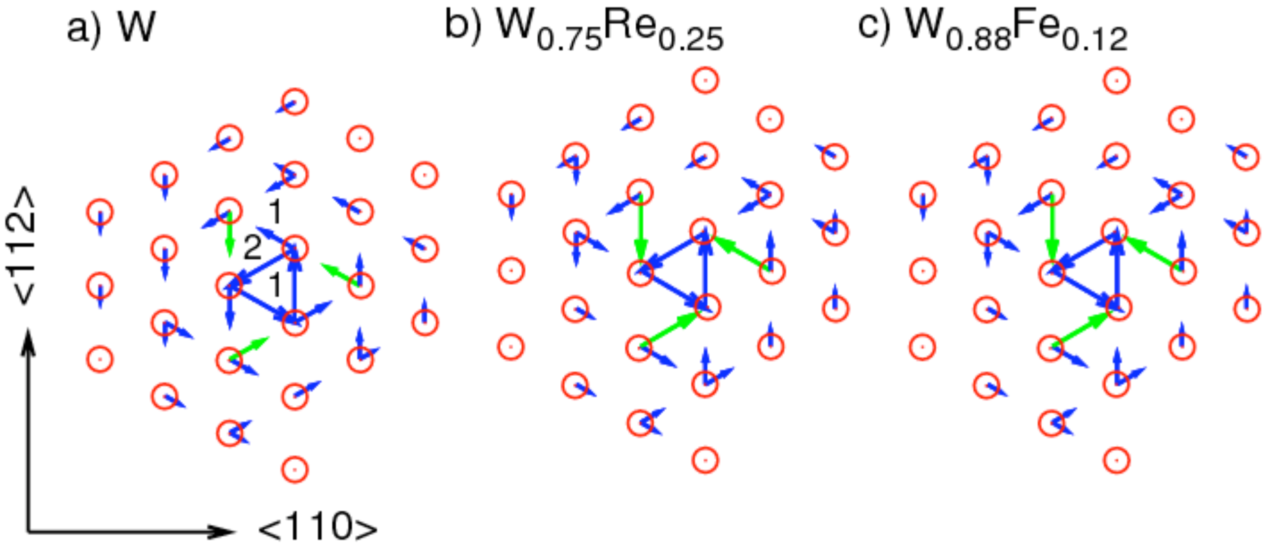

Figure 1. The easy core dislocation structure in $W_{1-x}Tm_x$ calculated in VCA.

Alloying with Re or any other Tm with the same value of (*e*/*a*) leads to change from a symmetric core structure to an asymmetric structure. It should be mentioned that increase of BZ grid size modifies Tm concentration at which the symmetry core change can bi visualized to larger concentrations. As was mentioned in Ref [5], the transition from symmetric to asymmetric cores changes the dislocation slip plane. The symmetric core dislocations move uniformly on {110} planes; asymmetric ones move in a zigzag manner [12] and the slip plane changes to {112}.

Along with the change of core symmetry the value of the Peierls barrier changes, see Fig. 2. As can be seen, alloying with Re, and Tm from VIII group with concentration which corresponds to (*e*/*a*)=6.05 reduces the barrier by ~25 %, whereas Zr increases the barrier and makes the tungsten alloy more brittle.

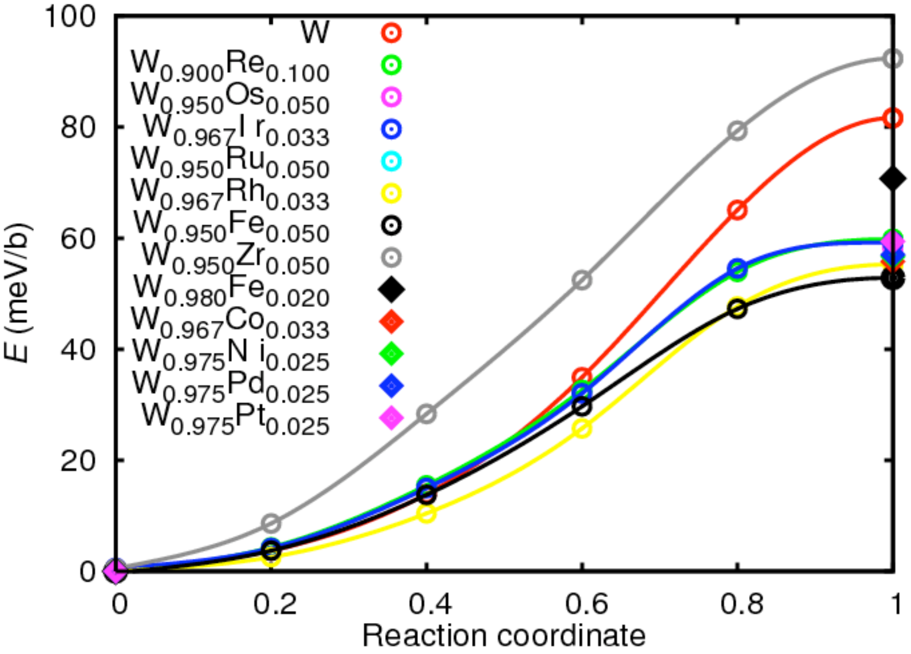

Figure 2. Calculated Peierls barrier in $W_{1-x}Tm_x$.

The concentration of Tm in these calculations was chosen thus that it keeps the same value (*e*/*a*). However the limit of solubility of Fe in W is < 2 %. The result for modification of Peierls barrier for 2 % Fe is shown by black diamond on Fig. 2 and equals ~ 10%. Although Peierls barrier is very important property of dislocation it's not directly determine value of Peierls stress, the stress should be applied to crystal to move dislocation from one easy core configuration to another one. The value of Peierls stress can be calculated directly by applying strain to modeling cell until the dislocation moves. The strain was applied by modification of lattice vector $\boldsymbol{b}_1=9/2\boldsymbol{u}_1+5/2\boldsymbol{u}_2+(1/2+\xi)\boldsymbol{u}_3$. On the Fig. 3 the dependence of modeling cell energy as a function of strain ξ is presented.

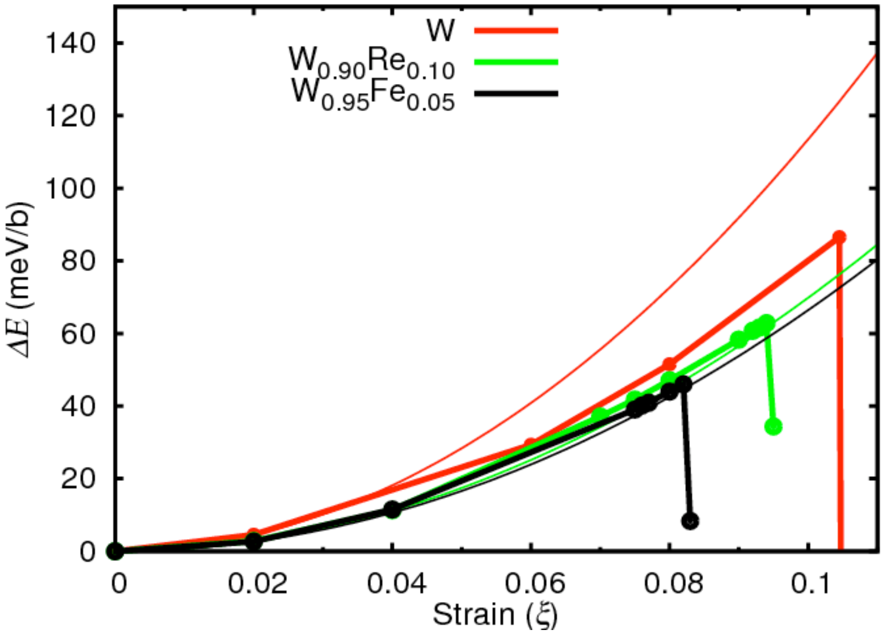

Figure 3. Energy of modeling cell as a function of strain ξ.

The drop in the total energy corresponds to dislocation glide and obtained value of the stress corresponds to Peierls stress. Thus the alloying reduces Peierls stress from 1.71 GPa to 1.37 GPa for 10 % Re and to 1.1 GPa for 5% of Fe. The correlation between Peierls barrier as a function of reaction coordinate (blue) and energy of the modeling cell as a function of strain (red) is illustrated on Fig. 4.

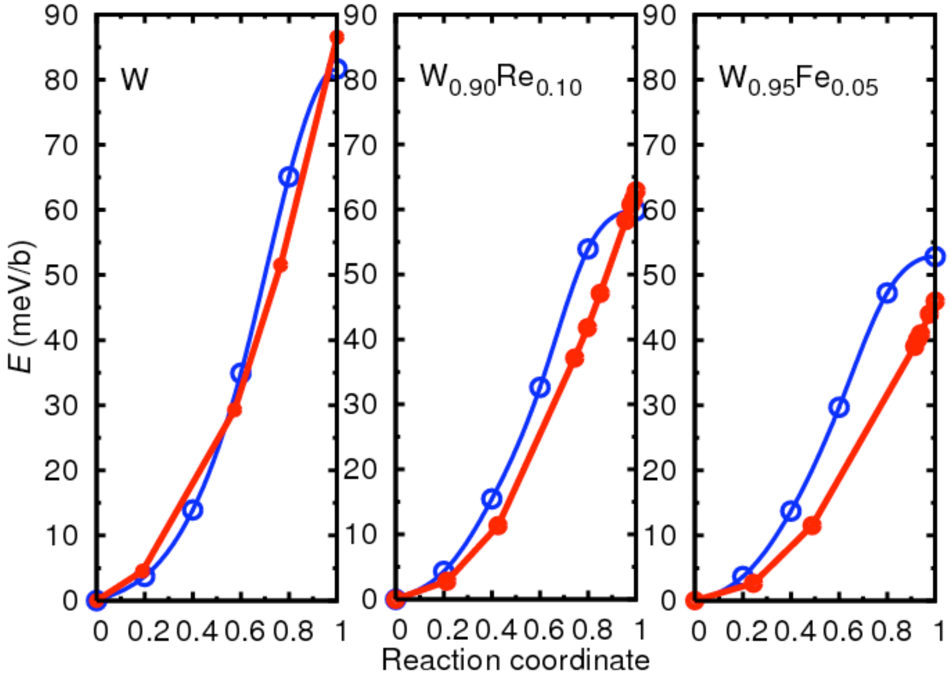

Figure 4. Energy of modeling cell as a function of strain ξ (red) and Peierls barrier (blue).

The energy as a function of strain is rescaled thus that zero corresponds to zero strain and one to Peierls stress. As it can be seen the value of total energy of cell at Peierls stress is qualitative agreement with value of Peierls barrier and modification of Peierls barrier can be used as a screening to gauge ductility.

Thus the alloying tungsten with any transition metal from VIIA and VIIIA groups leads to similar modifications of dislocation core structure and reduction of the Peierls barrier and Peierls stress and possible ductilizing effect.

References

[1] S. J. Zinkle, "Thermomechanical Properties of W-Re Alloys & Initial Survey of Molten Tin Corrosion Data," presented at APEX Study Meeting UCLA, November 2-4, 1998.

[2] R. A. Ayres, G. W. Shanette, and D. F. Stein, "Elastic Constants of Tungsten-Rhenium Alloys from 44 to 298 K," *J. Appl. Phys.* **46**, 1528 (1974).

[3] K. Persson, M. Ekman, and G. Grimvall, "Dynamical and Thermodynamical Instabilities in the Disordered Re_xW_{1-x} System," *Phys. Rev. B* **60**, 9999 (1999).

[4] M. Ekman, K. Persson, and G. Grimvall, "Phase Diagram and Lattice Instability in Tungsten-Rhenium Alloys," *J. Nucl. Mater.* **278**, 273 (2000).

[5] L. Romaner, C. Ambrosch-Draxl, and R. Pippan, "Effect of Rhenium on the Dislocation Core Structure in Tungsten," *Phys. Rev. Lett.* **104** 195503 (2010).

[6] P. Giannozzi, S. Baroni, N. Bonini, "QUANTUM ESPRESSO: A Modular and Open-Source Software Project for Quantum Simulations of Materials," *J. Phys.: Condensed Matter* **21**, 395502 (2009).

[7] N. J. Ramer and A. M. Rappe, "Virtual-Crystal Approximation That Works: Locating a Compositional Phase Boundary in $Pb(Zr_{1-x}Ti_x)O_3$," *Phys. Rev. B* **62**, R743 (2000).

[8] M. J. Mehl, et al., *Phys. Rev. B* **41** 10311 (1990).

[9] G. D. Samolyuk, Y. N. Osetskiy, and R. E. Stoller, "First-Principles Investigations of the Influence of Alloying Elements on the Elastic and Mechanical Properties of Tungsten," Fusion Materials Semiannual Reports DOE/ER-0313/48, June 30, 2010 pp. 96-101; and DOE/ER- 0313/49, December 31, 2010 pp. 90-93.

[10] R. A. Ayres, G. W. Shannette, and D. F. Stein. *J. Appl. Phys.* **46**, 1526 (1976).

[11] V. Vitek, *Cryst. Lattice Defects* **5**, 1 (1974).

[12] J. P. Hirth, and J. Lothe, **Theory of Dislocation** (Wiley-Interscience, New York, 1982).

6.2 Influence of Carbon on Helium – Defect Interactions in Single Crystal Iron Following Helium Implantation: Thermal Helium Desorption and Positron Lifetime Measurements and Modeling

— Xunxiang Hu (University of California, Berkeley), Donghua Xu, and Brian D. Wirth (University of Tennessee, Knoxville)

OBJECTIVE

The objective of this work is to identify the kinetics and energetics of helium-point defect interactions of helium implanted single-crystalline iron.

SUMMARY

The thermal desorption spectra of helium from single crystalline iron samples was obtained as a function of implantation conditions using the Berkeley thermal helium desorption spectroscopy (THDS). The implantation conditions were He ion implantation energies of 10, 20, or 40 keV at a consistent dose level 1×10^{15} He/cm^2. Constant rate heating ramps were employed to thermally desorb the implanted helium. The present results, in which the single crystalline iron has a lower carbon content, indicate a significant effect of carbon on the helium desorption behavior, when compared to our previous measurements. The results indicate that major helium releasing peaks of the iron samples with higher purity show up at lower temperatures. A spatially dependent cluster dynamics model is utilized to reproduce the helium spectrum in BCC region. Meanwhile it provides an opportunity to optimize the basic thermodynamic and kinetic energy parameters of helium and small helium-vacancy clusters. The combination of the modeling and THDS measurement allows identification of possible mechanisms (e.g. shrinkage of He_3V_2) responsible for the measured helium desorption peaks. Furthermore, the model is also used to predict the depth dependence of helium and helium-defect clusters as a function of time and temperature during the THDS measurement. The samples with the implantation condition of 40 keV, 1×10^{15} He/cm^2 have been measured by positron annihilation spectroscopy, as an initial attempt to correlate a second experimental technique of the vacancy cluster population against the modeling predictions. Good agreement is obtained between the positron lifetime analysis and the modeling calculation. The recent work provided an overview of the self-consistency of the model predictions based on the assumptions made in the helium-point defect binding and interaction energies and diffusivities.

PROGRESS AND STATUS

Introduction

A large quantity of helium will be generated in fusion structural materials (e.g. ferritic/martensitic steel) as a result of direct implantation or transmutation reactions induced by the large 14 MeV peaked neutron spectrum [1-3]. Since helium has extremely low solubility in most metallic alloys, it has a strong tendency to cluster with various types of defects and to precipitate out as bubbles. It has been observed that the production of helium in typical engineering alloys can lead to significant property degradation, such as hardening, fast creep rupture, swelling and embrittlement [1-4]. Therefore, studying helium effects on the microstructure and mechanical properties is of tremendous importance in fusion materials research. Since the macroscopic properties are determined by the microstructure and microscopic interactions, a major task of this study is to understand the helium effects by uncovering the mechanisms by which helium migrate and interact with various types of defects, and by which the interactions govern the subsequent nano/microstructural evolution in irradiated materials. This is an inherently multi-scale problem spanning from atomistic to macroscopic dimensions in both time and space.

The theoretical foundation of helium behavior was laid in the 1970s and 1980s with concern with mainly about the fission conditions [5-10]. Due to the increasing interest of fusion energy, a resurgence of research activities on helium is witnessed in recent years. BCC iron and ferritic alloys attract most of the concern, particularly. The kinetics, energetics and thermal stability of helium and small helium-containing clusters, and the helium interactions with grain boundaries and dislocations have been studied by atomistic simulations using molecular statics/dynamics and ab inito approaches. Rate theory models are also developed by different researchers to simulate the evolution of helium-defect clusters and fit the experimental results. Meanwhile, experiments using optical or electron microscopy, nuclear reaction depth profiling, positron annihilation spectroscopy, thermal helium desorption spectrometry and other techniques have been executed to analyze the behavior of helium and helium-containing clusters in BCC iron and ferritic alloys [11-16]. However, the overall picture of helium in BCC iron or ferritic alloys remains incomplete and not yet self-consistent. On one hand, there are still significant open questions such as the energetics of large He-V clusters. On the other hand, apparent discrepancies still exist in the literature regarding some basic subjects, such are the binding energy of HeV cluster.

A newly developed, parallel computer code for modeling the spatially-dependent cluster dynamics of helium, vacancy and interstitial clusters has been used to predict the earlier THDS experimental results in our research group [17,18]. A good agreement could be obtained by optimizing the values for the migration energy of single vacancy and the binding energies of small He-V clusters. These results were explained by invoking the presence of impurities in the experimental samples, which were not taken into account in the initial model. Since carbon is a common impurity in iron and since it strongly interacts with vacancies, as confirmed by ab initio calculation [19,20], carbon was proposed as the most likely candidate for the effect observed.

In this work, we conducted THDS measurements for the new batch of single crystalline irons implanted with 10keV, 20keV, 40keV to a constant dose $1x10^{15}$ He/cm^2. The comparison between the new helium desorption spectrum and the previous results of old samples give us a general picture of how the carbon's presence affects the helium outward flux. The cluster dynamic model is incorporated to fit the helium desorption spectrum and analyze the He-V clusters' evolution. The model's prediction will be verified by positron annihilation spectroscopy (PAS) measurements at selected annealing conditions of interest. This report will provide an overview of the self-consistency of the model predictions based on the assumptions made in terms of the He-point defect binding and interaction energies, and diffusivities.

Experimental Procedure

Two different batches of single crystalline irons were used in this project. The old samples with a purity of 99.94% were provided by Dr. S. A. Maloy at Los Alamos

National Lab. The new bacth of high purity (99.98%) single crystalline iron plates of 1mm in thickness, 4.5mm in diameter were purchased from Goodfellow. Before measurements, the samples were mechanically polished to 1 μm grade smoothness, and then commercially implanted at room temperature with He-4 ions.

Partial helium current was measured in Berkeley ultrahigh vacuum (~10^{-10} torr) thermal desorption system as a function of temperature during constant ramp rate (1 K/s) from room temperature up to 1300°C. The helium current was then converted to the instantaneous desorption rate by multiplying a proportionality coefficient, determined separately with a calibration procedure. More details of our system can be found in Ref. 21 and 22.

RESULTS

In order to study the effect of impurities, chemical analysis was conducted for both batches by Luvak Inc. to identify the compositions of samples. The following table shows the analysis details. No other elements were detected in excess of 0.01%.

Table 1. Composition of the two batches of single crystalline irons

	Carbon	Copper	Manganese	Nickel	Iron
Old samples	0.023%	< 0.01%	0.01%	< 0.01%	Balance
New samples	0.007%	0.0385%	0.049%	0.0135%	Balance

The analysis results indicate that carbon content of the old samples is three times more than that of new samples while the other impurities, such as Cu, Mg and Ni, of old samples are less than those present in the new samples. The substitutional solutes of copper, nickel and manganese should have very little impact on the binding energies of He-V clusters because of their similar properties (e.g. atom size) as iron. In contrast, carbon has a strong tendency to interact with vacancies, as confirmed by ab initio calculations. In this paper, we will focus on the effect of carbon on the helium desorption spectra. In the following, when the high purity of SC samples are mentioned, it represents the new samples with low carbon content; when low purity of SC samples are used, it means the old samples with relatively higher carbon content.

The facility experienced the change of tungsten crucible recently. A new tungsten crucible welded by a supporting tantalum rod replaced the separated ones used before. The new design will guarantee the stability of the thermal couple in the measurement in order to provide more accurate temperature control. Meanwhile, the facility accepted the new components after several runs. A relatively cleaner background was obtained whose helium current remains in the small region of low values, 1.4×10^{-13} A~3.2×10^{-13} A.

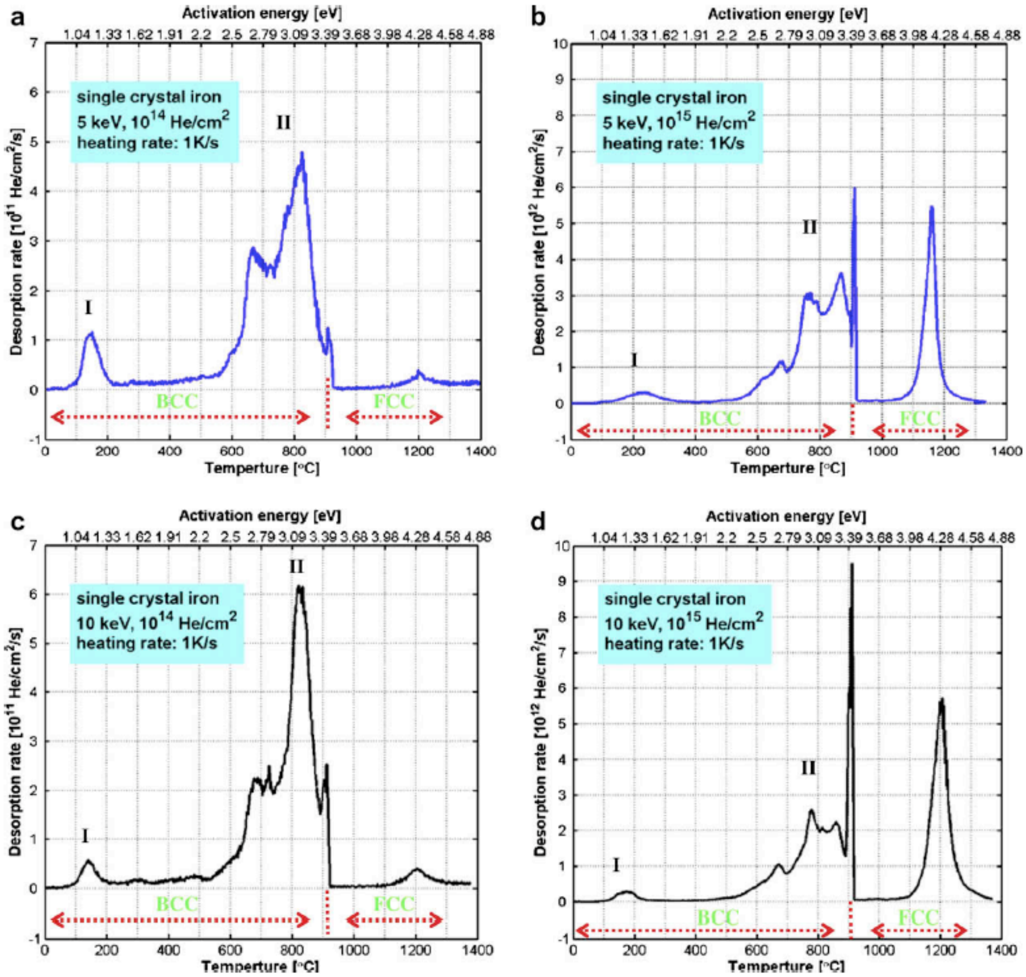

Fig.1 [22]. Desorption spectra of low purity single-crystalline iron implanted with ^{4}He at: (a) 5keV, 1x10^{14} He/cm^2; (b) 5keV, 1x10^{15} He/cm^2; (c) 10keV, 1x10^{14} He/cm^2; (d) 10keV, 1x10^{15} He/cm^2.

General features of low purity SC spectra

Fig.1 presents experimentally obtained thermal helium desorption spectra for the low purity single crystalline iron samples, which were implanted with either 5 or 10keV He ions to a fluence of 10^{14} or 10^{15} He/cm^2, during thermal annealing with a constant heating rate of 1°C/s. The data clearly show two well separated major desorption groups within the BCC temperature range (up to 912°C, where the appearance of the sharp peak marks the alpha-gamma phase transformation of iron): Group I below ~300°C and Group II from ~550°C to 912°C. Major helium releasing region is above 600°C. Further, increasing implantation fluence greatly enhances the fraction of retained helium that will not desorb until ~1200°C. The energy's difference dose not show significant discrepancy in the helium desorption spectra compared to the fluence's effect.

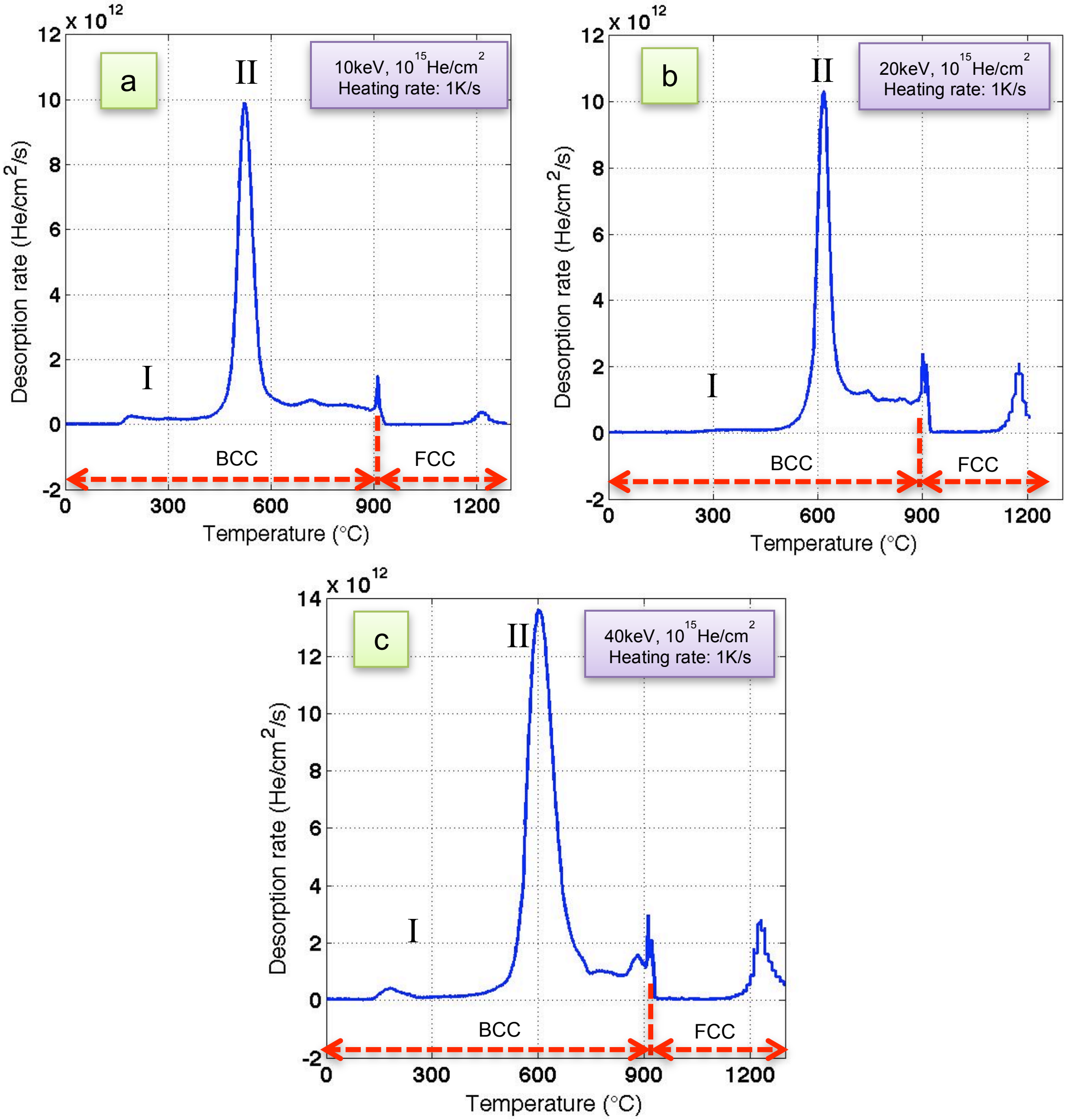

Fig. 2. Desorption spectra of high purity single-crystalline iron implanted with ^{4}He at: (a) 10keV, 1x10^{15} He/cm^2; (b) 20keV, 1x10^{15} He/cm^2; (c) 40keV, 1x10^{15} He/cm^2.

General features of high purity SC spectra

The helium desorption spectra obtained from high purity SC samples (new samples) for the three combination of implantation conditions used in the latest measurement are presented in Fig.2(a)-(c). There also exists a sharp peak for each of the spectra, which is also observed for other experimental conditions. In Ref. 21, it shows the strong evidence leading to the conclusion that this peak is primarily due to the alpha-gamma (BCC-FCC) phase transformation. Therefore, in this work, as what we did before, this peak is used to calibrate the temperature reading by setting this peak position to 912°C (the well known value of BCC-FCC phase transformation in pure iron) and utilizing a linear-correction to the other temperature values.

The new spectra also involve the existence of multiple helium release groups: Group I below ~300°C and Group II from ~450°C to 912°C. The group I here is similar to that in old spectra, although Fig.2(b) dose not show the obvious release peak around 200°C. In group II, a significantly large peak shows up around 600°C in the BCC region, which is not observed in the old spectra. From low implantation energy to higher implantation energy, the big peak switches to a position of higher temperature. Also, after the concentrated helium release in this big peak, a plateau with small fluctuations continues up to the phase transformation point. In Fig.2(c), there is an obvious peak in the plateau just before the BCC-FCC transformation. The other similar feature is that the retained helium will not be desorbed until ~1200°C. The Group II, major helium desorption region, starts from a lower temperature point (~450°C) compared to the old spectra. In general, the helium spectra of high purity SC look like more concise and less diffuse than old spectra of low purity SC.

It is reasonable to ascribe the less diffuse feature of the high purity SC spectra to the lower concentration of carbon. As mentioned earlier, the most crucial distinctions are the carbon content in the samples while the other impurities' effect can be neglected due to their substitutional positions. Carbon is known to affect the migration of self-defects in alpha iron, particularly vacancies. Some researchers [23,24] have pointed out that the effective migration energy of vacancies in BCC iron measured experimentally varies between 0.6 to 1.5 eV with higher values for specimens with higher carbon content. Some of these observations have been explained with the help of density functional theory calculations. Experiments also provide the evidence of the formation of various carbon-defect complexes, in particular carbon-vacancy clusters [25]. These can explain our experimental results from a very straight-forward point of view and approve our assumption that helium will be desorbed in a lower temperature range for the specimens with high purity due to the smaller effect of carbon.

However, how the energetics of helium and helium-vacancy clusters change cannot be seen clearly only by the experiment. Thus we next describe the use our spatially-dependent cluster dynamics code to model the new helium spectra and compare the energies applied here to the previous simulations. This will provide an overview of the energetic changes in detail.

Spatially-dependent Cluster Dynamics Model

Despite substantial effort, the overall picture of helium in BCC iron or ferritic alloys remains disconnected, incomplete and not yet self-consistent. A model that incorporates both temporally and spatially depent He and point defect diffusion, trapping and de-trapping kinetics during the implantation process and thermal annealing has been developed in our research group. The detailed ideas of this model can be found in Ref.17 and 18.

As shown in the Ref.17 and 18, the modeled desorption spectra can result in good overall agreement with the experiments by optimizing the parameters for the vacancy migration energy and the binding energy of very small helium-vacany clusters containing one to three vacancies and up to five helium atoms. The selection of optimized parameters has been guided from input from ab initio calculations, as well as from molecular dynamics and cluster dynamics simulation results.

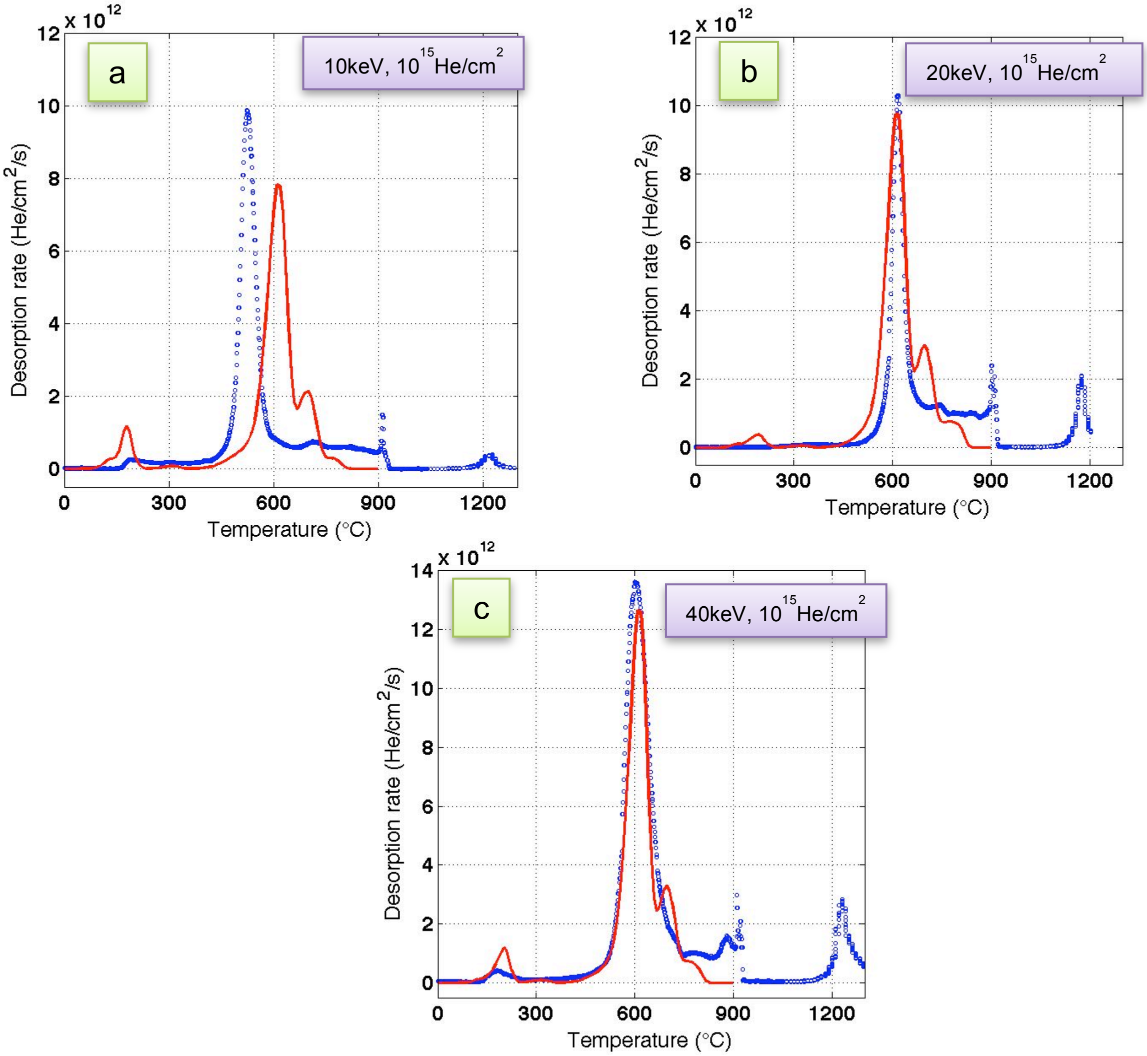

Fig.3. Experimental (open symbols) and predicted (solid lines) He desorption spectra in single crystalline iron of high purity following implantation of (a) 10keV, 1x10^{15} He/cm^2; (b) 20keV, 1x10^{15} He/cm^2; (c) 40keV, 1x10^{15} He/cm^2.

New Modeling Results

The new helium desorption spectra provides another opportunity to show the self-consistency of the code. A parameter optimization was performed, which is aimed at improving the agreement between the model and the experiments. The sold red lines in Fig. 3 represent the predicted desorption spectra with the best overall agreement with the experiments obtained so far using a different set of optimized parameters from previous model for low purity SC samples.

As shown in Fig.3, quite similar to the experimental spectra, the model reproduce the two well separated major desorption groups within the BCC temperature range, one below 300°C and the other above 450°C. Moreover, the small peaks in Group I are predicted well with a good position overlap. Although the model successfully generate the big peaks in Group II, the position for it in Fig. 3(a) does not fit the experimental result very well, shifting to the higher temperature region; while for Fig. 3(b), (c), the big peaks' positions are well produced. The other unfavorable aspect is that the plateau in the experimental spectra was not seen in the model prediction. Snuggling up to the big peaks in the modeled curves, a small peak show up and then helium desorption rate decreases abruptly. Furthermore, the model requires further improvement or optimization to better reproduce the intensities of the desorption peaks, the major peak's position for the lower implantation energy specimen as well as the plateau within Group II.

Influence of Carbon Existence on the Energetics and Kinetics

In our simulation, the migration energy of single vacancy is optimized to be the value of 0.82eV which is smaller than that used for the model of low purity samples. In the table 2, the major binding energies of helium for some important clusters are listed. It is very clear that the binding energies of the important clusters for modeling high purity samples are smaller than that for modeling low purity samples, except the value for the helium binding energy of He_2V. This situation has agreed with our experimental results and analysis. The other thing that should be mentioned is that all of the energies applied in the model are within the energy range computed by ab initio, molecular dynamics and thermodynamic.

Carbon's existence become a fetter for the mobility of helium and other mobile small clusters and induce the binding energies of helium-vacancy clusters to shift to higher values. A recent rate theory modeling work indicate that the explicit inclusion of a few small carbon-containing clusters $He_nV_mC_p$ (n,m,p=0,1,2) along with ab initio vacancy migration energy is shown to produce similar agreement with experiments to that obtained by an effective but larger vacancy migration energy without considering carbon.

Table 2. Comparison of the binding energies (eV) of helium for small He-V clusters.

Clusters	High purity	Low purity	Ab initio	MD	Thermodynamic
HeV	2.56	3.20	2.3	3.7	3.39
He_2V_2	2.98	3.17	2.75	3.8	3.17
He_2V	1.13	1.12	1.84	2.19	1.72
He_3V_2	2.25	2.45	2.07	2.81	2.29
He_4V_2	1.10	1.18	2.36	2.48	1.43
He_5V_3	1.70	2.17	n/a	3.11	1.92

Possible Mechanisms Responsible for He Desorption Peaks

The combination of the modeling and thermal desorption measurements allows identification of possible mechanisms governing helium desorption peaks. Actually, when we do the optimization of the binding energies of small clusters to fit the experimental results, the cluster distributions at different temperatures have been analyzed.

The case of high purity samples implanted by 40keV, $1x10^{15}$ He/cm^2 is taken as an example. The shrinkage of He_2V is responsible for the helium desorption peak in Group

I. The production of the big helium release peak derives from the large decrease of three small clusters, HeV, He_2V_2 and He_3V_2; the peak close to the major one within BCC region is due to dissociation of HeV. These are also our foundation to do the parameter optimization.

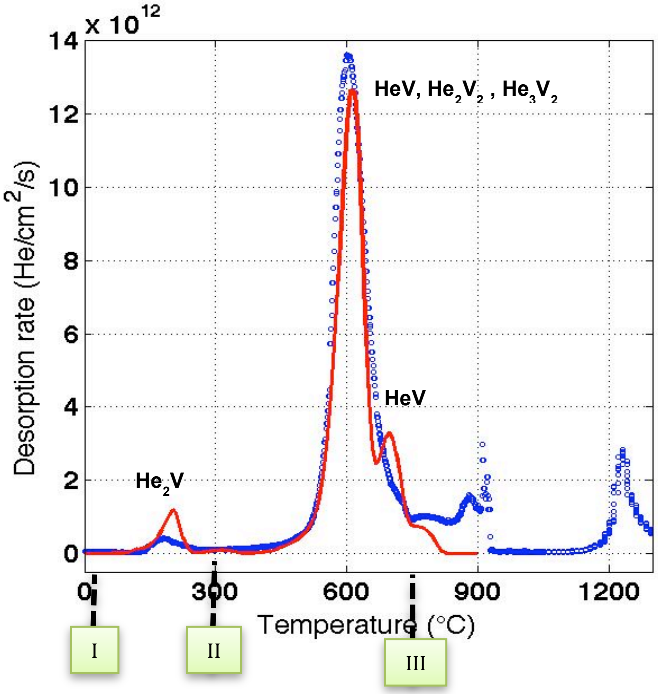

Fig.4. Experimental (open symbols) and predicted (solid lines) He desorption spectra in single crystalline iron of high purity following implantation of 40keV, $1x10^{15}$ He/cm^2; Major shrinkage of small clusters are labeled nearby the corresponding He desorption peaks; Three points of interest are marked to do the positron lifetime analysis.

Cluster Evolution Predicted by Model

While some small clusters listed above with optimized binding energies are important species to accurately model the desorption spectra, they are not the whole story. In fact, helium release is intimately coupled to the overall clusters evolution dynamics and each desorption group involves a collective action of a distribution of cluster size.

Here we picked up three interesting points covering the two major helium desorption groups within BCC region, as marked in Fig. 4, which are: I after irradiation, II at 300°C, III at 750°C.

In the model, we can obtain the cluster area concentration for various types of clusters along the depth of the sample at different temperatures. For the selected three points, the cluster concentrations come from the integration along the depth at each picked point. Fig.5 shows the cluster distribution.

From the calculation, the helium-vacancy cluster distribution is shown clearly. After irradiation by He-4, the clusters with vacancy number of 1~7 and helium number of 1~4 exist inside the sample where He_2V and HeV dominate the distribution. At point II after the first helium desorption peak, HeV occupies 75% of the total cluster concentration and the number of vacancy and helium in the cluster are 1~9 and 1~7, respectively. The clusters experience some significant changes after the second group of helium release peaks. At the third point, although HeV is still dominating, the size of the He-V clusters grow a lot with the helium number to be 24 and vacancy number up to be 18.

The change of the amount of helium-vacancy clusters can be seen clearly in the figure. The inclusion of clusters increases first because of the stronger mobility of helium and single vacancy, and then decreases due to helium desorption and recombination of interstitials and vacancies.

In the Ref.18, more simulating results of the cluster evolution for lower implantation fluence and higher implantation fluence are discussed. However, all of these predictions should be verified by transmission electron microscopy and/or positron annihilation spectroscopy measurements.

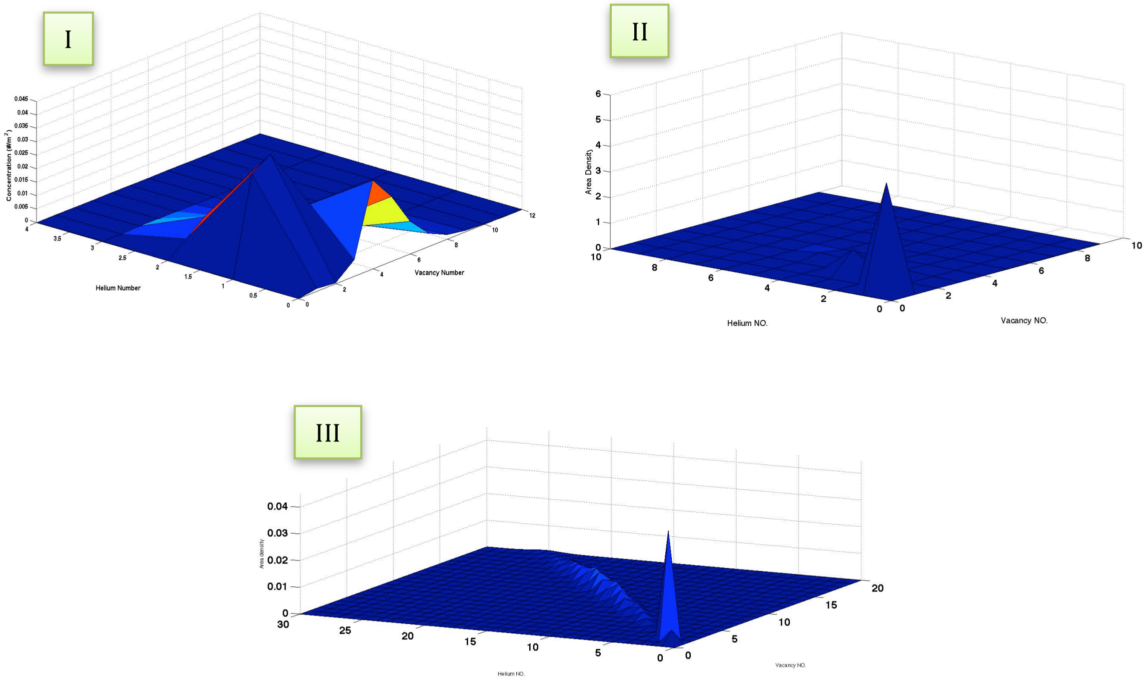

Fig. 5. Computed cluster distribution for the three selected points: I after irradiation, II at 300°C, III at 750°C.

Positron Annihilation Spectroscopy (PAS) Measurements

The use of positron annihilation spectroscopy for studies of defects in solids is mainly based on two facts. The first one is that positron may annihilate with an electron accompanying the emission of two gamma radiation who have the equivalent energy to the two particles. The second fact is that positrons injected into a material will become trapped in defects and annihilate there. By suitable measurements of the emitted gamma quanta, it is then possible to obtain useful information about the characteristics of those defects that trap positrons [26].

The positron lifetime measurements were conducted at room temperature on the Berkeley positron annihilation spectroscopy facility. Because the conventional sample-source-sample sandwich geometry was employed, an identical irradiation was given to both of the samples. The source was made from a ^{22}NaCl solution evaporated onto the surface of the samples.

The high purity SC iron samples in the implantation condition of 40keV, $1x10^{15}$ He/cm^2 were selected and two interesting points, labeled in Fig.4 are picked to do the annealing processes and PAS measurements. The annealing was performed in an ultra high vacuum environment used for THDS measurement, increasing the temperature to the set values with a heating rate of 1K/s which is the same with THDS in order to verify the cluster evolution mentioned before.

The data were analyzed by resolving two exponentials, which gave a satisfactory fit. Fig.6 shows the parameters of the lifetime spectra for the high purity SC iron as functions of the annealing temperature. As can be seen from this figure, the long lifetime, τ_2, decreases from 231ps to 214ps for the irradiation condition and 300°C annealing process; then it increases from 214ps to 278ps for the two annealing conditions, 300°C to 750°C. We can transfer the long lifetimes to the information of cluster size by comparing them to the Fig. 3 and Fig. 4 in Ref.27. The two figures show the positron lifetimes in vacancy clusters and helium-vacancy clusters in BCC iron. In our case, the positron lifetime of 231ps after irradiation represents the existence of small clusters, while the positron lifetimes in pure vacancy cluster V_4 and in helium-vacancy cluster HeV_6 are around this value of 231ps. Since it will not only one type of specie, the measured positron lifetime is a collective result. Based on this info, we can justify that the small cluster with the helium number up to 4 and vacancy number up to 8 present, conservatively. At the annealing point of 300°C, the lifetime is 213ps corresponding to V_2 or HeV_5 which means that small clusters still dominate and no large helium-vacancy cluster show up. The long lifetime for the condition of annealing at 750°C is 278ps aiming at the existence of V_{10} and/or He_2V_m(m>10). These results perfectly agree with our modeling calculations. For the mean lifetime indicated on the left in Fig.6, it has a decreasing tendency .

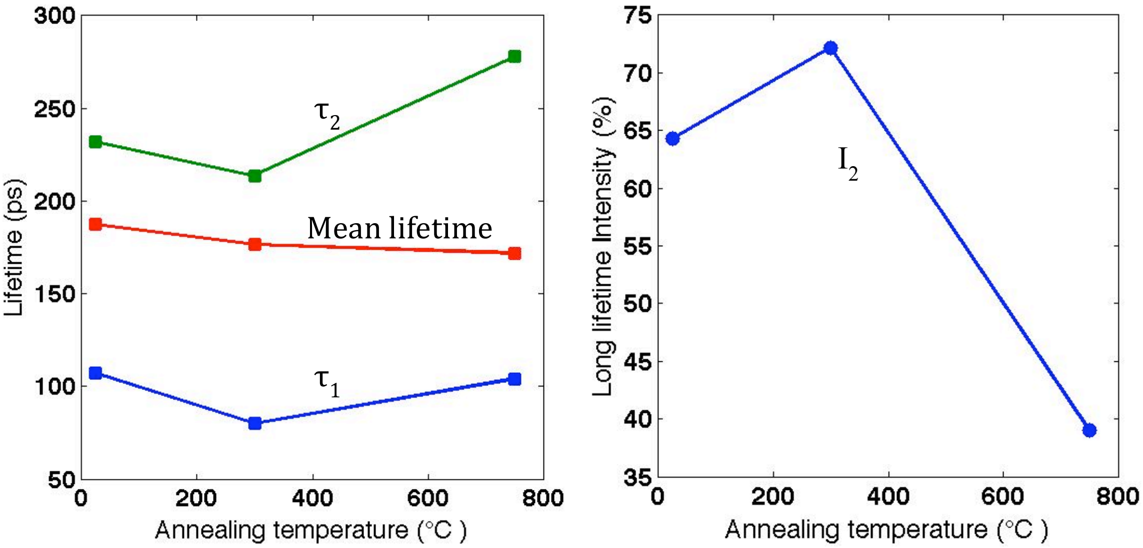

Fig.6. Two components analysis of the positron annihilation lifetime spectrum after each step of the annealing for the high purity SC irons implanted by He-4 of 40keV, $1\text{x}10^{15}$ He/cm^2.

The other important parameter is the intensity of the long positron lifetime. The intensity corresponds to the density of vacancy clusters. As shown in Fig.6, the intensity increases from 64.3% to 72.2% and then reduces to 39%. From the initial point to the 300°C annealing condition, the helium concentration grows because helium and single vacancy move fast and combine together to form helium-vacancy clusters with the temperature increasing. At this time, the helium release rate is not comparable to the formation of helium-vacancy clusters. For the 750°C annealing condition, it is located in the Group II region just after the major helium desorption. The retained helium is much less than initial condition. At this high temperature, the mobility of vacancy, helium and other small cluster is intense. The recombination of interstitials and vacancies will also induce the reduction of the clusters. These observations verify our model results in another way.

A Tentative Method to Compute the Overall Positron Lifetime

From the model calculations, we can obtain the detailed cluster distribution which can be compared to the information brought by the long positron lifetime. However, is there a straightforward way to predict the positron lifetime based on the model results?

Here, a tentative and rough method was conducted to combine the modeled helium-vacancy cluster distribution and the theoretical positron lifetime. The theoretical positron lifetime for various size of clusters are from the Fig. 3 and Fig. 4 in Ref. 27 directly or by interpolation. When the He-V cluster is big enough (e.g. He_mV_n , m>24, n>15), we assume that the positron lifetime is saturated, at a value of 308ps.

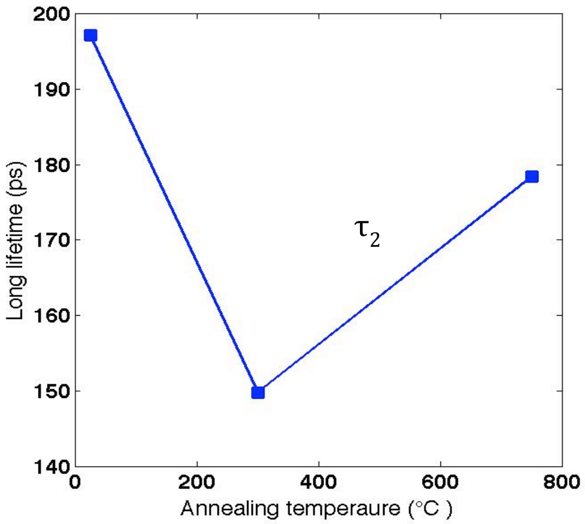

Fig.7. Calculated positron long lifetime for the three selected points.

The contribution of different clusters is based on their density fraction of the total cluster concentration. Then the contribution of each cluster shown in the model result is multiplied by the related lifetime. The sum of all of the computed values is considered the collective positron long lifetime in the defect region.

Although the method is simple, it can give a much more straightforward view of how the long lifetime of positron changes at different annealing stages. Fig.7 indicates the predicted results. As shown in the figure, the long lifetime decreases from 197ps to 149ps for the two stages of after irradiation and annealing at 300°C; then it goes up from 140ps to 178ps for the two annealing stages. The basic tendency of the curve is consistent with the experimental results. The disappointment is that the model underestimates the values of the positron lifetime and the increase value from I to II is larger than that from II to III, because the model method to calculate lifetime is simple and the samples used in the experiments are not ideally pure while some other defects exist, such as dislocations, small voids, etc. Furthermore, we are trying to develop a better way to model the measurements.

CONCLUSION

The impurities (carbon) effect on the helium desorption spectra was analyzed in details by comparing different batches of samples. The results show that the implanted helium will be released earlier for high purity single crystalline irons without more carbon's fetter. A spatially dependent cluster dynamics model is applied to reproduce the spectra which gives a overview of how the binding energies of small clusters and migration energy of vacancy change. The comparison shows that they are smaller for the high purity irons. Moreover, positron lifetime measurements are conducted for the high purity specimens at a selected implantation condition, of 40keV, $1\text{x}10^{15}$ He/cm^2. Three points were picked up to do the measurement, after irradiation, annealing at 300°C and annealing at 750°C. The PAS measurements are compared to the modeled cluster distribution at each stage. A good agreement shows up to prove the self-consistency of the model. Furthermore, a simple method to calculate the positron lifetime for different stages is indicated here and not bad results were obtained.

As to the future work, more efforts are necessary to study the impurity effects by both experiments and models. A more advanced model with He-V-C complex should be developed. For the PAS experiment and simulation, additional implantation conditions and more reliable modeling method are needed. Meanwhile, the combination of neutron irradiation and helium implantation should be done to push the research toward to the more real fusion environment.

REFERENCES

[1] H. Ullmaier, *Nucl. Fusion* **24** (1984) 1039.
[2] L. K. Mansur, M. L. Grossbeck, *J. Nucl. Mater.* **155** (1988) 130.
[3] L. K. Mansur, W. A. Coghlan, *J. Nucl. Mater.* **119** (1983) 1.
[4] H.Trinkaus, B. N. Singh, J*. Nucl. Mater.* **323** (2003) 229.
[5] K. C. Russell, *Acta Metall.* **20** (1972) 899.
[6] K. C. Russell, *Acta Metall.* **26** (1978) 1615.
[7] H. Trinkaus, *Rad. Eff. Defects in Solids* **78** (1983) 189.
[8] L. K. Mansur, E. H. Lee, P. J. Maziasz, A. P. Rowcliffe, *J. Nucl. Mater.* **141-143** (1986) 633.
[9] N. M. Ghoniem, S. Shafafat, J. M. Williams, L. K. Mansur*, J. Nucl. Mater.* **117** (1983) 96.
[10] R. E. Stoller and G. R. Odette, *J. Nucl. Mater.* **131** (1985) 118
[11] M. B. Lewis, K. Farrell, *Nucl. Instrum. Meth. Phys. Res. B* **16** (1986) 163.
[12] K. Ono, et al., J*. Nucl. Mater.* **329–333** (2004) 933.
[13] T. Ishizaki, Q. Xu, T. Yoshiie, S. Nagata, *Mater. Trans.* **45** (2004) 9.
[14] T. Iwai, Y. Ito, M. Koshimizu, *J. Nucl. Mater.* **329** (2004) 963.
[15] R. Sugano, K. Morishita, A. Kimura, *Fusion Sci. Technol.* **44** (2003) 446.
[16] R. Vassen, H. Trinkaus, P. Jung, *Phys. Rev. B* **44** (1991) 4206.
[17] D. H. Xu, B. D. Wirth, *Fusion Sci. Technol.* **56** (2009) 1064.
[18] D. H. Xu, B. D. Wirth, *J. Nucl. Mater.* **403** (2010) 184.
[19] C. Domain, C. S. Becquart, *J. Foct, Phys. Rev. B* **69** (2004) 144112.
[20] C. J. Först, J. Slycke, K. J. Van Vliet, S. Yip, *Phys. Rev. Lett.* **96** (2006) 175501.
[21] D. H. Xu, T. Bus, S. C. Glade, B. D. Wirth, *J. Nucl. Mater.* **367** (2007) 483.
[22] D. H. Xu, B. D. Wirth, *J. Nucl. Mater.* **386** (2009) 395.
[23] A. Hardouin-Duparc, A. Barbu, *Mater. Res. Soc. Symp. Proc.* **439** (1997) 509.
[24] M. Kiritani, *Ultramicroscopy* **39** (1991)135.
[25] S. Takaki, J. Fuss, H. K. U. Dedek, H. Schultz, *Radiat. Eff.* **79** (1983) 87.
[26] M. Eldrup, B. N. Singh, *J. Nucl. Mater.* **251** (1997) 132.
[27] T. Troev, E. Popov, P. Staikov, N. Nankov, *Phys. Status Solidi C 6* **11** (2009) 2373.

6.3 CLUSTER DYNAMICS MODELING OF NANO-SCALE DEFECT AGGLOMERATION IN THIN MOLYBDENUM FOILS BENCHMARKED BY IN-SITU ION IRRADIATION UNDER TEM

— Donghua Xu and Brian D. Wirth (Department of Nuclear Engineering, University of Tennessee, Knoxville, TN 37996, USA)

OBJECTIVE

Irradiation effects on materials are generally initiated by the creation of atomic scale defects and their subsequent agglomeration into nano- and larger size clusters. The objective of this study is to enhance the understanding of the defect dynamics in early stage of irradiation in structural metals through combined modeling and experiments.

SUMMARY

In a recent coordinated effort, we have studied defect cluster dynamics in nanometer-thick molybdenum foils under 1 MeV Krypton ion irradiation at 80°C through both cluster dynamics computation and in-situ TEM experiments. By making direct one-to-one comparisons with experimentally observed cluster number density and size distribution as functions of foil thickness and irradiation dose and dose rate, significant validation and optimization of the model have been conducted in terms of both physical contents (damage production mode, identities of mobile defects) and parameterization (diffusivities of mobile defects). The optimized model exhibits excellent agreement with the current set of experiments both qualitatively and quantitatively, while further validation of the model and parameterization will continue to be pursued in the future with respect to Kr ion irradiation at varied temperatures and neutron irradiations on Mo.

PROGRESS AND STATUS

Introduction

In coordination with a recent set of in-situ TEM irradiation experiments we simulated the defect dynamics in nanometer-thick molybdenum foils under 1 MeV Krypton ion irradiation at 80°C using the cluster dynamics code, PARASPACE (PARAllel SPAtially-dependent Cluster Evolution), developed by our group previously. In this report, the experimental conditions and main experimental results will be summarized first, and then detailed model validation and optimization through drawing direct comparisons with experiments will be presented. Both physical contents (damage production mode, identities of mobile defects) and parameterization (diffusivities of mobile defects) of the model will be examined in detail. Further, surface effect and additional factors that are relevant to the model or the comparison of the model with the experiments will be addressed, such as dislocation sinking effect.

Summary of Experiments

In-situ Kr^+ ion irradiation was performed at 80°C and 1 MeV ion energy using IVEM-Tandem on TEM molybdenum foils thinned to perforation in the center with a peripheral thickness around 150 nm. Each foil was irradiated at a fixed ion flux and there were totally three different fluxes, 1.6×10^{11}, 1.6×10^{10} and 1.6×10^{9} ions/cm^2/s used for all the foils. The irradiation as well as observation was performed up to a fluence of $1.5\text{x}10^{13}$ ions/cm^2 at the highest flux and $5\text{x}10^{12}$ ions/cm^2 at the two lower fluxes.

The damage production of 1 MeV Kr$^+$ in Mo was first calculated using SRIM-2008 with a displacement energy of 60 eV, assuming a Frenkel-pair production mode, which yielded an average production of 1.9 vacancies/ion/Å within the thickness range of the TEM foils. Then the nominal doses and dose rates corresponding to the above fluences and fluxes were evaluated based on the following equation:

$$\text{dose} = \frac{\Phi \times 10^8 \times \text{damage-production}}{N}, \tag{1}$$

where Φ is the fluence in ions/cm^2, the damage production is in vacancies/ion/Å obtained with SRIM, and

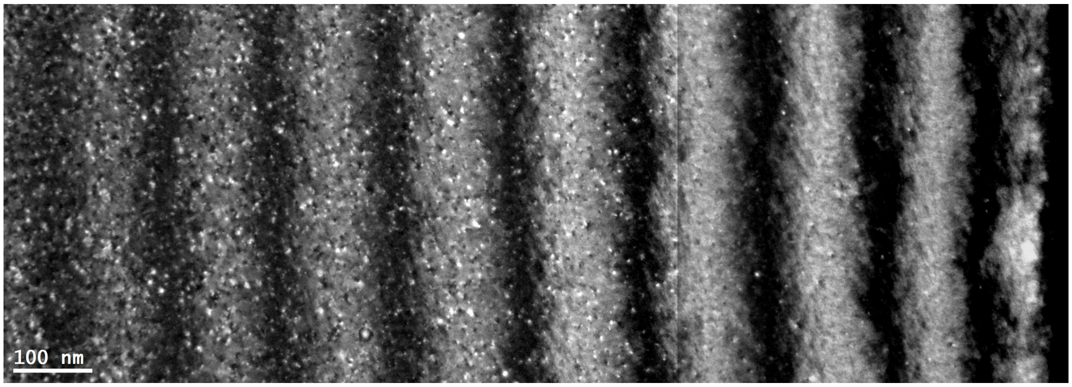

Figure 1. A composite of two plane-view dark-field micrographs showing defect structure distribution with increasing thickness (from right to left) in Mo in situ irradiated to 5×10^{12} ions/cm^2 at a flux of 1.6×10^{11} ions/cm^2/s and 80°C with 1 MeV Kr$^+$ ions.

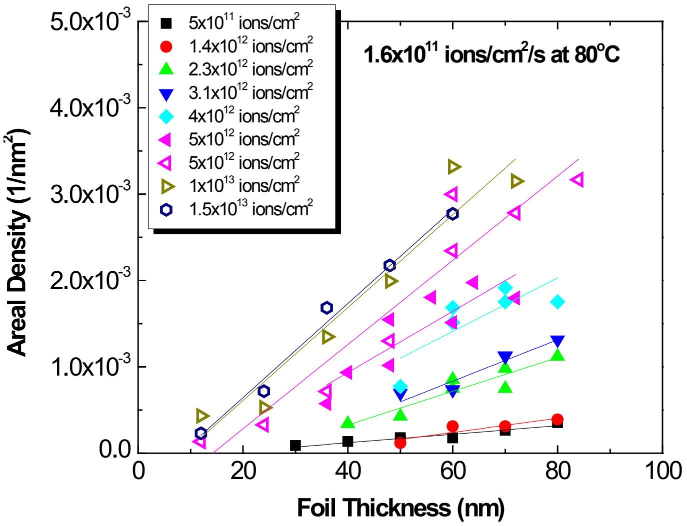

Figure 2. Areal density of defect clusters as a function of foil thickness and ion fluence in Mo in situ irradiated with 1 MeV Kr$^+$ ions at a flux of 1.6×10^{11} ions/cm^2/s at 80°C. Note that the solid symbols and the open symbols represent data from two different foils.

N is the atomic number density in atoms/cm^3. The nominal dose rates hence calculated are 5x10^{-4}, 5x10^{-5}, and 5x10^{-6} dpa/s, and the nominal finish doses are 0.045 dpa at the highest flux and 0.015 dpa at the two lower fluxes. As will be shown later, the assumed Frenkel-pair production mode is inadequate to satisfactorily reproduce the key experimental results, and intra-cascade cluster production has to be employed in the model in order to achieve good agreement with experiments. Hence, in the following text, ion fluences and fluxes rather than the doses and dose rates will be used in the comparisons between model and experiments.

During the in-situ irradiation of each foil at a selected flux, dark field (DF) micrographs (illustrated in Fig. 1) were taken at a series of selected fluences to record the defect (bright dots on the DF micrographs) evolution dynamics. Note that the fringes on a micrograph correspond to varying thicknesses (increasing from the foil center towards the foil periphery). From each DF micrograph, areal density and size distribution of defect clusters can be determined at different foil thicknesses, and overlaying such data from a series of micrographs taken from the same foil discloses the dose (fluence) dependence of the cluster evolution. Figure 2 provides such an example, showing the composite plot containing both thickness and fluence (dose) dependences of defect areal density for a foil irradiated at a flux of 1.6×10^{11} ions/cm^2/s to a fluence of 1.5×10^{13} ions/cm^2. Further, the dose rate dependence of defect evolution can be examined by comparing the above composite plots made for foils irradiated at different ion fluxes.

The defects observed are all dislocation loops and their Burgers vectors were analyzed. However, the defect character, interstitial- or vacancy-type, has yet to be determined, even though there is a reason to believe that the loops are of interstitial type.

Model Description

With 1D spatial dependence, the ODE (ordinary differential equation) system describing defect evolution changes to a PDE (partial differential equation) system, and the PDEs generally have the following generic form:

$$\frac{\partial C_i^{x_n}}{\partial t} = \varphi \times P_i(x_n) + D_i \frac{\partial^2 C_i^{x_n}}{\partial x^2} + GRT + GRE - ART - ARE \, , \tag{2}$$

where $C_i^{x_n}$ refers to the volumetric concentration (in 1/nm^3) of the *i*-th cluster at the depth position x_n (in nm), φ is ion flux (in ion/nm^2/sec), $P_i(x_n)$ is the production “probability” (in 1/ion/nm) of the *i*-th cluster by irradiation that is obtained through SRIM (combined with MD if not only Frenkel pairs are produced), D_i is the diffusivity of the *i*-th cluster, GRT is the rate of generation of the *i*-th cluster by trapping reactions ($A + B \rightarrow i$) among other clusters, GRE is the rate of generation of the *i*-th cluster by emission processes ($C \rightarrow i + B$) of other clusters, ART is the rate of annihilation of the *i*-th cluster by its trapping reaction with other clusters ($i + B \rightarrow C$), and ARE is the rate of annihilation of the *i*-th cluster by its own emission process ($i \rightarrow A + B$). The trapping (forward) and emission (backward) reaction constants are determined as follows (for a sample reaction $A + B \rightleftharpoons C$):

$$k^+ = 4\pi\left(r_A + r_B\right) \times \left(D_A + D_B\right), \tag{3}$$

and,

$$k^- = k^+ C_0 \exp\left(-\frac{E_b}{k_B T}\right), \tag{4}$$

where r_A and r_B are the trapping radii of clusters A and B typically taken as equivalent to the geometric radii of the clusters in the classical rate theory, D_A and D_B are the diffusivities, C_0 is the atomic number density of the matrix (here molybdenum) in 1/nm^3, and E_b is the binding energy of a single point defect to the cluster C (either A or B is a point defect or they both are). For trapping reactions among interstitials and/or interstitial clusters/loops k^+ and k^- are both scaled by a bias factor of 1.2. The diffusivity of a defect/cluster depends on the temperature according to Arrhenius law, i.e.,

$$D = D_0 \exp\left(-\frac{E_m}{k_B T}\right) \tag{5}$$

where D_0 is a prefactor and E_m is the migration energy. The monomer binding energy E_b is defined by the reduction in the summed formation energy (enthalpy, E_f) after binding occurs, for example, $E_b^{I_{10}} = E_f^{I} + E_f^{I_9} - E_f^{I_{10}}$. From Eqs. 2-5 it is evident that the diffusivities of various clusters, as determined by D_0 and E_m, play a very important role in the cluster evolution by affecting the trapping and emission kinetics within a certain depth grid as well as the diffusion kinetics across neighboring grids. The binding energies represent thermal stability of the clusters and determine (in combination with diffusivities) their emission rates, and their role in cluster evolution is limited at low temperature such as in the current study but may become significant at relatively high temperatures.

Initially, thermal equilibrium concentrations are set for point defects, i.e., single interstitial and single vacancy, and the concentrations of all other defects/clusters are set to zero at all depth grids. Note that values of 3 eV and 7 eV were used for the formation energy of single vacancy and single interstitial in Mo, respectively, similar to those reported from experiments and/or ab initio calculations. These E_f values correspond to extremely small thermal equilibrium concentrations of point defects. During the entire PDE solving and time integration process, the concentrations of all defects/clusters except the point defects are maintained at zero on the two surfaces of the foil whereas the point defects are maintained at their thermal equilibrium on the surfaces. With this boundary condition, the foil surfaces are treated explicitly as black sinks and thus the surface sinking effect is directly accounted for without having to use empirical formulations.

RESULTS

In this section, model calculations based on different assumptions with respect to damage production mode (Frenkel pair mode or intracascade cluster production mode) and mobile clusters (number of mobile clusters and their mobilities) will be compared against each other and directly against experiments. It will be shown that the simple model assumptions lead to large deviation from experiments unless abnormal parameter values are used, whereas more sophisticated model assumptions are able to produce excellent agreement with key experimental results after reasonable small amount of parameter optimization.

Numerous previous studies, both computational and experimental, have suggested interstitial clusters (I_n) exist in the form of two-dimensional loops in irradiated BCC metals. Hence their sizes are determined as:

$$d = 2r = 2\times\left(\frac{nV_a}{\pi b}\right)^{1/2}, \tag{6}$$

where d is the diameter, r is the radius, V_a is the atomic volume of Mo, and b is the Burgers vector length. The present experiments revealed two types of loops with Burgers vectors 1/2<111> and <100>, constituting an average of 77% and 23% of the total loop population, respectively. In the current modeling, we do not distinguish the two types of loops, and the Burgers vector length of 1/2<111> is used for all I_n clusters. Note that the diameter values corresponding to the two different Burgers vectors for a given n only differ by a factor of 1.07.

Vacancy clusters (V_n) have been frequently observed in previous studies as three-dimensional voids in BCC metals, in which case their sizes are determined as:

$$d = 2r = 2\times\left(\frac{3nV_a}{4\pi}\right)^{1/3}. \tag{7}$$

Frenkel Pair Production Mode and Only Single Interstitial & Single Vacancy Mobile

Frenkel pair production is a simple damage mode in which equal numbers of single interstitials and single vacancies are produced by irradiation. While it is often considered a good depiction of electron irradiations, it may not be sufficient to fully describe ion irradiations, particularly when high-energy ions are involved. In this subsection and the next we first explore the possibility of reproducing the experiments with this simple production mode.

Resistivity recovery experiments have been performed previously to determine the migration energies of single interstitials and single vacancies in Mo. Interstitial migration energy E_m^I was reported to be 0.083 eV based on a 2nd order rate equation fit to the recovery stage at 33~39 K, and values ranging from 1.35 to 1.89 eV were reported for vacancy migration energy E_m^V based on the slope change in the recovery stage at 520 K with an assumed sink density. These values provide at least a good estimate, although their accuracy may be worthy of more experimental verification, particularly the vacancy migration energy which may depend on material purity and the assumptions used to analyze the recovery data at 520 K where various vacancy and interstitial clusters may co-exist.

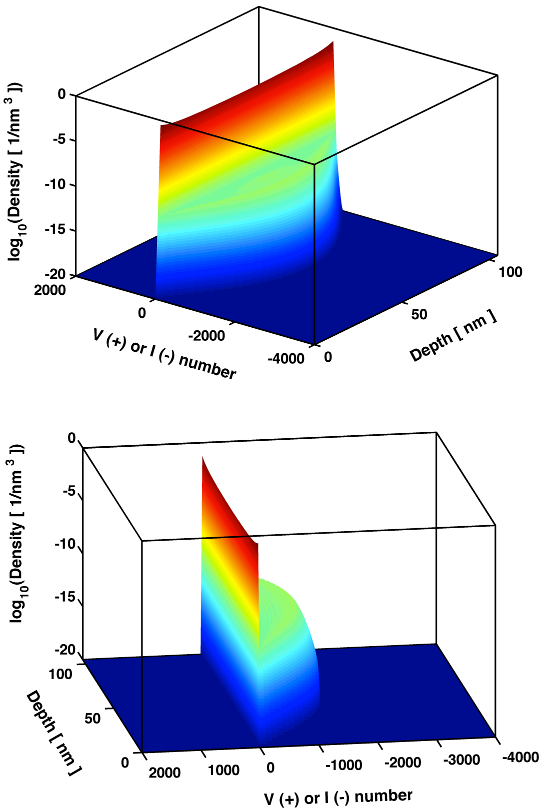

Figure 3. Model calculated volumetric density/concentration of all defect clusters plotted versus cluster composition and depth at the fluence of 5×10^{12} ions/cm^2 for a 105 nm thick foil assuming Frenkel pair production mode with only single interstitial ($E_m^I = 0.1$ eV) and single vacancy ($E_m^V = 1.3$ eV) being mobile at a flux of 1.6×10^{11} ions/cm^2/s.

We started our model calculation with $E_m^I = 0.1$ eV and $E_m^V = 1.3$ eV and focused on a 105 nm thick foil and an ion flux of 1.6×10^{11} ions/cm^2/s. Figure 3 illustrates the direct output of all the model calculations in this study, i.e., the volumetric density/concentration of all defect clusters at all depth grids and all doses/fluences. From Fig. 3 it can be seen that interstitials undergo significant clustering while the vacancies do not. This is because the interstitials are highly mobile but the vacancies are essentially immobile at 80°C, and this is consistently observed in the present study as long as a value above ~0.9 eV is used for E_m^V. The output from the model can be easily analyzed to extract the quantities that are measurable/observable in the experiments so that direct comparisons can be drawn between the model and the experiments.

It is important to note that not all the defects in the model, but only those with a diameter exceeding the TEM resolution limit, can be observed in experiments. The resolution limit in such TEM experiments varies slightly with material conditions as well as TEM operating conditions (e.g., plane-view vs. 3D tomography), in the range of 1.3~1.5 nm in the present study.

The areal density of *observable* interstitial loops obtained by applying a resolution limit of 1.5 nm to the model results for the 105 nm thick foil with $E_m^I = 0.1$ eV and $E_m^V = 1.3$ eV is plotted versus nominal dose in Fig. 4 (a). The density increases linearly until the fluence of 3×10^{11} ions/cm^2 after which it shows a tendency to saturate while slowly increasing. By the fluence of 5×10^{12} ions/cm^2 the modeled areal density reaches ~8×10^{-7} /nm^2. There was no experimental data for the 105 nm foil thickness at the same flux. However, the projection from the experimental data for other foil thicknesses at the fluence of 5×10^{12} ions/cm^2 (see Fig. 2) indicates an areal density of a few times 10^{-3} /nm^2 for a 105 nm thick foil, which is higher than the model prediction by four orders of magnitude. The size distribution of observable interstitial loops at the fluence of 5×10^{12} ions/cm^2 analyzed from this set of model results using the same resolution limit of 1.5 nm is shown in Fig. 5 (a). The modeled distribution shows a peak in the 8~8.5 nm size interval. In the experiments, nevertheless, the vast majority of observed loops have sizes less than 4 nm at the same nominal dose and same ion flux for foil thicknesses from 24 nm to 80 nm, and the size distribution shows only slight dependence on the foil thickness. It is thus clear that the model, with the assumed production mode and migration energies, over-predicts the growth of the loops. The under-prediction of loop density and over-prediction of loop growth both seem to suggest that the assumed mobility of interstitials is too high, since higher mobility is expected to enhance all the kinetic processes, including recombination with virtually immobile vacancies, diffusing and sinking to surfaces, and clustering with other interstitials. Thus, one is tempted to think that it is possible to resolve the large discrepancy between the model and the experiments by increasing E_m^I without changing the assumed Frenkel pair production mode.

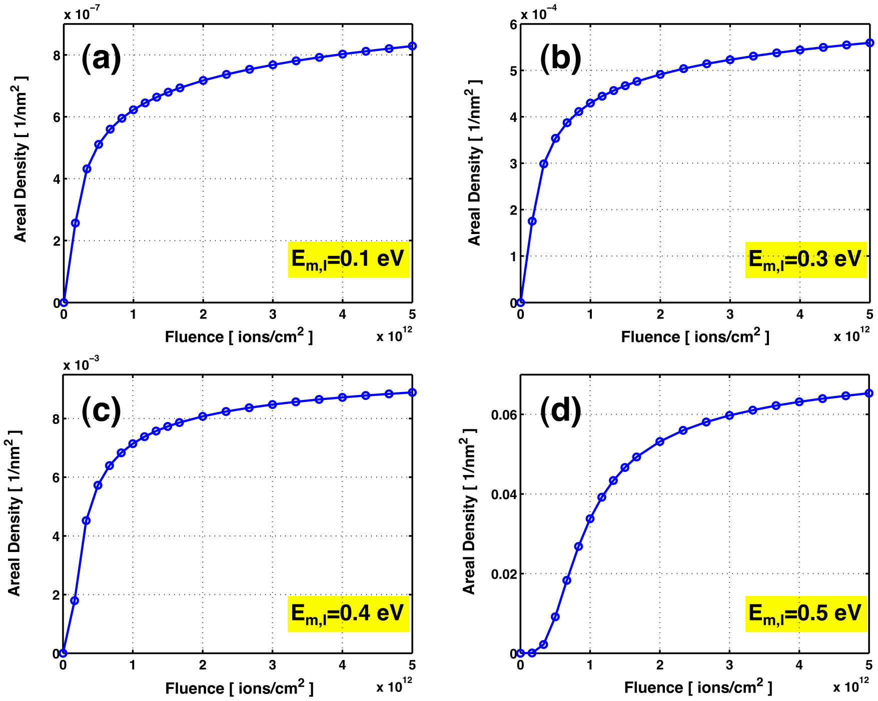

Figure 4. Model-predicted areal density of observable defect clusters (diameter no less than 1.5 nm) as a function of dose for a 105 nm thick foil assuming Frenkel pair production mode with only single interstitial ($E_m^I = 0.1,\ 0.3,\ 0.4, 0.5$ eV) and single vacancy ($E_m^V = 1.3$ eV) mobile at a flux of 1.6×10^{11} ions/cm^2/s.

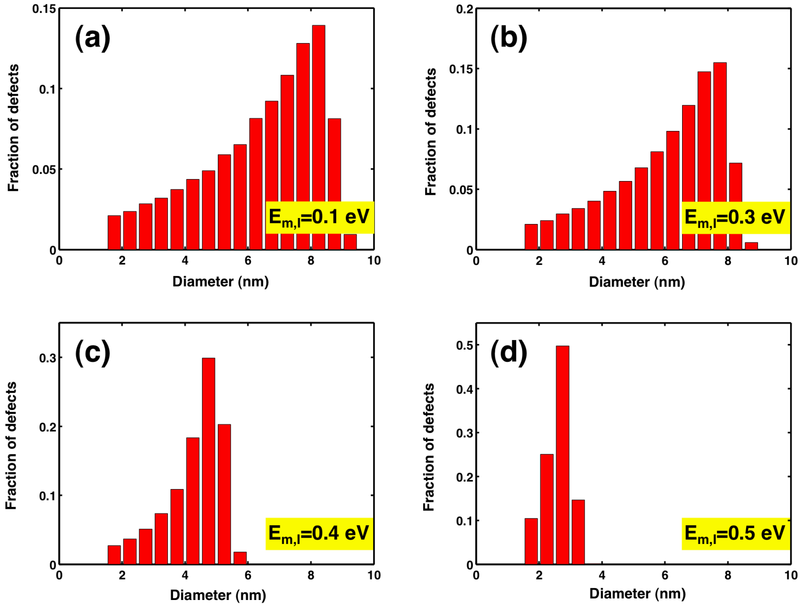

Figure 5. Model-predicted size distribution of observable defect clusters (diameter no less than 1.5 nm) at the fluence of 5×10^{12} *ions/cm*^{2} *for a 105 nm thick foil assuming Frenkel pair production mode with only single interstitial (*$E_m^I = 0.1,\ 0.3,\ 0.4, 0.5$ *eV) and single vacancy (*$E_m^V = 1.3$ *eV) mobile at a flux of 1.6×10*^{11} *ions/cm*^{2}*/s.*

Indeed, as shown in Fig. 4 (b-d), when E_m^I is increased from 0.1 eV to 0.3, 0.4 and 0.5 eV, the model-predicted areal density of observable loops increases by orders of magnitude. With $E_m^I = 0.4$ eV, the model predicts an areal density on the same order of magnitude as observed in the experiments, and with $E_m^I = 0.5$ eV the model predicts an areal density even higher than observed in the experiments by one order of magnitude. Meanwhile, the model-predicted size distribution also shifts to smaller loop sizes with increasing E_m^I, and, in particular, with $E_m^I = 0.5$ eV the model-predicted sizes fall very close to the sizes observed in the experiments. However, the 0.4 or 0.5 eV migration energy of interstitials that has to be used in order to bring the model close to the experiments is apparently too high to be realistic, given that a recovery stage occurs at 33~39 K in Mo following electron irradiation. Therefore, it can be concluded that either the assumption of Frenkel pair production or the assumption of only single interstitial and single vacancy being mobile is incorrect.

Frenkel Pair Production Mode and All Interstitial Loops Mobile

It has been consistently seen in many MD simulations that interstitial loops containing a few to several hundreds of single interstitials in BCC metals are highly mobile with nearly size-independent migration energies close to or even lower than the single interstitial migration energy E_m^I. In BCC iron, for example, MD simulations performed by Marian et al. disclosed a migration energy of I_n that initially decreases but quickly stabilizes with increasing n, following an expression of $E_m(n) = 0.06 + 0.07n^{-1.3}$ (eV), and diffusivity pre-factors expressed as $D_0(n) = 8.98\times10^{11} n^{-0.61}$ (nm^2/sec). Quite differently, however, ab initio calculations in BCC iron performed by Fu and Willaime revealed increasing migration energies from single interstitial to di-interstitial cluster, and the ab initio values, 0.34 and 0.42 eV, are very close to the E_m^I determined in earlier resistivity recovery studies in iron. The mobilities of other interstitial clusters containing three or more interstitials were not examined in the ab initio calculations unfortunately. More recently, in a TEM experimental study Arakawa et al. observed and analyzed the motion of interstitial loops in BCC iron containing thousands of single interstitials, and reported a size-independent migration energy of 1.3 eV for all the observed loops and pre-factors in the form $D_0(n) = (2.3 \pm 0.3) \times 10^{15} n^{-(0.80 \pm 0.02)}$ (nm^2/sec). Arakawa et al. explained this large migration energy value as the result of combined kink formation and impurity dragging mechanisms, and argued that by assuming typical values of impurity migration energies the migration energy of "naked" loops could be deduced to be ~0.4 eV, which is close to the values determined for I and I_2 in ab initio calculations and for I in resistivity recovery experiments.

In Mo, there have not been such intensive studies on the mobilities of interstitial clusters/loops. However, considering the structural similarity of Mo and BCC iron, it is not unlikely that interstitial clusters/loops in Mo also have mobilities, and that their mobilities, particularly for large clusters, are also subject to impurity dragging effect. It is thus interesting to examine how the model results presented in the last subsection may be modified by the cluster/loop mobilities. Table 1 lists the first set of mobility data we chose on an empirical basis for interstitial clusters/loops in Mo by considering the various studies in BCC iron mentioned above. In this set, loops containing more than 7 interstitials are assigned a constant migration energy of 1 eV and pre-factors with a power-law size dependence, whereas the migration energies and pre-factors of small clusters/loops are assigned in a way that gradually connects the single interstitial migration energy and pre-factor to those of large loops $I_{n>7}$.

Fig. 6 (a) and Fig. 7 (a) show the effects of the cluster/loop mobilities, with values listed in Table 1, on the areal density and size distribution, respectively, of observable loops for the 105 nm thick foil at the flux of 1.6×10^{11} ions/cm^2/s with $E_m^I = 0.4$ eV and $E_m^V = 1.3$ eV. By including the cluster/loop mobilities, the areal density saturates faster, at lower doses/fluences, than in the previous case where only single interstitial and single vacancy were considered mobile, and the new saturation value is lower than the previous value by almost three orders of magnitude. The sizes of the most populous loops shift from the bin at 4.5~5.0 nm to the bin at 8.5~9.0 nm, indicating significantly enhanced loop growth. Fig. 6 (b) and Fig. 7 (b) show similar effects of the cluster/loop mobilities with $E_m^I = 0.5$ eV. Although the effects in this case appear not so dramatic as in the case with $E_m^I = 0.4$ eV due to the fact that the different value of E_m^I leads to different migration energies of small clusters I_2~I_7 in the initial mobility set as shown in Table 1, the over one order of magnitude reduction in the saturation areal density by cluster/loop mobility is still significant.

Table 1. Initial set of interstitial cluster/loop mobility data

	$I_{n>7}$	I_7	I_6	I_5	I_4	I_3	I_2	I
D_0 (nm^2/sec)	$10^{12} \times n^{-0.7}$	$10^{12}/7$	$10^{12}/6$	$10^{12}/5$	$10^{12}/4$	$10^{12}/3$	$10^{12}/2$	10^{12}
E_m (eV)	1	E_m^I +0.5	E_m^I +0.35	E_m^I +0.15	E_m^I -0.05	E_m^I -0.05	E_m^I +0.05	E_m^I (varied)

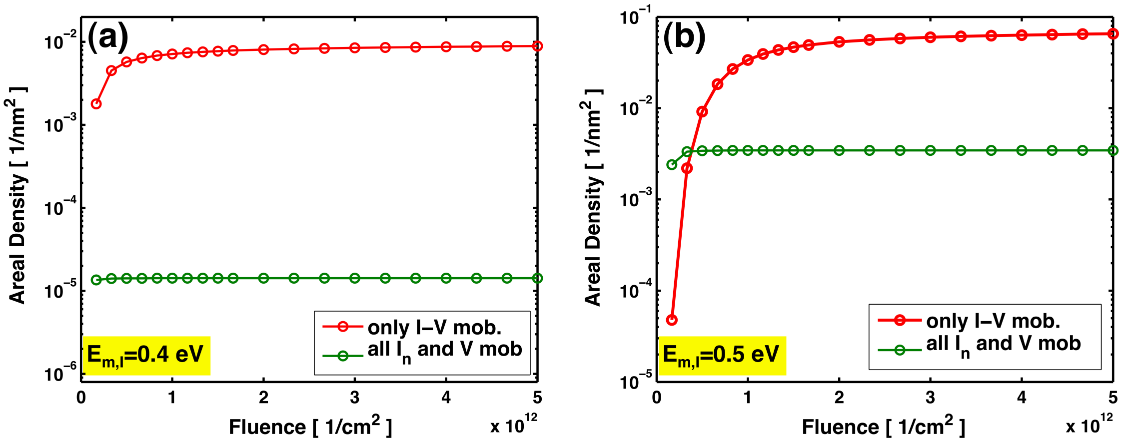

Figure 6. Comparison, for $E_m^I = 0.4,\ 0.5$ eV, of areal density of observable loops (diameter no less than 1.5 nm) predicted by two sets of model calculations for a 105 nm thick foil at a flux of 1.6×10^{11} ions/cm^2/s, both assuming Frenkel pair production mode, but one set considering only single interstitial and single vacancy mobile and the other considering all interstitial clusters/loops (with mobilities listed in Table 1) and single vacancy mobile.

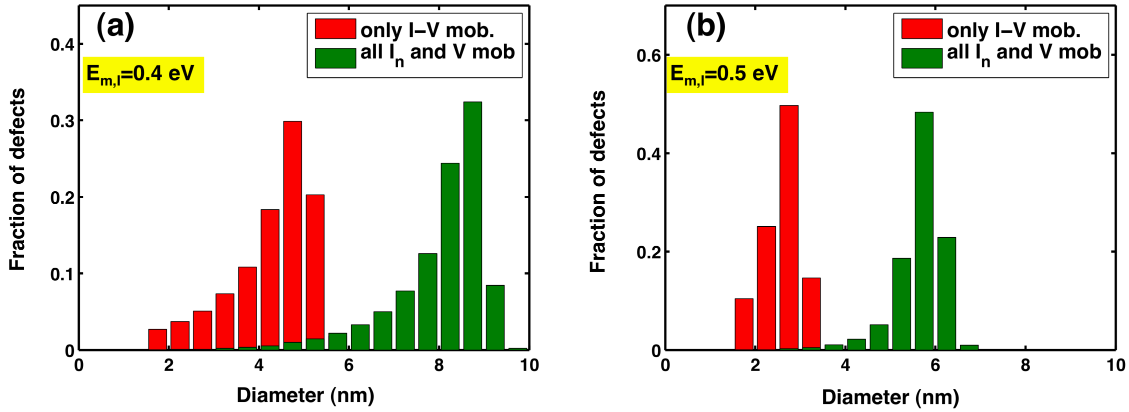

Figure 7. Comparison, for $E_m^I = 0.4,\ 0.5$ eV, of size distribution of observable loops (diameter no less than 1.5 nm) predicted by two sets of model calculations for a 105 nm thick foil at the fluence of 5×10^{12} ions/cm^2 with a flux of 1.6×10^{11} ions/cm^2/s, both assuming Frenkel pair production mode, but one set considering only single interstitial and single vacancy mobile and the other considering all interstitial clusters/loops (with mobilities listed in Table 1) and single vacancy mobile.

These effects of including cluster/loop mobilities can be understood in the same way as the effects of lowering E_m^I in the previous subsection. A case where only single interstitial and single vacancy are considered to be mobile, as in the previous subsection, is equivalent to a case in which the clusters/loops are mobile but with virtually zero mobilities (due to too high migration energies to be thermally activated, for example). From zero to the values listed in Table 1, the mobilities of interstitial clusters/loops are significantly enhanced, which leads to more severe loss of observable loops through capturing vacancies and thus shrinking, and diffusing and sinking to surfaces, while they form larger clusters by capturing single interstitials and other interstitial clusters/loops at a faster pace. Evidently, including the cluster/loop mobilities, regardless of their values chosen to use, can only aggravate rather than resolve the problem of under-predicting the areal density and over-predicting the loop sizes of the model based on Frenkel pair production assumption with reasonable migration energies of single interstitial and single vacancy.

Intra-cascade Cluster Production Mode and All Interstitial Loops Mobile

SRIM analysis shows that ~30% of all the PKAs induced by 1 MeV Kr^+ in Mo possess kinetic energies above 1 keV. Previous MD simulations on cascades in BCC metals showed that PKAs with a few keV or more kinetic energy can directly produce small interstitial and vacancy clusters rather than Frenkel pairs. There have unfortunately not been such MD studies in Mo, hence in this study we used the intra-cascade cluster production probabilities from MD simulations in BCC iron by Stoller et al. as a first order approximation for Mo with recognition that the true values in Mo may be somewhat different. Introducing the intra-cascade cluster production probabilities to the cases discussed earlier with the same initial set of cluster/loop mobilities as listed in Table 1 resulted in such dramatic increase in the areal density of observable loops and reduction in the cluster sizes that the previous under-prediction of density and over-prediction of size were excessively corrected, even when a low migration energy of 0.1 eV was used for single interstitial. This suggested that the small clusters being produced by cascades might have higher mobilities than those listed in Table 1. Therefore, optimization of the mobility parameters was carried out. Table 2 lists the currently achieved set of mobilities that have produced excellent agreement of the model with the key experimental results as to be shown in the following.

Figures 8-10 compare the areal densities of observable loops obtained in the in-situ experiments with those predicted by the model with intra-cascade cluster production and the optimized mobilities of clusters/loops, in foils of various thicknesses irradiated to various fluences at three ion fluxes, 1.6×10^{11} (Fig. 8), 1.6×10^{10} (Fig. 9) and 1.6×10^{9} (Fig. 10) ions/cm^2/s. Note that these density comparisons are made on the linear scale rather than the logarithmic scale typically used in rate theory modeling. For such close and detailed comparisons, a more realistic resolution limit of 1.3 nm that is slightly lower than the 1.5 nm in the previous subsections was used based on the consideration that the TEM image contrast of a dislocation loop produced by the strain field is always slightly larger than the actual loop size. Further, in the TEM experiments, for a given imaging condition (reflection vector) there were always loops with observable sizes falling out of contrast because of the $g\cdot b = 0$ extinction rule. Based on the detailed Burgers vector analysis, the difference between the resolved areal densities using the fixed g=110 (for all dark field images) and the actual areal densities was estimated to be a factor of 1.9. Therefore, to compare with experimental densities, the model-predicted densities were reduced by the factor of 1.9.

As can be seen in Figs. 8-10, the experiments and the optimized model show the same qualitative trends of the areal density with respect to varying ion fluence, foil thickness and ion flux. Specifically, they both show that the areal density of observable loops increases with increasing ion fluence and foil thickness, that for a fixed foil thickness the areal density tends to saturate as fluence increases, and that for a fixed foil thickness at a given ion fluence the areal density of observable loops is lower when a lower ion flux is used for irradiation.

Figure 8 (a) includes experimental data from two different foils irradiated at the same flux of 1.6×10^{11} ions/cm^2/s. The data from the two foils at a common fluence of 5×10^{12} ions/cm^2 indicate the statistical error/scattering in the experimental results. In view of this scattering and the linear scale of the comparisons, the model predicted areal densities as displayed in Figs. 8-10 can be regarded in excellent *quantitative* agreement with the experimental measurements.

Table 2. Optimized mobility set for interstitial clusters/loops and single vacancy.

	$I_{n>20}$	$I_{11\sim20}$	$I_{1\sim10}$	V
D_0 (nm^2/sec)	$2\times10^{11}n^{-0.7}$	$2\times10^{11}/n$		2×10^{11}
E_m (eV)	1.1	Linear-space (0.1 to 0.8)	0.1	0.9

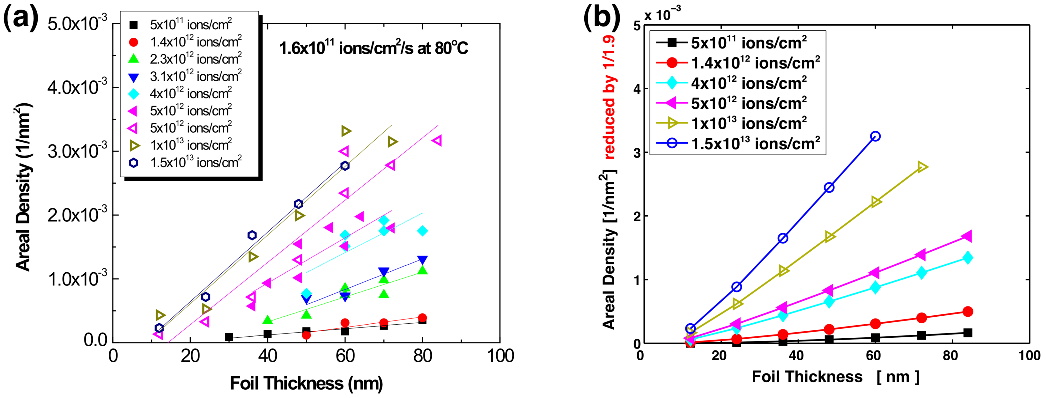

Figure 8. Experimental (a) and model-predicted (b) areal densities of observable loops (diameter no less than 1.3 nm) in foils of various thicknesses irradiated at the ion flux of $1.6{\times}10^{11}$ ions/cm^2/s to various fluences. The model adopted intra-cascade cluster damage production mode and interstitial clusters/loops mobilities listed in Table 2.

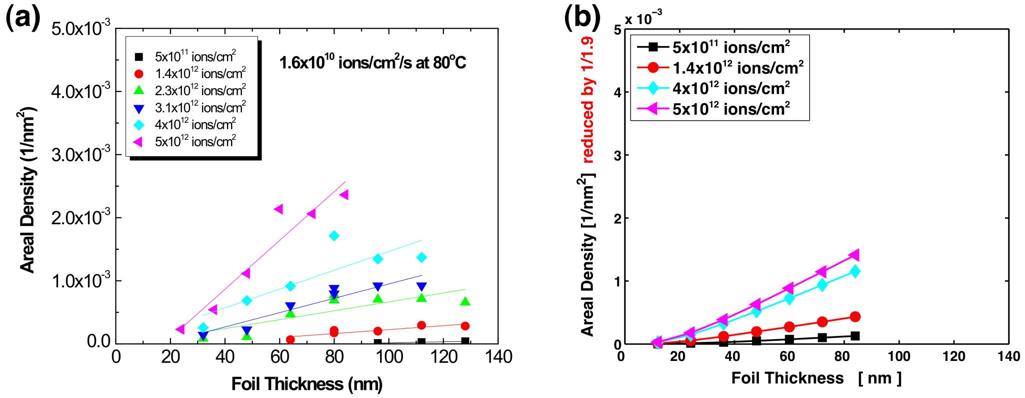

Figure 9. Experimental (a) and model-predicted (b) areal densities of observable loops (diameter no less than 1.3 nm) in foils of various thicknesses irradiated at the ion flux of $1.6{\times}10^{10}$ ions/cm^2/s to various fluences. The model adopted intra-cascade cluster damage production mode and interstitial clusters/loops mobilities listed in Table 2.

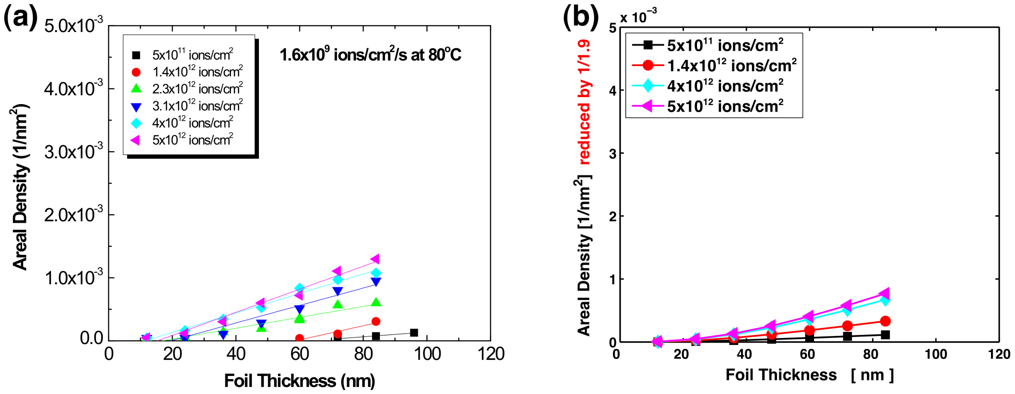

Figure 10. Experimental (a) and model-predicted (b) areal densities of observable loops (diameter no less than 1.3 nm) in foils of various thicknesses irradiated at the ion flux of 1.6×10^9 ions/cm^2/s to various fluences. The model adopted intra-cascade cluster damage production mode and interstitial clusters/loops mobilities listed in Table 2.

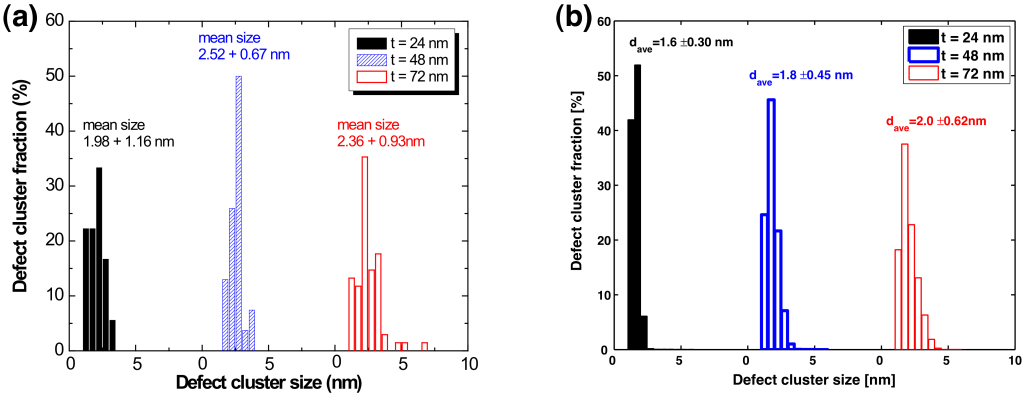

Figure 11. Experimental (a) and model-predicted (b) size distributions of observable loops (diameter no less than 1.3 nm) in foils of various thicknesses irradiated at the ion flux of 1.6×10^{11} ions/cm^2/s to the fluence of 5×10^{12} ions/cm^2. The model adopted intra-cascade cluster damage production mode and interstitial clusters/loops mobilities listed in Table 2.

Further, the size distributions of observable loops obtained in the experiments are compared with those predicted by the optimized model in Figure 11 for foils of three thicknesses, 24, 48, 72 nm, irradiated at the ion flux of 1.6×10^{11} ions/cm^2/s to the fluence of 5×10^{12} ions/cm^2. The model size distributions were obtained with a resolution limit of 1.3 nm, same as for the areal densities in the above. Despite some evident statistical scattering in the experimental size distributions, both the experiments and the model indicate that the size distribution broadens towards larger sizes as the foil thickness increases.

CONCLUSIONS

Nano-scale defect cluster dynamics in thin molybdenum foils under 1 MeV Krypton ion irradiation at 80°C was studied through both in-situ TEM irradiation experiments and coordinated cluster dynamics modeling. The in-situ TEM experiments have provided excellent references for comparing and validating different model assumptions (damage production mode, number of mobile defects/clusters) and for optimizing key kinetic parameters (defect mobilities). The main conclusions of the modeling are: Simple Frenkel pair damage mode with the assumption of only single interstitial and single vacancy being mobile is unable to account for key experimental observations, namely, defect areal density and size distribution, without introducing unrealistic mobility of single interstitials that significantly contradicts previous resistivity recovery experiments.

Introducing the mobilities of interstitial clusters/loops to the model based on simple Frenkel pair damage mode enlarges the discrepancy between the model and the experiments, regardless of the values chosen for the cluster/loop mobilities.

The model based on intra-cascade cluster production mode, with reasonable parameter optimization, generates excellent agreement with the experiments, both qualitatively and quantitatively, in terms of defect density and size distribution and their dose (fluence), dose rate (flux), and foil thickness dependencies.

8.1 Design of the Low Temperature DCT Experiment — M. A. Sokolov, J. McDuffee, D. Heatherly, (Oak Ridge National Laboratory)

OBJECTIVE

The low-temperature DCT experiment will provide F82H fracture toughness data in the high irradiation hardening regime. These data will be compared to data on specimens with other geometries, to calibrate effect of specimen size and geometry on fracture toughness parameters in material with a high level of irradiation hardening.

SUMMARY

An experiment has been designed, fabricated and assembled to irradiate disk compact tension (DCT) specimens of F82H in the flux trap of the High Flux Isotope Reactor (HFIR). Twelve DCT specimens with an outer diameter of 12.5 mm are exposed directly to HFIR coolant flow. The specimens are separated by perforated spacers to ensure cooling flow to the upper and lower surfaces of the specimens. Another experiment will use a perforated capsule to irradiate bend bar and tensile specimens to supplement this irradiation experiment, and provide the other specimen geometries for comparison with the DCT specimen data.

PROGRESS AND STATUS

Introduction

The fracture toughness response to high dose irradiation is a key factor in selecting ferritic-martensitic steel for fusion application. A large number of 3-point bend and DC(T) specimens of F82H RAFM steel were irradiated at 250-500°C in capsules RB11, RB12, JP26 and JP-27 to doses from 3.5 to 22 dpa. These specimens were tested in the hot cell and results are summarized in [1]. These irradiation studies rely on the ability of small specimens to adequately measure irradiation-induced shift in transition fracture toughness. Disk-shaped specimens with diameter 12.5 mm remain the largest fracture toughness specimen that can be irradiated in HFIR experiments. In capsules RB11 and RB12, both DC(T) and bend bars were irradiated up to 5 dpa. Results of these experiments indicated that for irradiation up to 5 dpa, shifts of transition fracture toughness temperature, T_o, are comparable for the two specimen types [1]. However, as goals and interests of the program evolve toward high-dose irradiation, the irradiation experiments are shifting to use of target capsules like JP26 and JP27 and rabbit capsules. Current target and rabbit capsule designs cannot accommodate DC(T) specimens. Thus, we have to rely on use of small 3-point bend specimens for post-irradiation fracture toughness measurement. Because of their small size, data from these specimens are evaluated using statistical, weakest-link, based size adjustments as well as constraint based adjustments. The statistical size adjustment is derived from the Weibul distribution function based on crack length and the widely used Master Curve methodology. The constraint corrections are volume based adjustments. The most commonly applied constraint adjustment for F82H data is the model developed by UCSB. However, the latest development of the UCSB model raises concerns about the validity of applying the constraint adjustment to materials with a high degree of hardening caused by irradiation [2]. That may make the small 3-point bend fracture toughness specimens unusable in high doses experiments.

The goal of this and the companion experiment is to irradiate large DC(T) and small 3-point bend specimens for one cycle (~1.6 dpa) at HFIR coolant temperature. This low-temperature irradiation will insure a high degree of hardening even at relatively low dose thus providing experimental data on the validity of using small bend bars to measure the fracture toughness shift as large specimens after high irradiation-induced hardening. The data can be used for any needed potential tuning of the UCSB constraint model.

Specimen Design and Preparation

Figure 1 shows the DCT specimen design. The specimen has an outer diameter of 12.5 mm (0.492 in) and a 4.62 mm thickness (0.182 in). Fracture toughness and tensile specimens were machined out of broken halves of previously tested 1T C(T) specimens. Figure 2 provides the schematic layout of specimens that were machined for this and the companion experiment.

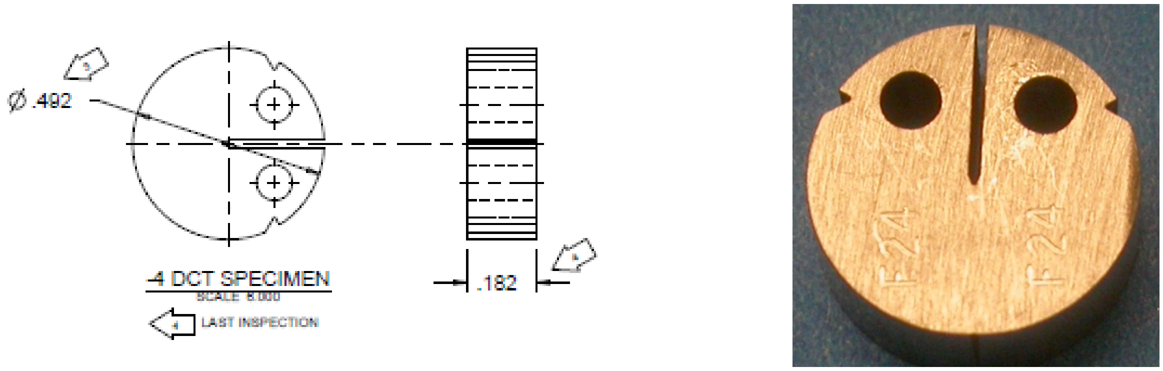

Figure 1. DCT specimen design.

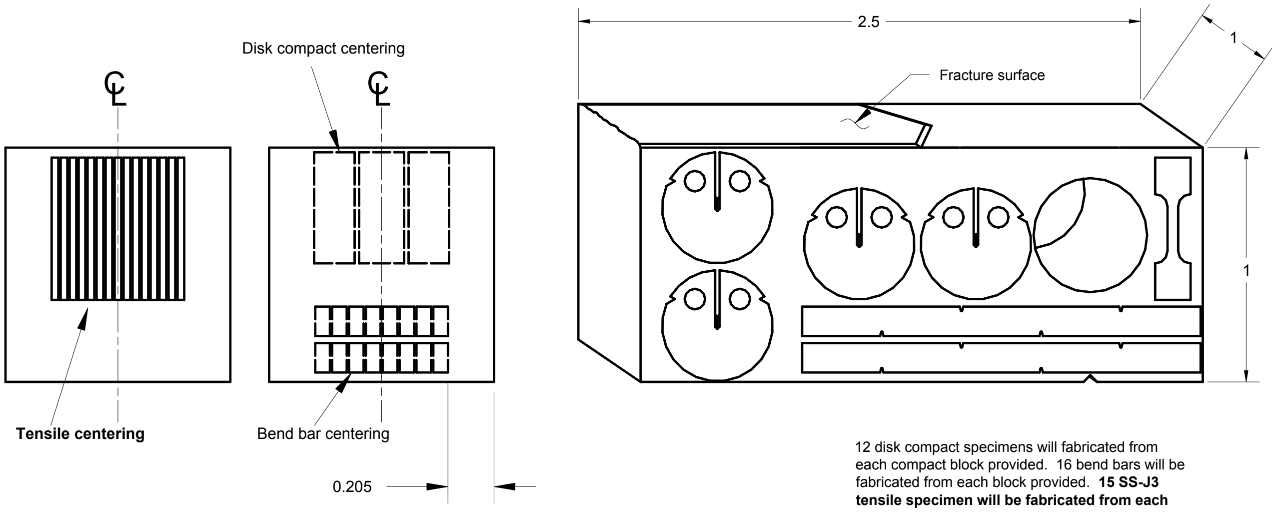

Cutting diagram for fabrication of bend bars, DCT and tensile specimens from a 1T Compact Specimen Half
Drawing number: NMST-071210
Drawn by: Eric Manneschmidt

12 disk compact specimens will fabricated from each compact block provided. 16 bend bars will be fabricated from each block provided. **15 SS-J3 tensile specimen will be fabricated from each block.** (2 blocks provided)

Specimens are to be machined from the center of the block in the orientation shown.

See attached drawing NMST-060810 for bend bars and NMST-090804-1 for disk compact fabrication details.

Figure 2. Cutting diagram for fabrication of bend bars, DCT and tensile specimens.
(Dimensions in inches)

Design Drawings

Table 1 lists design drawings and titles that were developed for the DCT experiment. The experiment consists of a stack of 12 DCT specimens with perforated spacers located between each specimen. Figure 3 shows the inner assembly in the specimen region.

Table 1. Low-temperature DCT experiment design drawings.

Drawing No.	Title
X3E020977A575	SHROUDED TARGET CAPSULE SHROUD TUBE
X3E020977A578	12-DCT LOW TEMPERATURE TARGET CAPSULE
X3E020977A579	12-DCT LOW TEMPERATURE TARGET CAPSULE DCT TOP CAP
X3E020977A580	12-DCT LOW TEMPERATURE TARGET CAPSULE DCT GUIDE PIN
X3E020977A581	12-DCT LOW TEMPERATURE TARGET CAPSULE SPECIMEN ASSEMBLY

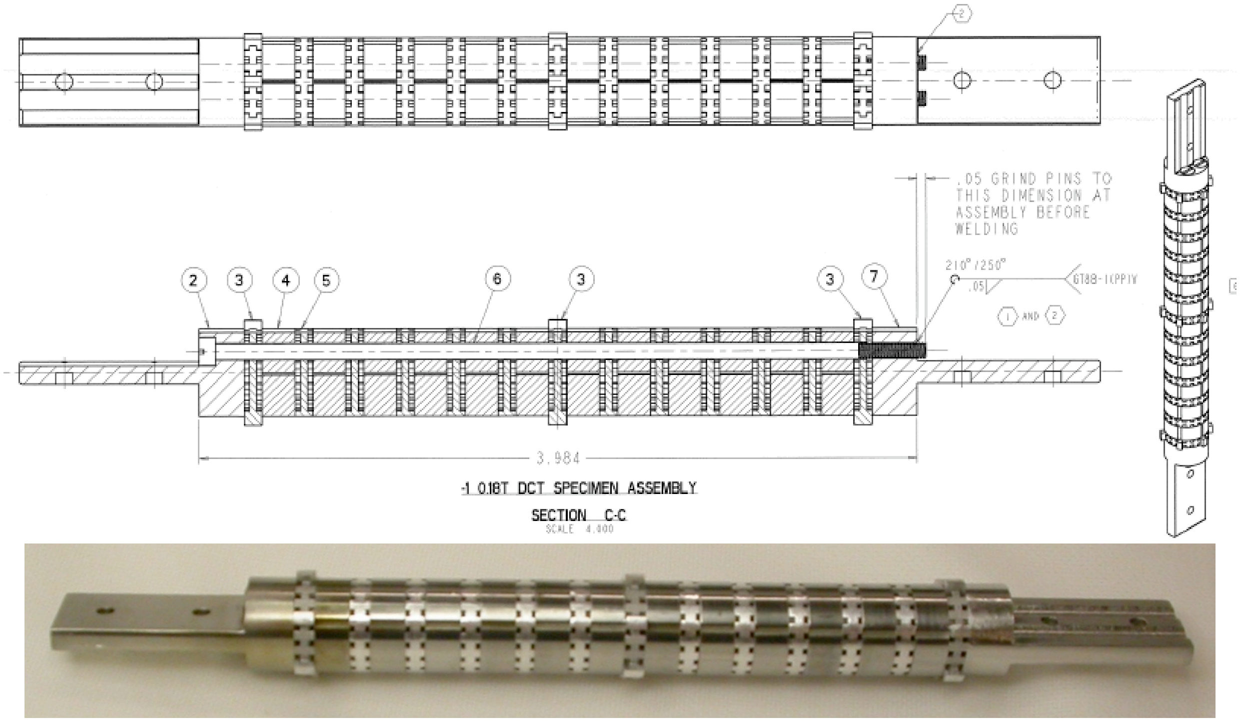

Figure 3. Specimen layout for the DCT experiment.

As shown in Figure 4, there are two types of spacers used in the experiment. The purpose of the primary spacer (right) is to ensure coolant flow to the upper and lower surfaces of the DCT specimens. The secondary spacer (left) has the added function of centering the assembly inside the coolant channel.

Figure 4. Specimen spacers for the DCT experiment.

The assembly is held together by two stainless steel rods that protrude through the matching holes in the DCT specimens and spacers. The connecting rod is sealed to retainers on either end of the specimen stack, and the inner assembly is then pinned to the upper and lower top cap and guide pin. The entire assembly is located inside a shroud tube, which directs coolant flow into the experiment region. Figure 5 demonstrates a partial assembly with just the retainers and connecting rods. Figure 6 shows a similar assembly with the first spacer and specimen installed. Figure 7 shows the entire completed target assembly.

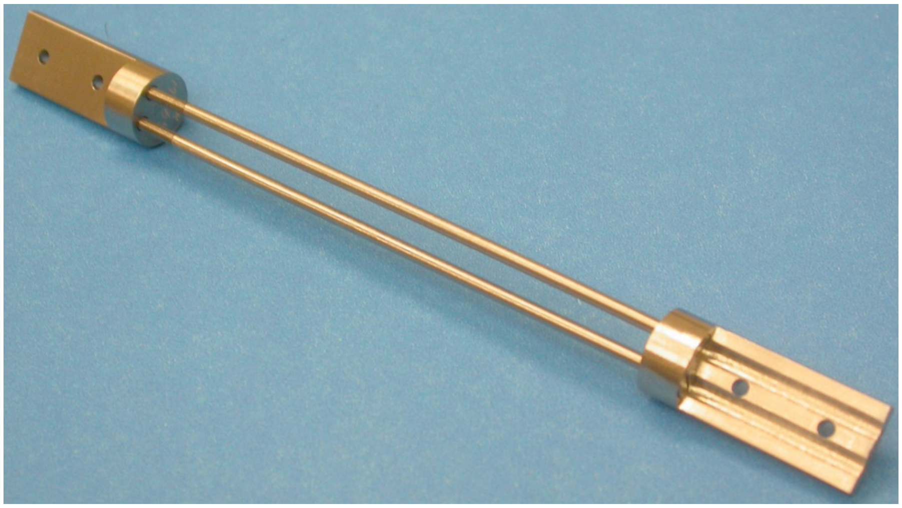

Figure 5. Partial assembly of the retainers and connecting rods.

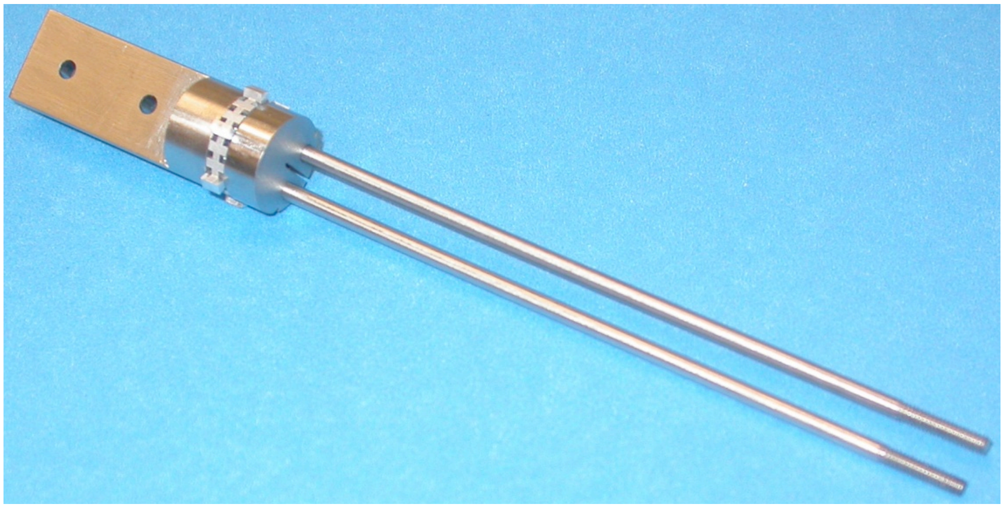

Figure 6. Partial assembly showing the first spacer and specimen.

Figure 7. Completed target assembly before loading into shroud tube.

Materials of Construction

The top cap, guide pin, spacers, and outer shroud are fabricated from aluminum alloy Al6061. Specimens are all F82H or variations of this steel alloy. The end retainers and guide pins are fabricated from 304L stainless steel.

Irradiation Environment

The reactor core, illustrated in Figure 8, consists of two concentric annular fuel regions, each approximately 61 cm in height. The flux trap is ~12.7 cm in diameter and is located inside the inner fuel annulus.

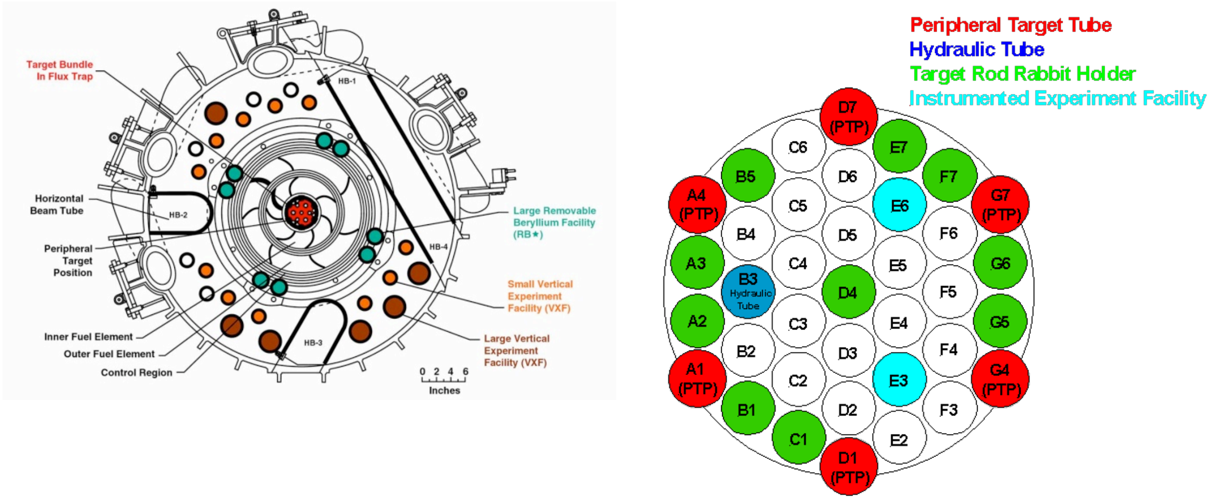

Figure 8. Cross section through HFIR illustrating the primary experimental sites in the reactor as a whole (left) and in the flux trap (right).

The DCT experiment will be located in one of the outer ring positions in the flux trap. Table 2 summarizes the neutron flux characteristics at these locations [3]. The fast fluence is based on a typical 24 day cycle and 7 cycles per year.

Table 2. Neutron Flux Characteristics of the Outer Ring Flux Trap Position

Parameter	**Outer Ring Flux Trap** (Greenwood, June 30, 1999)
Fast flux (10^{14} n/cm²·sec) [E > 1 MeV]	5.5
Fast flux (10^{14} n/cm²·sec) [E > 0.1 MeV]	10.8
Thermal flux (10^{14} n/cm²·sec) [E < 0.5 eV]	20.2
Fast fluence/cycle (10^{21} n/cm²) [E > 0.1 MeV]	2.24
Fast fluence/year (10^{21} n/cm²) [E > 0.1 MeV]	15.7
Axial peaking factor profile[1]	$1 - 1.06 \cdot 10^{-3} \cdot z^2$
dpa/cycle (iron)	1.6

[1] peaking factor is the ratio of the local flux at a distance z from the reactor midplane (in cm) to the flux at the reactor midplane

The design places the 12 DCT specimens in an 8.8 cm region centered at the HFIR midplane. Using the profile from Table 2 gives a peaking factor of $1 - 1.06 \cdot 10^{-3} \cdot (4.4)^2 = 0.98$. Therefore, all specimens in this experiment should receive a relatively constant 1.6 dpa/cycle.

CONCLUSIONS

An experiment has been designed, fabricated and assembled to irradiate DCT specimens of F82H in the flux trap of the HFIR. There are 12 DCT specimens with an outer diameter of 12.5 mm that are exposed directly to HFIR coolant flow. The specimens are separated by perforated spacers to ensure cooling flow on the upper and lower surfaces of the specimens.

REFERENCES

[1] M. A. Sokolov, G. R. Odette, T. Yamamoto, H. Tanigawa and N. Okubo, "Dose Dependence of Fracture Toughness Of F82H Steel," in Fusion Reactor Materials Program, Semi-annual Progress Report, June 30, 2010. DOE/ER- 0313/48 - Volume 48.

[2] T. Yamamoto, G. R. Odette and M. A. Sokolov, "On the Fracture Toughness of Irradiated F82H: Effects of Loss of Constraint and Strain Hardening Capacity," in Fusion Reactor Materials Program, Semi-annual Progress Report, December 31, 2010. DOE/ER-0313/47 - Volume 47.

[3] Greenwood, L. R., "Neutron Dosimetry and Damage Calculations for the HFIR-CTR-62 and 63," Fusion Reactor Materials Program, Semi-annual Progress Report, June 30, 1999. DOE/ER-0313/26 - Volume 26.

8.2 Reseach Plan and Status of High-Dose Rabbit irradiation Experiment for Silicon Carbide Composites

— T. Nozawa, K. Ozawa, H. Tanigawa (Japan Atomic Energy Agency), Y. Katoh, L. L. Snead, and R. E. Stoller (Oak Ridge National Laboratory)

OBJECTIVE

This report provides a brief summary of research plan and present status of the high-dose rabbit irradiation campaign for silicon carbide composites under the JAEA-DOE collaboration on fusion reactor materials.

SUMMARY

In order to examine the high-dose and high-temperature neutron irradiation effects on (1) mechanical properties of SiC, SiC/SiC composites and the fiber/matrix (F/M) interface, and (2) microstructural change of pyrolytic carbon (PyC) as the F/M interphase, new HFIR irradiation experiments were planned. Two types of rabbit capsules were designed: (1) composites' compact flexure rabbits for macro-strength evaluation and (2) mini-composites' rabbits for the F/M interfacial evaluation.

PROGRESS AND STATUS

Introduction

SiC/SiC composites are candidates for the advanced blanket system of a fusion DEMO reactor due to the excellent thermo-mechanical and physical/chemical properties [1-3]. Since these composite's functionalities are readily affected by the F/M interfacial properties, the irradiation stability of the interface needs to be proven for the practical design of the DEMO components. Specifically, understanding the correlation between the strength and microstructure is useful. The key issue is, therefore, to identify the dose-dependent strength of the F/M interface coupled with summarizing the irradiation-induced microstructural changes of SiC and PyC as a combined form of the F/M interface. High-dose irradiation effects data are lacking and specifically needed. Identifying the micro- and macro-strength interaction is another issue to be solved.

The effect of neutron irradiation on the F/M interfacial strength was evaluated by adopting the modified shear-lag model, which gives an interfacial debond shear strength and an interfacial friction stress [4-7]. Up to 10 dpa, they were revealed to slightly decrease by irradiation [4, 5]. The probable explanation for such changes is a decreasing surface roughness produced by the irradiation-enhanced change of the cracking path at the F/M interface from inside the PyC interphase to the fiber surface, although this is still uncertain because of the scarce of data of the irradiation-induced morphology change of the PyC interface. In contrast, at higher doses up to 40 dpa, there was no significant degradation of the bend strength, implying no potential degradation of the F/M interfacial strength [6]. Recent work by the authors has shown good irradiation tolerance of the interface up to 40 dpa for certain conditions [7]. This is somewhat surprising since it has been believed that carbon materials are generally unstable at higher dose irradiation. Therefore, the key mechanism of the good irradiation stability is still unsolved and needs to be identified by further experiments.

DETAILS OF THE TECHNICAL PLAN

Irradiation Matrix

The primary scope of this irradiation campaign is to examine the effects of neutron irradiation at high temperatures (~1000 ºC) and high-doses (~100 dpa). Specifically, the following two domains are to be evaluated: (1) mechanical properties of both monolithic chemical-vapor-deposited (CVD) SiC and "nuclear-grade" SiC/SiC composites and micromechanical properties of the F/M interface and (2) nano-structural change of the F/M interface, for materials such as PyC. This program includes 8 rabbits containing compact composite flexure specimens (hereafter JCR-CF) and 4 rabbits containing mini-composite specimens (hereafter JCR-MC). Table 1 shows the irradiation matrix including the specimen types to be irradiated.

Table 1 – Summary of irradiation conditions planned in high-dose rabbit experiments.

Rabbit ID	Configuration Type	Target Temperature [ºC]	Target Dose [x10^{25} n/m^2 fast]	Materials
JCR11-01	JCR-CF	950±50	10	· Composites for flexure · SiC for thermometry
-02	JCR-CF	950±50	10	
-03	JCR-CF	950±50	30	
-04	JCR-CF	950±50	30	
-05	JCR-CF	950±50	50	
-06	JCR-CF	950±50	50	
-07	JCR-CF	950±50	100	
-08	JCR-CF	950±50	100	
-09	JCR-MC	950±50	4	· Mini-composites for the F/M interfacial tests · SiC for equi-biaxial flexure and thermometry
-10	JCR-MC	950±50	10	
-11	JCR-MC	950±50	30	
-12	JCR-MC	950±50	100	

Materials and Specimens

Materials to be irradiated are summarized in Table 2. Four types of SiC/SiC composites are included for compact flexural tests: (1) P/W Hi-Nicalon Type-S/ PyC/CVI-SiC, (2) S/W Hi-Nicalon Type-S/ML/CVI-SiC, (3) P/W Tyranno-SA3/PyC/CVI-SiC and (4) P/W Tyranno-SA3/ML/CVI-SiC (Hyper-Therm High- Temperature Composites, Inc.); where P/W = plain-weave, S/W = satin-weave, and ML = multilayer. The multilayer interface consists of 150 nm PyC as the inner layer surrounded by 4 sequences of 100 nm SiC and 20 nm PyC. The size of the compact flexural specimen is 25 mm (L) x 2.8 mm (W) x 1 mm (T). At least two representative repeating fabric units are included in width of this rectangular composite specimen. The number of plies in thickness is in most cases five or more. The compact flexural tests after irradiation will use the four-point method with a support span of 20 mm and a loading span of 10 mm at room-temperature.

Table 2 – List of materials for irradiation.

ID	Fiber	Architecture	Interface		# of spec. per capsule	Capsule Type
			Type	e_{PyC} [nm]*		
PW-HS-150	Hi-Nicalon Type-S	P/W	Monolayer	150	5	JCR-CF
SW-HS-ML	Hi-Nicalon Type-S	5H S/W	Multilayer	150	5	
PW-SA-150	Tyranno-SA3	P/W	Monolayer	150	5	
PW-SA-ML	Tyranno-SA3	P/W	Multilayer	150	5	
UD-HS-70	Hi-Nicalon Type-S	UD	Multilayer	70	1	JCR-MC
UD-HS-240	Hi-Nicalon Type-S	UD	Multilayer	240	1	
UD-HS-1150	Hi-Nicalon Type-S	UD	Multilayer	1150	1	
UD-SA-70	Tyranno-SA3	UD	Multilayer	70	1	
UD-SA-230	Tyranno-SA3	UD	Multilayer	230	1	
UD-SA-1000	Tyranno-SA3	UD	Multilayer	1000	1	
UD-Syl-150	Sylramic	UD	Monolayer	150	1	
UD-iBN-0	Sylramic-iBN	UD	None	0	1	
R&H-CVD	-	-	-	-	4	

*e_{PyC}: thickness of the inner PyC interphase adjacent to the fiber

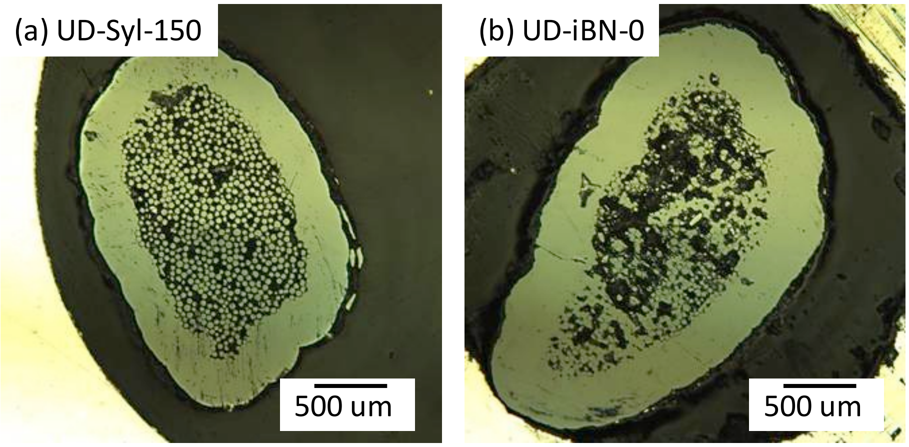

Fig. 1. Typical cross-sectional images of mini-composites: (a) Sylramic/PyC/CVI-SiC and (b) Sylramic- iBN/CVI-SiC.

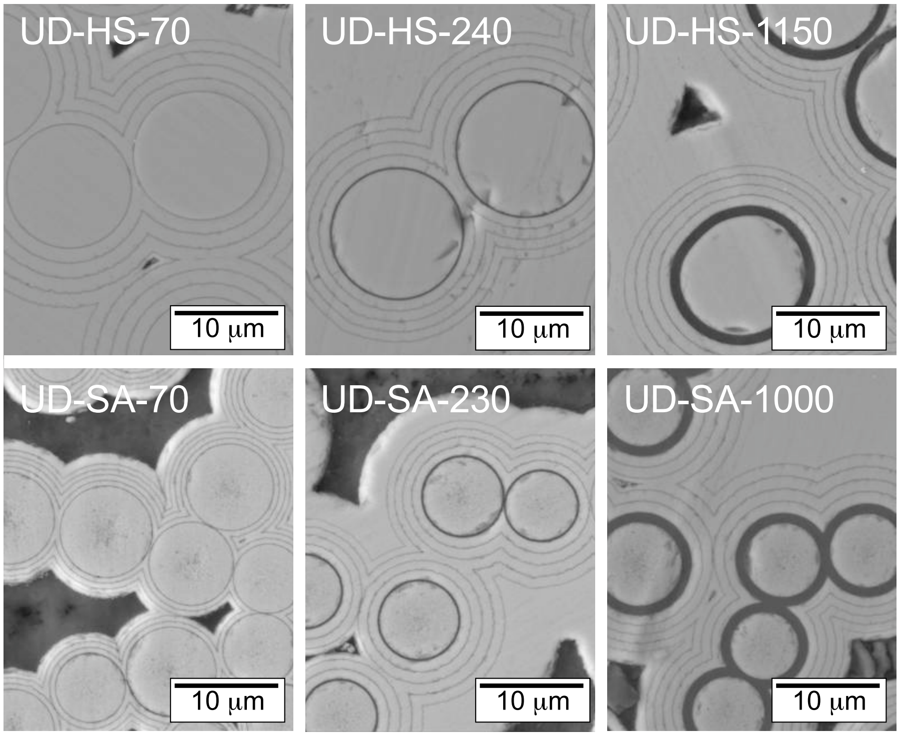

Fig. 2. Typical microstructural images of the F/M interface of mini-composites (UD-HS-70, UD-HS-240, UD-HS-1150, UD-SA-70, UD-SA-230 and UD-SA-1000). No image is presently available for UD-Syl-150 and UD-iBN-0.

Also, eight variations of mini-composites are included to evaluate irradiation tolerance of the F/M interface at high doses and high temperatures (Table 2). The F/M interfacial shear properties and microstructures of PyC will be evaluated by the single fiber push-out test and TEM observation, respectively. Typical cross-sectional images of mini-composites are as shown in Figs. 1 and 2. Thickness of the inner PyC was varied as shown in the table. The subsequent layers are fixed for all types of mini-composites: (1000 nm SiC + 20 nm PyC) x 4 sequences. Fiber volume fractions were approximately 42~50% for UD-Syl-150 and UD-iBN-0 and 5~10 % for the other types. Additionally, a high-resistivity CVD-SiC (Rohm and Haas Co., Ltd., presently The Dow Chemical Company) is used as mechanical test coupons (equi-biaxial flexure) and temperature monitors. A schematic drawing of the equi-biaxial flexural bar is as shown in Fig. 3. This bar has 7 V-shaped grooves on each surface and this can easily be broken into 6 mm x 6 mm pieces. This enables 8 tests from one coupon. A ring-on-ring test with 5 mm support diameter will be used to test these specimens. The experimental details are described elsewhere [8].

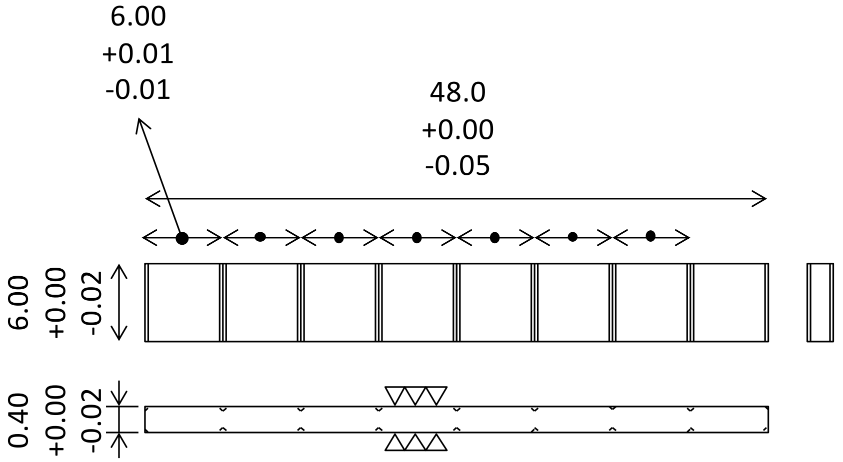

Fig. 3. Schematic drawing of the equi-biaxial flexural specimen (unit in mm).

Irradiation Capsules

The standard rabbit capsule design which has a volume of 6.2 x 6.2 x 50 mm and two bend bars can be stored in the standard employment was employed in this study, with the inner configuration modified to meet our requirements. The capsule was made of molybdenum.

A JCR-CF type capsule contains 20 compact flexural (CF) specimens (= 4 composites' type x 5 each) and 4 CVD-SiC temperature monitor (TM) specimens. The loading configuration is shown in Fig. 4. In this configuration, SiC liners should be used to prevent the specimen surfaces from touching the inner capsule surfaces.

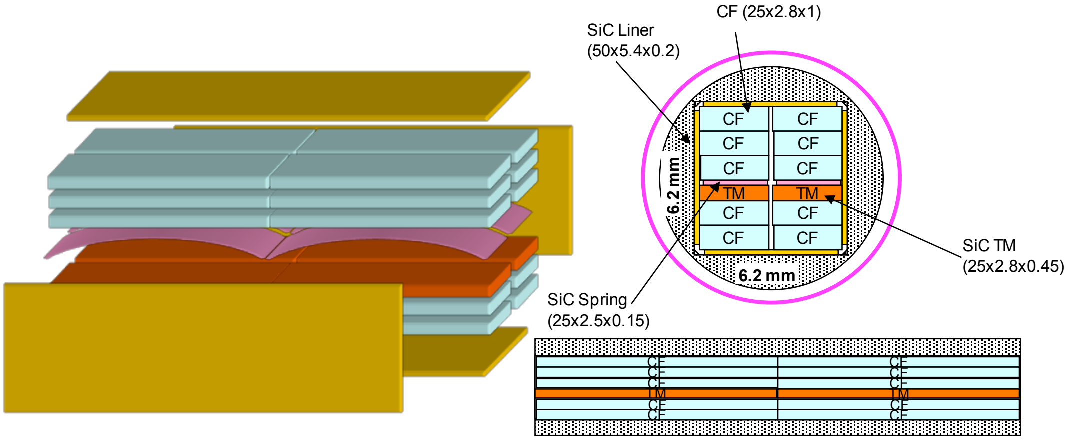

Fig. 4. Schematic drawing of the compact flexure rabbit capsule (unit in mm).

A JCR-MC type capsule contains 8 mini-composite (MC) specimens (= 8 mini-composites' type x 1 each), 4 equi-biaxial flexural (BF) specimens, and 2 CVD-SiC thermometry (TM) specimens.

The loading configuration is shown in Fig. 5. In this configuration, SiC springs (40 x 1.5 x 0.2 mm) will be used to hold mini-composites in place and in good thermal contact. The total number of the MC specimens will be adjusted to fit the available space.

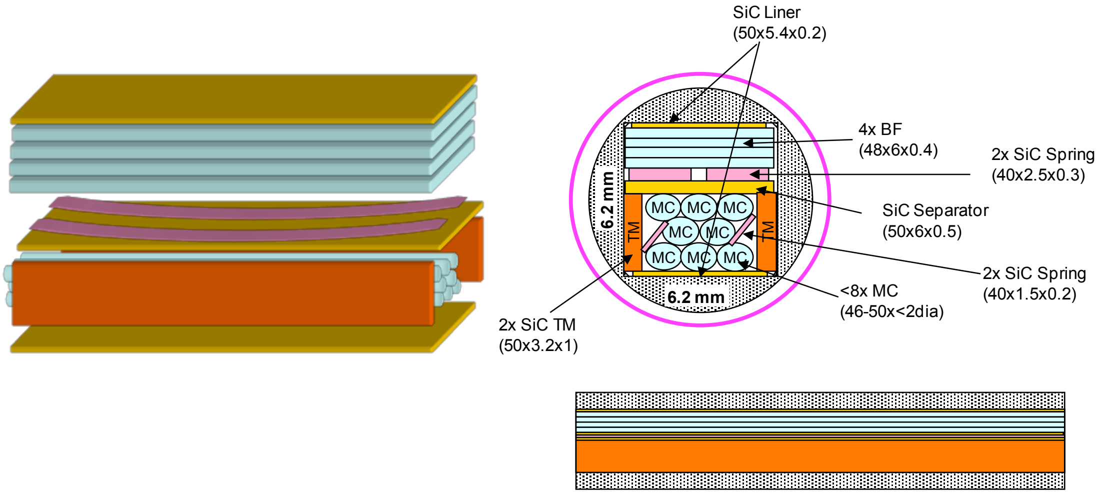

Fig. 5. Schematic drawing of the mini-composite rabbit capsule (unit in mm).

REFERENCES

[1] Y. Katoh, L. L. Snead, C. H. Henager, Jr., A. Hasegawa, A. Kohyama, B. Riccardi, and H. Hegeman, *J. Nucl. Mater.* **367-370** (2007) 659.

[2] T. Nozawa, T. Hinoki, A. Hasegawa, A. Kohyama, Y. Katoh, L. L. Snead. C. H. Henager Jr., and J .B. J. Hegeman, *J. Nucl. Mater.* **386-388** (2009) 622.

[3] L. L. Snead, M. Ferraris, Y. Katoh, R. Shinavski and M. Sawan, “Silicon Carbide Composites as Fusion Power Reactor Structural Materials,” *J. Nucl. Mater.* (2011) in press.

[4] T. Nozawa, Y. Katoh and L.L. Snead, *J. Nucl. Mater.* **384** (2009) 195.

[5] T. Nozawa, Y. Katoh and L. L. Snead, *J. Nucl. Mater.* **367-370** (2007) 685.

[6] Y. Katoh, T. Nozawa, L. L. Snead, K. Ozawa and H. Tanigawa, “Stability of SiC and its Composites at High Neutron Fluence,” *J. Nucl. Mater.* (2011) in press.

[7] T. Nozawa, P. Dou, K. Ozawa, L. L. Snead, H. Bei, Y. Katoh, H. Tanigawa and R. E. Stoller, “Strength and Microstructures of the Fiber/Matrix Interface of Neutron-Irradiated SiC/SiC Composites,” to be submitted to *J. Nucl. Mater.*

[8] S. Kondo, Y. Katoh and L. L. Snead, “Concentric Ring on Ring Test for Unirradiated and Irradiated Miniature SiC Specimens,” *J. Nucl. Mater.* (2011) in press.